GEMS & GEMOLOGY

About the Cover

This issue features a wall chart of inclusions in natural, treated, synthetic, and imitation opal. The platinum pendant shown on the cover features a 9.39 ct black opal accented by 0.25 ct pear-shaped diamond and 0.90 carats of round Paraíba tourmalines. Designed by Niveet Nagpal, courtesy of Omi Privé. The background is a photomicrograph of a black opal from Lightning Ridge, Australia, showing broad, angular flashes of play-of-color known as a harlequin or mosaic pattern. Diffuse reflected light, vertical field of view approximately 12 mm. Photomicrograph by Nathan Renfro.
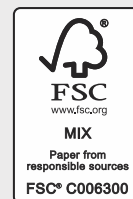
Dive Into Summer: Mozambique Ruby, Madagascar Sapphire, and Black Nephrite From China, Plus an Opal Inclusions Chart

With 2019 already past the halfway mark, we are very pleased to present our Summer edition. Inside you'll find new insights into a variety of gem materials.

The issue leads with a review of the past decade of ruby from Mozambique. Since 2009, Mozambique has become the world's leading supplier of ruby, transforming the market in the process. GIA has been visiting these deposits since the initial discoveries, and now Wim Vertriest and Sudarat Saeseaw from the Bangkok laboratory add a new chapter to this story with an overview of production and distribution, as well as a comprehensive gemological characterization and a discussion of the most common treatment processes applied to material from this important locality.

Next, Billie Hughes from Lotus Gemology and Rosey Perkins with Fura Gems present the results of low-temperature heat treatment experiments on sapphire from Madagascar. Increasing numbers of these stones are being heated to relatively low temperatures (below 1350°C) to lighten their color. The authors show the changes in these goods, providing a means of separating unheated and heated Madagascar sapphire.

> *"Since 2009, Mozambique has become the world's leading supplier of ruby, transforming the market in the process."*

Moving from Africa to Asia, the issue continues with a study of black nephrite from a deposit in southern China. Qian Zhong, a PhD student of mineralogy at Tongji University in Shanghai, leads a team of professors from that university in characterizing 12 nephrite samples from the Guangxi region.

In the fourth article, Jean-Pierre Gauthier from the Gemological Research Center of Nantes and his coauthors characterize "flame structure" in 37 pearls from bivalves of the Tridacnidae family. Careful observation revealed evidence of rotation during growth, a feature also seen in numerous pearls from *Pinctada margaritifera*.

The next article, also on pearls, presents an unusual identification challenge that confronted researchers at the Max Planck Institute for Chemistry, Johannes Gutenberg University, and GIA's New York and Bangkok laboratories. Two pearls were examined by the team of authors, who were unable to positively identify their origin (natural or cultured), their growth environment (freshwater versus saltwater), or the mollusk that produced the pearls.

In our last article, Nathan Renfro and coauthors present an opal inclusions chart, the fifth in their series on micro-features in gemstones. Laminated versions of all of these large, colorful wall charts are also available at store.gia.edu.

Highlights from the Lab Notes column include a rough diamond with a coating of fake green "radiation stains," a study on the separation of kornerupine and prismatine, and the first report of a color-change spessartine garnet examined by GIA. Gem News International features brief but thorough studies on the gemological characteristics of jadeite from the Polar Urals of Russia, more than 800 natural freshwater pearls from the Mississippi River system, and rubies from the Rock Creek deposit in Montana. As always, Micro-World reveals a fascinating gallery of inclusion scenes, while the Diamonds from the Deep section (now a year old) outlines the basic geological and practical features of kimberlites, the earth's diamond delivery system.

We hope you enjoy the Summer 2019 edition of *Gems & Gemology*!

Duncan Pay | Editor-in-Chief | dpay@gia.edu

A Decade of Ruby from Mozambique: A Review

Wim Vertriest and Sudarat Saeseaw

In less than a decade, Mozambique has become the world's most productive source for gem-quality ruby. Since the discovery in 2009, GIA has followed these deposits from the front lines, collecting data in the field and in the laboratory. The development of the deposit in Montepuez has been extremely interesting, with different players involved and different types of material unearthed. This article provides a summary and overview of the current knowledge about Mozambican ruby, including the history of mining and the market impact, as well as a comprehensive gemological characterization and discussion of the most common treatments applied to the stones. Much of the information in this article is based on the authors' observations in the field and market as well as several publications (Pardieu et al., 2009, 2013, 2015; Saeseaw et al., 2018).

Mozambique lies in southeastern Africa, with the city of Maputo as its capital. It shares borders with Tanzania to the north, Malawi and Zambia to the northwest, Zimbabwe to the west, and Swaziland and South Africa to the south. In the east, Mozambique is separated from Madagascar by the Mozambique Channel, which is part of the Indian Ocean. Many of these countries are known producers of gem corundum. Mozambique joined this club of ruby sources only in the last decade, a mere fraction of its long history.

Around 2,000 years ago, Bantu tribes settled in what is now Mozambique. In the eleventh century, traders from the northern shores arrived and set up trading posts. These were mainly Arab, Persian, and Somali merchants who merged their own customs with those of the local Bantu, leading to the development of the Swahili culture along the eastern coast of Africa.

In 1498, Vasco da Gama was the first European to arrive in Mozambique, en route to India. He encountered the Arab merchant ruler Mussa Bin Bique, whose name was given to the area. Vasco da Gama's arrival started the Portuguese influence in the East African country, which lasted until Mozambique gained independence in 1975. This independence sparked a civil war that tore the country apart until the mid-1990s, when its first elections with multiple

parties were held. Since these elections, the country has been relatively stable, although insurgent groups are still active.

The country's population of more than 29 million is largely Christian, with a significant number who follow Islam or traditional animistic beliefs. Portuguese remains the official language, though many

In Brief

- Mozambique entered the ruby market in 2009 and quickly became one of the most important producers on a global level.
- Small-scale artisanal miners and large companies have both played an important role in the rise and development of the Mozambican ruby mines and market.
- The Montepuez deposits produce rubies with different appearances. Two main types can be distinguished: "Maninge Nice"–type and Mugloto-type.
- Mozambican rubies are routinely treated, depending on the starting material. The goal is to improve either the color or the clarity.

people still speak local languages. Since the early 2000s, Mozambique has seen some of the world's largest gains in GDP, but it is still among the poorest and least developed countries. Most of the population and economic power are in the southern provinces.

Mozambique's economy is heavily focused on mineral resources and agriculture. More than 80% of the population is involved in agriculture.

Figure 1. This photo shows a variety of rubies from various areas in northern Mozambique (Niassa and Montepuez) that were mined in 2009–2010. It includes untreated and heated stones, weighing between 1.07 and 4.62 ct. Photo by Robert Weldon/GIA. Courtesy of Tommy Wu, Shire Trading Ltd.

Shrimp, timber, cashews, coconuts, tea, and tobacco are some of the main exports. Tourism is developing rapidly but remains small compared to other industries.

The mining sector includes building stones and granulates (marble and granite), industrial minerals (bentonite and sand), and metallic ores (gold, titanium, beryllium, tantalum, and bauxite). The country is also an important coal producer. Newly discovered offshore gas fields in northern Mozambique are generating considerable interest, though development is hindered by falling prices for oil and natural gas.

HISTORY OF RUBY IN MOZAMBIQUE

Mozambique holds large reserves of gemstones. Aquamarine and morganite are mined in Zambezia Province, while copper-bearing tourmaline is found at the Alto Ligonha field in Nampula Province (Rondeau and Delaunay, 2007; Laurs et al., 2008). Garnets and tourmaline varieties are found throughout the country, though most of the production is focused in the western and northern regions (Shigley et al., 2010; Sangsawong et al., 2016). The area around Ocua in Nampula produced pink spinel for a period in 2016 (Vertriest and Pardieu, 2016).

Early Discoveries. Corundum has been documented in Mozambique ever since Europeans first colonized the land. Although it was not discovered at the time, the presence of gem ruby (see figure 1) was suggested by the high volumes of Cr-bearing corundum (Lächelt, 2004).

The earliest mention of Mozambican ruby in the gemological literature came in 1991, when *Gems & Gemology* reported cabochon-grade rough samples at the Tucson gem shows. It was described as similar to some Tanzanian material (Koivula and Kammerling, 1991).

Ruby from Northwest Mozambique. The first confirmed sources of gem-quality ruby were found in northern Mozambique in the Niassa National Reserve in 2008. Near Ruambeze, in Cabo Delgado Province, cabochon-grade rubies were reportedly discovered in the early 1990s, according to officials from the Lichinga mining office. This deposit reportedly produced the cabochon-grade material reported in *G&G* in 1991. The material was heavily fractured and often contained considerable iron staining, obscuring the bodycolor (figure 2). Mining never really took off in this area due to the remote location and the mediocre quality (Pardieu et al., 2009a,b).

Figure 2. Rubies reportedly from the Ruambeze deposit obtained from a gem dealer in Lichinga. Photo by J.B. Senoble, September 2009.

The first facet-grade ruby was mined near the village of M'sawize, also located in the Niassa National Reserve. Artisanal miners worked a deposit about 40 km east of the village. It is assumed that this deposit was discovered in September 2008, when it began to attract large crowds of artisanal miners and buyers (Pardieu et al., 2009a,b). The deposit was closed to artisanal miners in 2009, but some mining licenses were granted to war veterans who attempted to further develop this deposit (V. Pardieu, pers. comm., 2019). According to some people, rubies from Niassa were already locally known for several years but had been overshadowed by the Winza deposit in Tanzania and Andilamena in Madagascar (Pardieu et al., 2009a,b).

The material ranges from pink to dark red, and faceted stones over 10 carats are produced (figure 3). However, the majority of this material would still require enhancement to solve clarity issues related to the fractures. This could be done by glass filling or flux healing.

Production in M'sawize was mostly abandoned in July and August 2009 due to the onset of the dry season and law enforcement efforts to control the illegal mining operations. Fortunately, another ruby deposit emerged.

Figure 3. Ruby associated with feldspar and amphibole, found at the mining site in M'sawize, November 2009. Photo by Vincent Pardieu/GIA.

Discovery Near Montepuez. In April 2009, rubies were discovered near the city of Montepuez in Cabo Delgado Province. This city is linked to the coastal city of Pemba by Road 242, the main transportation route in Cabo Delgado.

Unlike the other two deposits in northern Mozambique (M'sawize and Ruambeze), Montepuez is not located in a national reserve. This meant that there was potential for legal mining claims and larger-scale development. The initial production seen from the areas around Montepuez was more intensely colored and clearer than the material from Niassa, but its flatter shape resulted in lower yield after cutting.

At the time of the discovery, two deposits were known. The first was near the town of Namahaca, just north of the main road, where lower-quality material was found. The other was about 8 km southeast of the town of Namahumbire. This deposit yielded higher-quality ruby, with more facet-grade material available (Pardieu and Chauviré, 2012).

It is estimated that thousands of people started working this deposit in June or July 2009 without proper permits. Most of the miners were based out of the local villages. So were the "bush traders" who serve as middlemen between the miners and international buyers. These foreign buyers, located in Montepuez or Pemba, are mostly Thai, Tanzanian, and West African and have experience in the colored gemstone trade (Pardieu et al., 2013; Hsu et al., 2014).

This activity created new concerns for the government, though it was reluctant to take strong (and unpopular) measures since elections were coming up later that year. By November 2009, the artisanal mining situation had stabilized. The government had decided that artisanal, unlicensed mining would be tolerated in the area around Namahaca ("Areas Designadas"). The company that owned hunting rights on the ruby-bearing land (Mwiriti Limitada) was the first one to acquire several official mining licenses around Namahumbire (Pardieu et al., 2009a,b).

By 2010, material from the Montepuez deposit was widely available in the Asian market in all quality ranges. Fine untreated faceted stones were sold, as well as low-grade glass-filled cabochons and all qualities in between. Mwiriti officially had the mining license near Namahumbire but was unable to control and exploit the deposit at this stage. All of the production that reached the market in this period was taken out of the ground by artisanal miners known as *garimpeiros*, whose numbers kept grow-

Figure 4. Map indicating the main ruby mining areas around Montepuez.

ing. It is estimated that by the end of 2010, tens of thousands of them were working the ruby deposits around Montepuez (Pardieu et al., 2013).

With the rapid influx of miners, the working area was expanded and numerous other places with ruby were discovered in the following years. The most important ruby mining areas (figure 4) during this early period were:

- Maninge Nice (discovered in 2009): This area probably relates to the original Namahumbire discovery and translates to "good quality." Nova Mina and Central were often described as separate deposits in the older literature, but they are most likely a part of what is now considered Maninge Nice. This is a primary deposit, associated with an immature secondary deposit.
- Glass (2010): This area is named after the glass-like appearance of the finest stones found here. The deposit is very close to Maninge Nice, and the rubies share many similarities, but Glass is clearly a more mature secondary deposit with rounded rough rubies.
- Nacaca (2012): This secondary deposit is about 25 km southeast of Namahumbire, and a variety of material is found here. This area is east and downstream of all the other deposits.
- Ntorro (2012) and Mugloto (2014): This mature secondary deposit produces a lower volume than the others, but the rubies are of much higher quality.

Maninge Nice, Glass, and Mugloto-Ntorro are all located in the concession held by Mwiriti. Most of the Nacaca deposit is outside of the concession and

has been allocated to artisanal miners as Areas Designadas, similar to the area around Namahaca.

In June 2011, Mwiriti (25%) signed a joint venture agreement with Gemfields (75%), and Montepuez Ruby Mining (MRM) was formed to exploit the deposits near Namahumbire. After a year of mine development, MRM took its first rubies out of the ground in late 2012 (Lucas and Pardieu, 2014). The establishment of MRM drastically changed the dynamics of the Montepuez deposit. Unlicensed miners were restricted to certain areas while MRM developed the concession at an industrial scale. The large-scale development of MRM attracted other investors, and in 2016 several other mining groups started showing interest in the ruby deposits around Montepuez. The second company to commercially produce rubies was Mustang Resources, which worked on ruby mining concessions west and northwest of Namahumbire around the village of Napula (Lucas and Hsu, 2017; Pardieu, 2017). In late 2017, the newly formed Fura Gems acquired several exploration licenses north of Namahumbire. In mid-2018, Mustang Resources and Fura Gems merged their ruby assets, which are now handled by Fura.

Although the lion's share of ruby-bearing land is officially under control of large groups that obtained the legal mining/exploitation rights, unlicensed artisanal miners are still prevalent. The areas are simply too large to secure entirely. This has led to conflicts between private security forces, police forces, and artisanal miners (Hsu et al., 2014). Journalists have made claims of human rights abuses, both by police forces and private security firms, since 2015, most notably in a television documentary produced by Al Jazeera (Valoi and Macrae, 2015). In January 2019, Gemfields paid US$7.8 million to settle human rights abuses brought against it by the local community (Gemfields, 2019).

Over the years, a delicate balance was struck between the unlicensed miners and the license owners with regard to the ruby-bearing grounds. Although the mining rights belong to the license holder, unlicensed miners are often tolerated on parts of the concession. For example, Ntorro and Glass were worked by garimpeiros for years before the license owner started developing large-scale mining operations at these deposits.

At the time of this writing, there are two major players in the Montepuez ruby mining area: MRM and the artisanal mining community. The artisanal mining community around Montepuez has faced many challenges since the rubies were first discovered. For a while, they were able to work in the Areas Designadas around Namahaca and Nacaca, but these areas were later incorporated into larger mining licenses. Mining without a license was also not considered a major criminal offense until February 2016, which meant that garimpeiros who were caught could not be prosecuted. Mining without a license is now punishable by law, and the miners face considerable jail time and fines if caught (Vertriest and Pardieu, 2016). These factors, combined with the more established security of larger companies, have caused the supply from garimpeiros to drop considerably. In the early days (pre-2014), they accounted for nearly 100% of Mozambican ruby production; now it is far less.

It is important to note that only companies with a mining license are allowed to export gemstones out of Mozambique. This means that all rubies on the market that were mined by unlicensed miners left the country illegally.

MOZAMBIQUE RUBIES IN THE MARKET

Mozambican Ruby Trading. The first material from the Niassa deposits came to the international market through Tanzania. Before the discovery of Mozambican ruby, many buyers on the African mainland were based in Tanzania and Kenya. These international merchants had cash available and were knowledgeable about exporting procedures, so they were the first to see new goods. Since the initial material from Niassa was not of the highest grade, few merchants felt the need to pay attention to Mozambique. However, when the supply from Winza, Tanzania, began to decline, buyers started looking for other sources of ruby (Pardieu et al., 2009a,b).

By late 2009, the Montepuez deposit was starting to reveal its potential, and many merchants moved to Mozambique to establish a presence in Pemba or Montepuez. While the color of the material was very desirable, it often required treatment such as glass filling or heating with flux to address the abundant fractures. The Thai trading centers have a wealth of experience in enhancing ruby, with regard to both color (heat treatment is often required to optimize Thai and Cambodian ruby) and clarity (heating with flux to heal fractures, often done on Mong Hsu rubies, and glass filling, perfected on low-grade rubies from Madagascar). So nearly all production went to Thailand to be treated, cut, and sold in the trading centers of Bangkok and Chanthaburi. By the end of 2009, Mozambican ruby was flooding the Thai market.

In 2012, an important discovery was made in the Montepuez mining area, when rubies with a different

appearance were found. This was in an area called Ntorro. These stones had a more orangy bodycolor than the early Montepuez production, with subtle bluish color zones, bulky shapes, and a cleaner appearance overall. Furthermore, these rubies did not have abundant fractures and did not require clarity enhancement by heating with flux or glass filling. They do benefit from heat treatment to optimize the color, an area in which the Sri Lankans have great experience. Since the discovery of this type of material, Sri Lankan traders have also started buying material in the local market.

Mugloto-Ntorro produces a much lower volume than the others, but the value is much higher. This area has produced many important stones, including some of the most famous Mozambican rubies sold to date: the Dragon Eye rubies, the Rhino ruby, and the Rose of Mozambique.

In June 2014, Gemfields hosted the first auction of rough ruby from its mine near Montepuez (Lucas and Pardieu, 2014). This event, held in Singapore, represented the first legitimate public sale of Mozambican ruby since its discovery. The sale presented material from the Mugloto and Maninge Nice areas within MRM's concession. Some of the material was disclosed as treated, but the majority was guaranteed to be untreated. At the inaugural auction, 2.03 million carats were offered, of which 1.82 million carats were sold.

The material at these auctions is put in pregraded lots, where goods of similar quality and color are offered together (Shor and Weldon, 2015). The impact of Mozambican ruby became very clear when a well-known dealer said, "Before the Mozambique discovery, it would take several years to collect a full suite of color-matched rubies of equivalent quality. Now I can buy a full suite, and in six months a new one will be auctioned."

So far Gemfields has organized 12 ruby auctions, which have generated over US$500 million in revenue for nearly 10 million carats of rough ruby.

In October 2017, Mustang Resources held an auction in Mauritius that offered 22 lots of ruby and pink sapphire. Only eight of the lots were sold, generating US$550,000 (Pardieu, 2018). After the auction, they started selling the material through a sales office in Thailand ("Mustang Resources realizes maiden ruby sales…," 2018).

Apart from these auctions and some private sales by the mining companies, most of Mozambique's rubies have reached the market through unlicensed channels.

Presence in the Market. For centuries, the world's ruby supply was dominated by two sources: modern-day Sri Lanka and Myanmar (specifically Mogok). From the late 1800s until the 1990s, the border area of what is now Thailand and Cambodia also produced high-quality gems, although this deposit only became dominant in the 1960s, when the Burmese regime closed itself, and its ruby resources, from the rest of the world. Other historical sources such as Afghanistan have never produced comparable volumes or qualities.

Only in the last decades have other competitive sources appeared. These often showed great potential but lacked the volume (e.g., Winza, Morogoro, Vatomandry, or Luc Yen) or the facet-grade quality (e.g., Mangare) to cause a major shift in the global ruby trade. The most important new deposit in this period was Mong Hsu, Myanmar. This was the major source for rubies in terms of volume since its discovery in the early 1990s until the emergence of the Montepuez deposit (Hughes et al., 2017).

The Montepuez deposit has made ruby more accessible than ever before. Mozambique has joined an elite club of ruby producers and impacted the gemstone trade in ways never imagined before (Hughes, 2015). Mozambique offers everything from huge unheated stones with top color to sub-millimeter pinkish treated melee. This has increased the availability of ruby in all quality ranges and sizes.

We have to remember that gemstones are not perishable goods, and almost every stone that has entered the trade is still out there. A deposit such as Mogok has more than a thousand years' head start, yet nowadays the booths in major tradeshows offer the same volume of Burmese and Mozambican gems. The balance even shifts toward Mozambique.

GEOLOGY

The geology of northern Mozambique is very complex and not well understood. The area is sparsely inhabited, and very few geologic surveys have ever been carried out.

The large-scale geology is dominated by features related to the East African orogeny. The most important structure is the Mozambique Belt, a suture zone that developed during the formation of the Gondwana supercontinent. Currently it stretches from central Mozambique up into the Arabian Peninsula. Most of the islands in the Indian Ocean (including Madagascar and Sri Lanka) as well as parts of southern India and eastern Antarctica also belong to the Mozambique Belt. Though now exposed at the surface, it was once covered by more than 10 km of

rocks, which caused it to reach high temperatures and subjected it to large pressures (Lächelt, 2004; Grantham et al., 2008; Bingen et al., 2009).

The primary ruby deposits are hosted in the Montepuez complex. This wedge-shaped group of rocks deformed at high metamorphic conditions. Its main rock types are orthogneisses with various compositions (granitic to amphibolitic) and paragneisses including quartzite, meta-arkose, marble, and biotite gneiss. The age of these rocks is Meso- to Neoproterozoic (1.6–1.1 Ga). Numerous younger intrusions of granite, granodiorite, and tonalite can be found throughout the complex (Boyd et al., 2010).

During different orogenic phases, the Montepuez complex has been subjected to intense tectonism, resulting in a very complex structural framework. The rock units are tightly folded and cut by several shear zones that mainly trend northeast to southwest. This took place during the Mozambican orogeny (1100–850 Ma) and the East African orogeny (800–650 Ma). Another tectonic event altered these rocks around 538 Ma, when thrust faults, folds, and shear zones developed as a part of Pan-African mountain-building processes (Lächelt, 2004).

The geology on a more local scale is not well known, since outcrops are very scarce. Most of the bedrock is covered by up to 20 meters of soil. Due to the climate in northern Mozambique, rocks weather very quickly, and thus the top layers of the bedrock are intensely altered. This makes it very challenging to study the geology in outcrops or even in shallow drill holes.

Based on observations during field visits, the ruby mineralization is closely related to rocks rich in amphibole, mica, and feldspar. This is the reason we classify the Montepuez ruby find as an amphibole-related deposit (Hsu et al., 2014). Other studies mention the presence of kyanite and siderite associated with the amphibole-rich host rock of the rubies (Hänni and Krzemnicki, 2009).

DEPOSITS

Rubies are found in two types of environments around Montepuez: primary and secondary. The secondary deposits consist of more concentrated layers of gravel in which the host rock has been broken down and the more resistant material has been concentrated. There are several ways this could have happened: (1) the host rock weathered and the remaining stones were not transported (eluvial deposit); (2) the stones were transported by mass movement (colluvial); or (3) the stones were transported by water (alluvial). The earliest interpretations stated that the large secondary deposits in Mugloto-Ntorro were alluvial and caused by some sort of flash flood that was later reworked by river systems (Chapin et al., 2014; Hsu et al., 2014). However, field observations by the author and by one of the leading authorities on geological exploration in East Africa (Simonet, 2018) do not match this theory. In an alluvial system, rounded pebbles, well-sorted sediments, and various grain sizes would be found. The secondary deposits near Montepuez are unsorted and form one continuous layer of gravel that has sharp boundaries (figure 5). According to Simonet,

Figure 5. At the Mugloto pit, operated by MRM, a gravel layer containing rubies and quartz boulders in the secondary deposits is clearly visible. A tunnel that was supported by wooden structures is an indication that artisanal miners used to work in this area. Photo by Wim Vertriest.

this is consistent with the "weathering down" of rock masses. During this process, the rocks weather and erosion products get carried away. The most resistant material (garnet, corundum, and quartz boulders) is left behind and ultimately concentrated in one layer. This material has not been significantly transported by rivers or any other means.

Smaller-scale alluvial deposits are also present around Montepuez, where rivers and creeks have carried material of the different ruby-hosting rocks and dropped them in recent river sediments.

Primary deposits are those in which ruby is still found in its original host rock. In the case of the Mozambican ruby deposits, the original host rock is so strongly weathered as to be nearly unrecognizable. Most of the minerals are turned to clays and other alteration products. People working in the mine describe the host rock as "rotten" (figure 6). The primary deposit of Maninge Nice is overlain by a secondary deposit derived from it. This higher-grade deposit was probably the first discovered in Montepuez.

Because the primary deposits are so weathered, they are in a way easier to mine than the secondary deposits. This is counterintuitive, since we associate primary deposits with hard rock mining, tunnels, and blasting. However, the rock has been turned to clay, which is considerably easier to mine when it is dry. Pieces of dried clay can be crumbled between your fingers, turning everything except the rubies to dust. This makes excavation with excavators very simple, as opposed to the secondary deposits where large

Figure 6. The primary deposit in Maninge Nice contains extremely weathered amphibole-rich rock in which rubies are literally falling out of their host rock. Photo by Wim Vertriest.

quartz boulders make excavation more difficult. The situation reverses during the intense rainy seasons, with the clay turning into a sticky mass. Even the heaviest equipment cannot combat such conditions, and thus mining of the primary deposit only takes place for half of the year.

MINING

Artisanal miners usually work with very simple tools. Using shovels and picks, they dig into the earth to reach the gravel layers in the large secondary deposits (figure 7). Sometimes they support their shafts

Figure 7. A group of garimpeiros at their workings in the bush near Montepuez. Photo by Vincent Pardieu/ GIA, September 2014.

Figure 8. Large-scale mining in the Mugloto area. Photo by Wim Vertriest, July 2016.

and short tunnels with wooden structures, but in most cases they do not. Ruby-bearing gravel is taken from these pits and transported to a washing place. Using simple instruments such as washing pans or crude grids, they screen the material for rubies. In the early years of the deposits' development, several accidents happened due to poor mining conditions in artisanal workings. In the last three to four years, the number of garimpeiros has decreased and there have been fewer reports of accidents.

A similar process is followed at other alluvial deposits where rubies are found in recent gravels, often reaching the surface. This requires less work since no pit needs to be dug, but the ruby concentration is often a bit lower. These mining sites tend to be much smaller and localized, diminishing the chances of finding high-quality ruby.

The large-scale operations by major companies use industrial setups with excavators and dump trucks to move overburden and ruby-rich gravel. They build up a stockpile, mining material they can process later. This is because the rainy season makes it very difficult to extract the gravel for about half the year. The washing operations run year-round, using different techniques (figure 8).

Gemfields has opted for a series of screens and gravitational jigs to sort and concentrate the ruby. Mustang worked with rotary pans, where minerals are also concentrated based on their density. In 2017, Gemfields added dense media separation (DMS) techniques to pre-concentrate the gravels and optimize the efficiency of their jigs (Pardieu, 2017).

These techniques all require large amounts of water, so serious investments have been made to guarantee clean water supply, either in the form of artificial lakes, water treatment plants, or a combination of both.

The large companies also have extensive exploration programs that use a combination of core drilling, auger drilling, and geophysical analysis to determine the extent of ruby-bearing areas (Hsu et al., 2014).

GEMOLOGICAL ANALYSIS

Standard Gemological Properties and Appearance. Mozambican rubies generally have purplish red to red colors; some stones have an orange tint. Color intensities cover the spectrum from pale pink sapphires to deep red rubies. Standard gemological properties are consistent with gem corundum: a refractive index between 1.760 and 1.768 (+/– 0.001), a birefringence of 0.008–0.009, and a specific gravity average of 3.98–4.00. Fluorescence can be strong to medium red under long-wave UV radiation and medium to weak red under short-wave UV.

Based on their appearance, we can classify Mozambique's rubies in two major types. These types are named after the locality where they are most dominant, but they are by no means exclusive to these areas. Some Mozambican rubies share characteristics of both types, but these are considered rare.

The first type is named after Maninge Nice (figure 9). This material represents the first rubies mined around Montepuez in 2009. They show a strong flu-

Figure 9. Typical Maninge Nice–type rubies with a deep red color and strong UV reaction. Their flat hexagonal shape is typical of stones from a primary deposit. The coin shown as a reference has a diameter of 25 mm. Photo by Vincent Pardieu/GIA.

Figure 10. Typical Mugloto-type rubies with a nice red color. The blocky shapes are typical of a secondary deposit. These stones weigh around 1 gram each. Photo by Vincent Pardieu/GIA.

orescence reaction to long-wave UV exposure and have a variable color intensity ranging from pink to deep red. They tend to be associated with primary deposits. This means that the flat hexagonal crystal shape is often preserved.

The second type is called Mugloto (figure 10) and has been mined since 2012. The first Mugloto-type material was mined in Ntorro by artisanal miners, but since its discovery and large-scale exploitation in 2014, the nearby Mugloto area has been the main source for this type of material. Its fluorescence reaction to UV exposure is weaker, and its bodycolor appears to have a subtle orangy tint. Some Mugloto-type stones have bluish color zones. The material often has a bulkier shape since it is only found in weathered deposits.

Microscopic Observations. The most common inclusions are particles (McClure and Koivula, 2009; Pardieu et al., 2009a,b; Hänni and Krzemnicki, 2009; Pardieu et al., 2013, 2015; Saeseaw et al., 2018). In many cases, these oriented needles and particles appear in bands following the corundum growth structure (figure 11). These full hexagonal outlines are commonly seen in Maninge Nice–type rubies. Mugloto-type rubies seldom show the full hexagonal outline but often have straight or angular bands of particles.

Particles can have various shapes, but irregular and arrowhead forms are often seen. Finer particles and platelets can be challenging to observe without fiber-optic illumination under the correct angle (figures 12–14). Some of the needles and smaller particles are similar to rutile particles frequently found in

Figure 11. Bands of silk, often visible in a hexagonal configuration at 120° angles, are a common inclusion in Mozambican rubies. Photo by C. Khowpong; field of view 2.50 mm. Fiber-optic illumination.

Figure 12. Reflective particles and platelets are very common but take some practice to observe with a fiber-optic light. Photo by B. Kongsomart; field of view 1.35 mm. Fiber-optic illumination.

Figure 13. A Mozambican ruby appears clean when viewed in brightfield illumination. Photo by GIA; field of view 12.3 mm.

Figure 14. The ruby from figure 13 shows a variety of particles and platelets when a fiber-optic light is shined through it at the correct angle. Photo by GIA; field of view 12.3 mm.

other rubies, but the nature of the finer platelets is still unclear. Tubes, associated with twin planes, are also frequently observed (figure 15) (GIT Gem Testing Laboratory, 2009; Pardieu et al., 2013).

A variety of mineral inclusions are observed in Mozambican rubies. Rounded greenish amphibole crystals are often found in sub-spherical shapes (figure 16) but can be seen as elongated rods (figure 17). Pseudohexagonal mica platelets (figures 18 and 19) appear frosty and are often associated with fringes, indicating an alteration of the mica during the geological history of the ruby. Around these crystals, a planar feature of flat fluid "rosette" inclusions is

often seen. Opaque cubic crystals are common in rough crystals but not in faceted stones because they contrast very strongly with the reddish background color of the rubies (figure 20). On top of that, these black inclusions react very poorly to heat treatment, even at lower temperatures. These crystals have been identified as chalcopyrite (Pardieu et al., 2013).

Both types of Mozambican ruby have the same inclusions, but their abundance varies. We noticed that Mugloto rubies somehow contained fewer mineral crystals than rubies from Maninge Nice. Maninge

Figure 16. These two greenish amphibole crystals, identified by Raman spectroscopy, represent the most common crystal inclusion in Mozambican ruby. The smallest shows the typical rounded, elongated shape, while the larger crystal has a more irregular shape. Photo by C. Khowpong; field of view 1.42 mm. Brightfield illumination.

Figure 15. Intersecting tubes associated with twin planes are frequently seen in Mozambican rubies. Photo by Jonathan Muyal; field of view 2.65 mm. Darkfield illumination.

Figure 17. In some cases, amphibole occurs as elongated rod-like crystals. Photo by C. Khowpong; field of view 1.41 mm. Darkfield illumination.
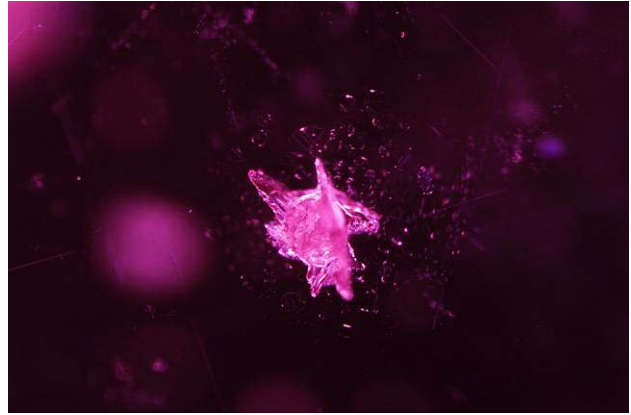
Figure 18. Pseudohexagonal mica with fringes (small expansion fractures) and a rosette pattern are a common sight in Mozambican rubies. Photo by C. Khowpong; field of view 1.12 mm. Darkfield illumination.

Nice rubies also have more fractures, which can be explained by their occurrence in a primary or near-primary deposit.

FTIR and UV-Vis-NIR spectroscopic analyses and LA-ICP-MS chemical analyses were done at GIA laboratories following GIA's internal procedures. These methodologies are outlined in full detail in Saeseaw et al. (2018).

Infrared Spectroscopy. Infrared spectroscopy analyzes the absorption in the infrared spectrum by a gem. Most instruments measure a range from 7500 to 370 cm^{-1}, but most useful is the functional group from 4000 to 1000 cm^{-1}.

This technique is best known from emerald analysis, where Fourier-transform infrared (FTIR) spectroscopy is used to identify fracture-filling material. In corundum, it can provide indications of heat treatment (Smith, 1995; Hughes et al., 2017). Very often FTIR spectra of untreated rubies show the presence of other mineral contaminants lining fractures or twin planes. Other peaks in the spectrum are commonly related to the presence of OH groups in the corundum lattice (Beran and Rossman, 2006).

Figure 19. A cluster of crystals following the hexagonal growth pattern of corundum is observed at the core of this ruby. Photo by C. Khowpong; field of view 2.85 mm. Darkfield illumination.

Figure 20. Opaque black-red crystals, presumably chalcopyrite, are common in rough rubies from Montepuez. They are rarer in finished stones because of their high contrast with the host material. Photo by C. Khowpong; field of view 1.00 mm. Fiber-optic illumination.
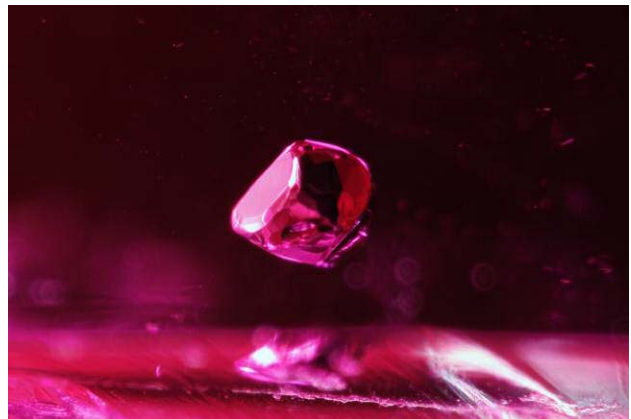
TABLE 1. FTIR spectrum types most commonly encountered in Mozambican rubies.

Number of samples	Spectrum A	Spectrum B	Spectrum C	Spectrum D	Other minerals	Total
Mugloto-type	97	17	42	17	2	175
Maninge Nice–type	55	9	19	6	16	105

Most FTIR spectra from Mozambican rubies can be grouped in one of four categories (table 1 and figure 21):

- Spectrum A is characterized by a single peak at 3309 cm⁻¹.
- Spectrum B shows the presence of boehmite, an aluminum oxide hydroxide, through a group of distinct bands in the 3600–2500 cm⁻¹ region.
- Spectrum C shows the presence of the clay mineral kaolinite, characterized by absorption peaks at ~3695, 3650, and 3620 cm⁻¹.
- Spectrum D has a peak at ~3161 cm⁻¹, accompanied by peaks at 3240 and 2420 cm⁻¹.

In some cases, these four patterns are obscured by peaks related to other mineral inclusion species. These are more common in Maninge Nice–type rubies.

Figure 21. Four different FTIR spectrum types seen in Mozambique rubies.
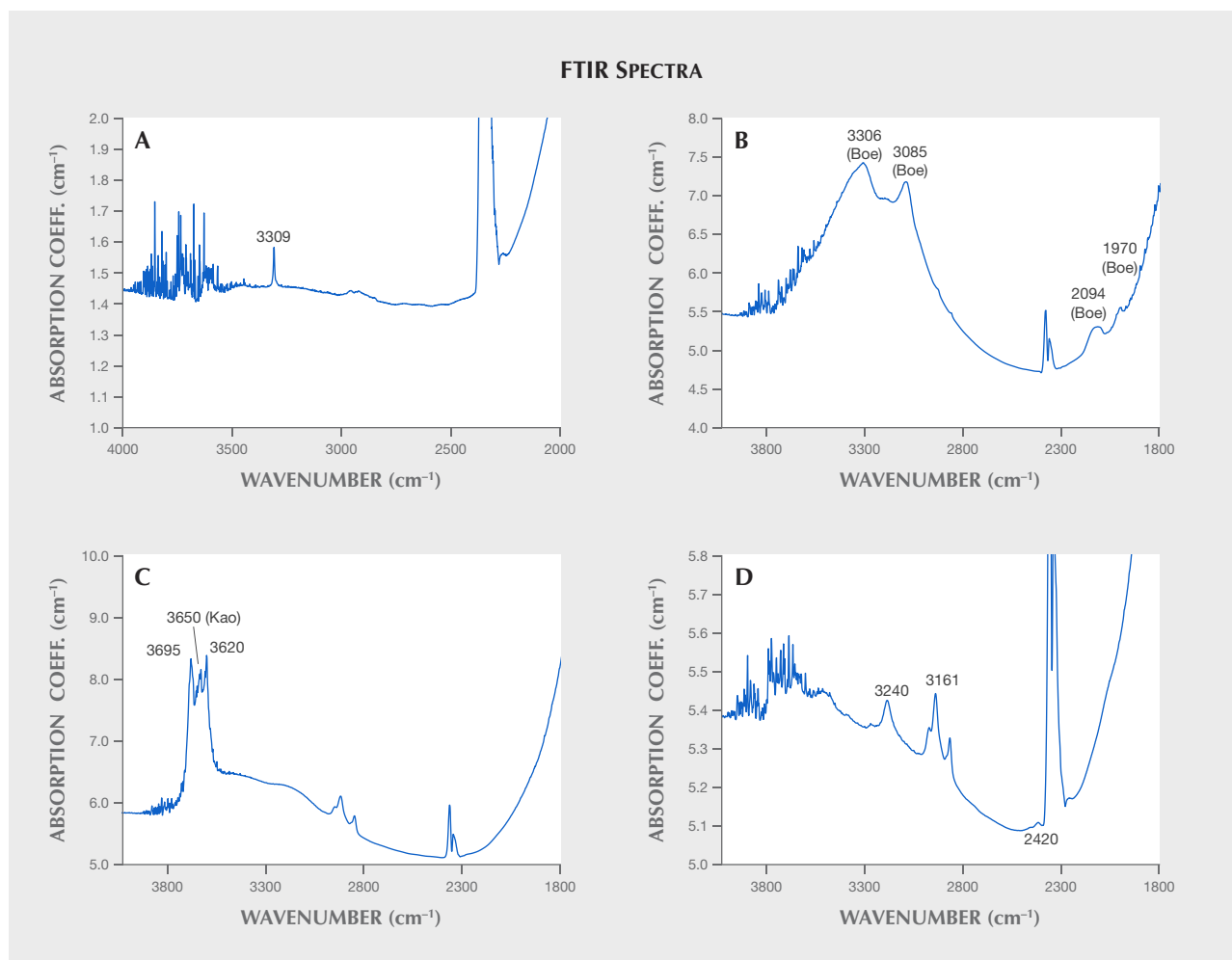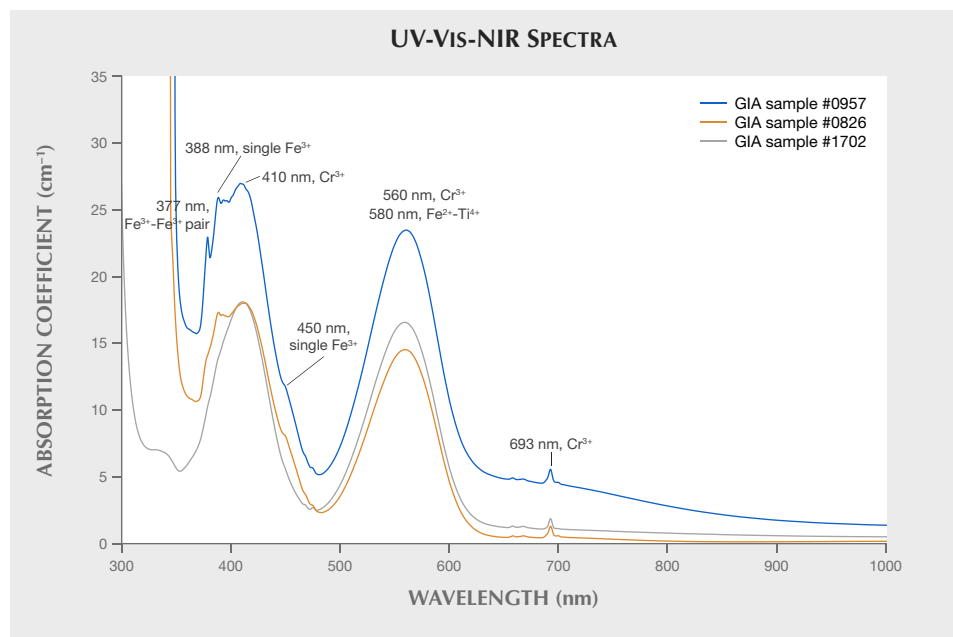
UV-Vis-NIR Spectra

Figure 22. Comparison of ordinary UV-Vis-NIR spectra from GIA samples 1702 (1.163 mm, Maninge Nice–type), 0826 (2.808 mm, Mugloto-type), and 0957 (1.960 mm, Mugloto-type).

UV-Vis-NIR Spectroscopy. Based on the different appearances of the two ruby types from Mozambique, a difference in their UV-Vis-NIR spectra is expected. To study these spectra, three samples were fabricated with windows perpendicular to the c-axis (see table 2). All the spectra are dominated by absorption due to chromium, characterized by bands around 410 and 560 nm (figure 22).

Maninge Nice sample no. 1702 shows a low shoulder at 330 nm, which is believed to be caused by pairs of trivalent iron. The Mugloto sample (no. 0826) also has this feature, but it is much stronger, so much so that it does not appear as a shoulder but as a cutoff. This is indicative of a much higher iron content, which also causes features at 377, 388, and 450 nm (Ferguson and Fielding, 1971, 1972). The third spectrum is from Mugloto sample no. 0957, which shows a subtle blue component. It differs from the other Mugloto sample by a minor shift of the 560 nm band and a slight increase of absorption over 600 nm, alterations caused by the presence of an Fe^{2+}-Ti^{4+} charge transfer.

Many Mugloto-type stones show this subtle color alteration, which can be removed by heat treatment (Pardieu et al., 2015; Sripoonjan et al., 2016; Saeseaw et al., 2018).

Treatments. Gems are often treated to improve their appearance, and Mozambican ruby is no exception. These gems commonly receive treatment to enhance their clarity and color. We distinguish two types of Mozambican ruby, which each have their own characteristics that can be improved by treatment. The most common treatments of Mozambican rubies are discussed below.

Flux Healing of Maninge Nice–Type Ruby. As discussed before, Maninge Nice–type rubies have a fine color but naturally occur as flat crystals with abundant fractures. These fractures will drastically reduce the durability of the gems. Heat treatment with the addition of flux (figure 23) can help heal the fractures and prevent the stones from breaking along these weak zones (Hänni, 1997–1998; Hughes and Galibert, 1998; Emmett, 1999; Pardieu et al., 2010). In this process, the stone is coated in a flux (usually borax) before heating. During heating, the flux will melt and flow into fissures. Fluxes have the capacity to lower the melting point of solid materials. This means that corundum will start to melt where the flux is in contact with the corundum (i.e., in the fractures and on the surface). Upon cooling, the molten compounds start to recrystallize, effectively closing the fracture. During this process, droplets of flux become trapped in the healed fissure, which we observe as fingerprints (figure 24). Where this fingerprint reaches the surface of a cut stone, a line of small cavities is often visible (Hänni, 1997–1998).

These flux-healed fractures often differ in appearance from natural fingerprints and can be recognized by their thicker droplets and more weblike configuration.

Since this process is associated with heating at high temperatures, crystals often become altered and/or form expansion fractures.

TABLE 2. Summary of trace-element concentrations in Mozambican ruby samples (in ppma) using LA-ICP-MS.[a]

GIA sample no. 1702 (Pink, 1.163 mm)	Spot number	^{24}Mg	^{47}Ti	^{51}V	^{53}Cr	^{57}Fe	^{69}Ga
	1	22	bdl	2	714	551	7
	2	23	33	2	671	573	8
	3	20	16	2	682	617	8
	4	25	24	3	875	665	7
	5	23	bdl	2	678	584	8
	6	16	17	2	682	548	7
	7	19	27	2	714	591	8
GIA sample no. 0826 (Red, 2.808 mm)	Spot number	^{24}Mg	^{47}Ti	^{51}V	^{53}Cr	^{57}Fe	^{69}Ga
	1	28	17	4	639	1504	9
	2	27	16	4	635	1501	9
	3	28	17	4	655	1493	9
	4	32	17	4	635	1490	9
	5	37	18	4	706	1519	9
	6	50	18	4	749	1523	9
	7	35	17	4	718	1515	10
	8	39	17	4	745	1555	9
GIA sample no. 0957 (Purplish red, 1.960 mm)	Spot number	^{24}Mg	^{47}Ti	^{51}V	^{53}Cr	^{57}Fe	^{69}Ga
	1	12	14	4	788	1501	10
	2	12	13	7	804	1563	10
	3	12	16	5	824	1566	10
	4	12	13	4	800	1566	10
	5	12	13	4	796	1479	10
	6	12	14	4	776	1493	10
	7	12	14	4	796	1512	10
	8	11	18	4	769	1457	10
	Detection limit	0.12	0.3	0.03	0.37	3	0.01

[a]All measurements were taken inside the circles indicated, which correspond to the area that was analyzed during UV-Vis-NIR spectroscopy (see figure 22).

Sometimes the fractures are simply filled with a glass that has a high lead content. In this case, the fractures are not healed and the glass can be easily removed with acids to expose the fractures again. Depending on the type of glass used, this process can be done at temperatures below 1000°C, which does not alter most inclusions. However, the glass filling is very characteristic, containing an abundance of bubbles, and it often has a characteristic colored flash under the microscope (figure 25). The lower durability of the glass also creates a luster difference with the corundum host (Pardieu, 2005; McClure et al., 2006; Pardieu et al., 2010; Scarratt, 2012).

Both of these treatments are associated with elevated temperatures that can alter natural inclusions as well. One of the most obvious telltale signs is expansion fractures around crystals. The opaque black inclusions commonly seen in Maninge Nice–type rubies are very susceptible to this and often appear as black discs after heat treatment (figure 26).

Low-Temperature Heat Treatment of Mugloto-Type Ruby. Rubies from Mugloto that have a dark color or strong blue color patches will be heat treated without any added chemicals to lighten their color (figure 27). In recent years, heat treaters have become very
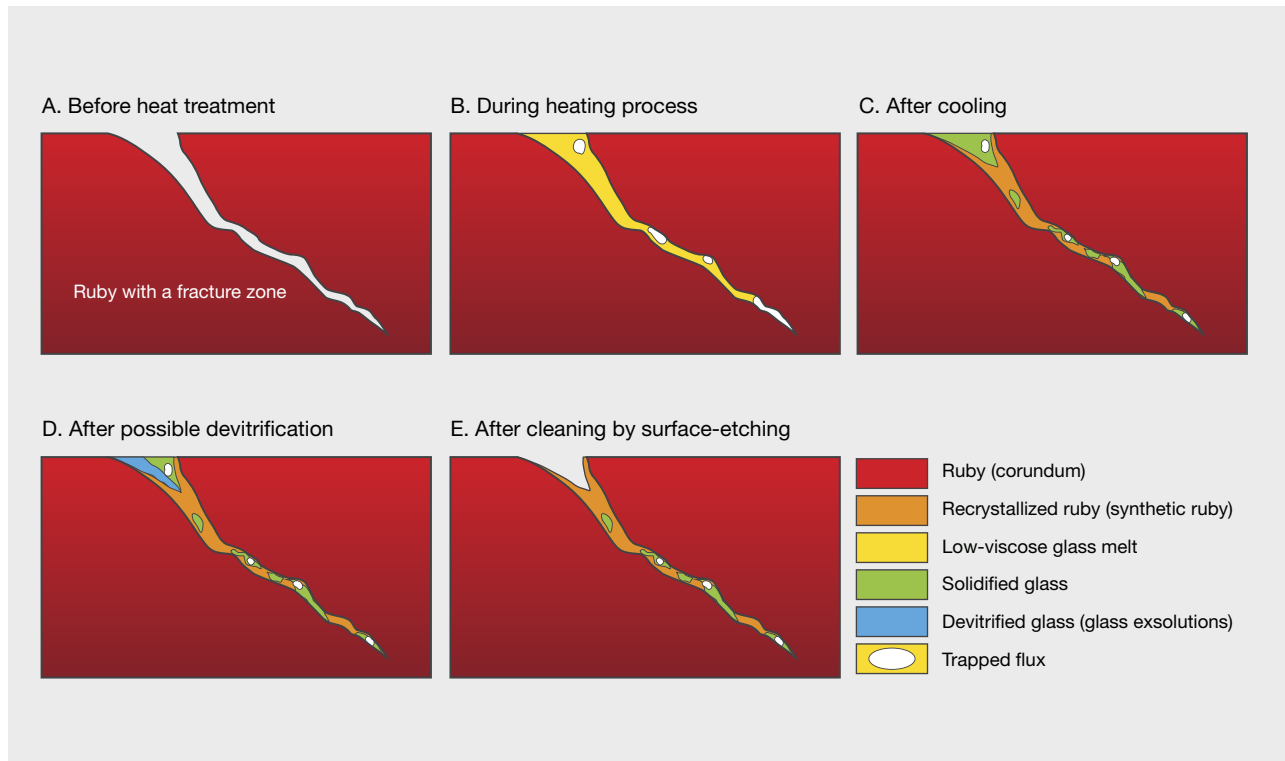
Figure 23. These images (from Hänni, 1997–1998) show the process of heat treatment with flux. During heating (step B), the flux flows into the fractures. When the temperature is raised further, the corundum near the fracture starts to melt. After cooling (step C), the mix of molten flux and corundum recrystallizes and "heals" the fracture. Bubbles of flux are trapped in the healing corundum, forming fingerprints.

skilled at this process, ever lowering the temperatures. These temperatures are low enough that inclusions are not severely altered. Below temperatures of 1200°C, even rutile silk is not dissolved into the lattice. GIA has conducted several studies of Mozam-

Figure 24. Flux-healed fracture in a ruby that was heated with borax flux. Photo by C. Khowpong; field of view 1.75 mm. Darkfield illumination.

Figure 25. Glass-filled fractures with bubbles and blue flashes are the most obvious features in this glass-filled ruby, but natural inclusions such as bands of silk can also be seen. Photo by C. Khowpong; field of view 4.60 mm. Darkfield illumination.
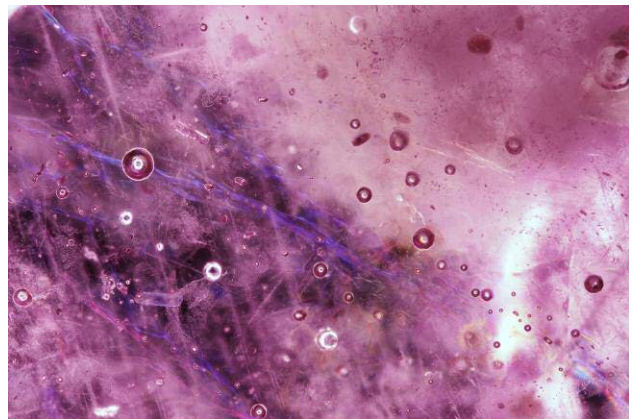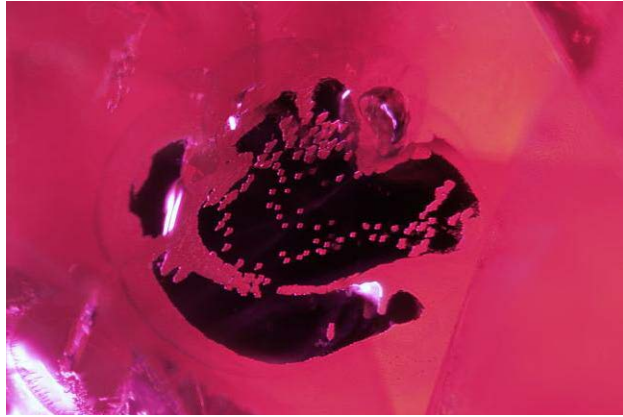
Figure 26. This opaque black inclusion expanded during heat treatment, creating a fracture around it. The molten crystal flowed into the fracture and solidified upon cooling, creating an opaque black disc. This is sometimes referred to as "bleeding out" of a crystal. Photo by C. Khowpong; field of view 1.20 mm. Darkfield illumination.

bican ruby treatment to determine the extent and detectability of heating at lower temperatures (Pardieu et al., 2015; Saeseaw et al., 2018). An initial experiment was done under unknown conditions by a professional offering his services to the trade; all follow-up experiments were carried out by GIA under known circumstances. Temperatures varied from 600°C to 900°C and heating times from 160 minutes to 24 hours. During all these experiments, the stones were fully documented before and after treatment, and some were treated multiple times. Identification of low-temperature heat treatment re-

quires inclusion study and FTIR spectroscopy (Pardieu et al., 2015; Saeseaw et al., 2018).

The reaction of crystal inclusions to heat treatment is unpredictable. In some cases, the crystals caused expansion fractures, while others did not change even when heated at more extreme conditions. Platelets can start to develop bright spots when heated at temperatures over 700°C (figure 28). It is important to note that this is not always seen after treatment, so the absence of spotted platelets does not conclusively indicate the absence of treatment. The platelets never showed alteration at 600°C, but under the conditions of this experiment the stone's color was not altered (Saeseaw et al., 2018). Fractures with iron staining showed a change from yellowish to brownish red, even when heated at low temperatures (Sripoonjan et al., 2016). However, these features are not commonly seen in faceted stones.

When the inclusion scene does not provide conclusive evidence of treatment, infrared spectroscopy can offer an indication of heating. In the majority of cases, minerals with an OH group such as boehmite and kaolinite are affected by heat treatment, so their presence in the FTIR spectrum indicates the absence of heating. By far the most common feature seen in the Mozambican rubies is a peak at 3309 cm^{-1}. Upon heating, the intensity of this peak always diminishes. When the peak before heating is strong enough, peaks at 3232 and 3185 cm^{-1} are formed (figure 29) (Pardieu et al., 2015; Saeseaw et al., 2018). Often called the 3309 series, this has only been observed in Mozambican rubies after heat treatment. Rubies with a weaker 3309 peak will not develop a

Figure 27. Left: An untreated Mugloto-type ruby clearly showing blue zones when viewed perpendicular to the c-axis. Right: The stone after heat treatment for 160 minutes at 800°C. Photos by S. Engniwat.
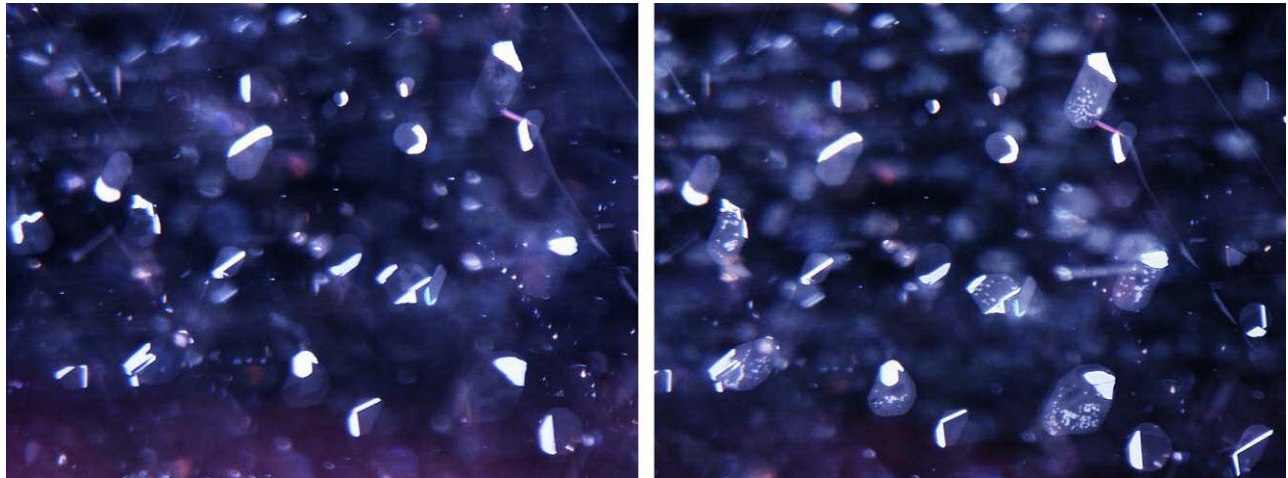
Figure 28. Left: Platelets in an unheated Mozambican ruby. Right: The platelets developed a spotted appearance after heat treatment at 900°C for 160 minutes. Photos by GIA; field of view 1.30 mm. Fiber-optic illumination.

3309 series after heating, so the absence of this series is not conclusive evidence of the absence of treatment (figure 30) (Saeseaw et al., 2018).

Distinguishing Rubies from Mozambique. Based on gemological data, Mozambican rubies can often be clearly distinguished. Many other ruby sources have a very different geological history, such as the marble-hosted deposits (e.g., Mogok and Mong Hsu in Myanmar, Luc Yen in Vietnam, and Jegdalek in Afghanistan) or the basalt-hosted deposits (Thailand-

Cambodia). These have very different inclusion scenes, allowing for a clear separation. Rubies from both of these geological origins usually have a more extreme reaction under UV light than Mozambican rubies, with marble-hosted rubies often being more fluorescent, especially under short-wave UV, and basalt-related stones being almost inert.

With rubies from other amphibole-related deposits such as those found in northeastern Madagascar (Didy, Andilamena, Zahamena, and Vatomandry) and Tanzania (Longido and Winza), the separation is

Figure 29. FTIR spectrum of a Mozambican ruby showing a strong 3309 cm⁻¹ peak in its unheated state (blue trace). The other spectrum (red trace) was taken after heating at 800°C for 160 minutes and clearly shows the development of 3232 and 3185 cm⁻¹ peaks and a decrease in 3309 cm⁻¹ peak intensity.
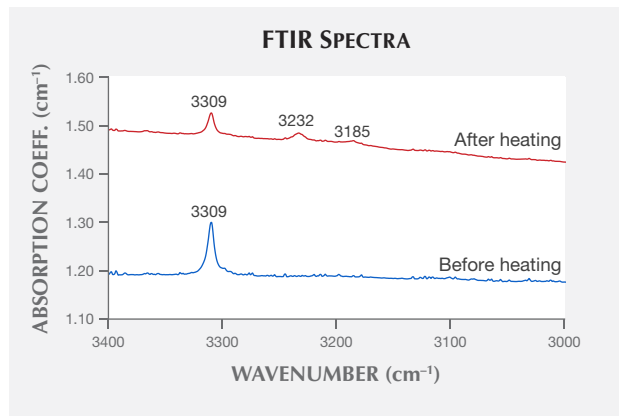
Figure 30. The FTIR spectrum of a Mozambican ruby (blue trace) shows a weak 3309 cm⁻¹ peak in its unheated state. The red trace, obtained after heating at 800°C for 160 minutes, shows a decrease in peak intensity but no formation of a 3309 series.
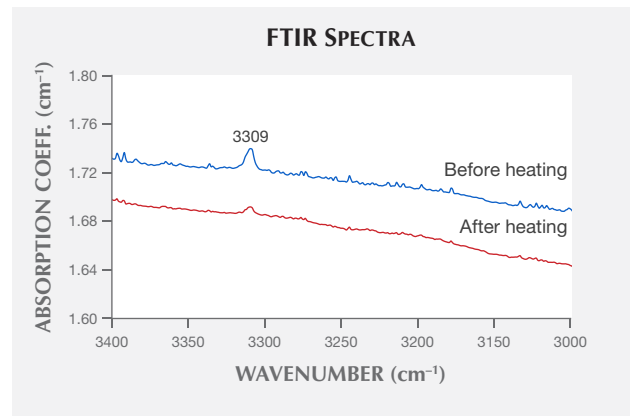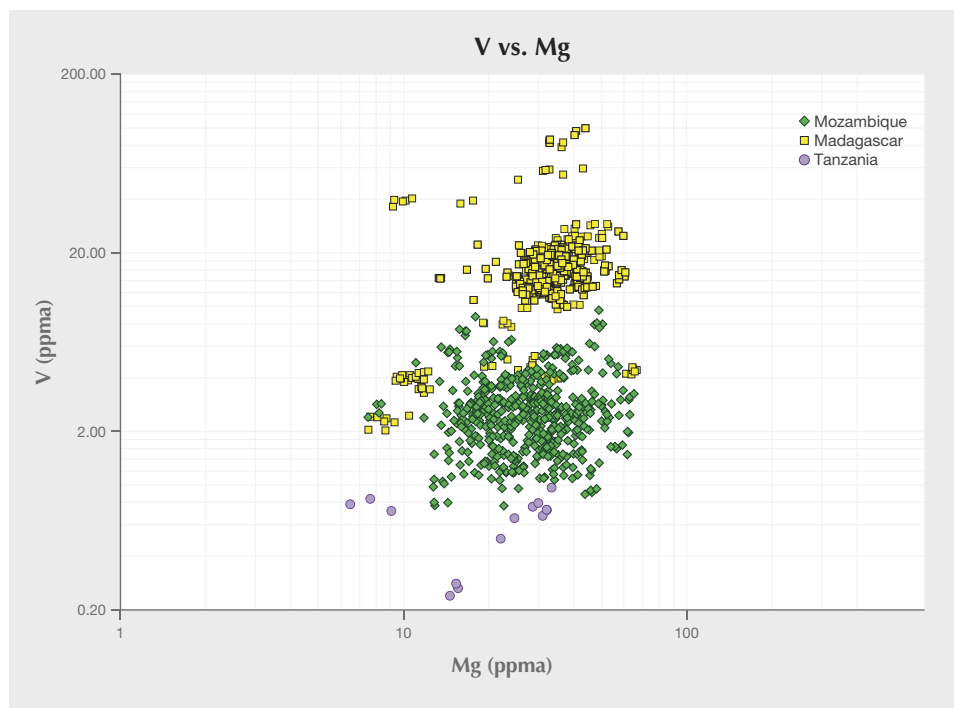
Figure 31. Trace-element chemistry plot of V vs. Mg (ppma, measured by LA-ICP-MS) following GIA protocols outlined in Saeseaw et al. (2018) for rubies from Mozambique, Madagascar, and Tanzania.

more challenging. All show a slightly similar inclusion scene and share the same gemological characteristics such as color intensity and UV reaction.

Trace-element chemistry can provide indications for origin discrimination between the East African ruby deposits in Mozambique, Madagascar, and Tanzania (figure 31). Vanadium content is often lower in rubies from the Winza deposit in Tanzania and higher in those from Madagascar, although some deposits yield V concentrations that overlap with Mozambican rubies.

CONCLUSIONS

GIA has been privileged to follow this discovery from the start and document its growth during the last decade. This work has shown that there are two varieties of Mozambican ruby: (1) Maninge Nice–type, characterized by strong color and fluorescence, a flatter shape, and abundant inclusions; and (2) Mugloto-type, with its weaker UV reaction but cleaner and bulkier stones.

In ten years, treatments of Mozambican rubies have evolved considerably, from copying existing recipes that worked with similar material, such as flux healing and glass filling, to adapting procedures of low-temperature heat treatment to specific Mozambican stones.

The first decade of Mozambican rubies from Montepuez was characterized by chaotic development and

plenty of opportunities (figures 32 and 33). New deposits were found, large crowds of garimpeiros dug up rubies, and foreign buyers operated from the shadows, all while a formal framework was being developed. Initially this caused a series of conflicts in the heat of the rush. The arrival of large companies disrupted the first equilibrium between miners, buyers, and local authorities. By now, a delicate balance has been

Figure 32. The 40.23 ct Rhino ruby was sold at a December 2014 Gemfields auction in Singapore. Photo by Robert Weldon.

Figure 33. In terms of value, fine Mugloto-type rubies are the most important stones being mined in the Monte-puez area. Their desirable color, high clarity, and blocky shape often yield attractive stones that are in high demand. Photo by Vincent Pardieu/GIA.

reestablished. At the moment, both MRM and the artisanal miners contribute significant amounts of ruby to the trade although the amount of ruby mined by the garimpeiros is decreasing.

Looking back on our initial experiences with Mozambican rubies, it is safe to say that this discovery will have a long-lasting impact on the ruby trade and perhaps the colored stone trade as a whole. Never

have so many rubies, in such a wide range of sizes and qualities, come out of the ground and into the market. Ruby is becoming more accessible than ever. This is disrupting the established market practices of secrecy and low transparency, creating some resistance from conservative (or nostalgic) dealers. However the Montepuez deposits evolve, this is already proving to be one of the most exciting ruby sources ever discovered.

REFERENCES

Beran A., Rossman G.R. (2006) OH in naturally occurring corundum. *European Journal of Mineralogy*, Vol. 18, No. 4, pp. 441–447, http://dx.doi.org/10.1127/0935-1221/2006/0018-0441

Bingen B., Jacobs J., Viola G., Henderson I.H.C., Skår Ø., Boyd R., Thomas R.J., Solli A., Key R.M., Daudi E.X.F. (2009) Geochronology of the Precambrian crust in the Mozambique Belt in NE Mozambique, and implications for Gondwana assembly. *Precambrian Research*, Vol. 170, No. 3-4, pp. 231–255, http://dx.doi.org/10.1016/j.precamres.2009.01.005

Boyd R., Nordgulen Ø., Thomas R.J., Bingen B., Bjerkgård T., Grenne T., Henderson I., Melezhik V.A., Often M., Sandstad J.S., Solli A., Tveten E., Viola G., Key R.M., Smith R.A., Gonzalez E., Hollick L.J., Jacobs J., Jamal D., Motuza G., Bauer W., Daudi E., Feitio P., Manhica V., Moniz A., Rosse D. (2010) The geology and geochemistry of the East African orogen in northeastern Mozambique. *South African Journal of Geology*, Vol. 113, No. 1, pp. 87–129, http://dx.doi.org/10.2113/gssajg.113.1.87

Chapin M., Pardieu V., Lucas A. (2014) Mozambique: A ruby discovery for the 21st century. *G&G*, Vol. 51, No. 1, pp. 44–54, http://dx.doi.org/10.5741/GEMS.51.1.44

Emmett J.L. (1999) Fluxes and the heat treatment of ruby and sapphire. *G&G*, Vol. 35, No. 3, pp. 90–92.

Ferguson J., Fielding P.E. (1971) The origins of the colours of yellow, green and blue sapphires. *Chemical Physics Letters*, Vol. 10, No. 3, pp. 262–265, http://dx.doi.org/10.1016/0009-2614(71)80282-8

——— (1972) The origins of the colours of natural yellow, blue, and green sapphires. *Australian Journal of Chemistry*, Vol. 25, No. 7, pp. 1371–1385, http://dx.doi.org/10.1071/CH9721371

Gemfields (2019) Gemfields press release, Jan. 29, https://mining.com/wp-content/uploads/2019/01/gemfields-press-announcement-jan29-2019.pdf, January 29.

GIT Gem Testing Laboratory (2009) Some characteristics of "Mozambique" ruby, Nov. 19, https://www.git.or.th/eng/testing_center_en/lab_notes_en/glab_en/2009/GIT_article_ruby_mozambique_web.pdf, November 19.

Grantham G.H., Macey P.H., Ingram B.A., Roberts M.P., Armstrong R.A., Hokada T., Shiraishi K., Jackson C., Bisnath A., Manhica V. (2008) Terrane correlation between Antarctica, Mozambique and Sri Lanka: Comparisons of geochronology, lithology, structure and metamorphism and possible implications for the geology of southern Africa and Antarctica. *Geological Society of London, Special Publication*, Vol. 308, No. 1, pp. 91–119, http://dx.doi.org/10.1144/SP308.4

Hänni H.A. (1997–1998) Short notes on some gemstone treatments. *Journal of the Gemmological Association of Hong Kong*, Vol. 20, pp. 44–52.

Hänni H.A., Krzemnicki M.S. (2009) Das neue Rubinvorkommen von Montepuez, Mosambik (The new ruby deposit of Montepuez, Mozambique). *Zeitschrift der Deutschen Gemmologischen Gesellschaft*, Vol. 58, No. 3-4, pp. 127–130.

Hsu T., Lucas A., Pardieu V. (2014) Mozambique: A ruby discovery for the 21st century. GIA Research News, https://www.gia.edu/gia-news-research-mozambique-expedition-ruby-discovery-new-millennium

Hughes R.W. (2015) Red rain: Mozambique ruby pours into the market. http://www.lotusgemology.com/index.php/library/articles/316-red-rain-mozambique-ruby-pours-into-the-market

Hughes R.W., Galibert O. (1998) Foreign affairs: Fracture healing/filling of Möng Hsu ruby. *Australian Gemmologist*, Vol. 20, No. 2, pp. 70–74.

Hughes R.W., Manorotkul W., Hughes E.B. (2017) *Ruby & Sapphire: A Gemologist's Guide*. RWH Publishing/Lotus Publishing, Bangkok.

Koivula J.I., Kammerling R.C. (1991) Gem News: Update on corundum. *G&G*, Vol. 27, No. 1, p. 48.

Lächelt S. (2004) The geology and mineral resources of Mozambique. Maputo: República de Moçambique, Monostério dos Recursos Minerais e Energia, Direcçâo Nacional de Geologia.

Laurs B.M., Zwaan J.C., Breeding C.M., Simmons W.B., Beaton D., Rijsdijk K.F., Befi R., Falster A.U. (2008) Copper-bearing (Paraíba-type) tourmaline from Mozambique. *G&G*, Vol. 44, No. 1, pp. 4–30, http://dx.doi.org/10.5741/GEMS.44.1.4

Lucas A., Hsu T. (2017) Gem News International: New ruby miner in Mozambique. *G&G*, Vol. 53, No. 1, p. 121.

Lucas A., Pardieu V. (2014) Gemfields inaugural rough ruby auction in Singapore. GIA Research News, July 17, https://www.gia.edu/gia-news-research-gemfields-ruby-auction-singapore

McClure S.F., Koivula J.I. (2009) Gem News International: Preliminary observations on new rubies from Mozambique. *G&G*, Vol. 45, No. 3, pp. 224–225.

McClure S.F., Smith C.P., Wang W., Hall M. (2006) Identification and durability of lead glass–filled rubies. *G&G*, Vol. 42, No. 1, pp. 22–34, http://dx.doi.org/10.5741/GEMS.42.1.22

Mustang Resources realises maiden ruby sales from new Thailand office (2018) *Mining Review Africa*, https://www.miningreview.com/diamonds-gems/mustang-resources-realises-maiden-ruby-sales-from-new-thailand-office, April 11.

Pardieu V. (2005) Lead glass filled/repaired rubies. www.aigslaboratory.com/Filearticle/55.pdf, Jan. 17

Pardieu V. (2017) Gem News International: Update on Mozambique ruby mining and trading. *G&G*, Vol. 53, No. 3, pp. 377–380.

Pardieu V. (2018) Tough lessons from Mustang's maiden ruby auction. *InColor*, No. 37, pp. 58–61.

Pardieu V., Chauviré B. (2012) Gem News International: Update on ruby mining and trading in northern Mozambique. *G&G*, Vol. 48, No. 4, pp. 309–311.

Pardieu V., Jacquat S., Senoble J.B., Bryl L.P., Hughes R.W., Smith M. (2009a) Expedition report to the ruby mining sites in northern Mozambique (Niassa and Cabo Delgado provinces). GIA Research News, Dec. 23, https://www.gia.edu/gia-news-research-nr121709

Pardieu V., Thanachakaphad J., Jacquat S., Senoble J.B., Bryl L.P. (2009b) Rubies from the Niassa and Cabo Delgado regions of northern Mozambique. GIA Research News, Sept. 13, https://www.gia.edu/gia-rubies-from-niassa-cabo-delgado

Pardieu V., Sturman N., Saeseaw S., Du Toit G., Thirangoon K. (2010) FAPFH/GFF treated ruby from Mozambique: A preliminary report. GIA Research News, May 11, https://www.gia.edu/gia-news-research-nr51110

Pardieu V., Sangsawong S., Muyal J., Chauviré B., Massi L., Sturman N. (2013) Rubies from the Montepuez area. GIA Research News, Oct. 1, https://www.gia.edu/gia-rubies-from-montepuez-area

Pardieu V., Saeseaw S., Detroyat S., Raynaud V., Sangsawong S., Bhusrisom T., Engniwat S., Muyal J. (2015) GIA reports on low-temperature heat treatment of Mozambique ruby. GIA Research News, April 28, https://www.gia.edu/gia-news-research-low-temperature-heat-treatment-mozambique-ruby

Rondeau B., Delaunay A. (2007) Les tourmalines cuprifères du Nigeria et du Mozambique. *Revue de Gemmologie a.f.g.*, No. 160, pp. 8–13.

Saeseaw S., Kongsomart B., Atikarnsakul U., Khowpong C., Vertriest W., Soonthorntantikul W. (2018) Update on "low-temperature" heat treatment of Mozambican ruby: A focus on inclusions and FTIR spectroscopy. GIA Research News, Apr. 30, https://www.gia.edu/ongoing-research/update-low-temperature-heat-treatment-mozambican-ruby-focus-on-inclusions-and-ftir-spectroscopy

Sangsawong S., Pardieu V., Raynaud V. (2016) Gem News International: Purple pyrope-almandine garnet from Mozambique. *G&G*, Vol. 52, No. 3, pp. 321–323.

Scarratt K. (2012) A discussion on ruby-glass composites & their potential impact on the nomenclature in use for fracture-filled or clarity enhanced stones in general. Feb. 3, http://www.giathai.net/pdf/Ruby-Glass_Composites.pdf

Shigley J.E., Laurs B.M., Janse A.J.A., Elen S., Dirlam D.M. (2010) Gem localities of the 2000s. *G&G*, Vol. 46, No. 3, pp. 188–217, http://dx.doi.org/10.5741/GEMS.46.3.188

Shor R., Weldon R. (2015) Gemfields bets on gemstone market's growth. GIA Research News, Jan. 26, https://www.gia.edu/gia-news-research-gemfields-bets-gemstone-markets-growth

Simonet C. (2018) The Montepuez ruby deposits, what's next? *In-Color*, No. 37, pp. 32–40.

Smith C.P. (1995) A contribution to understanding the infrared spectra of rubies from Mong Hsu, Myanmar. *Journal of Gemmology*, Vol. 24, No. 5, pp. 321–335.

Sripoonjan T., Wanthanachaisaeng B., Leelawatanasuk T. (2016) Phase transformation of epigenetic iron staining: Indication of low-temperature heat treatment in Mozambique ruby. *Journal of Gemmology*, Vol. 35, No. 2, pp. 156–161.

Valoi E., Macrae C. (2015) Mozambique's gem wars. Al Jazeera, *Africa Investigates*, Dec. 10, https://www.aljazeera.com/programmes/africainvestigates/2015/12/mozambique-gem-wars-151210075320384.html

Vertriest W., Pardieu V. (2016) Update on gemstone mining in northern Mozambique. *G&G*, Vol. 52, No. 4, pp. 404–409, http://dx.doi.org/10.5741/GEMS.52.4.404

For online access to all issues of GEMS & GEMOLOGY from 1934 to the present, visit:

gia.edu/gems-gemology

MADAGASCAR SAPPHIRE: LOW-TEMPERATURE HEAT TREATMENT EXPERIMENTS

E. Billie Hughes and Rosey Perkins

Madagascar has become one of the world's top sources of fine blue sapphire in recent times. In addition to beautiful untreated material, increasing numbers of treated stones have appeared in the market. Some have been heated to relatively low temperatures, below 1350°C, to lighten their color. To help separate unheated and heated Madagascar sapphire, the authors performed experiments to document the changes they undergo with low-temperature heat treatment in air, which is an oxidizing atmosphere.

This study was sparked by a 2017 comment from noted Australian gemologist Terry Coldham. In Bangkok he ran into a friend with a parcel of Madagascar sapphire. Mr. Coldham's friend said he was going "to the burner," hoping to "sweeten" the color with a low-temperature treatment that would lighten the hue. He indicated that the temperatures they were using were likely below 1000°C. This coincided with the sapphire rush at Bemainty (Perkins, 2016) that produced high-quality blue sapphires (figure 1), ranging from lighter colors with a lower iron content to much deeper blues with a higher iron content (Pardieu et al., 2017).

The abundance of blue sapphires from Madagascar being tested at Lotus Gemology in Bangkok, along with rumors of lower-temperature heat treatment (see "Defining 'Low' Temperature" below), suggested the need for further study and heat treatment experiments on this material. Our aim was to record the characteristics of Madagascar sapphires and to detect this type of heat treatment.

GEOLOGY

Approximately 750–500 million years ago, Madagascar was a part of the Gondwana supercontinent, sandwiched between what are now East Africa, southern India, and Sri Lanka. Today this region, known as the Mozambique (Pan-African) Orogenic Belt, is home to some of the world's richest corundum deposits (Hughes et al., 2017). Many regions that were a part of this belt are now the world's top producers of ruby and sapphire (see figure 2, left).

The majority of sapphire in Madagascar is metamorphic (though basalt-related sapphire is found in the far north) and recovered from secondary deposits (figure 2, right). It is not certain when these sapphires would have formed, but the literature suggests that they are likely 650–560 million years old (Kröner et al., 1999; Link, 2015).

Because of Madagascar's proximity to modern-day Sri Lanka at the time when sapphires were forming within the earth, it is understandable that there would be an overlap between sapphires from these two origins in terms of colors and internal features, sometimes making them difficult to separate.

> ## In Brief
> - Madagascar blue sapphire is of significant commercial importance and is gaining a reputation for producing high-quality material.
> - Untreated and heated specimens can be separated with FTIR spectroscopy, microscopy, and observation of short-wave UV fluorescence.
> - In heated samples, UV-Vis-NIR spectroscopy is not always a reliable way to separate metamorphic and magmatic blue sapphire.

The island of Madagascar, one of the most biodiverse in the world, offers an incredible wealth of gems. Some estimate that potentially 90% of the land is gem-bearing (Hughes, 2006). Most of the important ruby and sapphire finds are concentrated toward the
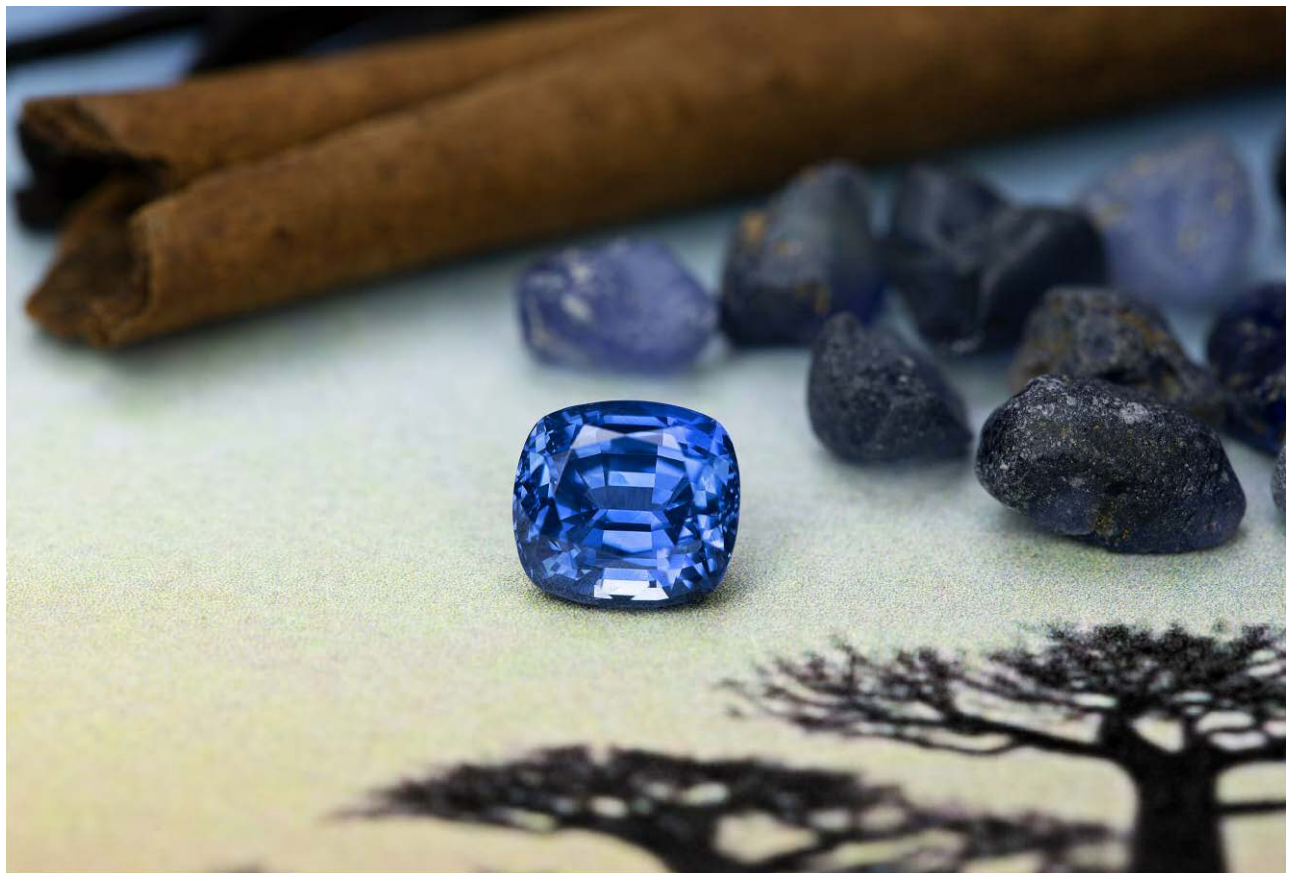
Figure 1. Sapphires from Madagascar: a beautiful 3.29 ct untreated faceted stone and an assortment of rough in the background. Madagascar has produced many high-quality stones in the last few years and is quickly gaining a reputation for fine sapphires equal to any on the planet. Photo by Wimon Manorotkul, courtesy of Neil Doohan.

eastern part of the island. Significant gem rushes at primary-type deposits near Andrebabe, Andilamena, and Didy lie on the boundary between the Antananarivo and Tsaratanana units (Rakotondrazafy et al., 2008; Pardieu et al., 2017). In the south there has been notable production of both blue and fancy-color sapphire, with mining and trading concentrated around the town of Ilakaka (figure 3).

EXPERIMENTS AND RESULTS

Samples. Twelve untreated Madagascar blue sapphire samples selected from parcels from three locations were prepared for the heating experiments. Samples 1–4 were collected by Rosey Perkins in 2017 in Bemainty, Madagascar. Samples 5–8 were purchased by a team from Lotus Gemology on a 2016 trip to Ilakaka, Madagascar. Samples 9–12 were obtained in Bangkok from a lot of rough Andranondambo sapphire from Simon Dussart of Asia Lounges and Isaac Stern. All stones were examined before heating and showed character-

istics consistent with untreated Madagascar sapphire (Peretti and Peretti, 2017; Krzemnicki et al., 2017).

Sample Preparation. Four samples were selected from each of the three parcels from Bemainty, Ilakaka, and Andranondambo, according to their color and inclusions. Preference was given to those of darker color with characteristic inclusions, and several showed color zoning. Darker samples were chosen because we were particularly interested in seeing what temperatures would lighten overly dark material. Then all 12 samples were polished into wafers measuring approximately 2–5 mm in thickness. The stones were acid cleaned in a mixture of 50% hydrochloric and 50% hydrofluoric acid for approximately 48 hours before being heated. After the final round of heating, the samples were repolished slightly to eliminate surface damage that occurred as a result of heat treatment.

Heating. After acid cleaning, we examined and recorded data on the 12 stones. Then we heated
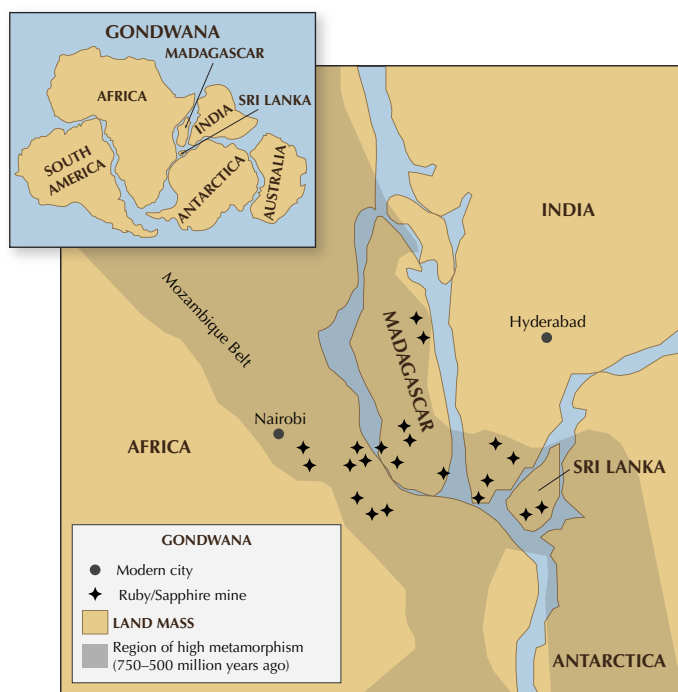
Figure 2. Left: This map of Gondwanaland illustrates how close Sri Lanka and Madagascar were to each other when their sapphire deposits were forming. This proximity may account for the similarities between much of the blue sapphire from the two origins. Right: Map of Madagascar, including the most notable corundum localities. Ilakaka, Bemainty, and Andranondambo, the sources of samples used in this experiment, are highlighted in red. Maps by Richard Hughes.

them in air, which is an oxidizing atmosphere, to 800°C, 900°C, 1000°C, and 1100°C for eight hours at each temperature with a Vulcan 3-550 oven (figure 4). They were further heated in air to 1300°C and 1500°C by John L. Emmett with a Lindberg 51333 oven. The stones were placed on corundum felt while being heated.

Defining "Low" Temperature. While some dealers that we spoke to defined low-temperature treatment as below 1000°C, for research purposes we define it slightly differently. High-temperature treatment involves the dissolution of secondary-phase microcrystals, while low-temperature treatment does not. The most common of these microcrystals in corundum is rutile silk. Rutile dissolution can occur around 1200–1350°C, which we use to define the approximate boundary between low- and high-temperature treatments (Hughes et al., 2017). Because of this, we focused our experiments on four "lower"-temperature rounds

of heat ranging from 800 to 1100°C, one "intermediate" round at 1300°C, which we can consider a borderline area, and one "high" round at 1500°C for contrast.

EDXRF. Energy-dispersive X-ray fluorescence (EDXRF) bulk analysis was performed using a Skyray EDX 6000B. We obtained chemical composition on all samples before heating (table 1). The detection limits were 1–3 ppmw (0.5–1 ppma) for Ti, 3–7 ppmw (1–3 ppma) for V, 3–7 ppmw (1–3 ppma) for Cr, 14 ppmw (5 ppma) for Fe, and 1–4 ppmw (1 ppma) for Ga. Dr. Andreas Burkhardt calibrated the corundum procedure with natural and synthetic corundum standards analyzed with laser ablation–inductively coupled plasma–mass spectrometry (LA-ICP-MS) and electron microprobe (EMPA) at the University of Bern and the University of Basel, Switzerland. The most interesting feature was the wide range of iron (Fe) levels, ranging from sample 10 at 243 ppma to sample 2 at 2465 ppma.

Figure 3. Miners move gem-bearing gravel near Ilakaka. Most of the sapphire production in Madagascar is by small-scale miners working with artisanal tools. Photo by E. Billie Hughes.

Macro Photography. Photos were taken with a Canon EOS 6D camera with a 65 mm lens clamped to a copy stand. Samples were placed on a light box powered by an XD-300 (xenon) light source. Photos were recorded before any heating and after each eight-hour round of heating at each temperature (figure 5).

Most of the samples started to show significant reductions in color after they were heated to around 900–1000°C (again, see figure 5). When temperatures rose to 1300–1500°C, the colors began to deepen again to medium to dark blues.

Sample 1, unlike the others tested, had a strong pink zone in addition to blue color zoning. This pink

Figure 4. E. Billie Hughes removes the samples from the Vulcan 3-550 oven after a heating session. Photo by Rosey Perkins.

TABLE 1. EDXRF chemical analysis of Madagascar sapphires prior to low-temperature heat treatment.

Sample no.	Concentration in ppmw (ppma in parentheses)				
	Ti	**V**	**Cr**	**Fe**	**Ga**
1	90 (38)	15 (5)	396 (155)	1764 (644)	57 (17)
2	206 (88)	bdl	48 (19)	6752 (2465)	86 (25)
3	154 (66)	9 (3)	bdl	5060 (1847)	26 (8)
4	107 (46)	8 (3)	bdl	4701 (1716)	25 (7)
5	86 (37)	10 (3)	bdl	3641 (1329)	92 (27)
6	107 (46)	bdl	bdl	1524 (556)	157 (46)
7	30 (13)	bdl	bdl	3531 (1289)	58 (17)
8	253 (108)	27 (9)	bdl	955 (349)	103 (30)
9	59 (25)	bdl	bdl	2626 (959)	154 (45)
10	21 (9)	bdl	bdl	667 (243)	74 (22)
11	297 (127)	bdl	bdl	2535 (926)	200 (59)
12	67 (28)	bdl	bdl	2064 (754)	187 (55)

bdl = below detection limits
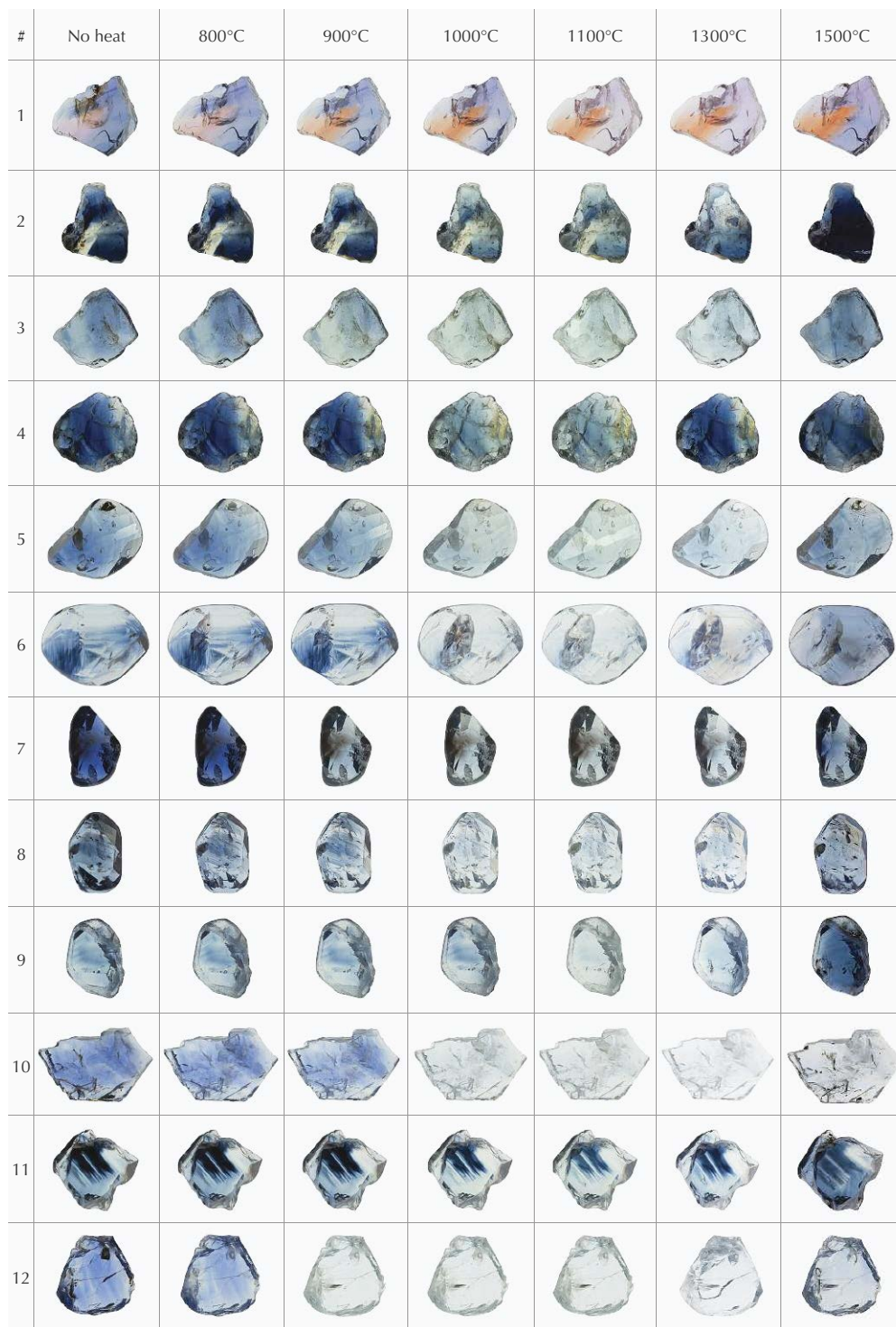
Figure 5. The 12 samples, shown before and after heating to each temperature. Most of the samples began to lighten significantly after heating to about 900–1000°C and started to deepen in color again around 1300°C. After heating to 1500°C, many pieces became significantly deeper in color. Photos not to scale. Photos by Rosey Perkins and Sora-at Manorotkul.

zone became a stronger orange with each round of heating (this has long been rumored to take place in Sri Lanka). The blue zoning in the piece started to lighten and turn a purplish color, particularly after heating to 1100–1300°C, and started to become more strongly blue again after heating to 1500°C.

Inclusions. Inclusion photomicrographs were taken with a Canon EOS 6D camera connected to an Olympus SZX16 microscope using an SDF PLAPO 0.8× lens. A variety of inclusions showed signs of alteration once the stones were heated. Some of the changes started to become evident after the first
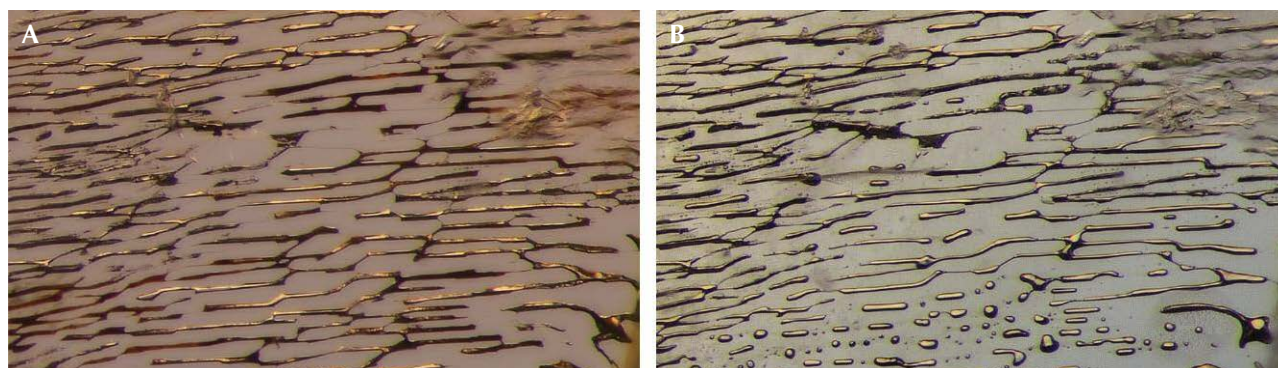
Figure 6. A: Partially healed fissure, or "fingerprint," in sample 3 before heating. Note the elongated, tube-like channels. B: After heating the stone to 1500°C, many of the jagged edges of the tubes have become rounded, and some even "neck down" to form smaller, rounded shapes in place of elongated tubes (Hughes, 2017). Diffuse transmitted light. Photomicrographs by E. Billie Hughes; field of view 1 mm.

round of heating at 800°C, while others developed at higher temperatures. Many of the changes that began at lower temperatures became increasingly dramatic as temperatures rose.

One of the first changes we began to notice was the development of fissures. Even after the first rounds of heating at 800°C and 900°C, shiny fissures appeared around many of the included crystals. As the stones were heated to higher temperatures, such fissures tended to grow larger, with glassy areas, evident in figures 7, 8, 9, and 11. Around 1300°C, some of these glassy areas started to "neck down" and form small bubbly channels that looked like "fingerprints" (Hughes and Emmett, 2004). In sample 3, which had a large partially healed fissure even before heat treatment, some of the tube-like channels in the fissure displayed clear signs of alteration after heat to 1500°C and developed rounded shapes (figure 6).

In several samples, the included crystals changed in appearance after heat. The crystals in sample 10, for example, developed small bubbles inside (see figure 10). Several included crystals developed a "frosty" appearance where their surfaces became rough and lighter in color, recorded in figures 10 and 11.

Figures 6–11 show a selection of inclusion photos of the stones both before and after heating. We kept the lighting conditions as similar as possible at each step, but because the bodycolor of the stones was changing, there are significant differences in the overall color of some images. In some cases, a blue color-correcting filter was used to neutralize the yellow tint of our microscope light.

UV-Vis-NIR. Ultraviolet/visible/near-infrared (UV-Vis-NIR) spectroscopy was conducted with a Magilabs GemmoSphere UV-Vis-NIR spectrometer. We

Figure 7. A: In sample 4 before heating, a cluster of transparent crystals surrounded by winged stress fractures has decolorized areas around them. B: After the first round of heating at 800°C, we can already observe small changes, as two of the crystals have developed larger glassy fractures than they had originally. C: By the time the sample is heated to 1100°C, significant differences have emerged. The previously smooth and glassy fissures around the crystals have become larger and begun to heal, creating a "fingerprint" appearance. Also note that the decolorized areas are much less prominent, and that the overall blue color of the stone has become lighter. Brightfield illumination, with blue and white diffusing filters. A blue diffusing filter is used to color-correct the light source, which has a yellow tint, to make it more neutral. Photomicrographs by E. Billie Hughes; field of view 1.8 mm.
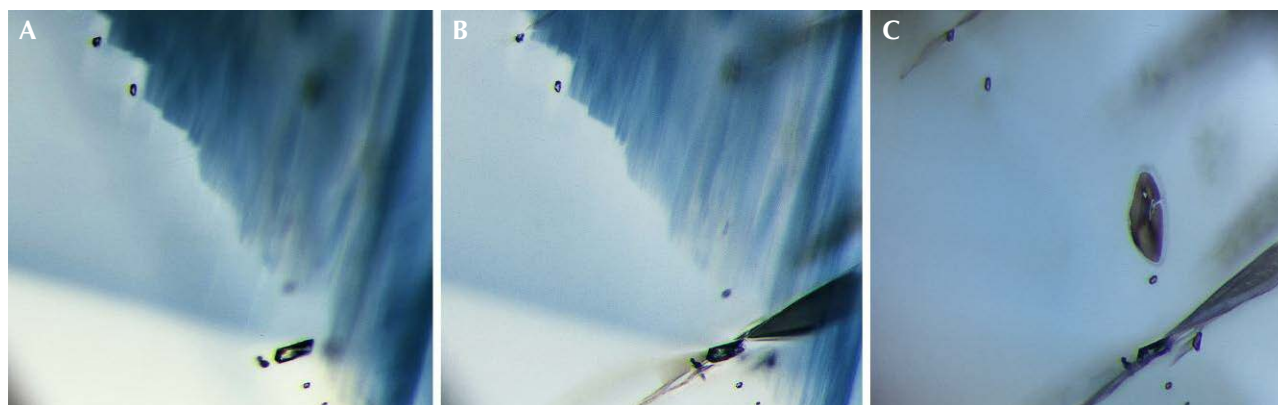
Figure 8. A: Before heat treatment, sample 6 shows a group of small crystals within decolorized areas as well as distinctive swaths of color zoning. B: At 900°C, the largest crystal has developed a large, shiny fracture around it, and the color zoning has lightened slightly. C: As we heat to higher levels, these fissures begin to heal at the edges. By our last round of heat, at 1500°C, other small crystals have also developed glassy fractures that are starting to heal. Any traces of the previously prominent color zoning are almost gone, and the stone has a more even light blue color. Brightfield illumination with blue and white diffusing filters. Photomicrographs by E. Billie Hughes; field of view 1.2 mm.

recorded UV-Vis-NIR spectra before heating and after each stage of heating. Before heating, 11 of the 12 stones showed spectra typical of metamorphic sapphire, with prominent absorption between 500 and 600 nm (figure 12A). Only sample 3 showed a spectrum that was not typical of metamorphic sapphire
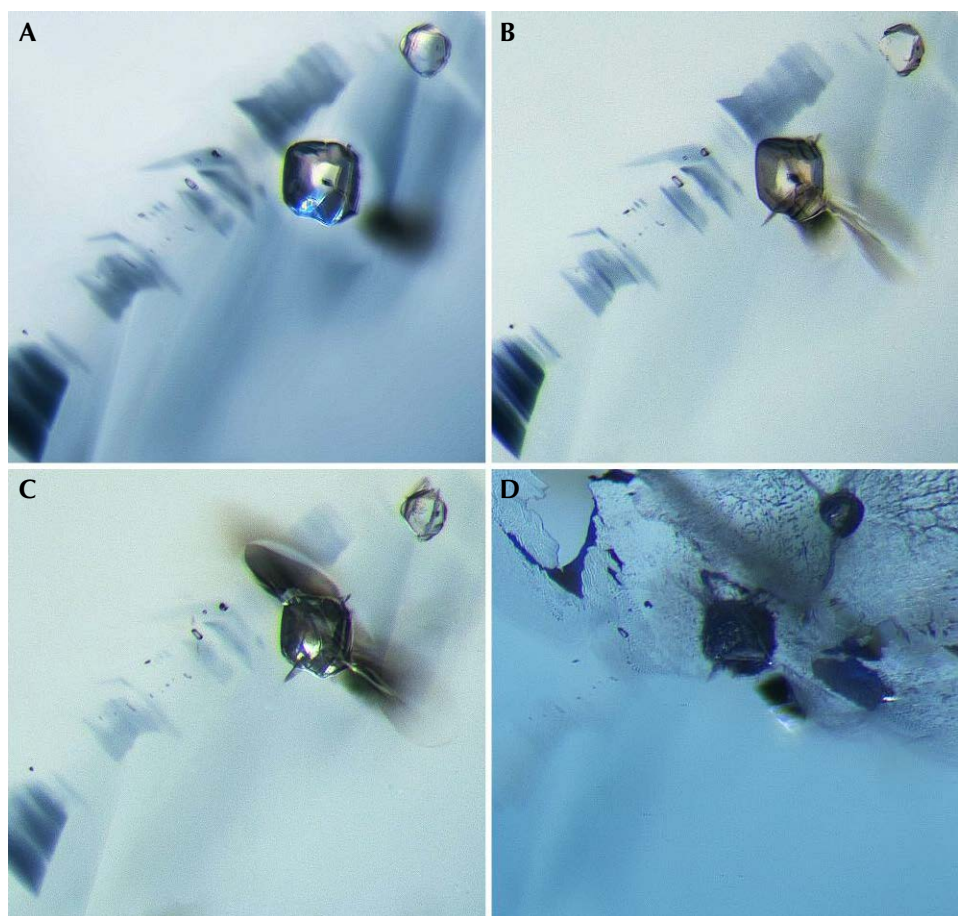
Figure 9. A: Before heating, sample 9 shows two transparent crystals next to a pattern of angular blue color zoning. B: With heating to 1000°C, the larger crystal shows heat damage, with a glassy fissure forming around it. Note how the background color has lightened. C: At 1100°C, the fissure has become larger, and a tiny fissure has begun to develop around the smaller crystal. D: At 1500°C, the inclusion scene is almost unrecognizable. Large fissures have developed around both crystals and begun to heal, creating melted-looking fingerprints. The blue color zones have lightened to a pale brown, but the overall bodycolor has become a stronger, even blue. Brightfield illumination with blue and white filters plus diffuse oblique fiber-optic light. Photomicrographs by E. Billie Hughes; field of view 1.7 mm.

Figure 10. A: Before heating, sample 10 is filled with elongated negative crystals, some of which branch into "Y" shapes. Many of these are filled with orange stains, but most are removed after acid cleaning. B: After the first round of heat, to 800°C, some changes are already apparent. The orange staining has turned a darker brownish shade. Some of the negative crystals, like the one on the right, have started to display a "frosty" white appearance on the surface. In the background behind the negative crystals, we can see faint signs of fissures and fingerprints beginning to develop. C: When heated to 1000°C, the changes become more pronounced. Some of the tubes, like the one in the center, have developed immobile bubbles inside. The fissures from previous rounds of heating have also begun to heal and create clear fingerprints composed of small channels. Also note how the background color has changed from medium blue to near-colorless. Diffuse oblique fiber-optic illumination. Photomicrographs by E. Billie Hughes; field of view 1 mm.

(figure 13). It displayed absorption between 500 and 600 nm as well as a prominent peak at 880 nm, which is often associated with magmatic sapphires (Hughes et al., 2017).

Eleven of the twelve stones also showed Fe-related peaks at 450 nm, ranging from weak to very strong. The only stone that did not initially display this peak was sample 1 (figure 14), which had both pink and blue zones. This stone showed transmission just below 700 nm in the red zone.

After each round of heating, we ran the spectra again. With heating at 800°C, all of the spectra were similar to those obtained prior to heating.

For the next round, we heated the samples to 900°C. We were surprised to see two of the spectra change significantly. In samples 7 and 12, the peak between 550 and 600 nm became less prominent and

a broad absorption band centered at 880 nm developed (figure 12B).

At first we suspected we had made an error, perhaps because we had focused on a slightly different area of the stones when running the spectra (see "Limitations of UV-Vis-NIR Results" below). We reran the spectra several times, with the same results. In the gemological literature, this shift has seldom been detailed. The earliest reference we found was with regard to heat-treated Montana sapphires, which also showed this shift after treatment (Emmett and Douthit, 1993). It was also reported in heated Madagascar sapphires in a master's thesis (Worawitratanagul, 2005).

By the next round of heating, to 1000°C, this aberration became the trend. Samples 7 and 12 still displayed the peak around 880 nm, but five more stones also showed this shift (samples 2, 4, 5, 9, and 10). At

Figure 11. A: A small, flat crystal is pictured in sample 10 before heat treatment. B: A reflective fissure begins to appear around the crystal after the first heating to 800°C. By 1100°C (pictured), the fissure has begun to heal at the edges. C: By the last round of heating, at 1500°C, the fissure around this crystal has begun to heal into a fingerprint. The crystal itself has also changed and developed a frosty, whitish appearance. Darkfield illumination. Photomicrographs by E. Billie Hughes; field of view 1 mm.

UV-Vis-NIR Spectrum

A

UV-Vis-NIR Spectrum

B
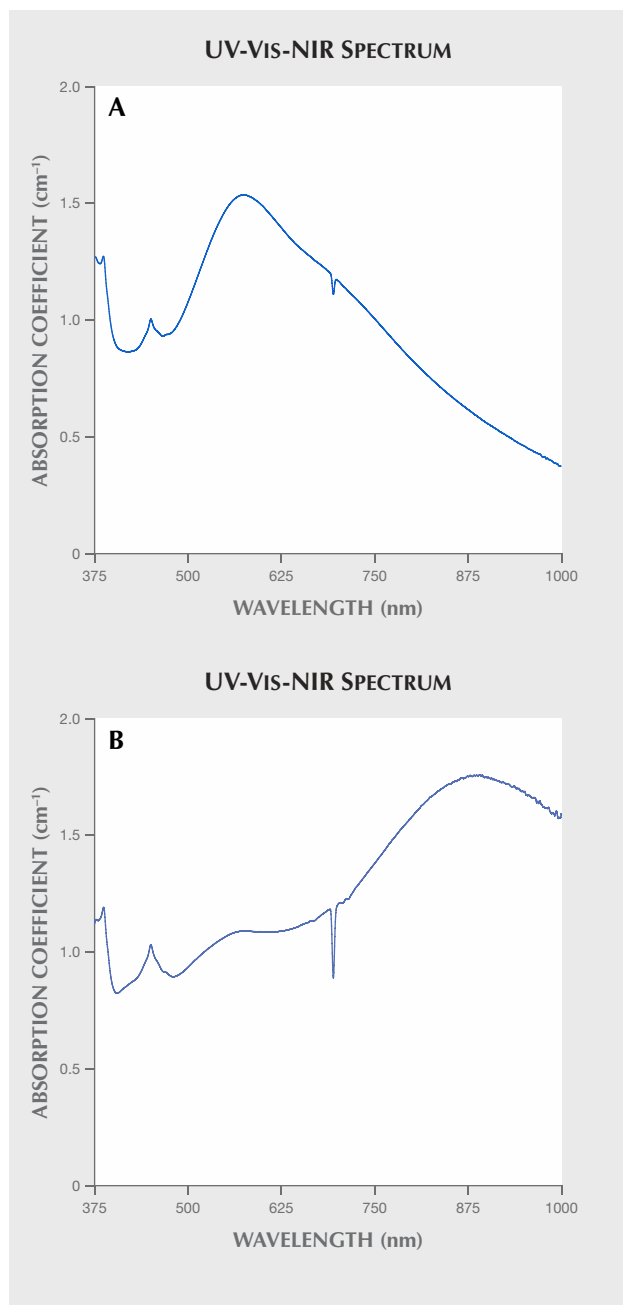
Figure 12. A: The UV-Vis-NIR spectrum of sample 7 before heat treatment. Note that the most prominent feature is the absorbance between 500 and 600 nm, as well as a small Fe-related peak around 450 nm. B: The UV-Vis-NIR spectrum of sample 7 after heating to 900°C. Note the development of a large peak at ~880 nm.

1100°C, the spectrum of sample 11 also displayed the shift, for a total of 8 out of 12.

Of the eight stones whose spectra changed to display this 880 nm peak, seven retained the peak after all subsequent rounds of heating. The only exception was sample 9, whose spectrum reverted to only showing absorption from 550 to 600 nm after heating at 1300°C. We are unsure of the cause. Further experimentation with samples aligned to the c-axis could be useful in exploring this further (again, see "Limitations of UV-Vis-NIR Results" below).

These significant spectral shifts showed a strong correlation with major changes in color after heat treatment. It has been suggested that there is a strong correlation between an 880 peak and a basalt-related origin. Given the fact that we have noted this peak in heated metamorphic sapphire, we would strongly caution against using the UV-Vis-NIR spectrum as the sole evidence of basaltic origin. As always, these spectra should be weighed with other factors.

Limitations of UV-Vis-NIR Results. We should note that the wafers were not oriented to the c-axis when they were polished, and spectra may have been taken from slightly different positions on the stone. This could affect the results.

However, the significant changes in a number of spectra (8 of the 12 stones) are strong evidence that this shift results from heat treatment, not just due to a different alignment of the stones while obtaining

Figure 13. Sample 3 was the only one to display absorption from 500 to 600 nm as well as around 880 nm before heat treatment.

UV-Vis-NIR Spectrum

UV-VIS-NIR SPECTRUM
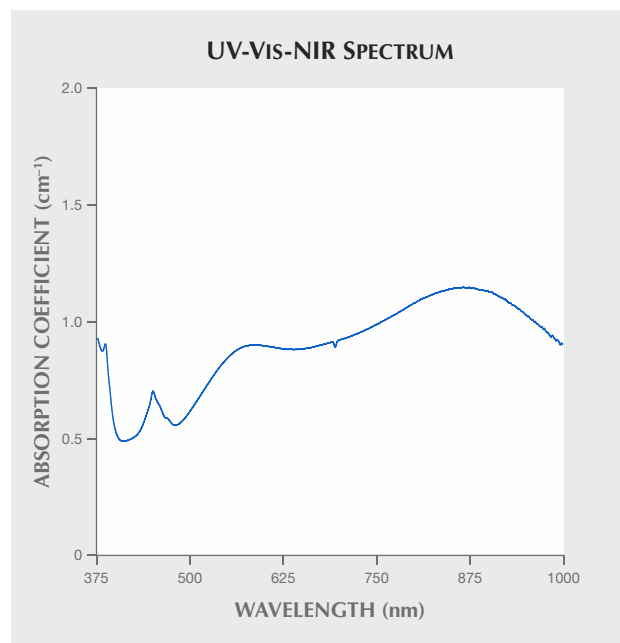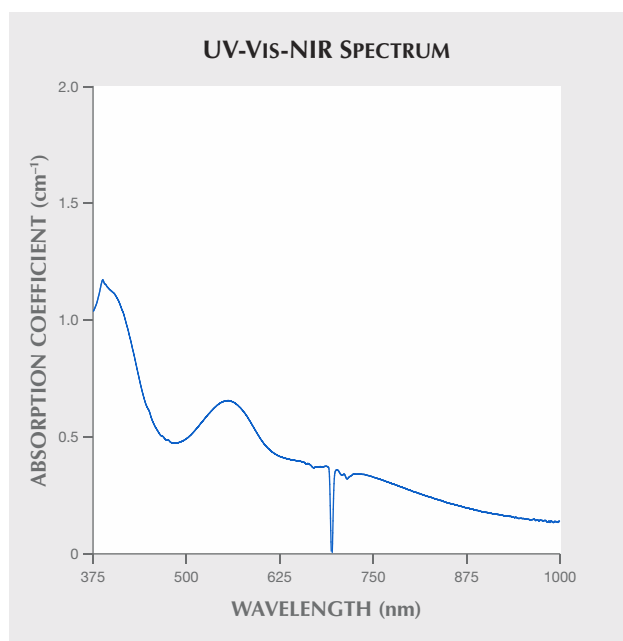
Figure 14. Sample 1 was the only one that did not display a peak at 450 nm.

IR SPECTRUM
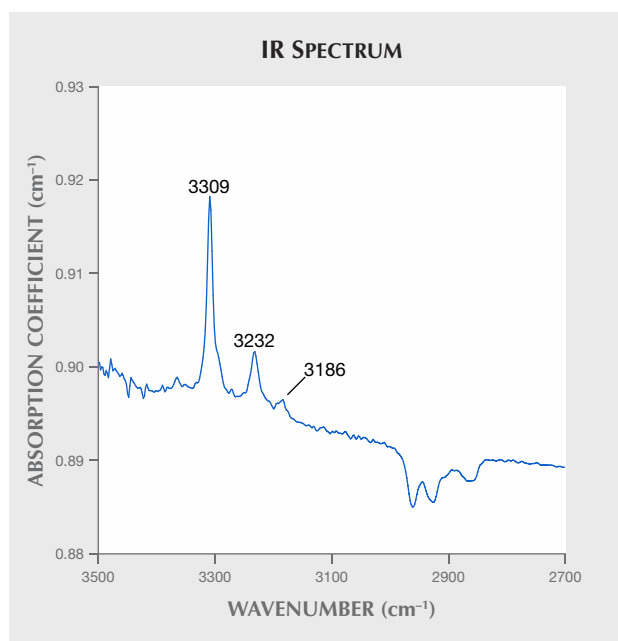
Figure 15. After heating to 1300°C, sample 2 developed a strong 3309 cm⁻¹ series with peaks at 3309, 3232, and 3186 cm⁻¹. In sapphires (and rubies) that have formed in metamorphic environments, the presence of the 3309 peak is not diagnostic; it is the appearance of the 3232 peak that provides strong evidence of artificial heat treatment.

spectra. Future experiments with samples oriented for the c-axis and positioned identically would strengthen these results.

FTIR. Fourier-transform infrared (FTIR) spectroscopy was performed using a Bruker Tensor 27 spectrometer, with the samples placed on a Pike DRIFTS attachment and scanned 64 times at a resolution of 4 cm⁻¹. Spectra were obtained before heating and after heating at each temperature, with the following results:

- In their unheated state and after heat treatment to 800°C and 900°C, none of the stones showed significant peaks.
- After heating to 1000°C, two of the samples started to show diagnostic peaks.
- Sample 2 showed very weak peaks at 3309 and 3232 cm⁻¹. Once it was heated to 1100°C, these features became more prominent. This trend continued after heating to 1300°C, where in addition to the 3309 and 3232 cm⁻¹ peaks, the 3186 cm⁻¹ appeared in this series (figure 15). After heating to 1500°C, only the 3309 and 3232 cm⁻¹ peaks were present. The presence of the 3309 peak by itself is not diagnostic evidence of artificial heat treatment in sapphire and ruby sourced from metamorphic rocks; however, the presence of a 3232 peak above the noise floor strongly suggests the stone has been artificially heated.

- Sample 8 displayed only a very weak 3309 cm⁻¹ peak after heating to 1000°C and did not display diagnostic features after heating at any other temperatures.
- Once the stones were heated to 1100°C, two more stones started to show additional features.
- Sample 4 displayed weak peaks at 3309 and 3232 cm⁻¹, which became more prominent after heating to 1300°C (figure 16). After heating to 1500°C, no diagnostic features were evident.
- Sample 6 also started displaying a very weak 3309 cm⁻¹ peak at 1100°C, which was also present after heating at 1300°C and 1500°C.
- The remaining eight stones showed no diagnostic features after heating at all temperatures.

Overall, the results suggest that the appearance of the 3309 cm⁻¹ series (with a 3232 cm⁻¹ peak) can be indicative of heat treatment in low-Fe metamorphic corundum. However, the lack of these features does not necessarily mean that a stone has not been heated. It is important to note that in high-Fe sapphires from basalt-related origins, a weak to medium 3309 cm⁻¹ series with the 3232 cm⁻¹ peak can often

IR SPECTRUM

Figure 16. A medium 3309 cm⁻¹ peak developed in sample 4 after heating to 1300°C.

be found naturally and is therefore not a reliable indication of heat treatment (Hughes et al., 2017).

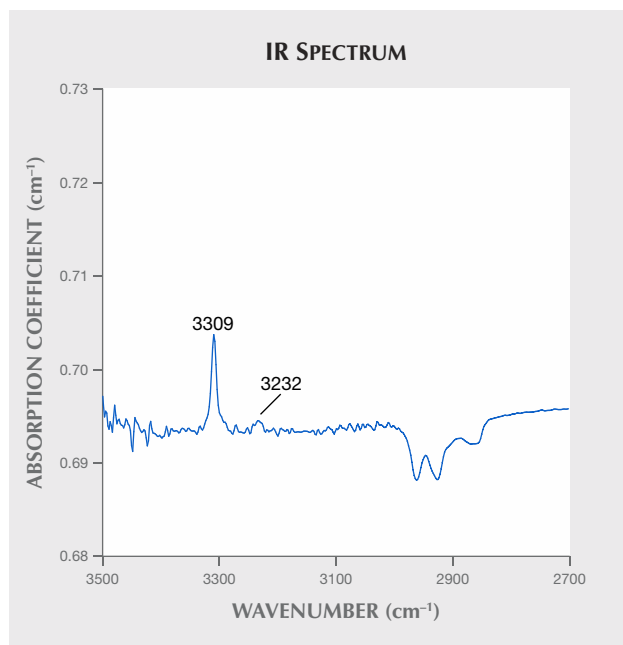**Limitations of FTIR Results.** As with the results of UV-Vis-NIR testing, the FTIR results may be limited by the fact that the stones were not oriented to the c-axis and the spectra were not taken in the exact same position.

Fluorescence Reactions. Examining the fluorescence reactions of the stones was a major area of focus for this project, with a particular emphasis on short-wave reactions. The value of examining short-wave UV fluorescence in the study of corundum has been recognized for decades (Crowningshield, 1966), and it has been connected to the detection of heat treatment.

Fluorescence was initially observed using an Ultraviolet Products UVLS-26 EL Series UV lamp using a six-watt bulb, with a long-wave light source at 365 nm and a short-wave light source at 254 nm. If a reaction was found, we also examined the sample with the Magilabs custom-designed deep-UV fluorescence system, consisting of a fluorescence microscope setup equipped with a high-intensity pulsed xenon flash lamp with an interference bandpass filter at 228 nm.

Short-wave fluorescence photomicrographs were taken with a Canon EOS 6D camera connected to a Wild M400 microscope and the Magilabs custom-designed deep-UV fluorescence system.

Long-Wave Fluorescence. Under long-wave UV, about half of the unheated stones were inert and showed no reaction. The other half showed mostly weak to medium zoned orange fluorescence. Heating did not produce any significant changes in the long-wave fluorescence reaction of most samples.

The one exception to this pattern was in sample 1, a stone with strong pink and blue color zoning. The pink zone (which turned orange after heat treatment) fluoresced a strong orange, and the blue zones fluoresced a medium to strong red. The stone did not show significant change in long-wave fluorescence after heating.

Short-Wave Fluorescence. Prior to heat treatment, all of the stones were inert under short-wave fluorescence. We initially checked for fluorescence in our standard UV light box. If we saw any sign of fluorescence, we photographed it with the Magilabs custom-designed deep-UV fluorescence system. It was not until the stones were heated to 1000°C that we started to see changes, where some stones began to display a weak chalky blue fluorescence (figures 17–19). This chalky appearance has been associated with heat treatment in sapphires.

In natural, heated sapphires, this chalky fluorescence is associated with the presence of rutile. Almost all natural blue sapphires contain some exsolved rutile (TiO_2). When these sapphires are heated, there is a slow dissolution of rutile, which creates Ti^{4+} ions and Ti-Al vacancies. These will fluoresce when illuminated in short-wave UV. The strongly chalky areas will follow the zoning patterns of the rutile, and the strongest fluorescence will be in areas with the lowest Fe and highest rutile concentrations (Hughes et al., 2017, pp. 154–155).

Once we started using the Magilabs fluorescence unit, we realized the reactions were much stronger and clearer than in our Ultraviolet Products UVLS-26 EL Series unit. Thus, after this round of heating at 1000°C, we started looking at all stones in the Magilabs system. We found that two of the stones appeared inert in the regular unit but showed weak chalky fluorescence in the Magilabs unit.

By the time we heated to 1300°C, all 12 stones were showing at least a weak zoned chalky blue fluorescence reaction. A few of these stones appeared inert in our regular UV light box. Again, when we checked each stone in our Magilabs system, we began to see reactions that were either extremely difficult or impossible to see in our regular fluorescence unit. It is possible that the fluorescence was apparent
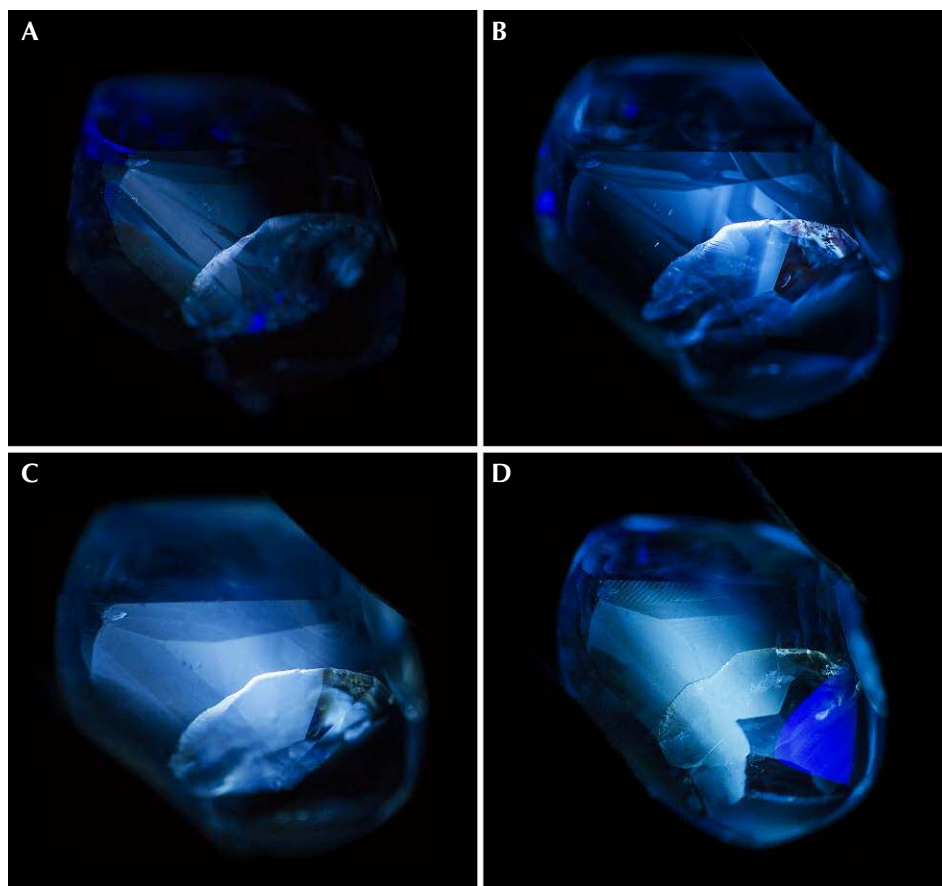
Figure 17. A: Once sample 6 was heated to 1000°C, we observed a weak zoned chalky fluorescence. The stronger whitish band is the fluorescence in a small fissure on one end of the stone, but an angular zoned chalky blue fluorescence can be seen in the body of the stone. B: After heating to 1100°C, the angular chalky fluorescence became more intense. C: By 1300°C the fluorescence reaction was even stronger, with the angular zoned areas barely visible as the stone took on a more chalky appearance overall. D: At 1500°C, the reaction was similar to the previous round, with an overall chalky blue appearance. A small triangular zone on one end, which was not apparent in previous rounds, may be due to the fact that we slightly repolished the stone to remove surface debris. Photos by E. Billie Hughes.

after heating below 1000°C (the temperature where we first noticed it) but that we did not see the reaction because our regular UV unit was not strong enough. In future experiments, we plan to conduct observations with the Magilabs unit after all stages of heating.

In fact, some stones that appeared inert even in this Magilabs unit showed extremely weak chalky fluorescence once photographed. It seems that our camera was able to capture reactions that are so weak as to be almost imperceptible to the human eye. This suggests that there is considerable information we may be missing when using the traditional UV light box. The development of better instruments to examine short-wave UV reactions would be a significant stride for gemology, and we believe this improvement could be of great use in determining heat treatment in corundum.

CONCLUSIONS

Heat treatment from lower to higher temperatures can have a significant impact on the color of metamorphic blue sapphires from Madagascar. In our study, temperatures between 800 and 1100°C in air

lightened the blue color, while higher temperatures, which can dissolve rutile, created deeper, more saturated blues.

Figure 18. Sample 10 did not show any short-wave fluorescence reaction until it was heated to 1000°C. At this point it displayed a strong chalky blue reaction, with complex angular fluorescent zones. Photo by E. Billie Hughes.
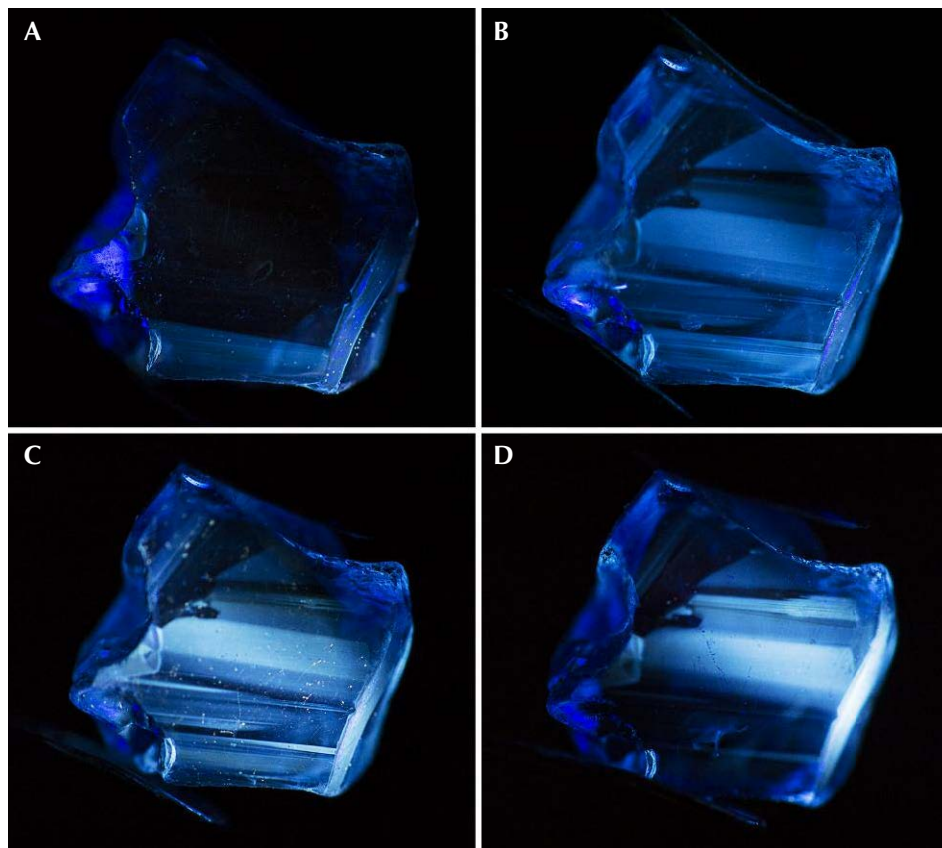
Figure 19. A: Sample 11 began to show a short-wave fluorescence reaction after heating to 1000°C. This was mainly limited to one side of the stone, where a chalky blue band can be seen. B: After heating to 1100°C, the chalky blue reaction became stronger and more widespread, with chalky blue bands across the stone. C: After heating to 1300°C, the reaction became even stronger, with a brighter, chalkier appearance. D: By the last round of heating at 1500°C, the fluorescence reaction still appears extremely strong and chalky, although the band at the bottom is less evident. This may be due to slight repolishing to remove surface debris. The overall appearance is still of a clear, strong chalky fluorescence reaction. Photos by E. Billie Hughes.

Detection of this treatment is possible by a combination of observing inclusion features and short-wave UV fluorescence, as well as infrared spectroscopy. We believe that the study of short-wave UV fluorescence shows great promise in determining heat treatment in sapphire. It would be beneficial to the gemological community to find more detailed and accurate ways to observe this reaction at stronger power and with magnification.

It is important to note that the authors found that for many of the stones, the UV-Vis-NIR spectra showed a shift from primarily having peaks be-tween 550–600 nm before heating to having a strong peak at 880 nm after heating. The experiments suggest that this 880 nm peak, which has often been correlated with sapphires of basalt-related origin, can also occur in heated metamorphic sapphires. Therefore, this peak should always be taken into consideration with other features before drawing a conclusion.

Our study of these stones demonstrates that heated metamorphic Madagascar blue sapphire can often be separated from unheated material, even when heated to temperatures as low as 800°C.

REFERENCES

Crowningshield R. (1966) Developments and Highlights at the Gem Trade Lab in New York: Unusual items encountered [sapphire with unusual fluorescence]. *G&G*, Vol. 12, No. 3, p. 73.

Emmett J., Douthit T. (1993) Heat treating the sapphires of Rock Creek, Montana. *G&G*, Vol. 29, No. 4, pp. 250–272, http://dx.doi.org/10.5741/GEMS.29.4.250

Hughes R.W., Emmett J.L. (2004) Fluxed up: The fracture healing of ruby. *The Guide*, Sept.–Oct., Vol. 23, No. 5, Part 1, pp.1, 4–9.

Hughes R.W., Pardieu V., Schorr D. (2006) Sorcerers and sapphires: A visit to Madagascar. *The Guide*, Jan.–Feb., Vol. 25, No. 1, pp. 1, 4–6.

Hughes R.W., Manorotkul W., Hughes E.B. (2017) *Ruby & Sapphire: A Gemologist's Guide.* RWH Publishing/Lotus Publishing, Bangkok, 816 pp.

Kröner A., Windley B.F., Jaeckelt P., Brewer T.S., Razakamanana T. (1999) New zircon ages and regional significance for the evolution of the Pan-African orogen in Madagascar. *Journal of the Geological Society*, Vol. 156, No. 6, pp. 1125–1135, http://dx.doi.org/10.1144/gsjgs.156.6.1125

Krzemnicki M., Cartier L.E., Wang H.A.O., Zhou W., Lefèvre P. (2017) Sapphires from a new deposit at Bemainty near Ambatondrazaka in Madagascar. *InColor*, No. 35, pp. 44–47.

Link K. (2015) Age determination of zircon inclusions in faceted sapphires. *Journal of Gemmology*, Vol. 34, No. 8, pp. 692–700.

Pardieu V., Vertriest W., Weeramonkhonlert V., Raynaud V., Atikarnsakul U., Perkins R. (2017) Sapphires from the gem rush Bemainty area, Ambatondrazaka (Madagascar). *GIA News from Research*, https://www.gia.edu/doc/Sapphires-Gem-Rush-Bemainty-area-Ambatondrazaka-Madagascar.pdf

Peretti A., Peretti F. (2017) Identification of sapphires from Madagascar with inclusion features resembling those of sapphires from Kashmir. *InColor*, No. 35, pp. 34–42.

Perkins R., Pardieu V. (2016) Gem News International: Sapphire rush near Ambatondrazaka, Madagascar. *G&G*, Vol. 52, No. 4, pp. 429–430.

Rakotondrazafy A.F.M., Giuliani G., Ohnenstetter D., Fallick A.E., Rakotosamizanany S., Andriamamonjy A., Ralantoarison T., Razanatseheno M., Offant Y., Garnier V., Maluski H., Dunaigre C., Schwarz D., Ratrimo V. (2008) Gem corundum deposits of Madagascar: A review. *Ore Geology Reviews*, Vol. 34, No. 1–2, pp. 134–154, http://dx.doi.org/10.1016/j.oregeorev.2007.05.001

Worawitratanagul P. (2005) Heat treatment of sapphires from Ilakaka, Madagascar. Master's thesis, Chiang Mai University, Thailand.

For online access to all issues of GEMS & GEMOLOGY from 1934 to the present, visit:

gia.edu/gems-gemology

Black Nephrite Jade from Guangxi, Southern China

Qian Zhong, Zongting Liao, Lijian Qi, and Zhengyu Zhou

Twelve black nephrite samples collected from the Guangxi region of southern China were investigated by standard gemological testing, polarized microscopy, scanning electron microscopy, and electron microprobe analysis, as well as infrared, Raman, and ultraviolet/visible/near-infrared spectroscopy. Originating from Ca-skarn contact metasomatism between limestone bearing siliceous rock and diabase intrusions, black nephrite from Guangxi consists mainly of actinolite or ferro-actinolite and minor stilpnomelane, andradite, apatite, epidote, quartz, diopside, pyrrhotite, and pyrite. Its high refractive index (1.625–1.650) and specific gravity (3.015–3.405), as well as its black color in natural light for plate samples and greenish yellow/brownish yellow or pale green/yellowish green/green color in transmitted light for thin-section samples, are primarily attributable to a high iron content: 11.67–25.75 wt.% Fe oxides and a Mg/(Mg + Fe^{2+}) ratio of 0.765–0.343. Mid- and near-infrared spectra and Raman spectra are characterized by four vibration bands corresponding to hydroxyl groups coordinated to three cations in M_1 and M_3 positions for $(M_1M_1M_3)$OH combinations (Mg)$_3$OH, (Mg$_2$Fe^{2+})OH, (MgFe$^{2+}_2$)OH, and (Fe^{2+})$_3$OH. Their relative intensities further indicate different iron contents and isomorphous substitution of Fe^{2+} for Mg^{2+} ions.

Nephrite is an essentially monomineralic rock composed primarily of tremolite-actinolite [Ca$_2$(Mg,Fe)$_5$Si$_8$O$_{22}$(OH)$_2$] amphiboles in a felted microcrystalline habit (Leake et al., 1997), making it greasy, tough, and easy to carve. Nephrite mainly forms in two settings (Harlow and Sorenson, 2005; Harlow et al., 2014). The first is dolomite replacement by silicic fluids commonly associated with granitic plutonism (i.e., D-type). Important deposits occur at Xinjiang, China (Liu et al., 2011a, 2015); Chuncheon, South Korea (Yui and Kwon, 2002); and Cowell, South Australia (Flint and Dubowski, 1990). The other type of setting is serpentinite replacement by Ca-metasomatism at contacts with more silicic rock (i.e., S-type). Related deposits include Siberia, Russia (Prokhor, 1991); South Island, New Zealand (Wilkins et al., 2003); British Columbia, Canada (Leaming,1998); and Fengtien, Taiwan (Yui et al., 2014). Nephrite found in the southern Chinese region of Guizhou forms in a different setting, within the metasomatic zone between diabase and limestone bearing siliceous rock (Yang, 2013).

In 2011, a new nephrite deposit was discovered in southern China at Yantan Town, Dahua County, in the Guangxi Zhuang Autonomous Region (Li et al., 2011). The Guangxi deposit is separated from the Guizhou deposit by the Hongshui River. Nephrite from Guangxi comes in a wide variety of colors such as white, green, brown, and black, and some varieties exhibit either a banded structure or a dendritic pattern (Wang et al., 2012; Yin et al., 2014). Among them, the nephrite with a homogeneous, pure black color reminiscent of Chinese calligraphic ink is the most prized by jade carvers and traders (figure 1). Several scholars have studied the mineralogy, spectroscopy, and genesis of black nephrite from Guangxi (Wang et al., 2014; Mo and Mao, 2016; Peng et al., 2017). The results suggest that it consists mainly of actinolite or ferro-actinolite and features a high iron content. Wang et al. (2014) proposed that the Guangxi deposit is a skarn-type occurrence and conducted preliminary analysis of its formation process. But few studies have discussed how high iron content influences its gemological properties or vibrational spectra. Moreover, detailed data and systematic research on its formation mechanism are still limited.

This study employed standard gemological testing, polarized microscopy, scanning electron microscopy, electron microprobe analysis, infrared spectroscopy, Raman spectroscopy, and ultraviolet/

Figure 1. A zun (Chinese ritual wine vessel) ornately carved from Guangxi black nephrite in the form of a tiger squatting on all fours with a bird on its back. Photo courtesy of Hongwei Ma.

visible/near-infrared spectroscopy to investigate the gemological properties, petrographic features, microstructures, chemical compositions, and vibrational spectra of black nephrite from Guangxi. The results demonstrate relationships between iron content and gemological properties as well as vibrational spectra. Additionally, the authors propose evidence for its deposit type and discuss the source rocks involved in its formation. This study will help in the identification of black nephrite from Guangxi and provide a basis for further research on the formation mechanism of nephrite from southern China.

GEOLOGICAL SETTING

Located in the intersection zone of the Tethys Tectonic Domain and the Circum-Pacific Tectonic Region, the Guangxi black nephrite deposit is between the southeast margin of the Yangtze Craton and the South China Caledonian Fold Belt, and adjacent to the Sanjiang Orogenic Belt in the southwest (Bureau of Geology and Mineral Resources of Guangxi Zhuang Autonomous Region, 1985; figure 2). According to the geologic map from the Chinese National Geological Archives (figure 3), the strata exposed here consist mainly of marine carbonate
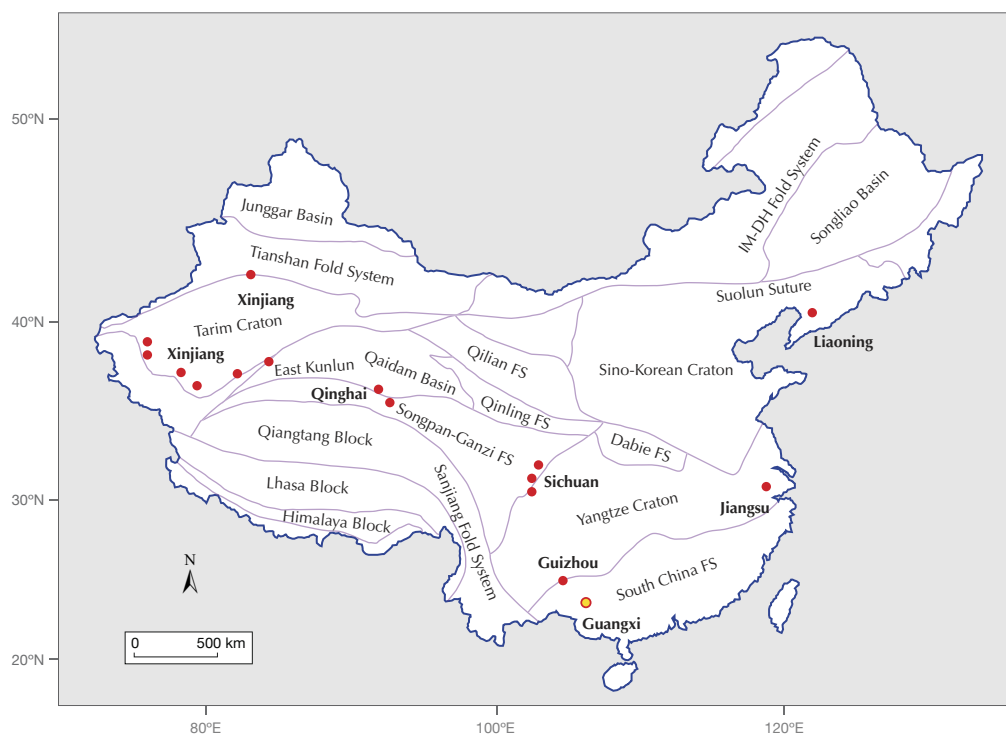
Figure 2. China is famous for its large-scale and high-quality nephrite production, as well as its long history of exquisite carving. Locations of the main deposits in Guangxi (this study), Guizhou (Yang, 2013), Xinjiang (Tang et al., 1994), Qinghai (Wang et al., 2007), Liaoning (Wang et al., 2002), Sichuan (Wang, 1993; Lu, 2005; Jin et al., 2014), and Jiangsu (He et al., 2002) are shown on this tectonic map of China (after Chen et al., 2010).

Figure 3. Regional geologic map of the Guangxi black nephrite primary deposit. The deposit occurs at the contact zone between marine carbonate rock bearing chert/siliceous rock/clay rock deposited from the Upper Carboniferous to Lower Permian periods (C_2–P_1) and diabase emplaced during the late Permian period ($\beta\mu_4$). The diabase displays an obvious circular structure in anticlines extending northwest to southeast and is controlled or transformed by several faults extending northwest by north, northeast by north, and northeast by east (modified after the 1:200000 geologic map from the National Geological Archives of China).

rocks deposited from the early Carboniferous to Middle Triassic periods (359–237 Ma). Basic igneous rock (i.e., diabase) emplaced during the late Permian period (260–252 Ma) within the Upper Carboniferous to Permian (323–252 Ma) limestone bearing banded chert/dolomite and Lower Permian (299–272 Ma) siliceous rock/clay rock/limestone bearing banded chert display an obvious circular structure in anticlines[1]. These anticlines extend northwest to southeast and are controlled or transformed by several faults extending northwest by north, northeast by north, and northeast by east. Black nephrite is situated in the southwest limb of an anticline and occurs at the contact zone between diabase[2] and carbonate rock.

According to local miners, the black nephrite was first discovered under houses in the village of Xiannv, and this was considered a secondary deposit. Mining of the primary deposit started in late 2012 but was prohibited by the local government the following year for conservation reasons. Fieldwork for this

---

[1]In structural geology, an *anticline* is a type of fold that is an arch-like shape with the oldest rock layer in the center and the younger rock layer lying on either side symmetrically. A typical anticline is convex up, in which the curvature is greatest at the hinge or crest, and the limbs are the sides of the fold that dip away from the hinge. On the regional geologic map of the Guangxi black nephrite primary deposit, the progressing age of the rock strata toward the core (from the Triassic to Carboniferous periods) is evidence of anticlines. In addition, each anticlinal fold plunges in all directions to form a circular or elongate structure, and the nephrite deposit is situated in the southwest limb of the middle fold, which extends northwest to southwest.

[2]*Diabase* (or dolerite or microgabbro) is a mafic, holocrystalline, shallow intrusive rock commonly occurring as dikes and sills and exhibiting a typically fine texture of euhedral lath-shaped plagioclase crystals set in a finer matrix of augite, with minor olivine, magnetite, and ilmenite. For example, igneous rocks in the Guangxi black nephrite deposit are diabase emplaced during the late Permian period.

Figure 4. Characteristics of the Guangxi primary deposit. A: Layers include a small exposed outcrop of marble and altered marble subjected to metasomatic diopsidization, silicification, albitization, and tremolitization/actinolitization; residual thin-bedded sedimentary sandstone/shale; and orebody bearing black nephrite. B: Marble formed by thermal metamorphism of limestone showing medium- to fine-grained crystalloblastic texture and flashes of calcite on cleavage planes. C: An alteration zone with a black nephrite vein about 30 cm thick underlies the altered marble. D: The banded structure of the alteration zone consists of typical metamorphic minerals such as garnet, clinopyroxene, stilpnomelane, and amphibole. E: A fracture in the black nephrite shows its compact and fine-grained texture. F: Diabase underlying the black nephrite vein shows the typical texture of lath-shaped plagioclase crystals set in a matrix of clinopyroxene. Photos by Qian Zhong and Lijian Qi.

study was done in August 2017 and August 2018 at the primary deposit, located 538 meters above sea level at 24°01'38.23"N, 107°27'39.61"E. The deposit contained many scattered diabase fragments due to previous mining activities. A small exposed outcrop of marble (figure 4B) and altered marble (figure 4C) was subjected to metasomatic diopsidization, silicification, albitization, and tremolitization/actinolitization. Residual thin-bedded sedimentary sandstone/shale and orebody bearing black nephrite are distributed from top to bottom (figure 4A). Underlying the altered marble is an alteration zone with an obviously banded structure and spatial inhomogeneity (figures 4C and 4D). Typical metamorphic minerals such as garnet, clinopyroxene, stilpnomelane, and amphibole occur in different bands. A black nephrite vein about 30 cm thick was layered in the lower part

(figure 4C). A fracture revealed that the jade is very compact and fine-grained (figure 4E). Diabase is mainly distributed under the vein, and the typical texture of the lath-shaped plagioclase crystals set in a matrix of clinopyroxene could be observed in the fracture (figure 4F).

Because of the subtropical climate, a thin yellowish brown to reddish brown weathering crust similar to iron rust is very common at the surface of the rocks in the primary deposit (figures 5A and 5B). The weathering crust on the black nephrite rocks from the secondary deposit has a yellow color like that of loess mud (figures 5C and 5D). Therefore, black nephrite rough mined from the Guangxi primary and secondary deposits is referred to in the market as "iron rust crust rock" and "loess mud crust rock," respectively.
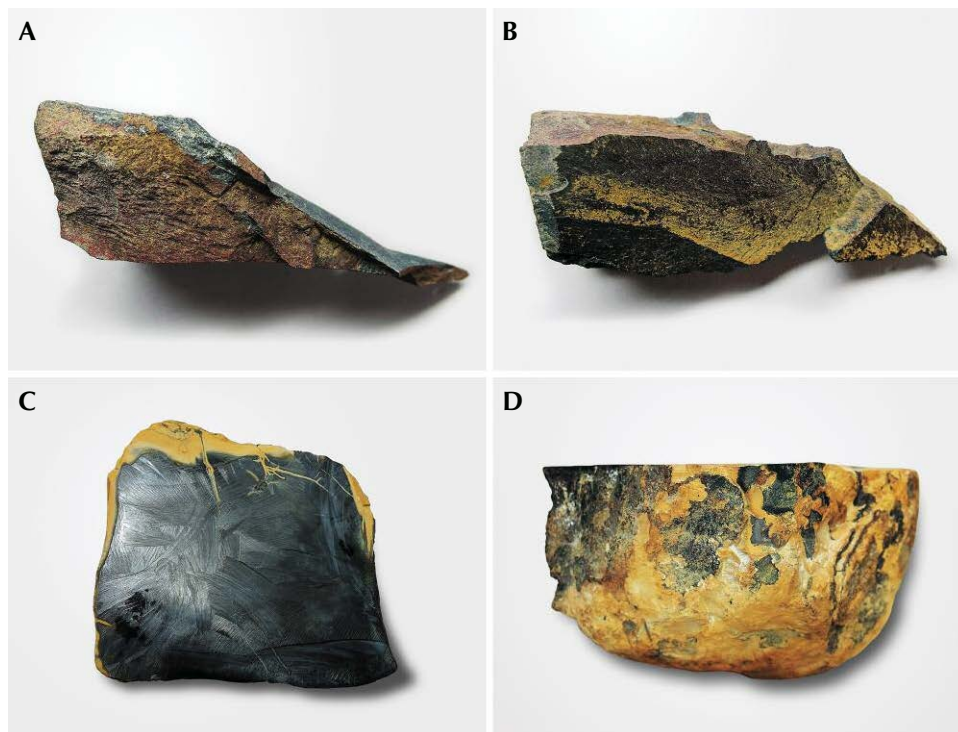
Figure 5. A and B: Black nephrite rough from Guangxi with a typical angular shape. These were collected from the jade vein in the primary deposit shown in Figure 4 and then analyzed as samples GB-11 and GB-12, showing a thin yellowish brown to reddish brown weathering crust similar to iron rust. C and D: Black nephrite jade rough with a typical round shape, collected from the secondary deposit. The rock weighs 2.1 kg and shows a yellow weathering crust similar to loess mud. Photos by Qian Zhong.

MATERIALS AND METHODS

Materials. Twelve pieces of black nephrite rough (GB-01 through GB-12) from Guangxi were investigated for this study. GB-01 through GB-09 were supplied by local miners, and GB-10 through GB-12 were collected from the primary deposit during fieldwork. We cut and polished the rough into plate samples, 1.10–6.13 mm thick and weighing 0.84–38.11 ct (see table 1 photos in natural light), and further polished them into thin sections with various thicknesses to meet the requirements of different measurements.

Analytical Methods. All measurements were collected with equipment at the Laboratory of Gem and Technological Materials of Tongji University, unless otherwise specified. The refractive indices of 12 black nephrite plate samples were measured using a refractometer (by normal reading from flat wafers), and specific gravity was measured hydrostatically with an electronic balance. Ultraviolet fluorescence reactions were examined with a long-wave/short-wave UV lamp. Color, luster, and transparency of the plate samples were observed in natural light, and the color of the thin sections (0.73–0.97 mm thick) was examined in transmitted light.

Petrographic features were studied with a Nanjing Jiangnan Novel Optics BM2100 polarized light microscope. Six thin sections (GB-04, GB-05, GB-06, GB-08, GB-09, and GB-10) with a standard thickness of 0.03 mm were observed in both plane- and cross-polarized light. Microstructures on the fractured surface of sample GB-06 were observed using a Hitachi S-4700 scanning electron microscope (SEM) with an accelerating voltage of 15 kV at the Analysis and Testing Center of Suzhou University.

In Brief

- Black nephrite from Guangxi in southern China exhibited a yellow or green color in transmitted light for thinner samples and displayed a high refractive index and specific gravity due to a high iron content.

- The relative intensities of $(Mg)_3OH$, $(Mg_2Fe^{2+})OH$, $(MgFe^{2+}_2)OH$, and $(Fe^{2+})_3OH$ vibration bands in the mid- and near-infrared and Raman spectra indicate Mg^{2+}-Fe^{2+} isomorphous substitution in M_1 and M_3 positions.

- Mineral assemblages including actinolite/ferro-actinolite, andradite, diopside, and epidote suggest a Ca-skarn metasomatism occurring at the contact zone between diabase intrusions and limestone bearing siliceous rock.

Backscattered electron (BSE) images and chemical compositions of minerals in 12 black nephrite thin

TABLE 1. Gemological properties and mineral compositions of black nephrite from Guangxi.

Sample no.	Weight (ct)	Luster	Transparency	UV fluorescence	Refractive index	Specific gravity	Natural light[a]	Transmitted light[b]	Mineral composition[c]
GB-01	0.84	Greasy to vitreous	Opaque	Inert	1.645	3.141			Actinolite (>98%)
GB-02	1.41	Greasy to vitreous	Opaque	Inert	1.645	3.149			Actinolite (>98%)
GB-03	2.07	Greasy to vitreous	Opaque	Inert	1.645	3.148			Actinolite (92–95%), stilpnomelane (5–8%)
GB-04	27.50	Greasy to vitreous	Opaque	Inert	1.625	3.062			Actinolite (75–80%), diopside (13–15%), quartz (5–8%), stilpnomelane (1–3%)
GB-05	23.09	Greasy to vitreous	Opaque	Inert	1.640	3.015			Actinolite (65–70%), stilpnomelane (23–25%), epidote (3–5%), apatite (1–3%), andradite (<1%)
GB-06	11.23	Greasy to vitreous	Opaque	Inert	1.645	3.146			Actinolite (97–99%), apatite (1–3%)
GB-07	23.71	Greasy to vitreous	Opaque	Inert	1.647	3.161			Ferro-actinolite (95–97%), stilpnomelane (3–5%)
GB-08	17.52	Greasy to vitreous	Opaque	Inert	1.650	3.405			Ferro-actinolite (60–65%), Fe sulfides (27–30%), stilpnomelane (8–10%)
GB-09	15.59	Greasy to vitreous	Opaque	Inert	1.650	3.251			Ferro-actinolite (75–80%), Fe sulfides (10–15%), stilpnomelane (3–5%), andradite (3–5%), diopside (<1%), quartz (<1%)
GB-10	8.80	Greasy to vitreous	Opaque	Inert	1.626	3.015			Actinolite (92–95%), stilpnomelane (5–8%)
GB-11	38.11	Greasy to vitreous	Opaque	Inert	1.645	3.142			Actinolite (93–95%), stilpnomelane (3–5%), apatite (1–3%)
GB-12	30.00	Greasy to vitreous	Opaque	Inert	1.648	3.197			Ferro-actinolite (97–99%), stilpnomelane (1–3%)

[a]Photos of plate samples with a thickness of 1.10 to 6.13 mm, taken in natural light.
[b]Photos of thin-section samples with a thickness of 0.73 to 0.97 mm, taken in white transmitted light.
[c]Volume percentage estimated by observing thin-section samples using a polarized light microscope or a gem microscope.

TABLE 2. Electron microprobe analysis and calculations of actinolite and ferro-actinolite in black nephrite from Guangxi.

Sample	GB-01	GB-02	GB-03	GB-04	GB-05	GB-06	GB-07	GB-08	GB-09	GB-10	GB-11	GB-12
Oxides (wt.%)												
SiO_2	54.07	53.44	54.20	55.69	53.93	54.65	53.36	52.33	52.33	56.14	55.09	53.38
Al_2O_3	0.33	0.36	0.33	0.47	0.39	0.27	0.32	0.43	0.27	0.32	0.24	0.31
TiO_2	0.02	0.01	0.01	0.02	0.01	0.02	bdl[a]	0.03	0.01	0.02	0.01	0.01
Cr_2O_3	0.01	0.01	bdl	0.01	0.02	0.01	bdl	0.02	0.01	0.01	0.01	0.01
FeO^b	19.42	19.49	19.46	11.67	19.31	19.50	21.70	25.61	25.75	15.31	19.66	23.39
MgO	11.48	11.25	11.45	16.90	12.08	11.19	9.70	7.47	7.23	14.13	11.15	8.94
MnO	0.21	0.20	0.21	0.18	0.23	0.25	0.24	0.21	0.16	0.33	0.20	0.19
CaO	11.55	11.29	11.53	12.31	11.60	11.36	10.85	11.43	11.60	11.09	11.25	11.74
Na_2O	0.09	0.09	0.06	0.07	0.10	0.08	0.13	0.11	0.08	0.10	0.17	0.05
K_2O	0.05	0.05	0.05	0.04	0.08	0.25	0.82	0.04	0.02	0.48	0.70	0.03
Total	97.22	96.18	97.29	97.36	97.75	97.59	97.12	97.68	97.46	97.92	98.47	98.04
Ions per 23 oxygens												
Si^{4+}	7.987	7.975	7.997	7.923	7.898	8.055	8.015	7.947	7.993	8.049	8.080	7.995
$^{IV}Al^{3+}$	0.013	0.025	0.003	0.077	0.068	bdl	bdl	0.053	0.007	bdl	bdl	0.005
ΣT	8.000	8.000	8.000	8.000	7.966	8.055	8.015	8.000	8.000	8.049	8.080	8.000
$^{VI}Al^{3+}$	0.044	0.038	0.055	0.002	bdl	0.046	0.057	0.025	0.041	0.054	0.041	0.050
Ti^{4+}	0.002	0.001	0.001	0.002	0.001	0.002	bdl	0.003	0.001	0.002	0.001	0.001
Cr^{3+}	0.001	0.002	bdl	0.001	0.002	0.001	bdl	0.002	0.002	0.001	0.001	0.001
Fe^{3+}	0.275	0.338	0.276	0.288	0.450	0.180	0.229	0.259	0.137	0.323	0.080	0.168
Fe^{2+}	2.124	2.094	2.125	1.101	1.915	2.224	2.496	2.993	3.152	1.513	2.332	2.762
Mg^{2+}	2.528	2.502	2.518	3.584	2.637	2.459	2.173	1.691	1.647	3.019	2.439	1.995
Mn^{2+}	0.026	0.025	0.026	0.022	0.029	0.032	0.030	0.027	0.020	0.040	0.024	0.024
ΣC	5.000	5.000	5.001	5.000	5.034	4.944	4.985	5.000	5.000	4.952	4.918	5.001
Ca^{2+}	1.827	1.805	1.822	1.877	1.820	1.793	1.745	1.860	1.899	1.703	1.768	1.883
Na^+	0.025	0.026	0.017	0.020	0.028	0.023	0.038	0.033	0.023	0.027	0.047	0.013
ΣB	1.852	1.831	1.839	1.897	1.848	1.816	1.783	1.893	1.922	1.730	1.815	1.896
K^+	0.010	0.010	0.010	0.007	0.015	0.046	0.156	0.007	0.004	0.088	0.130	0.005
ΣA	0.010	0.010	0.010	0.007	0.015	0.046	0.156	0.007	0.004	0.088	0.130	0.005
$Mg/Mg + Fe^{2+}$	0.543	0.544	0.542	0.765	0.579	0.525	0.465	0.361	0.343	0.666	0.511	0.419
Amphibole	Act[c]	Act	Act	Act	Act	Act	Fe-Act	Fe-Act	Fe-Act	Act	Act	Fe-Act

[a] bdl = below detection limit (0.01 wt.%)
[b] FeO = all iron oxide calculated as FeO
[c] Act = actinolite, Fe-Act = ferro-actinolite

sections (0.03 mm thick) and plate samples were obtained with a JEOL JXA-8230 electron microprobe at the State Key Laboratory of Marine Geology of Tongji University using an accelerating voltage of 15 kV, a beam current of 10 nA, and a beam diameter less than 5 µm in wavelength-dispersive spectrometry mode. Natural and synthetic mineral standards (SPI Supplies) were used to calibrate all quantitative analyses, and a ZAF program was used for data reduction. Two to six points per sample/mineral were analyzed.

Cations per formula unit of amphiboles were calculated based on 23 oxygen atoms and 15 cations. The total iron content was first estimated as FeO, and Fe^{2+}/Fe^{3+} ratios were then estimated by a charge-balance method on a stoichiometric sum of cations (Schumacher and Wang, 2001).

Infrared absorption spectra of 12 plate samples were obtained with a Bruker Tensor 27 Fourier-transform infrared spectrometer. For measurements in the 4000 to 400 cm^{-1} range, nearly 1.5 mg of pow-
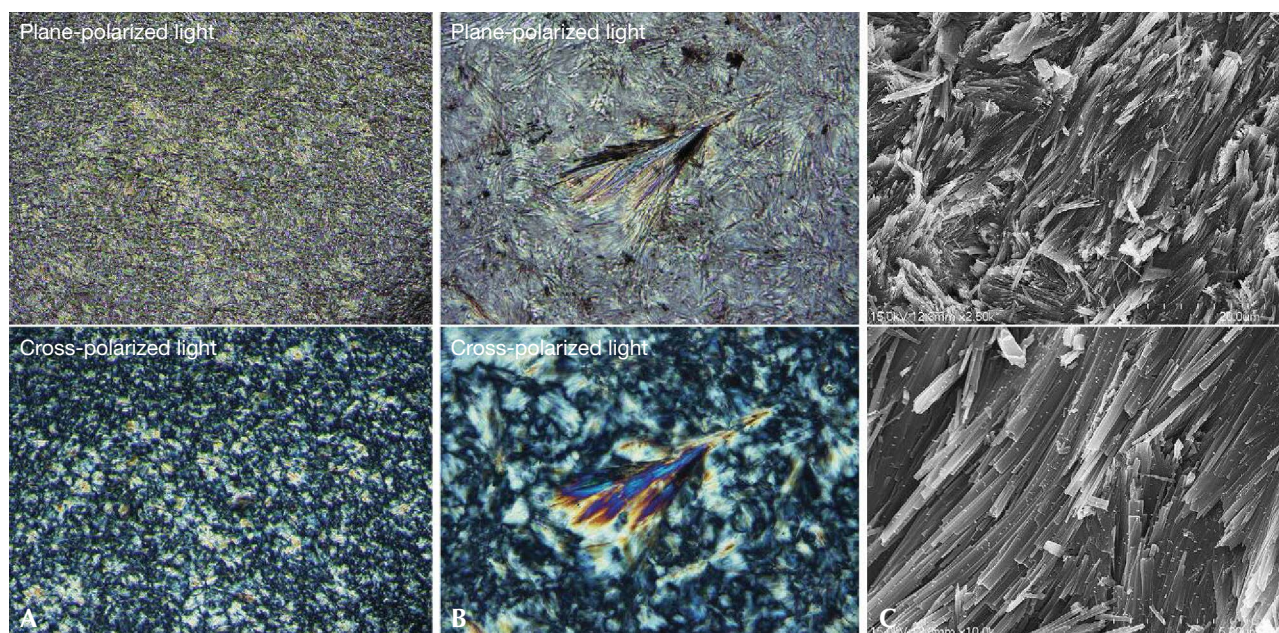
Figure 6. Polarized optical and scanning electron microscope (SEM) images of actinolite in black nephrite from Guangxi. A: In sample GB-06, fine-grained and felted actinolite fibers (top) show first-order orange to second-order bluish green interference colors in cross-polarized light (bottom). Image width 1.36 mm. B: In GB-04, some actinolite fibers are arranged to form a radial structure. Image width 0.68 mm. C: SEM images of GB-06 show actinolite fibers nearly 20×0.5 µm in size (top) and some actinolite fibers arranged to form a parallel structure (bottom). Photos by Qian Zhong.

der was scraped from each sample and dispersed in 150 mg of KBr to prepare pressed pellets. In the 8000 to 4000 cm^{-1} range, thin-section samples (0.73–0.97 mm thick) were tested directly. Both types of spectra were recorded in transmission mode at a resolution of 4 cm^{-1}, a scanning frequency of 10 kHz, and 32 scans. Infrared spectra in the 3700 to 3600 cm^{-1} range were obtained using a Bruker Lumos micro-Fourier-transform infrared spectrometer in attenuated total reflectance mode with medium pressures, at a resolution of 4 cm^{-1} and 32 scans per area (150 × 150 µm^2).

Raman spectra of 12 plate samples were collected using a Horiba Jobin Yvon LabRAM HR Evolution confocal micro-Raman spectrometer equipped with a 532 nm Nd:YAG laser. The laser was focused on the mineral surface using an optical microscope with a 100× objective, and the laser power was around 50 mW. Depolarized spectra in the 4000 to 100 cm^{-1} range were acquired using a grating with 600 gr/mm, a scan time of 20 s, and 3 scans.

Ultraviolet/visible/near-infrared (UV-Vis-NIR) spectra of 12 thin sections (0.13–0.49 mm thick) were obtained with a GEM-3000 spectrophotometer at a resolution of 1 nm, an integration time of 80 ms, a smoothness degree of 2, and 30 scans.

RESULTS

Gemological Properties. The gemological properties of the 12 nephrite samples from Guangxi are listed in table 1. All plate samples (1.10–6.13 mm thick) were black and opaque and exhibited a greasy to vitreous luster in natural light. The thin sections (0.73–0.97 mm thick) showed two different kinds of mottled color in transmitted light. Three samples (GB-01, GB-02, and GB-10) were greenish yellow to brownish yellow, while the remaining nine ranged from pale green to yellowish green to green. All samples were inert to both long- and short-wave UV radiation and displayed an RI of 1.625 to 1.650 and an SG of 3.015 to 3.405. In addition, different amounts of minor minerals were included in almost every sample. The most obvious were minerals with a typical metallic luster and brassy yellow color in plate samples GB-08 and GB-09.

Petrographic Features and Microstructures. Polarized optical images (figures 6A and 6B) combined with electron microprobe data (table 2) showed that the black nephrite samples from Guangxi consisted mainly of fine-grained, felted actinolite with first-order orange to second-order bluish green interference colors in cross-polarized light. (For more on orders of interference col-

The order of interference color is used to describe colors observed in thin sections with a petrographic microscope when identifying minerals, particularly anisotropic minerals. There is a path difference caused by the difference in velocity between the two rays resolved by the anisotropic (doubly refractive) substance between crossed polarizers, which is known as the retardation. The retardation (r) increases linearly with both the thickness (t) of a sample and the birefringence $(n_2–n_1)$: $r = t (n_2–n_1)$. When the two rays enter the upper polarizer, the retardation results in destructive interference for certain wavelengths to give the interference col-

ors. To distinguish the colors produced by different multiples of wavelengths, the interference colors are divided into "orders," with the end of each order marked by a red color representing one full wavelength retardation (Delly, 2003). For example, the first order starts with black and gray, followed by yellow and orange, and ends with "first-order red." The second order is made up of violet, blue, green, yellow, orange, and "second-order red." Interested readers should refer to the Michel-Lévy chart (see Delly, 2003), which shows the interrelationships between thickness, birefringence, and interference colors.

ors, see box A.) Faint light yellow/light green pleochroism was observed in plane-polarized light. SEM images (figure 6C) further indicated that the actinolite fibers were nearly 20 × 0.5 µm in size. Some fibers formed either a radial (figure 6B) or a parallel (figure 6C, bottom) structure. Polarized optical images and BSE images (figure 7) combined with electron microprobe data (table 3) revealed various amounts of Fe sulfides (up to 30%), stilpnomelane (up to 25%), diopside (up to 15%), quartz (up to 8%), epidote (up to 5%), andradite (up to 5%), and apatite (up to 3%) (table 1).

Chemical Compositions. Average chemical compositions and cations per formula unit of amphiboles for the 12 samples are shown in table 2. According to Leake et al. (1997) and Hawthorne et al. (2012), amphiboles in black nephrite belong to the calcic group, characterized by 7.898–8.080 atoms per formula unit (apfu) of Si, 0.004–0.156 apfu of K on the A site, and 1.703–1.899 and 0.013–0.047 apfu of Ca and Na on the B site, respectively. In addition, the $Mg/(Mg + Fe^{2+})$ ratio of amphiboles in GB-07, GB-08, GB-09, and GB-12 ranged from 0.343 to 0.465, and

TABLE 3. Electron microprobe analysis of minor minerals in black nephrite from Guangxi.

Mineral	Andradite		Epidote	Stilpnomelane		Quartz	Diopside		Apatite	Mineral	Pyrrhotite		Pyrite
Sample	GB-05	GB-09	GB-05	GB-05	GB-08	GB-04	GB-04-1	GB-04-2	GB-05	Sample	GB-08	GB-09	GB-09
Oxides (wt.%)										Elements (wt.%)			
SiO$_2$	35.51	37.28	38.24	45.34	45.65	99.05	55.46	52.89	0.29	Fe	61.05	61.14	47.52
Al$_2$O$_3$	0.56	1.56	27.08	5.84	5.71	0.05	0.42	0.14	0.01	Cu	0.05	bdl	bdl
TiO$_2$	bdl[a]	0.01	0.04	bdl	bdl	bdl	0.04	0.01	0.01	Zn	0.02	0.05	0.05
Cr$_2$O$_3$	bdl	bdl	0.01	0.00	0.08	0.01	0.00	0.04	bdl	S	39.83	39.77	52.29
FeO[b]	28.09	26.37	8.77	30.92	34.00	0.41	0.90	9.20	0.40	Total	100.95	100.96	99.86
MgO	0.03	0.14	0.03	5.58	3.43	0.61	17.88	12.28	bdl				
MnO	0.20	0.09	0.12	1.06	0.62	bdl	0.02	0.44	bdl				
CaO	33.14	33.28	23.37	0.51	0.28	0.35	25.75	23.58	55.73				
Na$_2$O	bdl	0.03	bdl	0.18	0.76	bdl	0.18	0.73	bdl				
K$_2$O	bdl	bdl	0.02	1.69	1.82	0.01	0.01	0.02	0.01				
P$_2$O$_5$	bdl	0.02	bdl	bdl	0.01	0.01	0.17	0.03	39.17				
F	bdl	bdl	bdl	bdl	bdl	bdl	0.00	0.00	1.73				
Cl	0.01	0.01	bdl	bdl	bdl	bdl	0.00	0.00	0.47				
Total	97.53	98.78	97.67	91.12	92.35	100.50	100.81	99.36	97.81				

[a]bdl = below detection limit (0.01 wt.%).
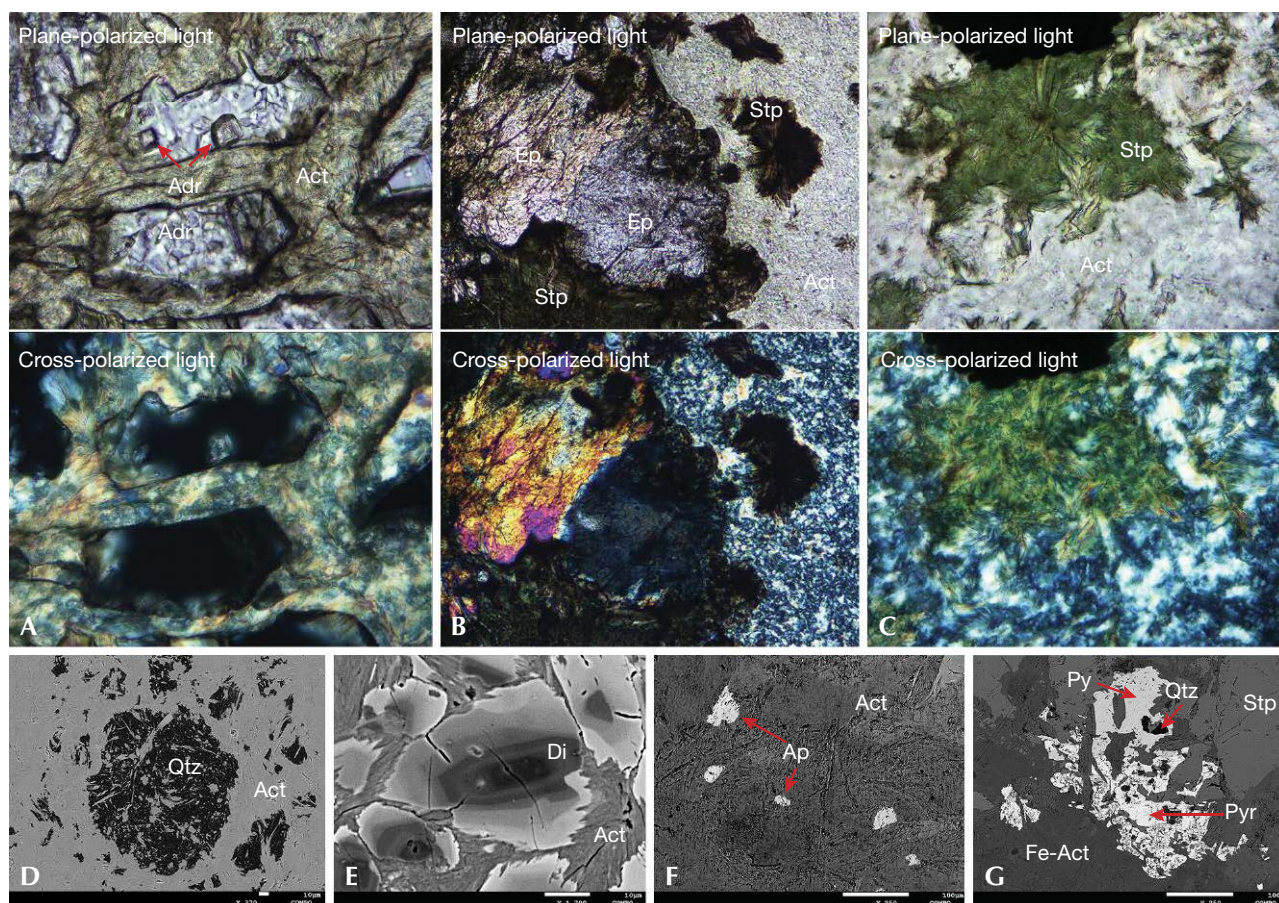[b]FeO = all iron oxide calculated as FeO

Figure 7. Polarized optical and back-scattered electron (BSE) images of minor minerals in black nephrite from Guangxi. A: In sample GB-10, actinolite veins cut the andradite, which includes two euhedral rhombic dodecahedral andradite crystals. Image width 0.68 mm. B: In GB-05, epidote crystals are replaced by fine-grained actinolite and needle-, rod-, or fiber radial-shaped stilpnomelane. Image width 2.72 mm. C: Sample GB-08 consists mainly of brownish green stilpnomelane with radial fiber arrangements. Image width 0.68 mm. D: The BSE image of sample GB-04 shows subhedral quartz crystals or relics up to 120 μm replaced by actinolite along fractures or cracks. E: GB-04 shows actinolite replacing subhedral diopside crystals up to 30 μm with zoning structures due to chemical compositional zonings. F: GB-05 shows anhedral apatite crystals up to 50 μm distributed within actinolite aggregates. G: GB-09 shows irregularly shaped pyrrhotite, pyrite, stilpnomelane, ferro-actinolite, and quartz grains of varying brightness due to different average atomic numbers. Abbreviations: actinolite (Act), ferro-actinolite (Fe-Act), andradite (Adr), epidote (Ep), stilpnomelane (Stp), pyrrhotite (Pyr), pyrite (Py), quartz (Qtz), diopside (Di), and apatite (Ap). Photos by Qian Zhong.

these were identified as ferro-actinolite. The ratio ranged from 0.511 to 0.765 in the remaining samples, which were identified as actinolite. Therefore, the black nephrite from Guangxi was composed mainly of actinolite or ferro-actinolite. All samples contained abundant iron (11.67–25.75 wt.% FeO) and minor manganese (0.16–0.33 wt.% MnO), titanium (below 0.03 wt.% TiO_2), and chromium (below 0.02 wt.% Cr_2O_3).

Representative chemical compositions of minor minerals including andradite, epidote, stilpnomelane, quartz, diopside, apatite, pyrrhotite, and pyrite (figure 7) are shown in table 3. The andradite was composed mainly of CaO (33.14–33.28 wt.%), FeO (26.37–28.09 wt.%), and SiO_2 (35.51–37.28 wt.%). The stilpnomelane (brown in GB-05 and green in GB-08) was characterized by a high iron content (30.92 and 34.00 wt.% FeO, respectively). In diopside, iron was lower and magnesium was higher in the core (table 3, GB-04-1) than in the rim (table 3, GB-04-2), which explains its zoning structure of darkness and brightness in the BSE image (figure 7E). The pyrrhotite in sample GB-09 had a typical chemical composition of 61.14 wt.% iron and 39.77 wt.% sul-
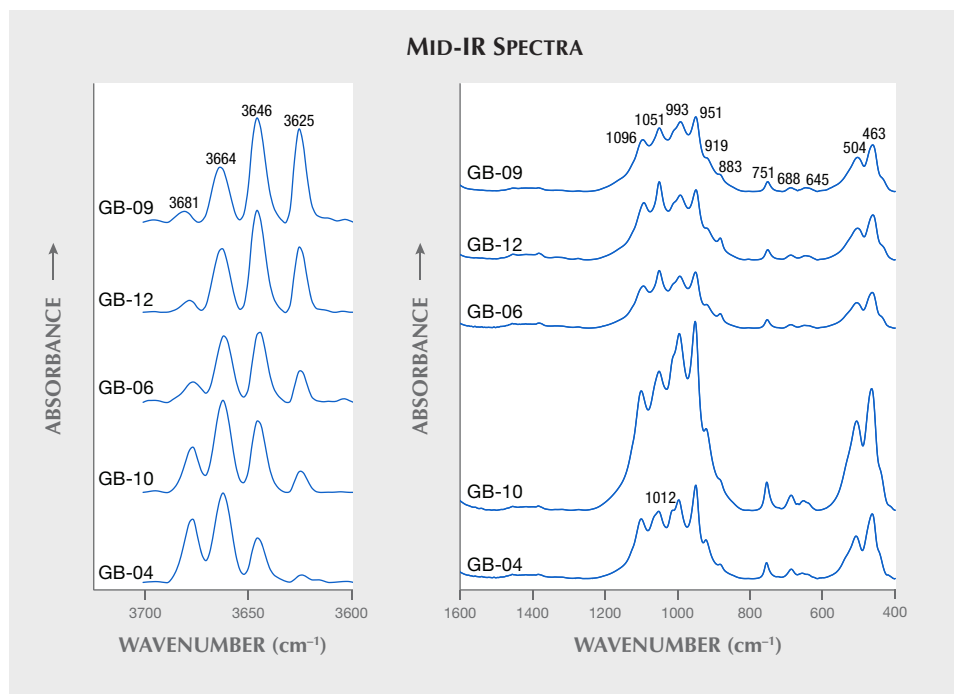
MID-IR SPECTRA

Figure 8. Mid-infrared spectra of five typical plate samples from Guangxi in the 3700–3600 cm⁻¹ (left) and 1600–400 cm⁻¹ (right) ranges. The spectra show bands related to M_3-OH asymmetric stretching modes; Si-O-Si, O-Si-O, and M-O stretching modes; Si-O bending modes; and O-H translational modes of actinolite or ferro-actinolite. (M is an abbreviation for a metal ion.) Spectra are offset vertically for clarity.

fur, while the pyrite's was 47.52 wt.% iron and 52.29 wt.% sulfur.

Infrared Spectroscopy. *Mid-Infrared Spectroscopy.* Mid-infrared spectra (figure 8) of the black nephrite plate samples were characterized by one set of bands in the 3700 to 3600 cm⁻¹ range and three sets (1200–800 cm⁻¹, 800–600 cm⁻¹, and 600–400 cm⁻¹) in the 1600 to 400 cm⁻¹ range, typical of M_3-OH (M is an abbreviation for a metal ion) and [Si_4O_{11}] vibrations in actinolite or ferro-actinolite, respectively (Wen et al., 1988). The asymmetric and symmetric stretching modes of the Si-O-Si and O-Si-O groups appear mainly at approximately 1096, 1051, 1012, 993, 951, 919, 883, 751, 688, and 645 cm⁻¹. The bands near 504 and 463 cm⁻¹ are related to the bending modes of the Si-O group, stretching modes of the M-O group, and translational modes of the O-H group. The bands around 3681, 3664, 3646, and 3625 cm⁻¹ are related to the asymmetric stretching modes of the M_3-OH group. No absorption bands related to minor mineral phases were observed.

Near-Infrared Spectroscopy. Near-infrared spectra (figure 9) of the black nephrite thin sections were mainly characterized by the combination modes of the M_3-OH, Si-O groups, or water and the multiple vibration modes of the hydroxyl group in actinolite or ferro-actinolite. Four strong and sharp bands around 7185, 7156, 7117, and 7078 cm⁻¹ are related to the first overtone of M_3-OH asymmetric stretching modes (Burns and

Strens, 1966). The broad band centered at nearly 5226 cm⁻¹ is assigned to the combination modes of water adsorbed within the actinolite or ferro-actinolite aggregates. The combination modes of the M_3-OH and Si-O groups appear at approximately 4295 and 4161 cm⁻¹.

Figure 9. Near-infrared spectra of five typical thin-section samples (0.73–0.97 mm thick) from Guangxi showing bands related to the first overtone of M_3-OH asymmetry stretching modes as well as the combination modes of water, M_3-OH, and Si-O groups of actinolite or ferro-actinolite in the 8000–4000 cm⁻¹ range. Spectra are offset vertically for clarity.
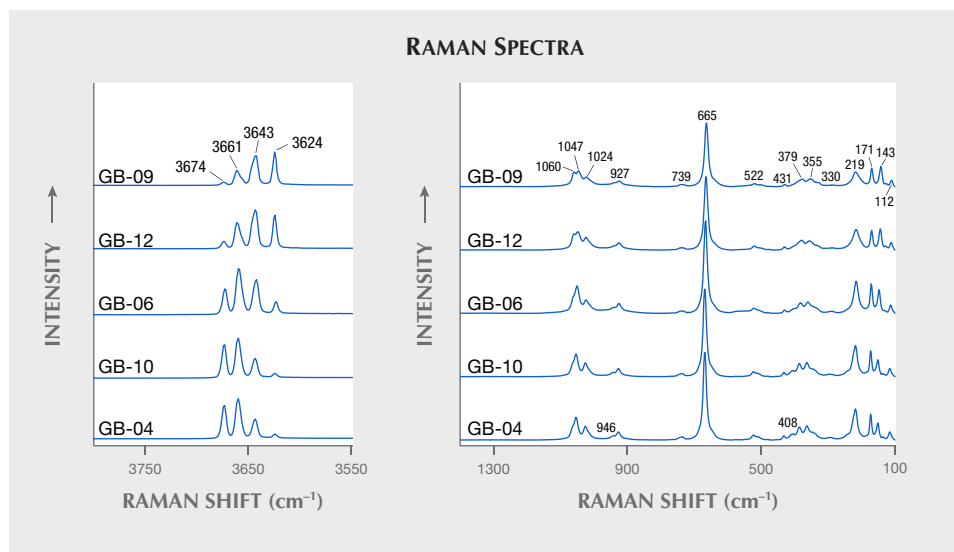

NIR SPECTRA
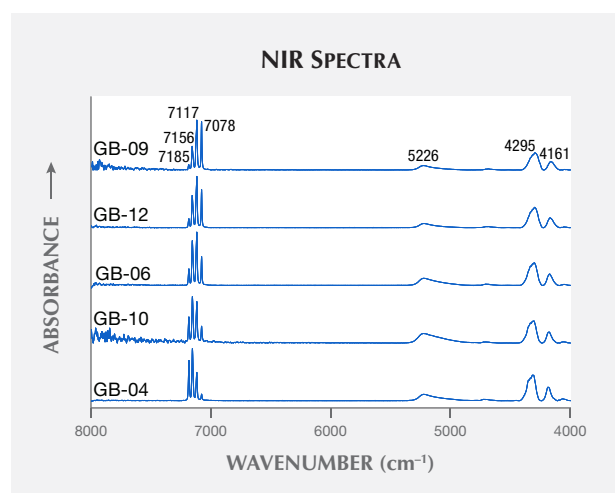
Figure 10. Raman spectra of five typical plate samples from Guangxi showing peaks related to M_3-OH stretching modes of actinolite or ferro-actinolite in the 3700–3600 cm^{-1} range, as well as Si-O and Si-O-Si stretching modes, Si-O bending modes, and lattice vibration modes in the 1200–100 cm^{-1} range. Spectra are offset vertically for clarity.

Raman Spectroscopy. Raman spectra (figure 10) of the black nephrite plate samples were primarily characterized by peaks in the 3700 to 3600 cm^{-1} and 1200 to 100 cm^{-1} ranges, which are typical of M_3-OH and $[Si_4O_{11}]$ vibrations in actinolite or ferro-actinolite. Peaks at approximately 1060, 1047, 1024, 946, and 927 cm^{-1} are related to the stretching modes of the Si-O group, and those at 739 and 665 cm^{-1} are related to the stretching modes of the Si-O-Si group. The bending modes of the Si-O group appear mainly at approximately 522 and 431 cm^{-1}. Peaks at around 408, 379, 355, 330, 219, 171, 143, 128, and 112 cm^{-1} are assigned to the lattice vibration modes. Four sharp Raman peaks near 3674, 3661, 3643, and 3624 cm^{-1} are related to the stretching modes of M_3-OH groups (Lu, 2005; Feng et al., 2017).

UV-Vis-NIR Spectroscopy. Black nephrite thin sections (0.13–0.49 mm thick) with greenish yellow to brownish yellow (samples GB-01, GB-02, and GB-10) and pale green to yellowish green to green (samples GB-04, GB-06, and GB-09) colors in transmitted light exhibited similar but slightly different absorption features in the 220 to 1000 nm range; these are named type I (figure 11, left) and type II (figure 11, right) spectra. Considering chemical composition (table 2) and previous studies (Marfunin, 1984; Lu, 2005), the significant transition metals that contributed to the colors and UV-Vis-NIR spectra of the Guangxi black nephrite were iron and manganese. In both types of spectra, there are two broad bands centered at 726–737 nm and 916–935 nm, which are due to $Fe^{2+} \leftrightarrow Fe^{3+}$ intervalence charge transfer and combinations of Fe^{2+} and Fe^{3+} electron transition, respectively. The strong

absorptions in the blue-ultraviolet range with a maximum at 440–460 nm for type I spectra and 355–405 nm for type II spectra are both due to $O^{2-} \leftrightarrow Fe^{3+}$ charge transfer. In type II spectra, shoulders at 445 nm and 625–635 nm are due to Fe^{3+}/Mn^{2+} and Fe^{3+} electron transition, respectively. Absorptions mentioned above result in a transmission centered at 628–645 nm or 515–553 nm in the visible range, which leads to a greenish yellow/brownish yellow or pale green/yellowish green/green bodycolor, respectively.

However, there is no obvious difference in transition metal contents between the samples with two types of color. We infer that differences in their UV-Vis-NIR spectra result from different modes of occurrence of iron and manganese in black nephrite.

DISCUSSION
Iron's Influence on RI, SG, and Vibrational Spectra. The samples from Guangxi have an iron content (11.67–25.75 wt.% FeO) that is higher than that of white nephrite (0.07–1.09 wt.% FeO, four deposits; Siqin et al., 2012), green nephrite (0.12–4.93 wt.% FeO, nine deposits; Siqin et al., 2012), and even other black nephrite (4.11–14.39 % FeO, Xinjiang; Liu et al., 2011a). For that reason, they have a higher RI (1.625–1.650) and SG (3.015–3.405) than any nephrite previously reported (see Zhang, 2006). Likewise, significant substitution of iron for magnesium indicates that black nephrite from Guangxi is primarily composed of actinolite or ferro-actinolite instead of tremolite. Figure 12 shows that the samples' RI and SG values increase with iron content. Due to a large amount of minor minerals included in some samples (see table 1), related data can deviate from the normal
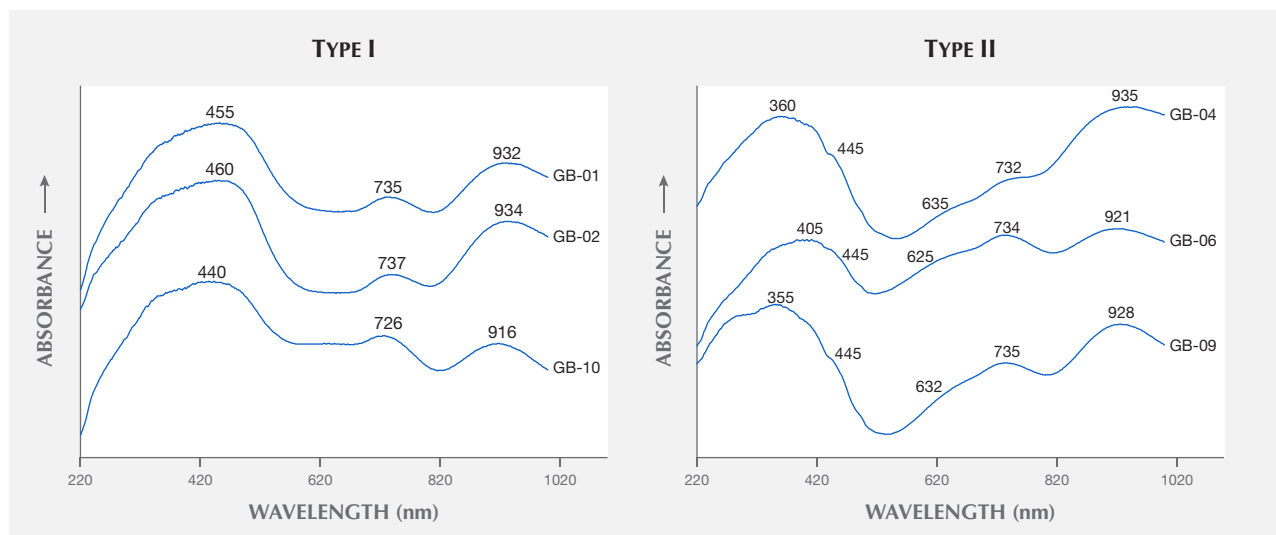
Figure 11. UV-Vis-NIR spectra of six typical thin-section samples (0.13–0.49 mm thick) from Guangxi with greenish yellow/brownish yellow (type I) and pale green/yellowish green/green (type II) colors in transmitted light. The peaks in the 220–1000 nm range are attributable mainly to iron and manganese.

trend. For sample GB-04, the relatively high RI and SG are believed to result from the diopside content. The relatively low RI and SG of GB-05 are likely caused by its stilpnomelane content. The highest SG, in sample GB-08, is probably related to Fe sulfides in addition to a high iron content.

As seen in figure 13, the mid-infrared, near-infrared, and Raman spectra of the black nephrite are characterized by four M_3-OH vibration bands in the

3700 to 3600 cm^{-1} or 7240 to 7020 cm^{-1} range. In the crystal structure of calcic amphiboles, each hydroxyl group is coordinated to three neighboring metal ions at two M_1 positions and one M_3 position, forming a pseudo-trigonal symmetrical $(M_1M_1M_3)$OH group. M_1 and M_3 positions are occupied mainly by Mg^{2+} or Fe^{2+}, forming a perfect isomorphous substitution. For white nephrite composed of tremolite nearly free of iron, there exists only one sharp $(Mg)_3$OH band. For

Figure 12. Scatterplots showing that the refractive index (left) and specific gravity (right) of the samples increase with iron content as FeO. Data deviating from the normal trend likely due to included minor minerals such as diopside (GB-04), stilpnomelane (GB-05), and Fe sulfides (GB-08) are specially marked. For detailed data, see tables 1 and 2.
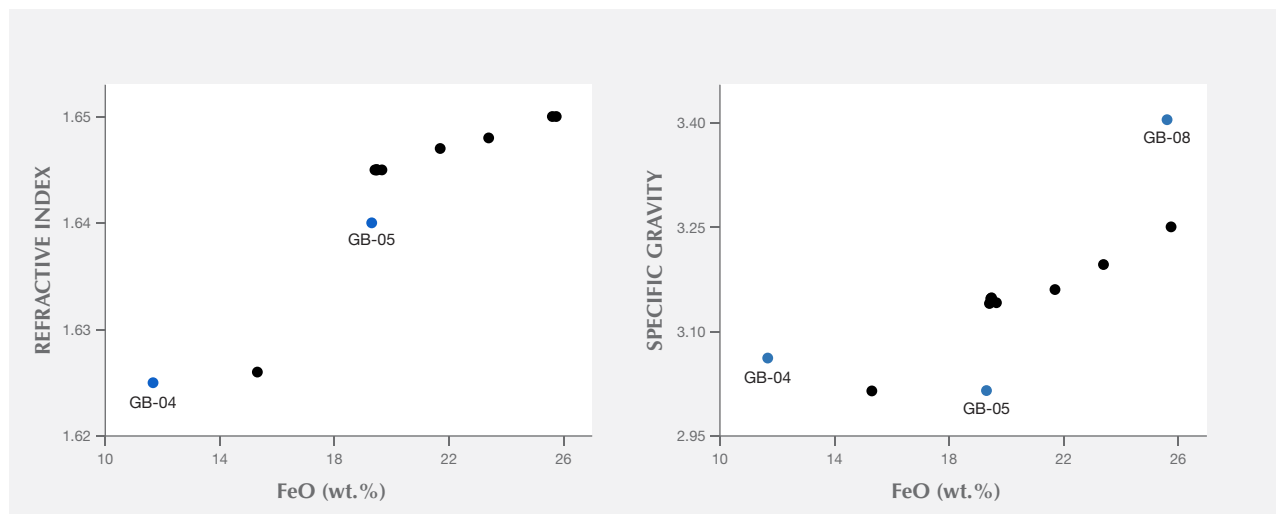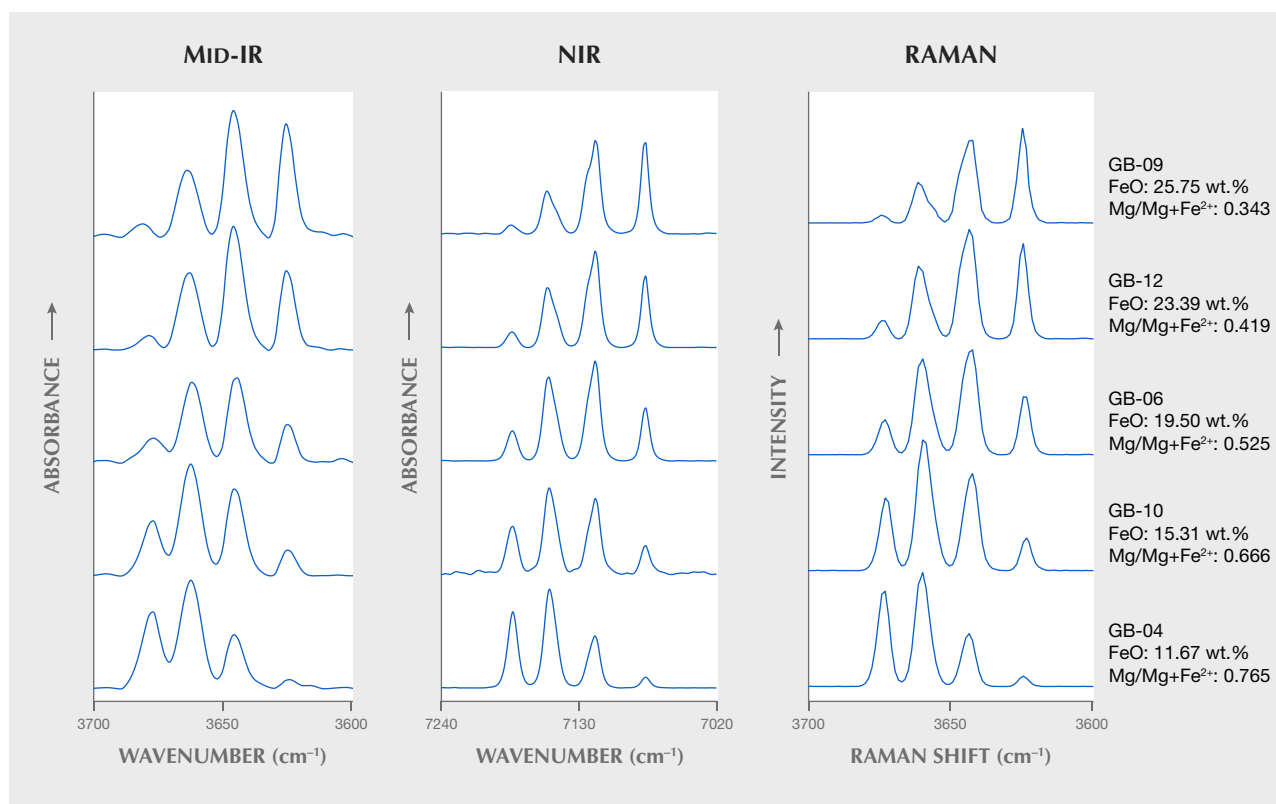
Figure 13. Mid-infrared, near-infrared, and Raman spectra of the samples are characterized by four $(Mg)_3OH$, $(Mg_2Fe^{2+})OH$, $(MgFe^{2+}_2)OH$, and $(Fe^{2+})_3OH$ bands in the 3700–3600 cm^{-1} or 7240–7020 cm^{-1} range. With rising iron content, relative intensities of $(Mg)_3OH$ and $(Mg_2Fe^{2+})OH$ bands decrease while relative intensities of $(MgFe^{2+}_2)OH$ and $(Fe^{2+})_3OH$ bands increase. Spectra are offset vertically for clarity.

greenish white and green nephrite, bands related to $(Mg_2Fe^{2+})OH$ and $(MgFe^{2+}_2)OH$ gradually appear as iron content increases (Burns and Strens, 1966; Feng et al., 2017). For the black nephrite from Guangxi, M_3-OH vibration bands are split into four bands due to high iron content. According to Burns and Strens (1966) and Lu (2005), four bands in the mid-infrared and Raman spectra near 3681/3674, 3664/3661, 3646/3643, and 3625/3624 cm^{-1} are respectively attributed to $(Mg)_3OH$, $(Mg_2Fe^{2+})OH$, $(MgFe^{2+}_2)OH$, and $(Fe^{2+})_3OH$ fundamental vibrations. Four bands in the near-infrared spectra near 7185, 7156, 7117, and

7077 cm^{-1} are respectively attributed to the first overtone of $(Mg)_3OH$, $(Mg_2Fe^{2+})OH$, $(MgFe^{2+}_2)OH$, and $(Fe^{2+})_3OH$ fundamental vibrations (table 4).

For sample GB-04, with the lowest iron content—11.67 wt.% FeO, and an Mg/(Mg + Fe^{2+}) ratio of 0.765)—the relative intensity of the M_3-OH bands is $(Mg_2Fe^{2+})OH > (Mg)_3OH > (MgFe^{2+}_2)OH > (Fe^{2+})_3OH$. The $(Fe^{2+})_3OH$ band is very weak (figure 13). For GB-10, GB-06, and GB-12, with increasing iron content, $(MgFe^{2+}_2)OH$ and $(Fe^{2+})_3OH$ bands are increasingly stronger as they are more closely related to Fe^{2+}, while $(Mg_2Fe^{2+})OH$ and $(Mg)_3OH$ bands are

TABLE 4. Frequencies (cm^{-1}) of $(M_1M_1M_3)$-OH bands in vibrational spectra and their assignments in black nephrite from Guangxi.

Type of $(M_1M_1M_3)$-OH group	$(Mg)_3OH$	$(Mg_2Fe^{2+})OH$	$(MgFe^{2+}_2)OH$	$(Fe^{2+})_3OH$
Mid-infrared frequency	3681–3677	3664–3662	3646–3645	3625–3624
Near-infrared frequency	7185–7183	7156–7154	7117	7077
Raman frequency	3674–3673	3661–3660	3643–3642	3624–3623

increasingly weaker. For sample GB-09, with the highest iron content—25.75 wt.% FeO, and an $Mg/(Mg+Fe^{2+})$ ratio of 0.343—the relative intensity is $(Fe^{2+})_3OH≈(MgFe^{2+}_2)OH > (Mg_2Fe^{2+})OH > (Mg)_3OH$, and the $(Mg)_3OH$ band is very weak. Therefore, iron content and Mg^{2+}-Fe^{2+} isomorphous substitution affect the relative intensity of M_3-OH vibration bands, in addition to their number and frequency.

There are also differences in the Raman spectra of the black nephrite samples in the 1400–100 cm^{-1} range (figure 10, right). For instance, with increasing iron content, the strongest peak at 669 cm^{-1} gradually shifts toward the lower frequency to 665 cm^{-1}. The relative intensity of the 1060 cm^{-1}/1047 cm^{-1} peaks becomes stronger, while the peaks at nearly 946 and 408 cm^{-1} become weaker. And in mid-infrared spectra (figure 8, right), the intensity of the band at approximately 1012 cm^{-1} becomes weaker with increasing iron content.

Genesis of Black Nephrite. Located at the boundary zone between diabase and limestone bearing siliceous rock, Guangxi black nephrite is a product of contact metasomatism[3] occurring after basic magma intrusion into carbonate rock. Therefore, this deposit is of contact metasomatic and skarn origin. Skarn deposits can generally be grouped into Ca-, Mg-, and Mn-skarn by their mineral assemblages. Typical Mg-skarn nephrite from Xinjiang, which is related to dolomitic marbles rich in magnesium (29.61–30.76 wt.% CaO, 22.08–22.52 wt.% MgO, and a Ca/Mg ratio of 0.94–1.01; Liu et al., 2011b), contains Mg-bearing minerals such as olivine, spinel, phlogopite, serpentine, and talc (Tang et al., 1994; Liu et al., 2015). Low-magnesium marbles (54.19 wt.% CaO, 0.21 wt.% MgO, and a Ca/Mg ratio of 183) found in the deposit and the presence of calcic minerals such as actinolite/ferro-actinolite, andradite, diopside, and epidote in the samples (figure 7 and table 3) strongly suggest that the Guangxi deposit is a Ca-skarn deposit. The skarn appears to be spatially zoned as the Xinjiang deposit, with different minerals distributed at different distances from the intrusive rock (figure 4). Moreover, it is remarkable that stilpnomelane, a minor mineral in the black nephrite from Guangxi, can be used as a fingerprint, as it has not been reported to exist in other nephrite deposits.

The $Fe^{2+}/(Mg + Fe^{2+})$ ratio of actinolite/ferro-actinolite in black nephrite from Guangxi (0.235–0.657) is much higher than that of tremolite-actinolite in D-type (0.001–0.074) and S-type (0.064–0.118) nephrite (Siqin et al., 2012), which is determined by diabase related to its formation. From a chemical composition perspective, basic diabase is richer in iron and magnesium and poorer in silicon (12.00–15.50 wt.% FeO, 3.02–6.59 wt.% MgO, and 45.90–48.30 wt.% SiO_2; Zhang and Xiao, 2014), compared to intermediate-acid diorite/granodiorite (2.68–6.16 wt.% FeO, 2.27–4.39 wt.% MgO, and 50.57–58.62 wt.% SiO_2; Tang et al., 1994). Hence, diabase and siliceous rock in limestone are likely sources of magnesium and silicon, respectively, whereas the limestone itself is the source of calcium. Rare earth elements (REE) with patterns more similar to limestone than diabase (Wang et al., 2014) suggest that the Guangxi black nephrite formed by the replacement of limestone. In addition, hydrous minerals such as actinolite/ferro-actinolite, stilpnomelane, and epidote formed in the metasomatism stage indicate that fluids were also involved. Therefore, it is proposed that actinolite/ferro-actinolite in black nephrite from Guangxi formed by a reaction between limestone bearing siliceous rock and aqueous solutions bearing iron, magnesium, and silicon:

$$2CaCO_3 + 8SiO_2 + xFeO+ (5–x)MgO +H_2O→$$
limestone

$$Ca_2(Fe_x,Mg_{5-x})Si_8O_{22}(OH)_2 + 2CO_2$$
actinolite/ferro-actinolite
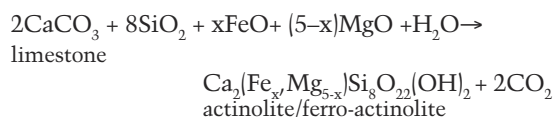
The rocks involved in black nephrite formation are limestone bearing siliceous rock and diabase. These are similar to the rocks in the Guizhou deposit. Considering similarities in geographical and tectonic locations and orebody characteristics, we believe that Guangxi and Guizhou represent another large-scale nephrite formation belt in China in addition to the east-west Kunlun Mountains.

CONCLUSIONS
With a pure color and delicate texture, carvings of black nephrite jade from Guangxi in southern China (figure 14) have been favorably received in the market since mining began in 2012. The material is com-

---

[3]*Contact metasomatism* refers to a process of chemical change in the composition of rock in contact with an invading magma, from which fluid constituents are carried out to combine with some of the country-rock constituents to form a new suite of minerals. The Guangxi black nephrite deposit is a typical contact-metasomatic (or skarn) deposit formed in the contact zone between mafic magma intrusions (i.e., diabase) and carbonate rock.

Figure 14. This censer delicately carved from Guangxi black nephrite has a mountain-shaped cover and a bamboo-shaped stem, with decorative patterns on its body as well as dragon patterns on its joint and pedestal. Courtesy of Hongwei Ma.

posed mainly of fine-grained and felted actinolite or ferro-actinolite, with minor minerals stilpnomelane, andradite, apatite, epidote, quartz, diopside, pyrrho- tite, and pyrite. An abundant iron content—11.67–25.75 wt.% Fe oxides and an $Mg/(Mg + Fe^{2+})$ ratio of 0.765–0.343—is the main reason for its high refractive

index (1.625–1.650) and specific gravity (3.015–3.405). High iron content is also the reason for the black color in natural light for samples with a normal thickness (1.10–6.13 mm) and the greenish yellow/brownish yellow or pale green/yellowish green/green color in transmitted light for thinner samples (0.73–0.97 mm). Moreover, significant isomorphous substitution of Fe^{2+} for Mg^{2+} at M_1 and M_3 positions in the crystal structure of actinolite or ferro-actinolite is responsible for bands with different intensities appearing at approximately 3681/3674, 3664/3661, 3646/3643, and 3625/3624 cm^{-1} in the mid-infrared/Raman spectra,

as well as bands at approximately 7185, 7156, 7117, and 7077 cm^{-1} in the near-infrared spectra. These are respectively related to $(Mg)_3OH$, $(Mg_2Fe^{2+})OH$, $(MgFe^{2+}_2)OH$, and $(Fe^{2+})_3OH$ fundamental vibrations as well as their first overtones. As a product of Ca-skarn metasomatism occurring at the contact zone between diabase intrusions and limestone bearing siliceous rock, Guangxi black nephrite originated from source rocks similar to those of Guizhou. It is proposed that the Guangxi and Guizhou nephrite deposits are part of a large-scale jade formation belt in southern China.

ABOUT THE AUTHORS
Ms. Zhong (Zhongqian2012@163.com) is a PhD student of mineralogy, Dr. Liao (liaozt@tongji.edu.cn, corresponding author) is a professor of tectonic geology, Mr. Qi is a professor of gemology, and Dr. Zhou is an associate professor of gemology, in the State Key Laboratory of Marine Geology, the School of Ocean and Earth Sciences, and the Laboratory of Gem and Technological Materials of Tongji University, Shanghai.

REFERENCES

Bureau of Geology and Mineral Resources of Guangxi Zhuang Autonomous Region (1985) *Regional Geology of Guangxi Province.* Geological Publishing House, Beijing, pp. 156–212, 363–395.

Burns R.G., Strens R.G.J. (1966) Infrared study of the hydroxyl bands in clinoamphiboles. *Science,* Vol. 153, No. 3738, pp. 890–892, http://dx.doi.org/10.1126/science.153.3738.890

Chen Y.L., Niu F.L., Liu R.F., Huang Z.B., Tkalcic H., Sun L., Chan W. (2010) Crustal structure beneath China from receiver function analysis. *Journal of Geophysical Research,* Vol. 115, No. B3, http://dx.doi.org/10.1029/2009JB006386

Delly J.G. (2003) The Michel-Lévy interference color chart—microscopy's magical color key. https://www.mccrone.com/the-michel-levy-interference-color-chart-microscopys-magical-color-key

Feng X.Y., Zhang Y., Lu T.J., Zhang H. (2017) Characterization of Mg and Fe contents in nephrite using Raman spectroscopy. *G&G,* Vol. 53, No. 2, pp. 204–212, http://dx.doi.org/10.5741/GEMS.53.2.204

Flint D.J., Dubowski E.A. (1990) Cowell nephrite jade deposits. In F.E. Hughes, Ed., *Geology of the Mineral Deposits of Australia and Papua New Guinea.* Institute of Mineralogy and Metal-lurgy, Melbourne, Australia, Vol. 14, pp. 1059–1062.

Harlow G.E., Sorensen S.S. (2005) Jade (nephrite and jadeitite) and serpentinite: metasomatic connections. *International Geology Review,* Vol. 47, No. 2, pp. 113–146, http://dx.doi.org/10.2747/0020-6814.47.2.113

Harlow G.E., Sorensen S.S., Sisson V.B., Shi G.H. (2014) Chapter 10: The Geology of Jade Deposits. In L.A. Groat, Ed., *The Geology of Gem Deposits,* 2nd ed. Short Course Handbook Series 44. Mineralogical Association of Canada, Quebec, Canada, pp. 305–374.

Hawthorne F.C., Oberti R., Harlow G.E., Maresch W.V., Martin R.F., Schumacher J.C., Welch M.D. (2012) Nomenclature of the amphibole supergroup. *American Mineralogist,* Vol. 97, No. 11–12, pp. 2031–2048, http://dx.doi.org/10.2138/am.2012.4276

He M.Y., Zhu Y.N., Li H.B. (2002) Gemmological characteristics of Meiling jade from Liyang, Jiangsu Province. *Acta Petrologica et Mineralogica,* Vol. 21, No. S1, pp. 99–104.

Jin X.T., Qiu Z.L., Dai S.L., Yi J.H., Li L.F., Zhang Y.F. (2014) Gemological and mineralogical characteristics of nephrite from Ya'an, Sichuan Province. *Journal of Gems and Gemmology,* Vol. 16, No. 5, pp. 1–8, http://dx.doi.org/10.3969/j.issn.1008-214X.2014.05.001

Leake B.E., Woolley A.R., Arps C.E.S., Birch W.D., Gilbert M.C., Grice J.D., Hawthorne F.C., Kato A., Kisch H.J., Krivovichev V.G., Linthout K., Laird J., Mandarino J.A., Maresch W.V., Nickel E.H., Rock N.M.S., Schumacher J.C., Smith D.C., Stephenson N.C.N., Ungaretti L., Whittaker E.J.W., Youzhi G. (1997) Nomenclature of amphiboles: Report of the Subcommittee on Amphiboles of the International Mineralogical Association Commission on New Minerals and Mineral Names. *American Mineralogist*, Vol. 82, No. 9/10, pp. 1019–1037, http://dx.doi.org/10.1180/minmag.1997.061.405.13

Leaming S.F. (1998) *Jade in Canada: Geological Survey of Canada Papers*, Vol. 78, pp. 1–59.

Li X., Yu X.J., Wang S.Q., Mo Y.Y. (2011) The discovery and a preliminary study of Dahua tremolite jade in Guangxi. *Acta Petrologica et Mineralogica*, Vol. 30, No. Supp., pp. 47–52.

Liu Y., Deng J., Shi G.H., Sun X., Yang L.Q. (2011a) Geochemistry and petrogenesis of placer nephrite from Hetian, Xinjiang, Northwest China. *Ore Geology Reviews*, Vol. 41, No. 1, pp. 122–132, http://dx.doi.org/10.1016/j.oregeorev.2011.07.004

Liu Y., Deng J., Shi G.H., Yui T.F., Zhang G.B., Abuduwayiti M., Yang L.Q., Sun X. (2011b) Geochemistry and petrology of nephrite from Alamas, Xinjiang, NW China. *Journal of Asian Earth Sciences*, Vol. 42, No. 3, pp. 440–451, http://dx.doi.org/10.1016/j.jseaes.2011.05.012

Liu Y., Zhang R.Q., Zhang Z.Y., Shi G.H., Zhang Q.C., Abuduwayiti M., Liu J.H. (2015) Mineral inclusions and SHRIMP U–Pb dating of zircons from the Alamas nephrite and granodiorite: Implications for the genesis of a magnesian skarn deposit. *Lithos*, Vol. 212–215, pp. 128–144, http://dx.doi.org/10.1016/j.lithos.2014.11.002

Lu B.Q. (2005) The Gemological Mineralogy and Spectroscopy of Nephrite Cat's Eye and Serpentine Cat's Eye from Shimian, Sichuan Province, Southwest of China. PhD thesis, Shanghai University, Shanghai.

Marfunin A.S. (1984) *Physics of Minerals and Inorganic Materials: An Introduction*. Translated by Li G.S, He Y.X., He S.W. Geological Publishing House, Beijing, pp. 149–187.

Mo Z.R., Mao Y.J. (2016) Gemological study of a black jade. *Technology Outlook*, Vol. 26, No. 21, pp. 258–259, http://dx.doi.org/10.3969/j.issn.1672-8289.2016.21.227

National Geological Archives (2013) 1:200000 geologic map of Guangxi and Guizhou Province. http://www.ngac.org.cn/Document/Map.aspx?MapId=EC7E1A7A782D1954E0430100007F182E

Peng F., Zhao Q.H., Pei L., Wang C., Yin Z.W. (2017) Study of mineralogical and spectroscopic characteristics of black nephrite from Dahua in Guangxi. *Spectroscopy and Spectral Analysis*, Vol. 37, No. 7, pp. 2237–2241, http://dx.doi.org/10.3964/j.issn.1000-0593(2017)07-2237-05

Prokhor S.A. (1991) The genesis of nephrite and emplacement of the nephrite-bearing ultramafic complexes of east Sayan. *International Geology Review*, Vol. 33, No. 3, pp. 290–300.

Schumacher J.C., Wang L.B. (2001) Estimation of Fe^{3+} percentage from the electron microprobe data of amphiboles. *Acta Petrologica et Mineralogica*, Vol. 20, No. 2, pp. 189–198, 207.

Siqin B., Qian R., Zhuo S.J., Gan F.X., Dong M., Hua Y.F. (2012) Glow discharge mass spectrometry studies on nephrite minerals formed by different metallogenic mechanisms and geological environments. *International Journal of Mass Spectrometry*, Vol. 309, No. 1, pp. 206–211, http://dx.doi.org/10.1016/j.ijms.2011.10.003

Tang Y.L., Chen B.Z., Jiang R.H. (1994) *Chinese Hetian Nephrite*. Xinjiang People's Publishing House, Urumqi, China, pp. 103–237.

Wang B., Shao Z.Y., Liao Z.T., Zhou Z.Y. (2012) Gemmological and mineralogical characteristics of nephrite from Guangxi. *Journal of Gems and Gemology*, Vol. 14, No. 3, pp. 6–11, http://dx.doi.org/10.3969/j.issn.1008-214X.2012.03.003

Wang C.Q., Sun P., Wang S.Q. (2014) Mineralogical characteristics of Dahua dark nephrite, Guangxi. *Acta Petrologica et Mineralogica*, Vol. 33, No. S2, pp. 1–9.

Wang C.Y. (1993) Geological and physical, chemical characteristics of Longxi nephrite. *Mineral Resources and Geology*, Vol. 7, No. 35, pp. 201–205.

Wang J.J., Gan Y.H., Li J., Wei J. (2007) Analysis on nephrite conditions and discovery prospects in Dazaohuo area in Qinghai Province. *Plateau Earthquake Research*, Vol. 19, No. 4, pp. 47–51, http://dx.doi.org/10.3969/j.issn.1005-586X.2007.04.008

Wang S.Q., Duan T.Y., Zheng Z.Z. (2002) Mineralogical and petrological characteristics of Xiuyan nephrite and its minerogenetic model. *Acta Petrological et Mineralogica*, Vol. 21, No. S1, pp. 79–90.

Wen L., Liang W.X., Zhang Z.G., Huang J.C. (1988) *The Infrared Spectroscopy of Minerals*. Chongqing University Press, Chongqing, China, pp. 85–89.

Wilkins C.J., Tennant W.C., Williamson B.E., McCammon C.A. (2003) Spectroscopic and related evidence on the coloring and constitution of New Zealand jade. *American Mineralogist*, Vol. 88, No. 8–9, pp. 1336-1344, http://dx.doi.org/10.2138/am-2003-8-917

Yang L. (2013) Study on Petromineral Features and Genetic Mechanism of Luodian Jade, Guizhou Province. Ph.D. thesis. Chengdu University of Technology, Chengdu, China.

Yin Z.W., Jiang C., Santosh M., Chen Y.M., Bao Y., Chen Q.L. (2014) Nephrite jade from Guangxi Province, China. *G&G*, Vol. 50, No. 3, pp. 228–235, http://dx.doi.org/10.5741/GEMS.50.3.228

Yui T.F., Kwon S.T. (2002) Origin of a dolomite-related jade deposit at Chuncheon, Korea. *Economic Geology*, Vol. 97, No. 3, pp. 593–601, http://dx.doi.org/10.2113/97.3.593

Yui T.F., Usuki T., Chen C.Y., Ishida A., Sano Y., Suga K., Iizuka Y., Chen C.T. (2014) Dating thin zircon rims by NanoSIMS: The Fengtien nephrite (Taiwan) is the youngest jade on Earth. *International Geology Review*, Vol. 56, No. 16, pp. 1932–1944, http://dx.doi.org/10.1080/00206814.2014.972994

Zhang B.L. (2006) *Systematic Gemmology*. Geological Publishing House, Beijing, pp. 367.

Zhang X.J., Xiao J.F. (2014) Zircon U-Pb geochronology, Hf isotope and geochemistry study of the Late Permian diabases in the northwest Guangxi Autonomous Region. *Bulletin of Mineralogy, Petrology and Geochemistry*, Vol. 33, No. 2, pp. 163–176, http://dx.doi.org/10.3969/j.issn.1007-2802.2014.02.003

Evidence of Rotation in Flame-Structure Pearls from Bivalves of the Tridacnidae Family

Jean-Pierre Gauthier, Jacques Fereire, and Thanh Nhan Bui

Thirty-seven pearls originating from bivalves of the Tridacnidae family were analyzed to determine their gemological properties and to characterize the optical features of their distinctive flame structure, terminating at the apex and base with patterns like those of blade impellers. All but two of the samples exhibited cylindrical symmetry around a fixed axis, suggesting a rotating movement during growth, as with numerous pearls from *Pinctada margaritifera*. One quite unusual feature, which is difficult to detect and to our knowledge has never before been described, consisted of spiral patterns at the apex and base of the pearl, and one of these patterns suggested the possibility of rotation. Other details that supported the conclusion of rotation during growth included comets associated with spot defects and pseudo-chatoyancy that appeared shifted to one side.

A number of marine organisms produce aragonitic pearls with microstructures different from the nacreous layers generally observed in various bivalves such as the saltwater *Pinctada* and *Pteria* species or the freshwater *Hyriopsis* species. These non-nacreous pearls have a microstructure consisting of crossed aragonitic lamellae (Jiao et al., 2016; Agbaje et al., 2017). These specimens possess a "flame" structure that can be observed under the microscope, with a large base and an elongated tail terminating in one or more tips. They sometimes display an optical phenomenon resembling chatoyancy.

Some marine gastropods produce concretions with a flame structure. One of the most famous is the pink conch "pearl" from *Strombus gigas*, a gastropod that has been fished for its flesh and concretions, and these concretions have even been cultured (Davis, 2000; Davis and Shawl, 2005; Segura and Fritsch, 2015). In addition to salmon pink, these concretions can display white, brown, golden, or yellow hues. The history and gemology of the conch pearl have been reported by Fritsch and Misiorowski (1987) and Federman and Bari (2007). Similar to these are *Lambis*

truncata pink pearls (Bari and Lam, 2009, p. 68). Less well documented are flame-structure pearls from the *Melo* species (Htun et al., 2006), with a color ranging from orange to brown and in light, vivid, or dark hues

In Brief

- Like nacreous pearls from various bivalves, non-nacreous pearls from the Tridacnidae family may display an axial symmetry.
- Distinct flames develop in a crisscross pattern around the rotation axis and converge toward the poles as blade impellers.
- These figures, in addition to other features such as polar spirals, comets, and pseudo-chatoyancy, are evidence of the rotation during formation in flame-structure pearls.

(Scarratt, 1999; Htun et al., 2006). Even rarer in the literature are the flame-structure pearls from *Cassis cornuta* (Bari and Lam, 2009, pp. 73–75) and *Pleuroploca gigantea* (Koivula et al., 1994).

The flame structure is encountered in some bivalves. Except for rare cases of species from the *Spondylus* genus (Ho and Zhou, 2014; Homkrajae, 2016a,b), these belong to the Tridacnidae (also referred to as Tridacninae) family, which contains two genera, *Tridacna* and *Hippopus* (figure 1). *Tridacna gigas* has

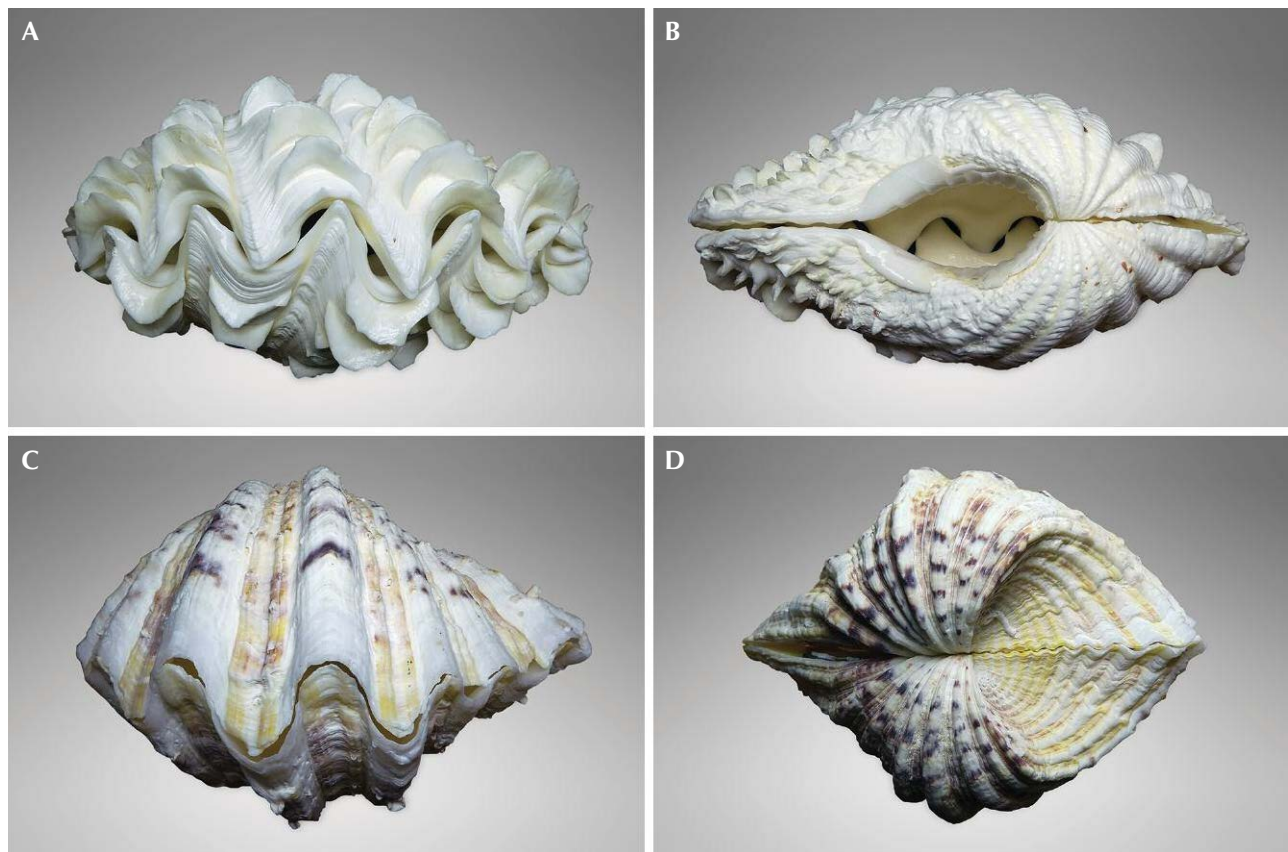*Figure 1. Examples of shells (front and back side) from both Tridacnidae genera:* Tridacna maxima *(A and B, shell length 18.5 cm) and* Hippopus *(C and D, shell length 19 cm). Photos by T.N. Bui.*

yielded very large non-nacreous concretions, such as the approximately 6.37 kg "Pearl of Allah" (Strack, 2006) and the "Pearl of Elias." Both are blister pearls: The former has been cut from the shell, and the latter is still attached to its shell. But the species has also produced beautiful flame-structure pearls weighing several tens of carats. The pearls from *Hippopus* or other *Tridacna* species are significantly smaller, weighing only a few carats. From these species we obtained an assortment of 37 pearls, mainly from *Tridacna gigas*, *Tridacna maxima*, and *Tridacna squamosa*, and possibly from *Hippopus hippopus* (figure 2).

The largest species in the Tridacnidae family, the giant clam (*Tridacna gigas*), possesses a shell that can reach 1.5 m in length and produces non-nacreous pearls of significant size (Bidwell et al., 2011). While the size of most naturally grown pearls is in the range of one to several centimeters, the previously mentioned "Pearl of Allah" measures 23 cm in length. Such pearls, described as chalky concretions, are of poor quality and usually do not present a visible flame structure (Bari and Lam, 2009).

Other species from the family (*Tridacna derasa*, *Tridacna maxima*, *Tridacna squamosa*, and *Hippopus hippopus*) have shells that only measure up to tens of centimeters in length, and they produce smaller concretions and pearls. These present a flame structure that is visible to the unaided eye.

All species of the Tridacnidae family are protected under the European Union (Council of the European Union, 1997), the Convention on International Trade in Endangered Species of Wild Flora and Fauna (CITES), and the International Union for Conservation of Nature (IUCN). However, *Tridacna maxima* is bred in ponds for the aquarium market. It is also cultivated at the French Research Institute for Exploitation of the Sea (IFREMER) in Tahiti for research purposes (Garen, 2003). Unlike conch pearls, for which cultivation has been reported (Acosta-Salmón and Davis, 2007), to the best of our knowledge no pearls have been harvested from bivalves of the Tridacnidae family.

Geographic distribution varies within the Tridacnidae family. For all species combined, the popula-
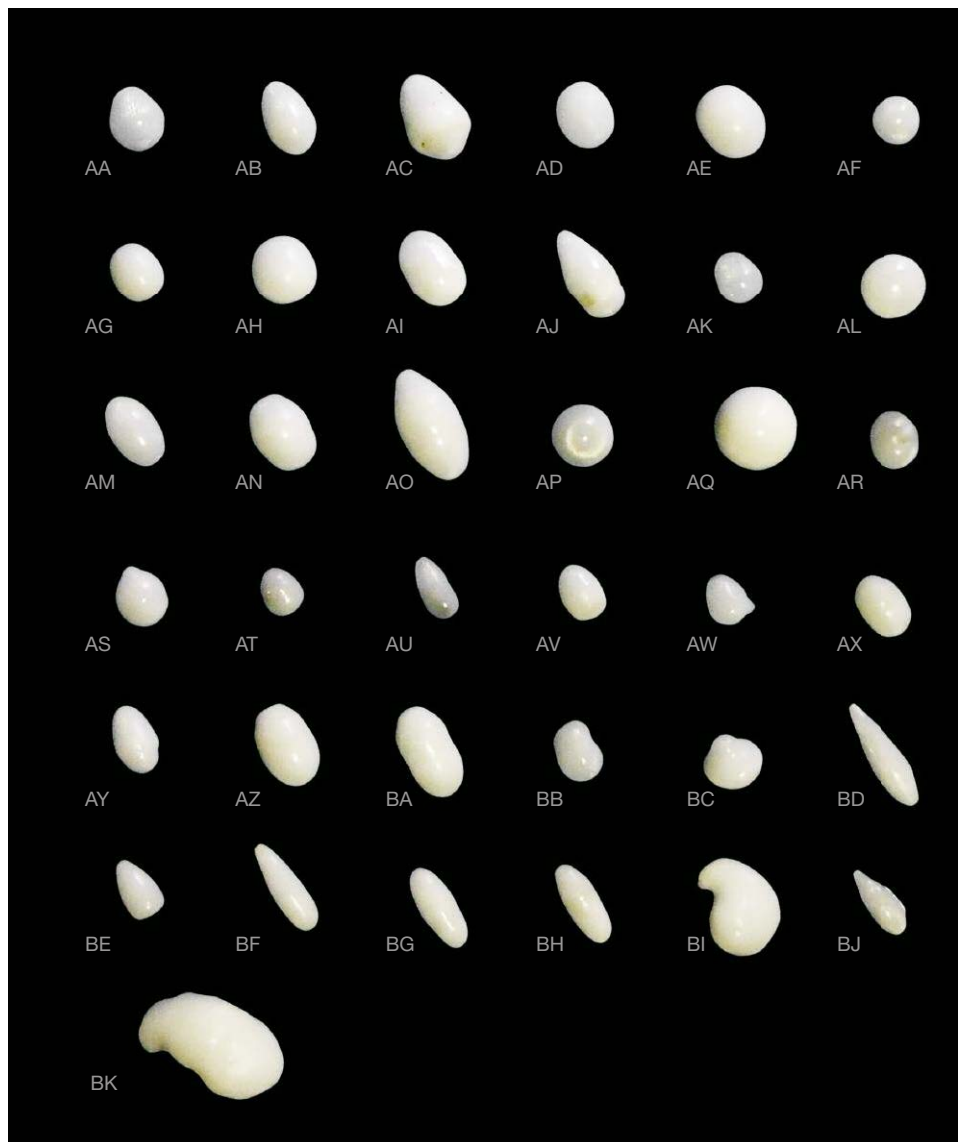
Figure 2. The 37 pearls from this study, ranging from 1.67 to 20.28 ct. Photo by J.-P. Gauthier.

tion of this bivalve extends from the seas south of China to the north of Australia and from Myanmar to Fiji. *Tridacna squamosa* and *Tridacna maxima* are distributed across the Indian Ocean to the east coast of Africa and far into the Pacific Ocean (Copland and Lucas, 1988; Hui, 2012).

Other species such as *Tridacna crocea*, *Tridacna rosewateri*, *Tridacna tevoroa*, and *Hippopus porcellanus* are probably also able to produce pearls, despite not having been mentioned by merchants of natural pearls or in the gemological literature. This may be explained by the small size of their shells (*Tridacna crocea)*, their limited geographic distribution, and the absence of known specimens.

Our set of 37 pearls from the Tridacnidae family originated from Indonesia. They were purchased from traders who collected them from several islands. These traders had taught locals to check for pearls inside the mollusk before cooking the meat. Most of the time the exact origin of the *Tridacna* species was not documented, but systematic tracking was requested for recent acquisitions.

This article will describe the main gemological characteristics of these pearls and detail the features visible to the unaided eye or under the microscope. We will also discuss the characteristics that strongly suggest a rotation of the forming pearl inside the mollusk, similar to that demonstrated in pearls from *Pinctada margaritifera* (Gueguen et al., 2015). Pearl rotation is a frequent phenomenon that occurs around several random axes for round pearls or around one fixed axis for pearls that display an axial

symmetry (see Gauthier et al., 2014, 2015, 2018). In fact, these authors observed that the circles found in Tahitian pearls are induced by spot defects, which are the emergence of tubular cavities perpendicular to the pearl surface and similar to chimney-like structures, sometimes opening out on the surface. The circles form as an asymmetrical comet-shaped structure, which allows us to infer the rotation direction of the pearl.

GEMOLOGICAL DATA

Table 1 presents data on all 37 pearl samples from the Tridacnidae family.

Shape and Symmetry. Figure 3 illustrates the forms observed in the 37 samples from this study. Most of these pearls, labeled in figure 2, exhibited an axial symmetry, except for two baroque pearls with a bean shape (BI and BK). Some presented a classical symmetry in pear or drop shapes. There were no round pearls but two near-round (AF and AQ). Quite a few had an oval shape (AD, AE, AG, AM, AN, AR, AX, AZ, BA, and BB) and some a spindle (AO, BD, BF, BG, BH, and BJ) or bullet shape (AJ, AV, AW, AY, and BE).

For the sake of clarity, the photo labels will refer to the:

1. apex (a): the sharpest upper pole (for example, "AG-a" on the far right of figure 4)
2. base (b): the more rounded lower pole for axially symmetric pearls
3. side (s): the lateral surfaces of the pearls

Figure 3. The main shapes observed in pearls from the Tridacnidae family. N-R = near-round, P = pear, D = drop, O = oval, S = spindle, Bt = button, Bl = bullet, Ba = baroque. The green arrows point to the apex, the red arrows to the base.
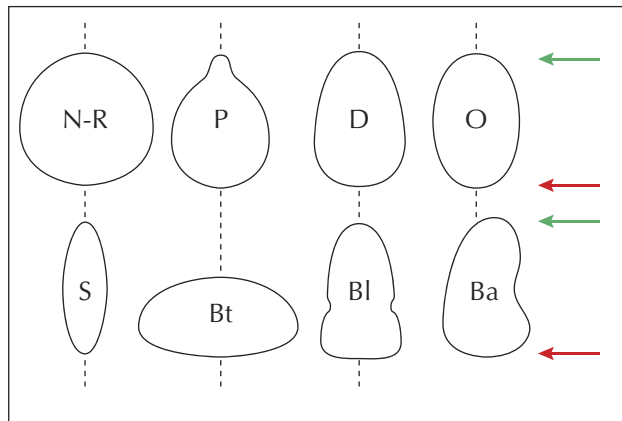
For the oval-shaped pearls, the choice of apex and base is obviously arbitrary.

Dimensions and Weight. With previously reported flame-structure pearls, dimensions have varied from a few millimeters to several centimeters and weights reaching tens of carats. These were reported for *Tridacna gigas* (Bidwell et al., 2011) and different *Melo* species (Scarratt, 1999) or other gastropods (Hyatt, 2008; Chang and Hyatt, 2011). The pearls in the present study, from *Tridacna gigas*, *T. maxima*, and *T. squamosa*, as well as *Hippopus* species, are smaller, measuring 16 mm or less and weighing between 1.67 and 20.28 ct.

Density. Each sample's density was obtained using a Sartorius CP323S scale and given as the average of three measurements. Values fell mostly between 2.70 and 2.86, comparable to aragonitic conch pearls (Fritsch and Misiorowski, 1987). In a few cases where the recorded value was low, ranging from 2.31 to 2.63, we assume the existence of an internal cavity, particularly in two samples (AC and AR) that contained a pit, which was also demonstrated in an X-ray radiograph by Singbamroong et al. (2015).

Refractive Index. As the pearls did not have flat surfaces, we had to estimate the refractive indices using the distant vision or spot refractive index method. Most of the samples were elongated and had to be laid down on their sides in the refractometer. Measured RI values ranged from 1.620 to 1.655. Our range of values lies in the mid to high range of the refractive index of aragonite. Among the less-pointed pearls, we tried a single measurement along the pole axis. The measured indices were often weak but did not systematically yield a value close to the lowest index.

Crystallochemical Nature of Pearl AC. X-ray diffraction analysis conducted on sample AC revealed peaks typical of aragonite and no component attributable to calcite. This is consistent with the aragonitic composition of Tridacnidae shells (Dauphin and Denis, 2000; Gannon et al., 2017).

Short-Wave and Long-Wave UV. No reaction to ultraviolet radiation was observed.

Color. Thirty-three of the pearl samples presented a white bodycolor with no additional hues. Four pearls (see figure 15) had a slightly yellowish pit-type defect.

TABLE 1. Gemological data for the set of 37 pearls from the Tridacnidae family.												
											Spiral and/or blade impeller[b] (figure 13)	
Sample no.	Symmetry	Shape	Diameter (mm)	Height (mm)	Weight (ct)	Density	RI ($\perp$)	RI ($\parallel$)	Flame + Ψ_{CE}[a]		Apex	Base
AA	Axial	Pear	9.71	8.36	4.68	2.80	1.64	1.67	Flame			
AB	Axial	Drop	11.90	7.66	4.73	2.79	1.63	—	Flame		n.d.[c]	n.d.
AC	Axial	Pear	9.71	14.10	8.35	2.63	—	—	Flame + Ψ_{CE}			
AD	Axial	Oval	9.90	8.20	5.20	2.85	1.66	1.60	Flame			
AE	Axial	Oval	11.25	9.20	7.24	2.84	1.645	1.67	Flame			
AF	Axial	Near-round	7.24	7.00	2.60	2.80	1.64	1.59	Flame + Ψ_{CE}			
AG	Axial	Oval	9.00	7.55	4.04	2.84	1.64	1.58	n.d.		n.d.	n.d.
AH	Axial	Drop	10.21	9.62	7.11	2.81	1.64	1.59	Flame			n.d.
AI	Axial	Drop	12.20	8.40	6.61	2.81	1.63	1.58	Flame + Ψ_{CE}			
AJ	Axial	Bullet	7.52	14.46	5.58	2.82	1.61	1.58	Flame + Ψ_{CE}			
AK	Axial	Pear	7.98	6.78	2.72	2.82	1.655	1.60	Flame			n.d.
AL	Axial	Button	8.16	9.43	5.31	2.82	1.60	1.56	Flame			
AM	Axial	Oval	11.72	7.24	4.59	2.81	1.65	1.56	Flame			
AN	Axial	Oval	11.95	8.98	7.09	2.79	1.65	1.63	Flame			n.d.
AO	Axial	Spindle	17.59	9.33	10.67	2.79	1.64	1.59	Flame + Ψ_{CE}			
AP	Axial	Button	8.37	9.21	4.76	2.70	1.65	1.59	Flame			n.d.
AQ	Axial	Near-round	11.32	12.05	11.96	2.84	1.64	1.60	Flame			
AR	Axial	Oval	8.75	6.80	2.63	2.31	1.65	1.60	Flame			
AS	Axial	Pear	9.56	7.73	3.78	2.70	1.64	1.56	Flame + Ψ_{CE}			n.d.
AT	Axial	Pear	7.42	6.52	1.90	2.53	1.65	1.56	Flame		n.d.	
AU	Axial	Drop	10.06	5.17	1.83	2.62	1.63	1.62	Flame			
AV	Axial	Bullet	8.69	6.55	2.75	2.76	1.65	1.57	Flame			n.d.
AW	Axial	Bullet	7.69	6.11	2.10	2.82	1.64	1.58	Flame			
AX	Axial	Oval	10.11	7.7	3.79	2.81	1.63	1.60	Flame			
AY	Axial	Bullet	10.81	6.85	3.39	2.80	1.65	1.61	Flame		n.d.	n.d.
AZ	Axial	Oval	12.73	8.70	7.77	2.77	1.63	1.63	Flame			
BA	Axial	Oval	14.31	7.88	7.37	2.82	1.65	1.57	Flame		n.d.	n.d.
BB	Axial	Oval	9.16	6.85	3.38	2.79	1.62	1.63	Flame			n.d.
BC	Axial	Pear	9.00	9.10	4.20	2.77	1.64	1.61	Flame			n.d.
BD	Axial	Spindle	17.76	5.25	3.11	2.82	1.64	—	Flame + Ψ_{CE}			n.d.
BE	Axial	Bullet	9.53	5.94	2.53	2.80	1.64	1.57	Flame			n.d.
BF	Axial	Spindle	15.42	5.08	2.88	2.82	1.64	—	Flame			n.d.
BG	Axial	Spindle	13.60	5.70	3.24	2.81	1.65	—	Flame			
BH	Axial	Spindle	13.46	5.50	3.04	2.81	1.64	—	Flame		n.d.	n.d.
BI	None	Baroque	L = 14.42 W = 12.25 H = 8.71		9.40	2.78	1.64	—	n.d.		n.d.	n.d.
BJ	Axial	Spindle	12.33	0.30	1.67	2.76	1.64	—	Flame + Ψ_{CE}		n.d.	n.d.
BK	None	Baroque	L = 22.44 W = 13.45 H = 8.92		20.28	2.86	1.64	—	n.d.		n.d.	n.d.

[a] Ψ_{CE} = pseudo-cat's-eye
[b] The two last columns indicate the direction of spirals or blade impellers described in the "Optical Features" section.
[c] n.d. = not detected
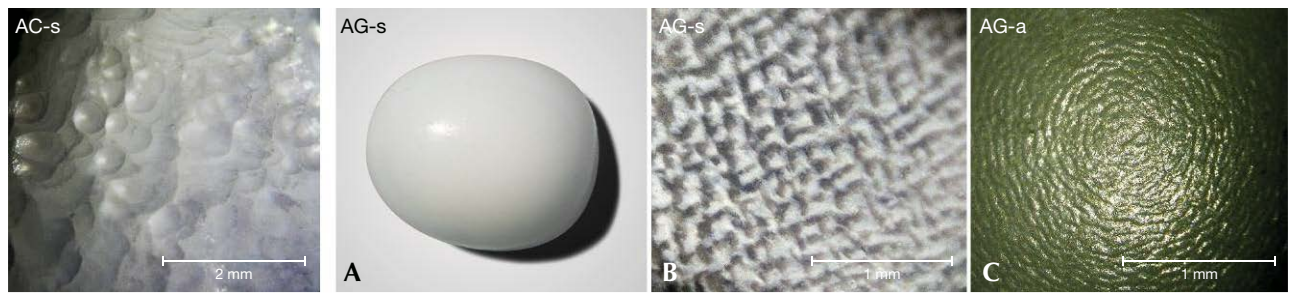
Figure 4. The photo on the far left reveals the texture of concave areas on flame-structure pearl AC. Pearl AG shows a satin-like appearance (A) and an orange peel structure along one side (B) and at the apex (C). Photos by J.-P. Gauthier.

OPTICAL FEATURES

By far the most distinctive optical feature of the Tridacnidae samples was their flame structure. Some of the samples simply showed porcelaneous surfaces or appeared rather dull.

Surface Texture. At first, the brilliant surfaces of the flame-structure pearls appeared smooth. With low-angle lighting, however, one could observe numerous small, joined depressions (far left in figure 4, pearl AC). Most of the pearls had a high luster and displayed a porcelaneous sheen. Some pearls lacking flames (AG, BI, and BK) had a satin luster (figure 4A, pearl AG); at higher magnification, they presented an orange peel texture (figure 4B), axially centered in circles at the poles (figure 4C). No evidence of polishing or peeling (Strack, 2006) on the surface was found.

Flames. Lateral observation revealed a flame structure fanning out in one main direction, in a bright helix, around the rotation axis. The winding helices displayed a characteristic crisscross pattern (figure 5, pearls AE and AU). These helicoidal lines converged

toward the poles, resulting in dramatic patterns (figure 6). Moreover, a top view showed a non-radial convergence to the poles that resembled the structure of blade impellers oriented in the same direction and confirming the existence of a rotation axis (see figure 12).

Figure 6. Flame patterns observed at the apex or base of six pearls from the Tridacnidae family. Photos by J.-P. Gauthier.

Figure 5. Lateral observation of samples AE (left) and AU (right) shows a crisscross flame structure. Photos by J.-P. Gauthier.
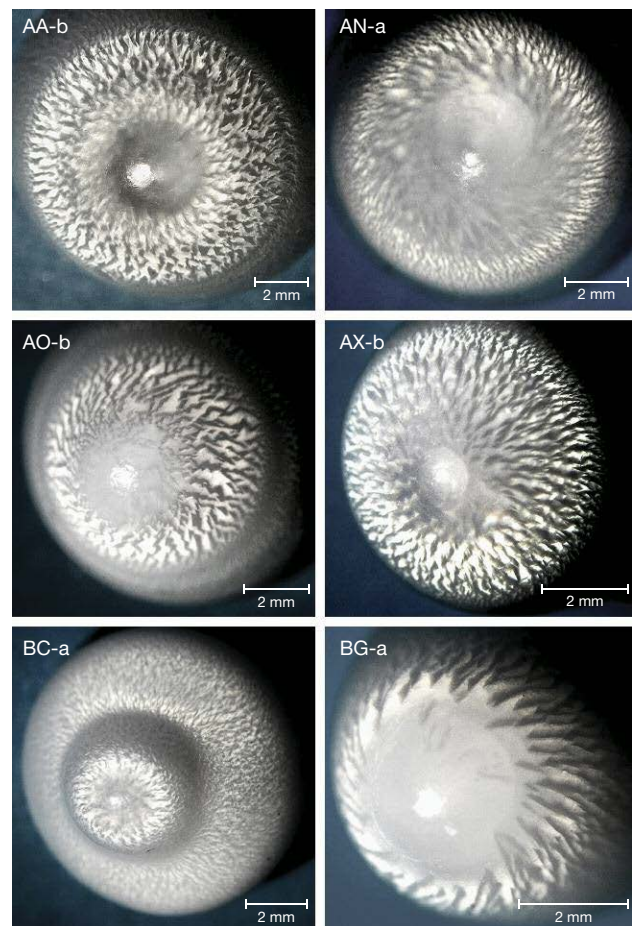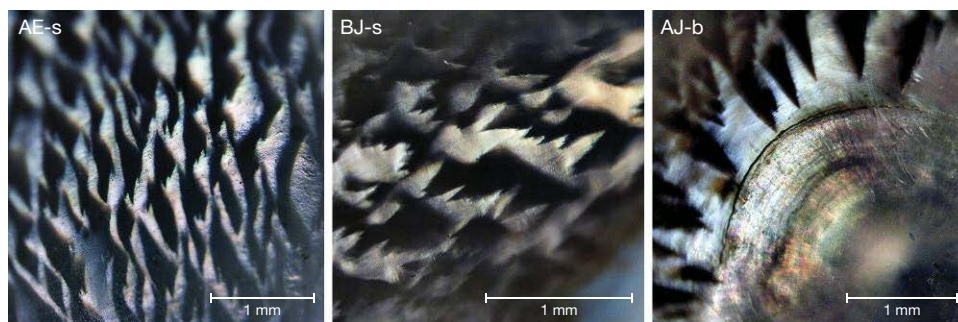
Figure 7. Left and center: These images of pearls AE and BJ show the directional growth of flames. Right: In pearl AJ, flames start from a pole with a two-dimensional spiral. Photos by J.-P. Gauthier.
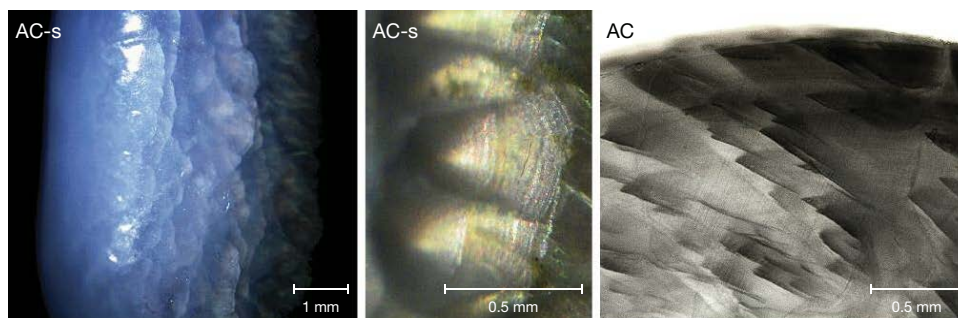
Figure 8. Left and center: Overlapping layers merging at the surface of pearl AC and their lamellar iridescent structure. Right: A thick slice cut perpendicular to the rotational axis of pearl AC shows the flames inclined with respect to the surface. Photos by J.-P. Gauthier.

In their finer structure, the shape and positions of the flames are more difficult to grasp, as their appearance changes depending on the light exposure. The term "flame" is justified by a wide base and a pointed tip, all oriented in the growth direction (figure 7, pearls AE and BJ). Alternating bright and dark areas are noted by Hänni (2010), while the cross-lamellar structure observed in conch pearls and shells is reminiscent of a previous study on the fracture toughness of the *Strombus gigas* shell (Kamat et al., 2000). Binocular microscopy allows us to better appreciate the three-dimensional configuration of the flames, which are less visible in two-dimensional photographs. Through this process, we came to understand that these flames are not totally localized on the surface, but rather come from inside the pearl. This is confirmed by a photograph of a slice cut perpendicular to the rotation axis of pearl AC, as illustrated in figure 8 (right).

In some cases, the reflective parts instead have a scale-like shape (figure 8, left) perpendicular to the rotation axis. We then observe a pseudo-chatoyancy, shifted to the right or the left of the axis (figure 9, pearls AI and BD). The origin of this effect will be discussed later. It is also worth noting the helicoidal

Figure 9. Pseudo-chatoyancy in pearls AI (left) and BD (center) and a helical effect in pearl AF (right). The bright spots in pearls AI and AF and the shiny median line close to the apex of pearl BD correspond to specular reflection. Green arrows represent the direction of rotation (according to figure 17). Photos by J.-P. Gauthier.
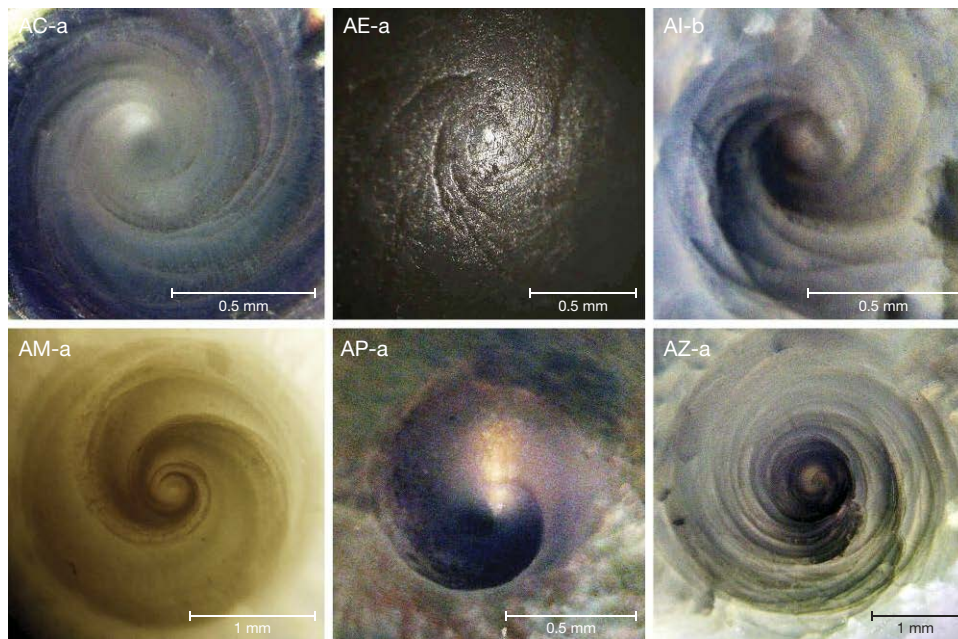
Figure 10. Three-dimensional spirals (or helices) merging at the poles of some Tridacnidae pearls. The images are processed using a high-pass filter. Photos by J.-P. Gauthier.

cat's-eye effect, visible in some samples but especially in pearl AF (figure 9, right).

The scales on the lateral part of the pearl (figure 8, left), which developed in laminated layering, are similar to nacre in their optical effect (interference and diffraction colors; see figure 8, center), as observed on the polished outer surface of *Pinctada margaritifera* shells (see figure 1 in Liu et al., 1999).

MAJOR OBSERVATIONS

Spirals. One of the most astounding characteristics found in some of the pearls is the spiral observed at the apex or base. This characteristic appears to be absent from the literature. Due to the difficulty of microscopic observation of the smooth white pearls, it was necessary to process the images and enhance the outlines by using a high-pass filter and forcing the contrast. Having gathered a number of images of these spirals, we determined that they fell into two types:

- The first has sharp outlines, often constituted by several branches, unfolding from the pole axis. Given the pearls' translucency, an internal helical structure seems to be emerging toward the surface. However, they exhibit no particular optical feature (figure 10).

- The second type has more tenuous outlines and presents only one branch at first glance. These spirals are flat and formed by radial crystallites in angular sectors of only a few degrees. Interference colors reveal that these spirals develop in thin layers. Examination at higher magnification also reveals narrow areas parallel to the edge of each spiral, constituting growth steps of low height (figure 11). In the case of pearl AI, the spiral is highlighted by air bubbles in water. This defines a local depression on the apex surface suitable for the deposition of these bubbles rather than for a smooth surface.
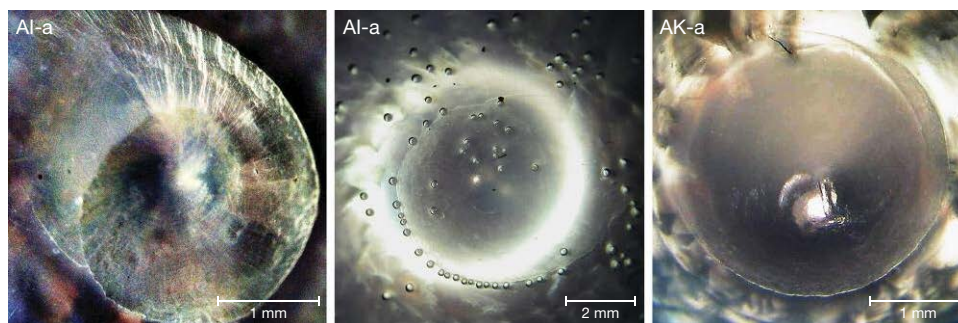
Figure 11. Two-dimensional spirals with radial sectors at the poles of some Tridacnidae pearls. The spiral of immersed pearl AI is highlighted by air bubbles in the depression on the surface. The images are processed using a high-pass filter. Photos by J.-P. Gauthier.
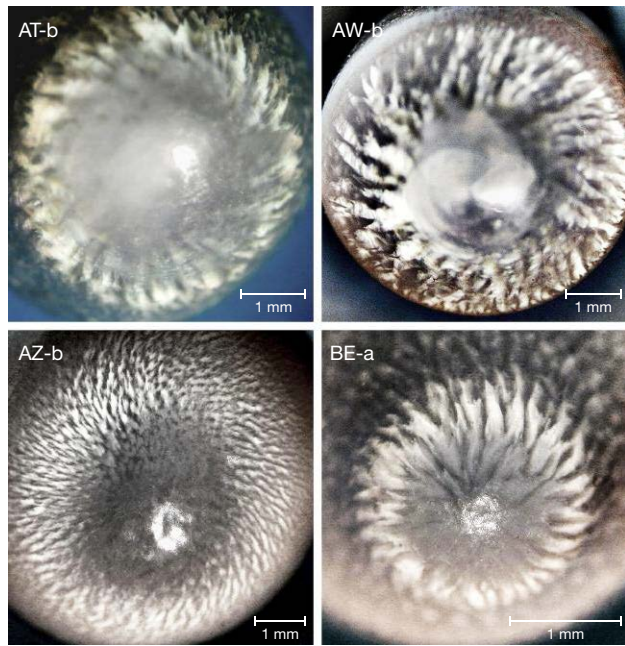
Figure 12. Some flame structures display a pattern at the poles that is reminiscent of blade impellers. Photos by J.-P. Gauthier.

Figure 13. Clockwise and counterclockwise line drawings of two- and three-dimensional spirals (first four drawings from the left) and blade impellers (last two drawings on the right).

Unfortunately, most of the spirals were barely visible and only a few were correctly identified, which made it impossible to evaluate statistics on their effective presence on one or both poles. In addition, these two types of spirals are likely to superimpose on each other. Note that the two types of spirals can be left- or right-handed.

Blade Impellers. At either the apex or the base, the flames often formed attractive patterns reminiscent of blade impellers or fan blades. These blades were all curved in one direction on a given pearl. Figure 12 shows typical examples.

Spirals and blade impellers, when present, do not always coexist. For an overview of the whole sample set of pearls, see table 1, which includes the rotation direction of spirals and blades for the apex as well as the base. The multiple branches of spirals represent the internal helices. The surface spirals have a single branch in addition to centripetal rays, suggesting angular growth sectors. A corona-shaped representation with directional blades is adopted for both the clockwise and counterclockwise blade impellers. The basic patterns are represented in figure 13. Depending on the orientation of the spirals and blade impellers, they can be used individually or combined. Figure 14 displays the superimposition of spirals and blade impellers, oriented in the same direction (left, pearl AN) or the opposite direction (right, pearl AE).

OTHER OBSERVATIONS

Defects. Four pearls (AC, AJ, AR, and BC) presented a surface defect visible to the eye (figure 15). These were related to a spot defect that extended into a depressed groove with a light yellowish hue, possibly consisting of organic material. Two of the four spot defects formed a depression and exhibited a chimney-like hole (pearls AC and AR).

Uncommon Features. Three pearls (AA, AB, and AO) presented a sharp and relatively thin circle perpendi-
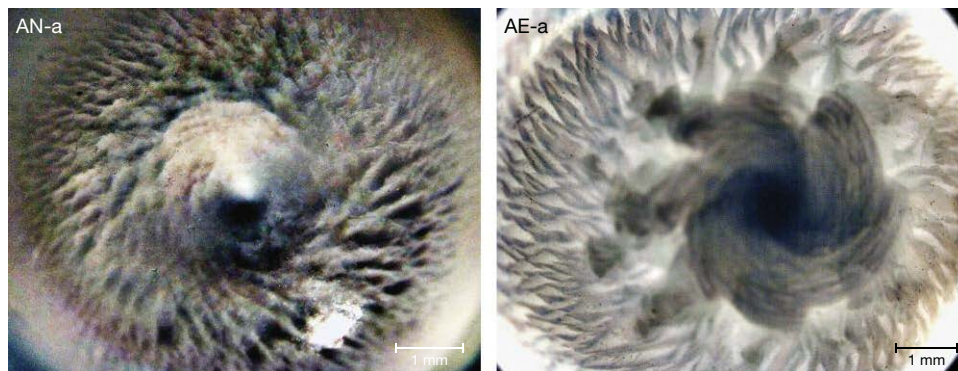
Figure 14. The flame structure at the apex, similar to blade impellers; the internal spiral shows a common (pearl AN) or opposite (pearl AE) direction. Photos by J.-P. Gauthier.
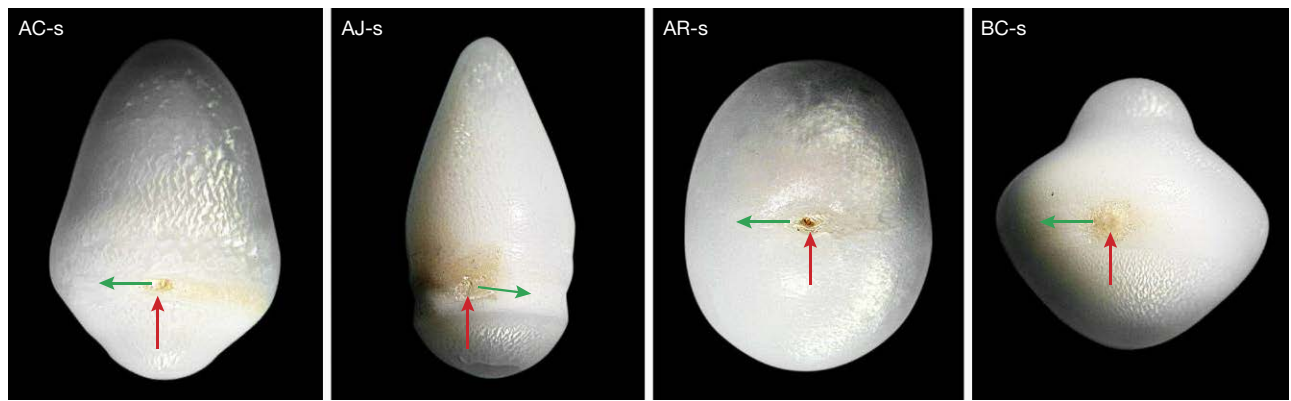
Figure 15. Spot defects observed on Tridacnidae pearls (red arrows) are accompanied by a comet, which indicates the direction of rotation (green arrows). Photos by J.-P. Gauthier.

cular to the rotation axis. These were not related to the circles observed in barrel-shaped pearls from *Pinctada* that are associated with spot defects (Gauthier et al., 2014). Rather, the circles revealed a separation line on the surface, characterized by a discontinuity of the flame growth direction (figure 16). Their origin remains unclear.

Translucency of Poles. In some cases, the flames did not cover the apex or the base. The light penetrated inside the pearl when the poles were illuminated in the direction of the rotation axis and was therefore not reflected by the flames. Subsequently the light was stopped by the lateral flames, which appeared dark (see figure 6, pearl BG). This translucency allowed for the observation of three-dimensionality in one spiral type, as described above.

DISCUSSION
Routine analyses confirmed the aragonitic nature of these pearls. They are exclusively white in color and do not fluoresce under UV light. While the exact origin of these pearls remains unknown, the variations observed in the visual features could be linked to differences between *Tridacna* and *Hippopus* species. This hypothesis requires confirmation based on samples from known species and their respective shells, but such an analysis is outside the scope of the present study.

Several elements support the probability of pearl rotation during the growth phase:

Axial Symmetry. Among the set of 37 pearls, 35 exhibited cylindrical symmetry (see figure 2 and table 1). The pearls, which developed in the mantle tissue of the mollusk, did not grow around spherical nuclei and were not confined to limited spaces (as opposed to those cultivated in the gonads of saltwater oysters). Therefore, we must examine the rotation of these pearls to explain this symmetry. The rotation around a fixed axis takes place when the pearl settles in the mantle on anchorage points, specifically due to its nonspherical shape (Gauthier et al., 2014). Incidentally, the circle surrounding the three pearls in figure 16, perpendicular to their rotation axis, supports the likelihood of rotation.
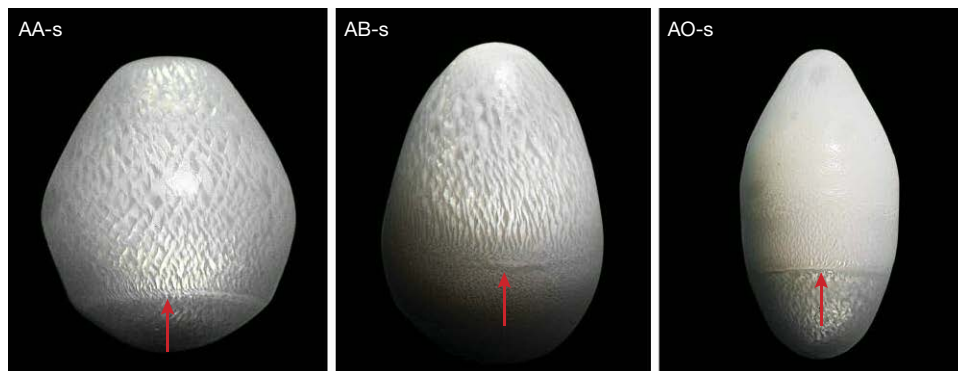
Figure 16. Circles observed at the bases of some pearls from Tridacnidae. Photos by J.-P. Gauthier.

Presence of Spirals at the Poles. As mentioned earlier, the spirals fell into two types. One was a three-dimensional spiral, most probably with internal helices from a genetic origin and possibly not related to rotation (see figure 10). The second type, a quasi-two-dimensional flat spiral of mechanical origin, was due to the deposition of aragonite at the poles, which grew in small angular sectors (see figure 11). The direction of rotation was opposite to the direction of the spiral development, as is the case with pearls from *Pinctada margaritifera* (Gueguen et al., 2015).

Flame Growth and Blade Impellers. Flames often developed along a helix, sometimes a double helix, located on or near the pearl surface. When looking at a coil spring, whether left- or right-handed, nothing indicated the direction in which it would turn. However, the flame spikes of a helix were all oriented in the same growth direction. The name "blade impellers" refers to the flames being displayed in a pattern, centered on the pearl's axis when it reaches the pole (see figure 12). Whether by lateral or vertical observation, the pearl normally rotated in the direction opposite to the aragonite growth (Cartwright et al., 2013).

Pseudo-Chatoyancy. Some flame-structure pearls presented a bright line rising along their axis of symmetry (see figure 9) that resembled a cat's-eye effect. Unlike chatoyancy in cabochon-cut gems, this does not result from a lattice of parallel acicular inclusions diffusing the light (Wüthrich and Weibel, 1981), but is instead due to a series of reflective blades oriented in the same direction, on or near the pearl surface (see figure 8, left and center). The pseudo-chatoyancy is produced by the reflection from this scale-like structure.

Observing the line of pseudo-chatoyancy is crucial to infer the direction of rotation. When both the light source and the observer are positioned upright over the pearl axis, which is horizontal, the bright line should be symmetrical if the blades lie on the surface (see the light path shown in red in figure 17). However, the blades come from the inner pearl in successive layers, as shown in figure 8. Consequently, the bright line is not observed in the median plane. Rather, it is off-center (see the light path marked in black in figure 17 as well as the pseudo-cat's-eye in figure 9, pearls AI and BD). The rotation should then occur in the direction opposite the blade growth, again according to the theory of Cartwright et al. (2013). They suggest a rotation mechanism due to fundamental forces, acting
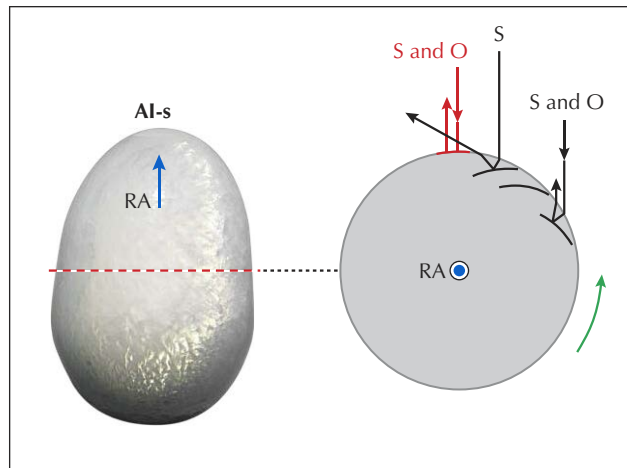
Figure 17. Left: As shown in figure 9, pearl AI displays a pseudo-chatoyancy. The red dashed line corresponds to the cross-section of the pearl, perpendicular to the rotational axis (RA) and represented in the sketch on the right. Right: Centered reflection on a hypothetical blade at the surface (in red), for light source (S) and observer (O) above the pearl. In fact, an off-center reflection on an inner pearl layer (in black) results in a pseudo-chatoyancy effect. The green arrow indicates the rotation derived from the position of the pseudo-cat's-eye and the direction of scale-like growth. Photo by J.-P. Gauthier.

toward the growth steps of nacreous pearls. The findings regarding the layer-by-layer growth in pearls of *Pinctada margaritifera* (Gauthier et al., 2014) support this theory of rotation direction. Accordingly, in the blade configuration illustrated in figure 17, the rotation should be counterclockwise.

The direction of rotation suggested by the pseudo-cat's-eye of pearls AI and BD (see figure 9) is consistent with the observation of the two-dimensional flat spiral at the apex (table 1). Additionally, the helical bright line related to the flames in figure 9 (pearl AF) is the consequence of pseudo-chatoyancy, which accounts for both the helical growth of flames and the pearl rotation.

Presence of Spot Defects. The spot defects located near the bases of four pearls (see figure 15) are accompanied by comets, defining the arc of the circles perpendicular to the rotation axis. As established with pearls from *Pinctada margaritifera* (Gauthier et al., 2014), these spot defects allow us to determine the direction of rotation, as shown by the green arrow.

The rotation direction of each pearl cannot be inferred from the figures due to their complexity. An unambiguous answer lies in less common but more
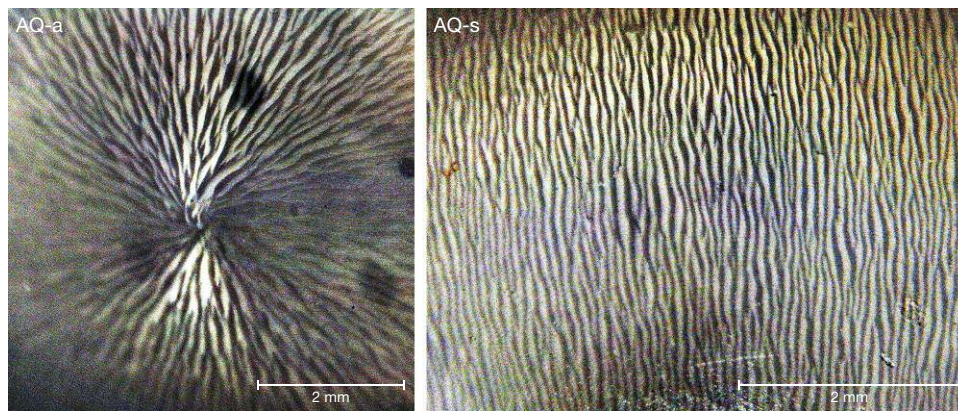
Figure 18. Observations of flame structures at the apex and equator of pearl AQ. Photos by J.-P. Gauthier.

reliable features, namely the two-dimensional spirals and comets associated with spot defects.

CONCLUSIONS

Besides the intrinsic gemological properties of flame-structure pearls from the Tridacnidae family, this study has stressed the predominance of axial symmetry, including unusual shapes unlike those generally encountered in nacreous pearls.

The two types of spirals, which have rarely been photographed, were often highlighted at the poles. The growth of flames produces some peculiar patterns on the pearls: blade impellers in the apex regions, pseudo-cat's-eyes on the sides, or circles resulting in caps at the two poles. Surface defects were identified, such as spot defects accompanied by comets. The axial symmetry, the directional growth of the flames, the pseudo-chatoyancy, the circles and

comets, and the blade impellers are all features that suggest the rotation of these pearls—if not during their formation, then at least during the growth phase preceding their harvest.

The unknown species origin of each Tridacnidae pearl leaves open the reasons for the observed visual differences, for example in the polar and equatorial flame patterns on pearl AQ (figure 18). Investigation of the internal structure definition, probably constituted of internal helices, will require the sacrifice of some pearls through cuts made parallel and perpendicular to the rotation axis.

It would also be interesting to investigate the flame-structure concretions of gastropods, such as conch "pearls," that show evidence of rotation. However, these pearls rarely present an axial symmetry, and their scarcity is a major obstacle to the systematic study of this property.

ABOUT THE AUTHORS
Dr. Gauthier is a professor of physics retired from the University Claude Bernard Lyon I and now with the Gemological Research Center of Nantes (CRG) and the Association Française de Gemmologie (AFG). Mr. Fereire is also a member of CRG and AFG. Mr. Bui is a civil engineer and researcher working at the Catholic University of Louvain in the field of nanophysics. He is a lecturer at HRD Antwerp and collaborates with that institute and the CRG on gemological research.

REFERENCES
Acosta-Salmón H., Davis M. (2007) Inducing relaxation in the queen conch *Strombus gigas* (L.) for cultured pearl production. *Aquaculture*, Vol. 262, No. 1, pp. 73–77, http://dx.doi.org/10.1016/j.aquaculture.2006.09.032

Agbaje O.B.A., Wirth R., Morales L.F.G., Shirai K., Kosnik M., Watanabe T., Jacob D.E. (2017) Architecture of crossed-lamellar

bivalve shells: the southern giant clam (*Tridacna derasa*, Röding, 1798). *Royal Society Open Science*, Vol. 4, No. 9, 170622, http://dx.doi.org/10.1098/rsos.170622

Bari H., Lam D. (2009) *Perles.* Skira Ed., Milan, 335 pp.

Bidwell D., DelRe N., Widemann A., Epelboym M. (2011) Natural non-nacreous pearls from the giant clam *Tridacna gigas. G&G,*

Vol. 47, No. 2, pp. 144–145.

Cartwright J.H.E., Checa A.G., Rousseau M. (2013) Pearls are self-organized natural ratchets. *Langmuir*, Vol. 29, No. 26, pp. 8370–8376, http://dx.doi.org/10.1021/la4014202

Chang J.W., Hyatt A. (2011) Lab Notes: Large conch pearl. *G&G*, Vol. 47, No. 3, pp. 230–231.

Copland J.W., Lucas J.S. (1988) *Giant Clams in Asia and the Pacific*. ACIAR Monograph No. 9, 274 pp.

Council of the European Union (1997) Council Regulation (EC) No 338/97 of 9 December 1996 on the protection of species of wild fauna and flora by regulating trade therein. *Official Journal of the European Communities*, L61, Vol. 40, p. 60.

Dauphin Y., Denis A. (2000) Structure and composition of the aragonitic crossed lamellar layers in six species of Bivalvia and Gastropoda. *Comparative Biochemistry and Physiology Part A*, Vol. 126, No. 3, pp. 367–377, http://dx.doi.org/10.1016/S1095-6433(00)00213-0

Davis M. (2000) Queen conch (*Strombus gigas*) culture techniques for research, stock enhancement and growout markets. In M. Fingerman and R. Nagabhushanam, Eds., *Recent Advances in Marine Biotechnology, Volume 4: Aquaculture, Part A: Seaweeds and Invertebrates*. Science Publishers, Inc., Enfield, New Hampshire, pp. 27–59, and other references in this chapter.

Davis M., Shawl A.L. (2005) A guide for culturing queen conch. In A.M. Kelly and J.T. Silverstein, Eds., *Aquaculture in the 21st Century: Proceedings of an American Fisheries Society Symposium Special Symposium on Aquaculture in the 21st Century*, August 22, 2001, Phoenix, Arizona, pp. 125–142. American Fisheries Society, Bethesda, Maryland.

Federman D., Bari H. (2007) *La perle rose: trésor naturel des Caraïbes*. Skira Ed., Milan, 176 pp.

Fritsch E., Misiorowski E.B. (1987) The history and gemology of queen conch "pearls." *G&G*, Vol. 23, No. 4, pp. 208–221, http://dx.doi.org/10.5741/gems.23.4.208

Gannon M.E., Pérez-Huerta A., Aharon P., Street S.C. (2017) A biomineralization study of the Indo-Pacific giant clam *Tridacna gigas*. *Coral Reefs*, Vol. 36, No. 2, pp. 503–517, http://dx.doi.org/10.1007/s00338-016-1538-5

Garen P. (2003) Ponte et élevage larvaire de bénitier (*Tridacna maxima*). IFREMER, Note technique, 5 pp.

Gauthier J.-P., Gutierrez G., Serrar M. (2014) La "piqûre", un défaut à l'origine du cerclage de perles chez *Pinctada margaritifera*. *Revue de Gemmologie a.f.g.*, No. 187, pp. 4–6.

Gauthier J.-P., Gutierrez G., Serrar M., Bui T.N. (2015) Rares perles cerclées à double axe de rotation. *Revue de Gemmologie a.f.g.*, No. 194, pp. 4–7.

Gauthier J.-P., Fereire J., Bui T.N. (2018) An explanation of a specific type of circling as observed on Ming cultured pearls. J*ournal of Gemmology*, Vol. 36, No. 3, pp. 152–160, http://doi.org/10.15506/jog.2018.36.3.240

Gueguen Y., Czorlich Y., Mastail M., Le Tohic B., Defay D., Lyonnard P., Marigliano D., Gauthier J.-P., Bari H., Lo C., Chabrier S., Le Moullac G. (2015) Yes, it turns: experimental evidence of pearl rotation during its formation. *Royal Society Open Science*, Vol. 2, No. 7, p. 150144, http://dx.doi.org/10.1098/rsos.150144

Hänni H.A. (2010) Explaining the flame structure of non-nacreous pearls. *Australian Gemmologist*, Vol. 24, No. 4, pp. 85–88.

Ho J.W.Y., Zhou C. (2014) Lab Notes: Natural pearls reportedly from a *Spondylus* species ("thorny" oyster). *G&G*, Vol. 50, No. 3, pp. 241–242.

Homkrajae A. (2016a) Micro-World: Iridescent *Spondylus* pearl. *G&G*, Vol. 52, No. 2, pp. 202–203.

——— (2016b) Lab Notes: Non-nacreous purple and white pearls reportedly from *Spondylus* species. *G&G*, Vol. 52, No. 3, pp. 303–304.

Htun H., Larson W., Cole J.E. (2006) Melo "pearls" from Myanmar. *G&G*, Vol. 42, No. 3, pp. 135–136.

Hui M. (2012) Connectivity and evolution of giant clams (Tridacnidae): A molecular genetic approach. PhD thesis, University of Bremen, 85 pp.

Hyatt A. (2008) Lab Notes: Large baroque multicolored conch pearl. *G&G*, Vol. 44, No. 1, p. 72.

Jiao D., Liu Z.Q., Qu R.T., Zhang Z.F. (2016) Anisotropic mechanical behaviors and their structural dependences of crossed-lamellar structure in a bivalve shell. *Materials Science and Engineering C*, Vol. 59, pp. 828–837, http://dx.doi.org/10.1016/j.msec.2015.11.003

Kamat S., Su X., Ballarini R., Heuer A.H. (2000) Structural basis for the fracture toughness of the shell of the conch *Strombus gigas*. *Nature*, Vol. 405, No. 6790, pp. 1036–1040, http://dx.doi.org/10.1038/35016535

Koivula J.I., Kammerling R.C., Fritsch E. (1994) Gem News: Horse conch "pearls." *G&G*, Vol. 30, No. 3, p. 195.

Liu Y., Shigley J.E., Hurwit K.N. (1999) Iridescence color of a shell of the mollusk *Pinctada margaritifera* caused by diffraction. *Optics Express*, Vol. 4, No. 5, pp. 177–182, http://dx.doi.org/10.1364/OE.4.000177

Scarratt K. (1999) Orange pearls from the Melo volutes (marine gastropods). In D.J. Content, Ed., *The Pearl and the Dragon: A Study of Vietnamese Pearls and a History of the Oriental Pearl Trade*. Rare Books Incorporated, Houlton, Maine, pp. 80–107.

Segura O., Fritsch E. (2015) Gem News International: Nonbead-cultured pearls from *Strombus gigas*. *G&G*, Vol. 51, No. 2, pp. 201–202.

Singbamroong S., Ahmed N., Ahmed A.R., Karam M., Hassan G., Mohamed S., Al Muhairi N. (2015) Observations on natural non-nacreous pearls reportedly from Tridacna (clam) species. *34th International Gemmological Conference IGC*, pp. 125–127.

Strack E. (2006) *Pearls*. Rühle-Diebener-Verlag, Stuttgart, Germany, 707 pp.

Wüthrich A., Weibel M. (1981) Optical theory of asterism. *Physics and Chemistry of Minerals*, Vol. 7, No. 1, pp. 53–54, http://dx.doi.org/10.1007/BF00308202

A PEARL IDENTIFICATION CHALLENGE

Nicholas Sturman, Laura M. Otter, Artitaya Homkrajae, Areeya Manustrong, Nanthaporn Nilpetploy, Kwanreun Lawanwong, Promlikit Kessrapong, Klaus Peter Jochum, Brigitte Stoll, Herman Götz, and Dorrit E. Jacob

Nacreous pearls are usually found in saltwater (SW) or freshwater (FW) environments, yet there are some reports of pearls originating from a brackish environment. Likewise, nacreous pearls may form naturally or by human manipulation (bead and non-bead cultured), but in some cases the origin is hard to prove and professional opinions are not always unanimous. Two pearls were examined by the authors, who were in the unique situation of being unable to positively identify either their origin (natural or cultured) or growth environment (FW versus SW). This in turn had a direct impact on the ability to determine which mollusk produced the pearls, a factor that would have helped answer the former two questions. It is very rare to find pearls for which all three of these criteria are in doubt, as usually it is straightforward to determine at least two of them. The results of this study illustrate the challenges that laboratories sometimes face when testing pearls.

When a gemological laboratory receives pearls for examination, a series of tests are carried out to reach a conclusion on their identification (natural, cultured, imitation, or assembled); whether they formed in a saltwater (SW) or freshwater (FW) environment; and whether any treatments have been applied (color modification, filling, or coating). Some laboratories, such as GIA, also provide an opinion, whenever possible, on the mollusk that produced the pearls. The two pearls described in this work (figure 1) were submitted to GIA's Bangkok laboratory at different times by different clients. They were subsequently purchased for further analysis after their identity (natural/cultured), their growth environment (FW/SW), and consequently the mollusk in which they formed proved challenging to determine. Trace element chemistry is an important factor to consider when identifying the environment in which a pearl-producing mollusk lived (Wehrmeister et al., 2007; Karampelas et al., 2019). A clear answer to this question, in turn, yields potential information about the cultured versus natural origin of pearls produced and may assist with mollusk identification (Hänni, 2012).

The initial results from the work carried out by GIA revealed internal structures that were not typical of either natural pearls or non-bead cultured pearls. Bead cultured pearls were quickly ruled out, as were assembled and imitation pearls. The most unusual initial findings related to the pearls' chem-

In Brief

- Pearls are found within mollusks that inhabit either saltwater or freshwater environments. The species of mollusk is usually directly related to the environment in which it is found. For example, *Pinctada* species bivalves and *Melo* species gastropods live in saltwater conditions.

- It is usually straightforward for any gemological laboratory to determine the environment from which a pearl originated. The saltwater or freshwater nature is routinely identified by EDXRF and optical X-ray fluorescence analyses.

- Encountering pearls with mixed chemistry (saltwater and freshwater) is very unusual unless the pearls are atypical "bead" cultured pearls in which the overlying saltwater layers are so thin that the underlying freshwater nucleus impacts the chemistry results obtained.

istry and their optical X-ray fluorescence reactions. In fact, the questions that arose from the initial work carried out on the pearls led to discussions with other colleagues in the industry, and additional complementary tests at the Max Planck Institute for Chemistry and Johannes Gutenberg University, both

Figure 1. The two challenging pearls discussed in this report. Pearl A sits on a freshwater shell (top) and pearl B on an iridescent saltwater shell (bottom). Photo by Nuttapol Kitdee.

located in Mainz, Germany, were carried out in order to compare the results with those obtained by GIA. The GIA authors felt that taking this approach would yield helpful data and discussions, which indeed turned out to be the case.

MATERIALS AND METHODS

Two pearls weighing 8.52 ct (sample A) and 10.66 ct (sample B) and measuring 11.81 × 10.45 × 9.21 mm and 13.77 × 11.82 × 8.67 mm, respectively, were examined with a variety of gemological, structural, and chemical analyses. Analysis of the pearls' surfaces was carried out with gemological microscopes (magnification range between 10× and 60×) and documented by photomicrographs using a Nikon SMZ18 microscope (various magnifications up to 176×) incorporating Nikon NIS-Elements photomicrography software and a Canon Power-Shot G16 camera. The pearls' ultraviolet fluorescence reactions were observed under an 8-watt UV lamp with both long-wave and short-wave UV at

365 and 254 nm excitation wavelengths, respectively. A DiamondView unit provided deep-ultraviolet (<230 nm) luminescence reactions.

As X-ray film imaging has become largely obsolete, the two main X-ray techniques used to identify pearls today are real-time microradiography (RTX) (Karampelas et al., 2017) and X-ray computed microtomography (μ-CT) (Karampelas et al., 2010; Krzemnicki et al., 2010; Otter et al., 2014a). The former allows the tester to obtain results on the whole volume of the sample, while the latter reveals a pearl's structure from micron-thin slices while reconstructing a three-dimensional model of the sample. While the vast majority of pearls submitted undergo only RTX investigation, as this technique is significantly faster and more cost-efficient, some require more in-depth μ-CT analysis. This technique allows the non-destructive investigation of finer structural details with high spatial resolution in three dimensions. Its higher sensitivity permits structural differences to be discerned down to the order of a few microns per

voxel (or 3D pixel), depending on the overall size of the sample volume (e.g., Wehrmeister et al., 2008; Karampelas et al., 2010; Otter et al., 2014a).

In Bangkok the internal structures were examined using a Faxitron CS-100 2D real-time RTX unit (90 kV and 100 μA excitation) and a Procon CT-Mini μ-CT unit fitted with a Thermo Fisher 8W/90 kV X-ray tube and a Hamamatsu flat-panel sensor detector. Additional X-ray computed microtomography scans were obtained using a Scanco μ-CT 40 unit with an acceleration voltage of 70 kV together with a 114 μA target current at the University Medical Center of Johannes Gutenberg University in Mainz, Germany. The resulting images were processed using OsiriX, an open-source visualization software.

A custom-modified FocalSpot Verifier FSX-PF100 optical X-ray fluorescence unit (100 kV voltage and 3.2 mA current) incorporating a Canon EOS Rebel T4i camera was subsequently used in Bangkok to check whether the pearls originated from a marine or freshwater environment, as pearls from each react differently when exposed to X-rays (Hänni et al., 2005; Kessrapong et al., 2017). The results of energy-dispersive X-ray fluorescence (EDXRF) analysis provided further data to be used in conjunction with the optical fluorescence results.

The pearls' chemical composition was initially analyzed in Bangkok using a Thermo Scientific ARL Quant'X EDXRF spectrometer. Since the results were inconsistent with those expected during routine pearl analysis, more thorough investigations were obtained by means of laser ablation–inductively coupled plasma–mass spectrometry (LA-ICP-MS) carried out in different laboratories. First, spot analyses were performed using a Thermo X Series II ICP-MS system in combination with a New Wave Research UP-213 laser ablation system at GIA laboratories in Bangkok and New York. U.S. Geological Survey (USGS) microanalytical carbonate reference materials MACS-1 and MACS-3 were used as matrix-matched calibration standards. A pulse repetition rate of 7 Hz, energy density of 10 J/cm^2, and spot diameter of 40 μm were applied. The pearls were further investigated in Germany, with depth profiles obtained using a Thermo Fisher Element 2 single-collector sector-field ICP-MS paired with the same laser ablation system as before. A pulse repetition rate of 10 Hz, energy density of 8 J/cm^2, and spot diameter of 80 μm were applied. Here, pearls A and B were analyzed with 33 and 36 spots, respectively, distributed in groups of three over their entire surface. Probing the pearls in groups of three adjacent spots permitted the techni-

cian to monitor the reproducibility of the trace element pattern in every location. Data reduction and elimination of obvious outliers were performed following a programmed routine in Microsoft Excel described in Jochum et al. (2007). The calibration followed the method for accurate trace element analysis of biogenic calcium carbonates published in Jochum et al. (2012), where refractory lithophile elements are calibrated with NIST glasses (SRM 610 and 612), while chalcophile and siderophile elements with low boiling points were calibrated using matrix-matched calibrated standards USGS MACS-1 and -3. A Leica DMRX incident-light microscope with well-defined zoom steps for each grid on its focusing adjustment screw was used to measure the depth of the ablation spots left in the pearls after analysis.

RESULTS

External Appearance. In most cases, gemologists and experienced members of the trade are able to visually identify pearls based on their external characteristics (luster, color, shape, etc.). However, these two pearls did not exhibit typical SW or FW features, and as a result their external appearance did not fit particularly well with either natural or cultured pearls. Based on the authors' experience handling countless pearls of all types, the form of the platy overlapping nacreous structures (i.e., platelet size, spacing, and shape/appearance of the platelet edges—see figure 2) could be considered more indicative of FW than SW. The flat surfaces on one side of each pearl could also have been taken as an indicator of freshwater origin. The pearls did not display enough characteristic features to sway the decision one way or the other, however.

RTX and μ-CT Analysis. Both pearls in this study showed structures that were ambiguous when examined with the RTX units in Bangkok. Similarities in the darker organic-rich arcs extending from near the center to the outer surfaces and in small organic-rich areas adjacent to the centers were revealed. A straight organic-rich feature (figures 3 and 4), related to the flat surfaces visible on the exterior, was also observed in each pearl. Such structures are not conclusive of any particular type of pearl and do not match the SW or FW structures usually associated with non-bead cultured pearls (see box A), so natural origin remained a possibility. In order to identify the true origin, more work was considered necessary, so both pearls were further examined by μ-CT. The resulting μ-CT work provided more detail but did not resolve the origin to the complete satisfaction of those who

Figure 2. Platy structure typical of nacreous pearls was evident on both pearls (sample A on the left, field of view 2.34 mm; sample B on the right, field of view 1.76 mm). The platelets of both were finely to moderately spaced, while areas of pearl B also showed some distortions in the platelet patterns similar to those observed by the authors on some freshwater pearls. However, the nature of the platelets was not specific enough to indicate a freshwater or saltwater growth environment. Photomicrographs by Artitaya Homkrajae.

examined the data. As can be seen from the sample µ-CT images in figures 3–6, the structures were inconclusive, although the majority of opinions favored a cultured origin based on previous testing experience. However, an idea of their chemistry was also needed before reaching any conclusions, as linking

Figure 3. Three µ-CT slices obtained during the analysis of pearl A in Bangkok (the top row shows the whole pearl, the bottom row the magnified areas). All three slices show a suspicious feature: a small dark linear-appearing void (red arrows) that some gemologists might associate with NBC formation, within a dark gray organic-rich area (around the green arrows). The linear structure related to the flat surface area is indicated by the blue arrows. Blue arrows are absent from the upper and lower right-hand images, as the structure does not show due to the pearl's orientation. Note the similarity to the features observed in pearl B (figure 4). The weak white rings on the lower right image are artifacts and not pearl-related structures.

Saltwater
NBC Structures

Freshwater
NBC Structures
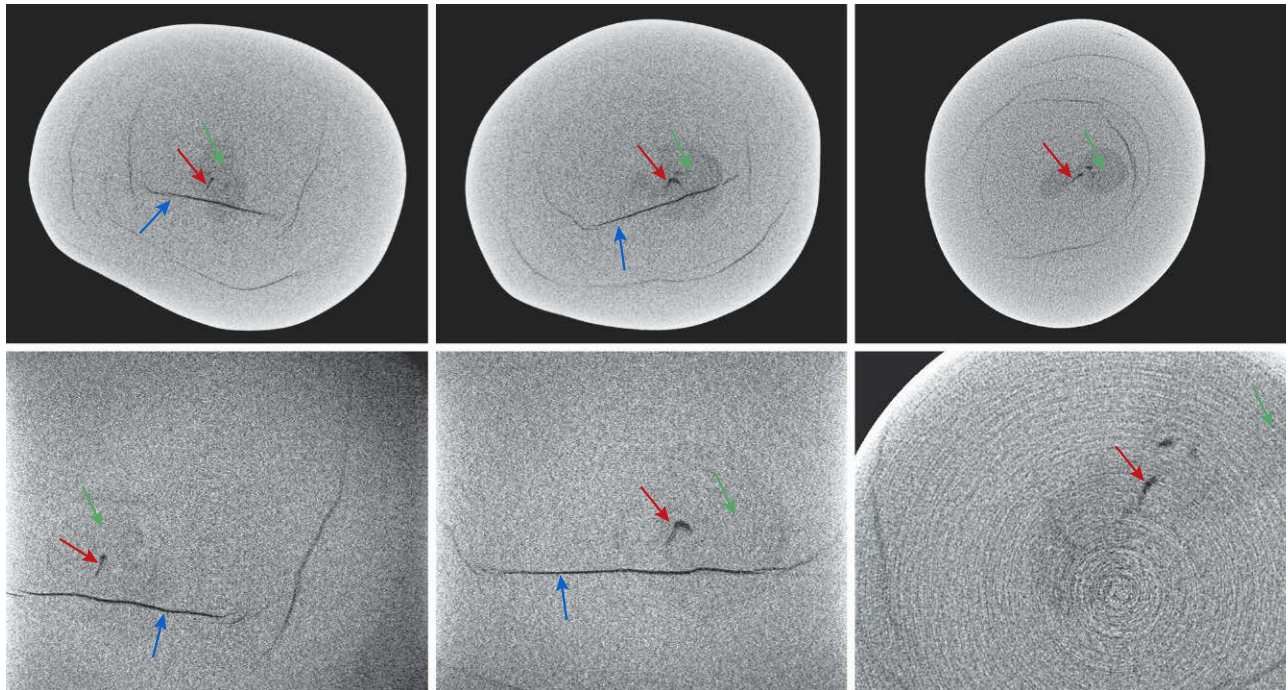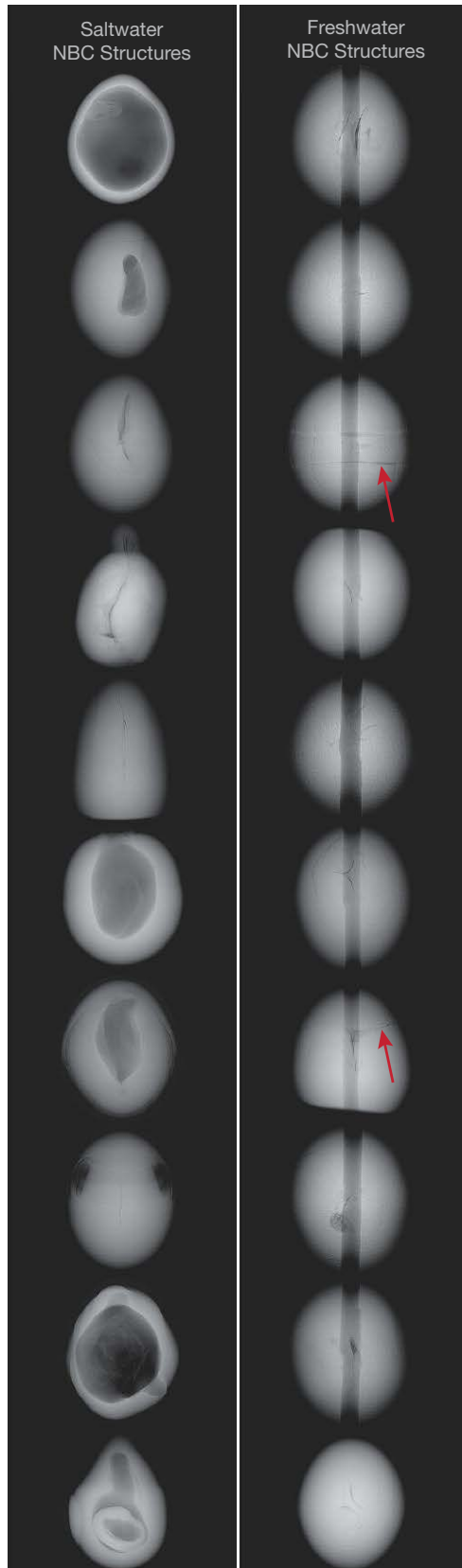
Box A: Typical Saltwater and Freshwater NBC Pearl Microradiographic Structures

A selection of NBC pearls showing structures representative of those encountered in saltwater (left) and freshwater (right) varieties. The saltwater pearls tend to show pronounced void and/or organic-rich structures or more linear features that are often elongated rather than short, but examples of the latter are also observed and can be more challenging to distinguish as proof of cultured formation. On the other hand, freshwater pearls tend to show distinct twisted linear structures or voids, quite often with distinct associated growth rings around them, and sometimes boundary-like features as indicated by the red arrows on a couple of the microradiographs. Unlike saltwater pearls, the linear/void structures observed in freshwater pearls are sometimes hard to resolve and require examination in several directions. Additional work using X-ray computed microtomography (μ-CT) is not unusual when it comes to those examples that do not readily reveal their identity. It is also possible to understand how suitably positioned/sized drill holes within some samples may complicate the identification work and lead to differing opinions between gemologists and laboratories.

RTX images of known undrilled saltwater (left) and drilled freshwater (right) NBC pearls showing the differences in their internal structures.
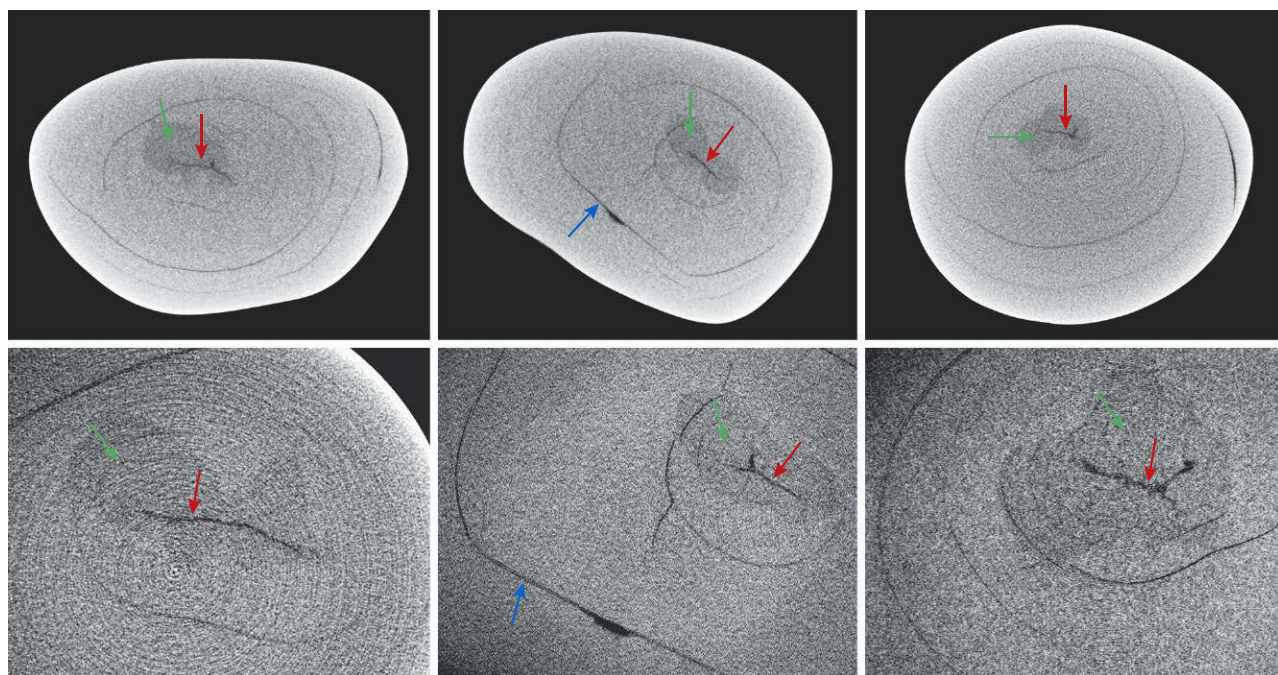
Figure 4. Three μ-CT slices obtained during the analysis of pearl B in Bangkok (the top row shows the whole pearl, the bottom row the magnified areas). All three slices show a suspicious feature: a small dark linear-appearing void (red arrows) indicating a possible NBC formation, within a dark gray organic-rich area (around the green arrows). The linear structure related to the flat surface area is indicated by the blue arrows in the middle slice, although it does not show on the other slices due to the pearl's orientation.

the internal structures to a known formation environment is an important part of pearl identification.

Complementary μ-CT and trace element characterization were performed at Mainz University and the Max Planck Institute for Chemistry, respectively. The additional findings matched those of GIA's, as can be seen in figures 5 and 6. However, GIA's analysis time was 16 minutes, compared with 5.4 hours at Mainz University, which prompted another analytical run in which the pearls were positioned closer to the tube to increase magnification. The acquisition time difference is due to the equipment used and the software/parameters applied, which is why a second opinion was sought, since the lengthier analysis usually yields

Figure 5. Three μ-CT slices obtained during the analysis of pearl A in Germany. All three slices show a suspicious feature: a small dark linear-appearing void feature (red arrows) within a dark gray organic-rich area (around the green arrows). A blue arrow is absent from the right-hand image, as the structure does not show due to the pearl's orientation. Note the similarity to the features observed in pearl B (figure 6).
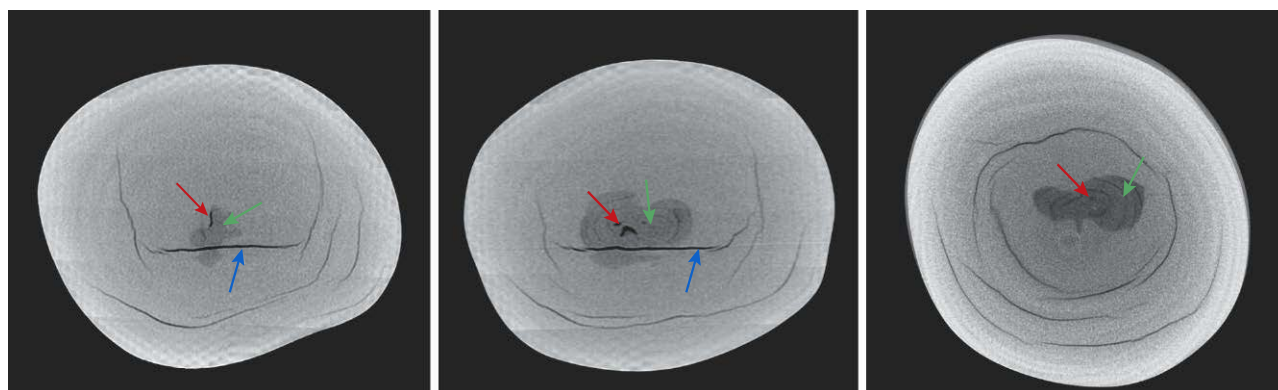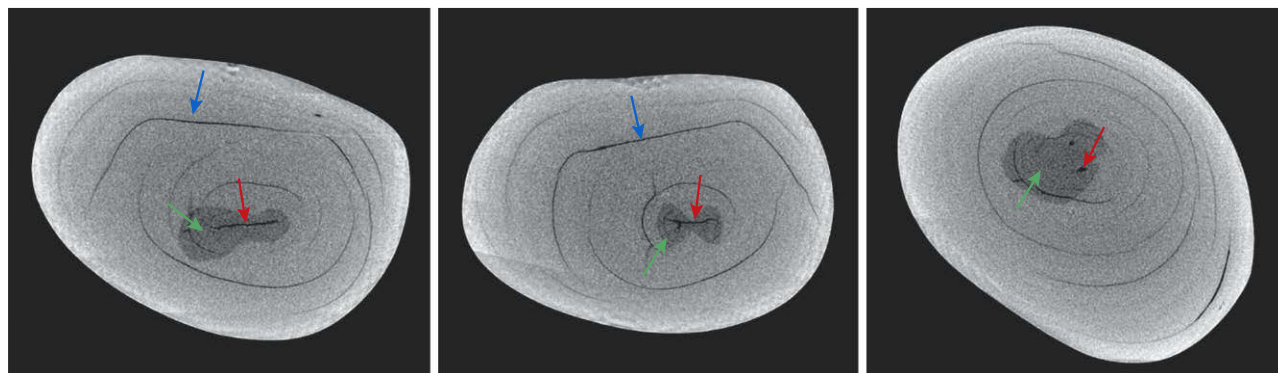
Figure 6. Three μ-CT slices obtained during the analysis of pearl B in Germany. All show a suspicious feature: a small dark linear-appearing void (red arrows) within a dark gray organic-rich area (around the green arrows). A blue arrow is absent from the right-hand image, as the structure does not show due to the pearl's orientation. Note the similarity to the features observed in pearl A (figure 5).

sharper features. Following the μ-CT results, the trace element results were considered even more important for the identification of these particular pearls.

In Germany, OsiriX 5.8.5 data visualization and analysis software was used to further investigate the pearls using orthoslices and 3D volume rendering (figure 7). The results indicated that the composition of the layers varied significantly in density, with four internal layers showing an unenclosed profile—visible as yellow structures in the figure— different from the main body of the pearl. The introduction of such software in pearl identification has

Figure 7. Additional imaging revealed four layers of different density (yellow structures) within the pearls that did not appear to reach the surface. Pearl A is shown on the top row and pearl B on the bottom row.
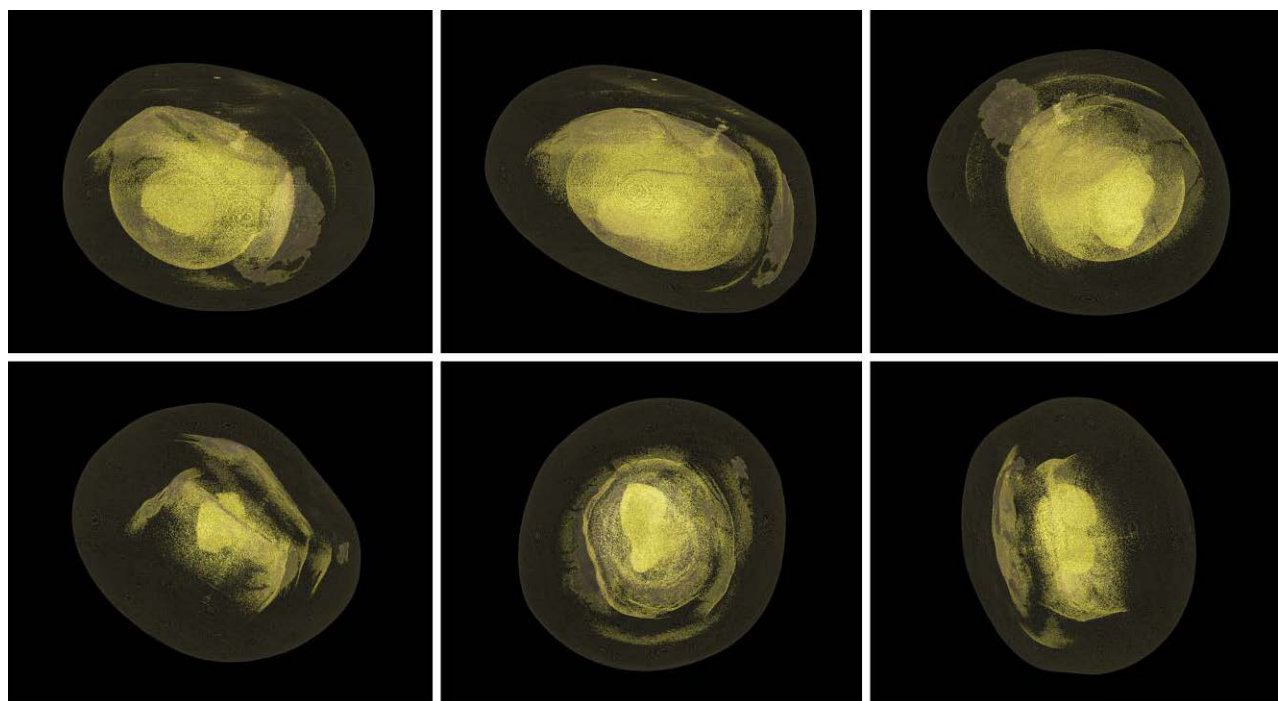
TABLE 1. EDXRF results (in ppm) obtained from the two pearls in six different positions.

Pearl ID	Mn[b]	Sr[b]
A_Position 1	<5	1364
A_Position 2	<5	1284
A_Position 3	<5	2073
A_Position 4	<5	1524
A_Position 5	<5	1261
A_Position 6	<5	1497
B_Position 1	<5	1293
B_Position 2	<5	1128
B_Position 3[a]	1006	588
B_Position 4	<5	1422
B_Position 5	1501	538
B_Position 6	66	1107
Detection limit	5	6

[a]The two shaded rows for pearl B reveal freshwater signatures, while the remaining results for both pearls indicate saltwater origin.
[b]Note the correlation of higher Mn and lower Sr with a freshwater environment, while low Mn coupled with high Sr points toward marine origin.

been used to provide more detail in cases worthy of additional study (Otter et al., 2014a; Zhou et al., 2016). The yellow areas in question did not appear to reach the surface, so it is unlikely that they are related to the trace element characteristics, although the only way to verify this would require cutting the pearls in half and analyzing their trace element chemistry in more detail.

EDXRF. Since the interpretation of the RTX and μ-CT data failed to reach a conclusive identity, other tests had to be considered in order to help establish either a natural or cultured origin. One of the main supporting techniques available to gemologists is trace element analysis. By confirming whether a pearl is SW or FW and linking the environment to the RTX and/or μ-CT structure, the decision on a pearl's identity can often be made easier.

In order to determine their formation environment, the pearls were each tested in an EDXRF spectrometer. While lower manganese (Mn) levels (below detection limits of around 20 parts per million) usually indicate a SW origin, higher values (most often from 150 ppm into the low- to mid-thousands) identify a FW origin (Wada et al., 1988; Wehrmeister et al., 2007). Some of the gemologists who examined the pearls favored a FW origin based on the internal structures observed via the X-ray work. Therefore,

further EDXRF analysis was carried out in more positions on the pearls to provide additional data (table 1). This produced very interesting and conflicting results that GIA had not encountered previously, which led to further research on these pearls. Based on the EDXRF results, the decision was made to check the pearls' reactions under optical X-ray fluorescence conditions. Pearls that fluoresce strongly when tested by this method tend to originate in FW environments, as the Mn content is higher and is thought to cause the strong visible reaction; in SW pearls, Mn is low or absent, and hence no reaction is observed (Hänni et al., 2005; Kessrapong et al., 2017). Strontium (Sr), on the other hand, is known to reach high concentrations for biogenic calcium carbonates (i.e., pearls and shells from SW environments), while low Sr values are characteristic of FW origin (Wehrmeister et al., 2007). Mn and Sr concentrations, combined with those of other elements, are useful tools to determine the habitat of the pearl-forming mollusk (saltwater or freshwater).

According to the results from EDXRF analysis, pearl A should in theory be of saltwater origin, as the consistent results from the six different positions tested did not find detectable amounts of Mn. On the other hand, pearl B seemed to be a mixture of saltwater and freshwater origin, which came as rather a surprise. This is the first time GIA has encountered such mixed trace element signatures in a pearl, and to our knowledge there are no other recorded cases of such testing results in the literature.

Optical X-Ray Fluorescence. To further examine the pearls and see how the data from the EDXRF results would be reflected in the visual reactions of the elemental distributions throughout the pearls, we turned to the simple but effective method of optical X-ray fluorescence. A pearl with mixed trace element signatures should in theory show a mixed reaction corresponding to the areas of freshwater and saltwater composition detected. The saltwater pearl, based on known saltwater pearl reactions, should show no reaction or at best a very weak reaction. Pearls that exhibit moderate to strong greenish fluorescence usually contain sufficient Mn to generate the effect, while those that show very weak fluorescence or are inert lack sufficient levels of Mn and are usually associated with saltwater environments (Hänni et al., 2005). The results obtained for pearls A and B are shown in figure 8.

The reactions were completely at odds with the testing results already described. Instead of a hetero-
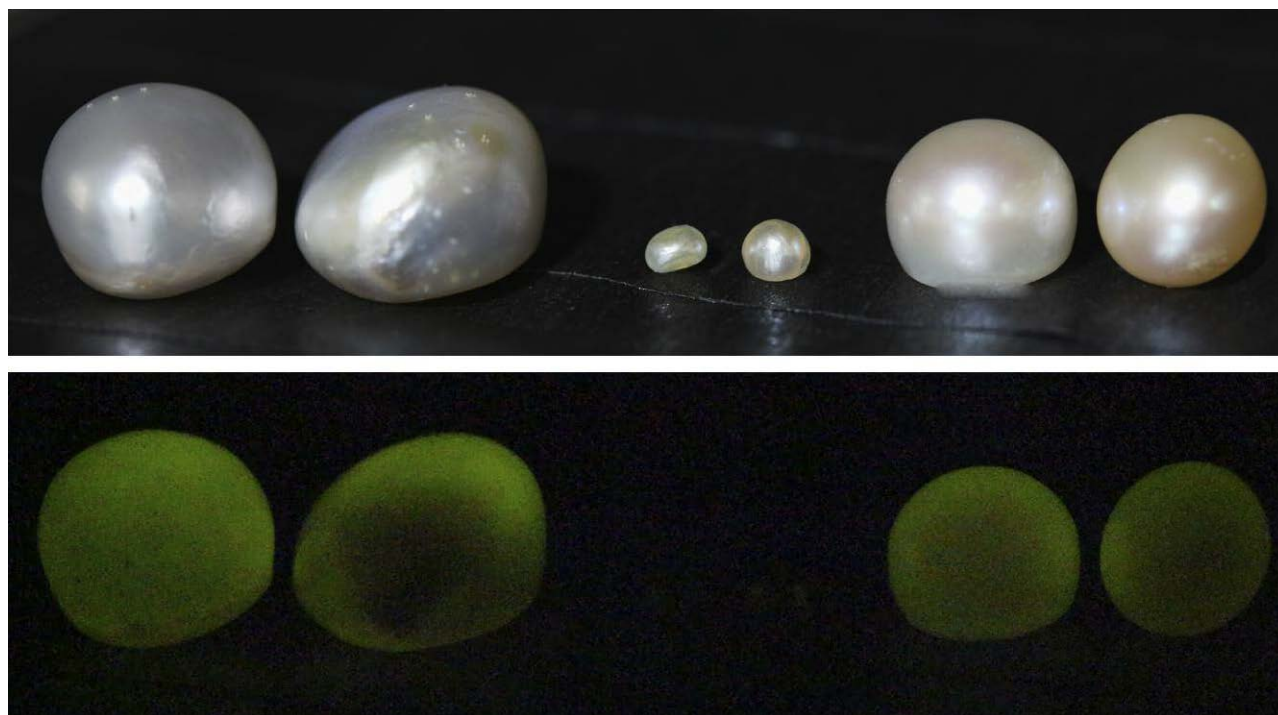
Figure 8. The optical X-ray fluorescence reactions of the two pearls from this study (left), shown with two natural saltwater pearls from Venezuela in the center and two known non-bead cultured freshwater pearls from China on the right. Pearl A (far left) should not show any reaction according to its trace element characteristics, while pearl B (second from left) shows a predominantly freshwater reaction, which again does not conform entirely to the trace element observations. Camera settings used to record the luminescence were ISO speed 12800, F-stop of 5, and exposure time of 5 seconds. Photos by Chunhui Zhou.

geneous reaction, pearl B exhibited a fairly homogenous moderate to strong greenish yellow reaction, while the apparent SW pearl (A) revealed a very similar reaction to the known FW samples, which was very surprising given the trace element data. This added to the identification challenges: Not only was the nature of their origin (natural or cultured) in doubt, but so was the environment in which they formed. On top of this, the question about Mn and its role in fluorescence immediately came into focus. This relationship is not yet fully understood, so it was decided that even further analysis was needed for these two examples.

LA-ICP-MS Analyses. Since the EDXRF results and subsequent optical X-ray fluorescence analysis produced unusual results, we turned to LA-ICP-MS to obtain more accurate trace element data for comparison. In routine pearl testing, LA-ICP-MS analysis is not usually applied since the EDXRF and optical X-ray fluorescence techniques provide suffi-

ciently accurate and distinct data to reach a conclusion on the exact environmental origin. When combined with the pearls' external appearance, the form of their platy structure, and their internal structures, the identification of the environment becomes even more accurate. For the two pearls under discussion, their external appearances, platelet form, internal structure, chemistry results, and optical X-ray fluorescence reactions were all inconsistent with regard to any particular type of pearl, environment, or mollusk.

The initial ICP work was carried out in Bangkok after the pearls were acquired. We chose two preliminary spots for pearl A and six spots for pearl B, and the results are shown at the top of table 2. Surprisingly, the results from the Bangkok unit on pearl A still fell within those expected from SW pearls, so it was decided to hold the pearl until the results of pearl B were known.

Since the results from two spots on pearl B agreed with two of the areas tested by the EDXRF spec-

TABLE 2. LA-ICP-MS data (in ppm) obtained in three different laboratories for both pearls from this study.

Pearl ID	B	Mg	Mn	Fe	Sr	Ba
GIA, Bangkok						
A_Position 1	12	210	16	238	1561	1
A_Position 2	11	180	21	186	1287	1.5
B_Position 1	16	127	45	130	1119	0.6
B_Position 2	15	195	44	236	1373	2
B_Position 3[a]	bdl	39	1672	287	438	57
B_Position 4	11	145	19	168	1137	0.7
B_Position 5	bdl	35	2307	152	523	77
B_Position 6	16	204	21	194	1261	bdl
Detection limit	3	0.5	2	50	0.1	0.5
GIA, New York						
B_Position 1	19	208	47	209	1570	2.5
B_Position 2	16	149	50	216	1290	0.6
B_Position 3	bdl	51	1632	152	460	47
B_Position 4	14	174	27	180	0.3	0.1
B_Position 5	bdl	49	2110	183	579	72
B_Position 6	18	187	26	179	1455	bdl
Detection limit	3	1	1	60	0.3	0.1
Mainz, Germany[b]						
A_Position 1	10	207	156	51	1026	5.5
A_Position 2	10	204	236	51	1003	9
A_Position 3	11	213	23	48	1064	0.7
A_Position 4	12	181	22	38	1115	0.5
A_Position 5	12	213	21	36	1129	0.5
A_Position 6	11	213	20	35	1144	0.5
A_Position 7	7	147	476	53	1010	16
A_Position 8	11	212	16	49	1218	0.6
A_Position 9	7	147	476	53	1010	16
A_Position 10	10	211	19	62	1281	0.7
A_Position 11	11	221	20	61	1211	0.5
B_Position 1	3	51	768	52	480	29
B_Position 2	3	58	783	54	481	28
B_Position 3	1.5	36	885	54	388	38
B_Position 4	12	172	87	38	1127	8
B_Position 5	12	162	29	38	1170	0.5
B_Position 6	1	24	1252	58	464	49
B_Position 7	1	22	1371	58	445	48
B_Position 8	0.8	20	1071	57	424	44
B_Position 9	12	131	39	67	1157	1
B_Position 10	3.6	62	746	68	578	31
B_Position 11	0.9	17	939	69	377	63
Detection limit	0.1	0.3	0.1	4	0.9	0.1

[a]Shaded spots mark freshwater-like trace element compositions.
[b]Values from Germany are expressed as averages of three spots each.

trometer, the decision was made to send the pearl to GIA's laboratory in New York for examination using their LA-ICP-MS unit to check for consistency. The results proved very similar and are shown in table 2 for comparison.

As the chemistry of the pearls and their fluorescence reactions were so intriguing, we also sent them to one of the co-authors (LMO) for more detailed chemical analysis in Mainz. In order to obtain a good set of results with which to perform their calculations, that team tested in total 33 spots (measured as 11 groups of 3 adjacent spots) on pearl A and a total of 36 spots (measured as 12 groups of 3 adjacent spots) on pearl B. The estimated depth of these ablation spots was around 270 µm. The results of the analysis were consistent with GIA's findings for both pearls (see table 2). While the positions of the spots analyzed by GIA in New York and Bangkok were in similar positions, those analyzed by researchers in Mainz differed slightly owing to the greater number of spots examined.

The greater number of spots evaluated as depth profiles over a greater surface area revealed deeper Mn-rich areas (figure 9, A and B). Pearl B showed a higher concentration of Mn closer to the surface in several spots (figure 9, C and D). Both pearls showed a pattern of low Mn values of around 20 ppm, characteristic for SW conditions, rising steadily to high values of over 1000 ppm, which are characteristic for FW conditions. These high Mn values are found generally closer to the surface in pearl B, on average at about 100 µm depth, whereby the depth of the Mn-rich areas was found to be very heterogeneously dis-

Figure 9 (opposite page). Depth profiles obtained by LA-ICP-MS show significant fluctuations for Mn with depth for pearl A (plots A and B) as well as pearl B (plots C and D). Plots A through D each show one of the representative depth profile groups consisting of three spots ablated adjacent to each other. Bivariant double-logarithmic plots of Mn versus Mg (E) and Mn versus Sr (F) show a mixture of saltwater and freshwater environments: High Mn together with low Mg or Sr values indicates a freshwater (FW) origin, while low Mn in combination with high Mg or Sr points toward a marine (SW) origin. Pearl B generally exhibits a higher proportion of Mn than pearl A, which falls more within a saltwater environment. The fine trace of data points connecting the SW-like and FW-like compositions (black circles) have never been observed in any pearls to the authors' knowledge. All together, the trace element patterns of both pearls were atypical of pearls tested by GIA over the years.
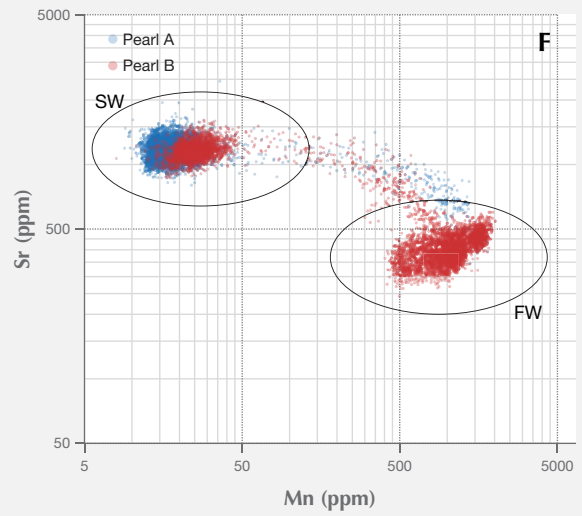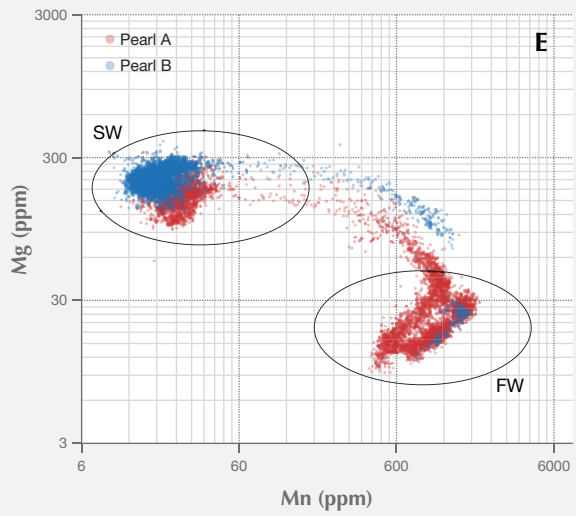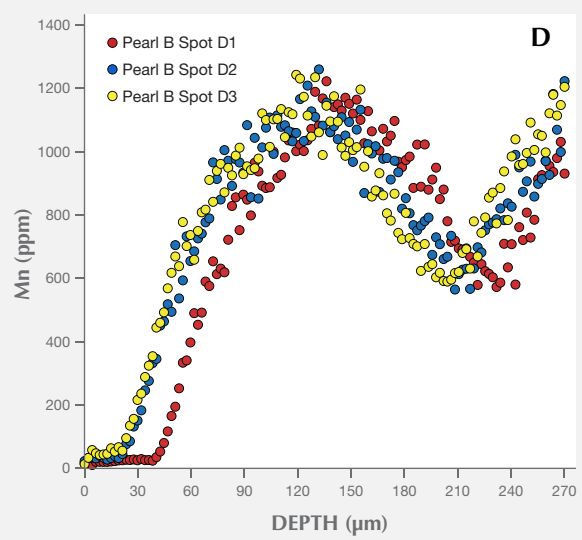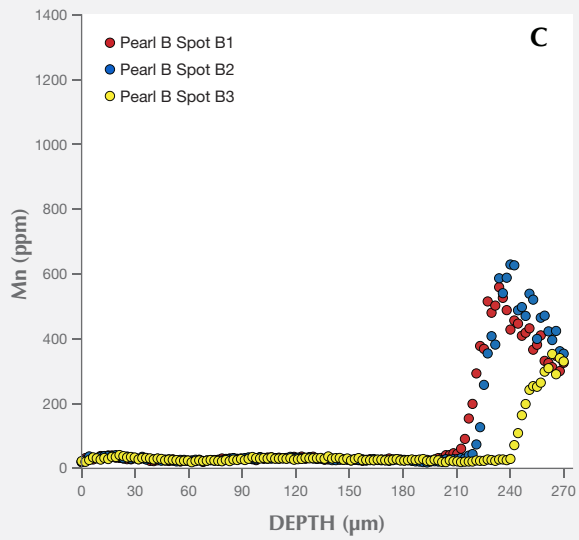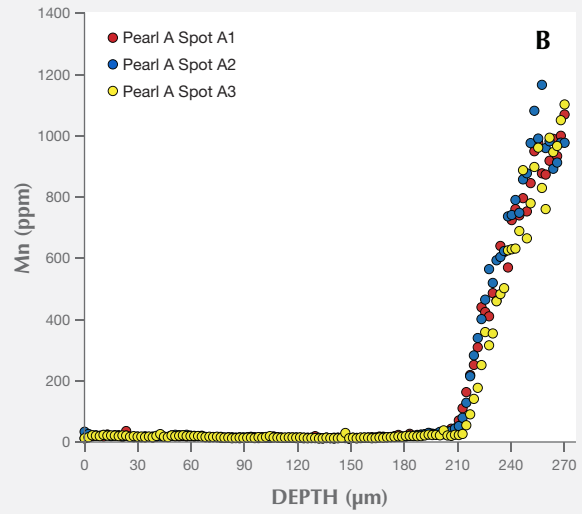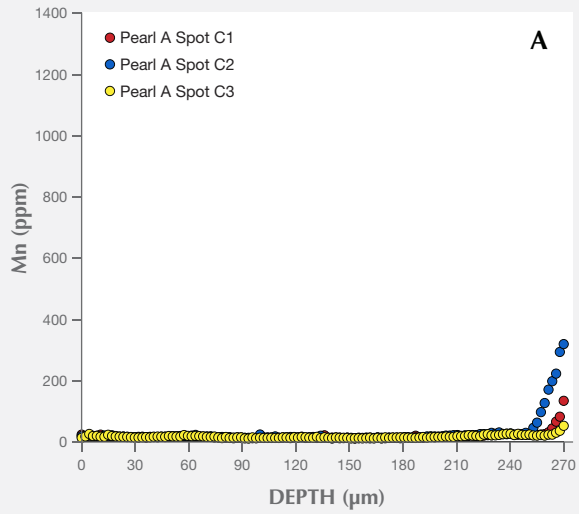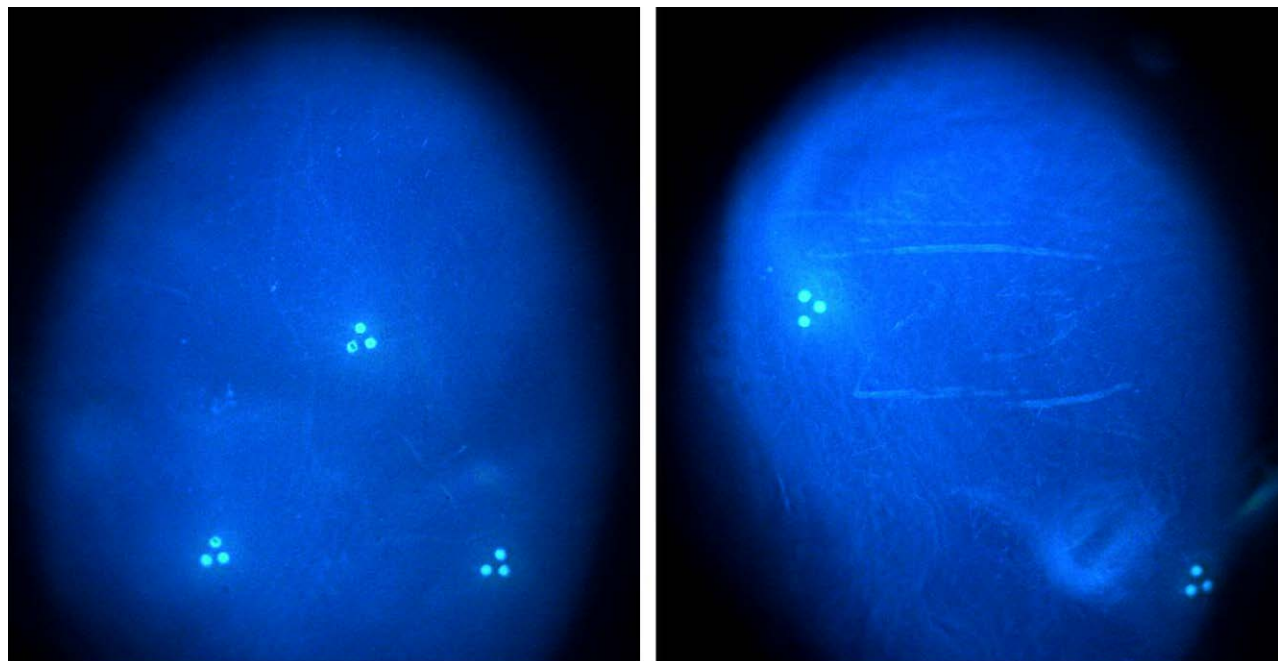
Figure 10. The DiamondView results for pearl A (left) and pearl B (right) show the characteristic blue reaction of untreated pearls. Each small triangular group of dots consists of three laser ablation holes that react with a stronger bluish white fluorescence, which from GIA's experience is typical of pearls where the underlying surface structure has been exposed by different means (e.g., LA-ICP-MS analyses, drilling, working, or heavy polishing). This reaction is seen not only in the DiamondView but also under short-wave and long-wave UV radiation.

tributed over the surface of the pearl, ranging from its presence directly at the surface to its absence within the profile. Pearl A showed the Mn-rich area at around 240 µm depths on average. In addition, bivariate double-logarithmic plots showing the full datasets of both pearls for Mn versus Mg (figure 9E) as well as Mn versus Sr (figure 9F) reveal further mixed FW-like (high Mn and low Mg/Sr) and SW-like (low Mn and high Mg/Sr) compositions. The heterogeneity observed in Mg and Sr shows that the concentration of these elements changes similarly within the depth profiles. Thus, it is clear to see that while both pearls appear to contain areas of both saltwater and freshwater trace element characteristics, pearl A trends generally more toward saltwater than pearl B, even if neither pearl's chemistry is specific to a defined environment.

UV Radiation and DiamondView Reactions. The majority of white to cream-colored nacreous pearls exhibit a weak to strong, chalky yellow to bluish fluorescence (depending in part on the mollusk species) under short-wave and long-wave UV radia-

tion. These reactions may be further influenced by various processes, including treatments (Strack, 2006). Such treatments may also provide some indications about the nature of the pearls. For example, bleaching is commonly applied to cultured freshwater and akoya pearls and may show as a stronger bluish reaction in some examples. Both samples studied fluoresced a weak chalky yellow under short-wave UV, while pearl A reacted with a moderate chalky yellow fluorescence under long-wave UV and pearl B showed a similar reaction but with more of a blue component. The reactions were not those typically associated with cultured FW pearls or akoya pearls that have undergone bleaching. The DiamondView unit, although not always useful in distinguishing natural from cultured or saltwater from freshwater pearls, may aid in determining treatments. However, since these were white pearls that usually show a marked blue reaction within the DiamondView, we did not expect to see anything unusual, and that turned out to be the case when both pearls exhibited a characteristic blue reaction (figure 10).

DISCUSSION

The results obtained from the analysis described so far led to two main questions: First, did the pearls form naturally in a mollusk without any human intervention? Second, did the mollusks live in a SW or FW environment? Most of the time these questions are relatively straightforward to answer, but in this case we were still uncertain after examining these two pearls.

The first method of identification employed was RTX analysis. The results showed suspicious structures, although not enough to prove they were non-bead cultured. It was still possible that the pearls were natural, and many pearls examined by GIA over its history have shown odd natural structures. The results led to the next identification method, μ-CT analysis. Again the results revealed structures that could be considered either natural or non-bead cultured and were not definitive.

The chemistry was considered next, and in this case the exact formation environment (saltwater or freshwater) could not be determined. EDXRF data raised more questions. Pearl A yielded <5 ppm Mn in every spot and an average concentration of 1500 ppm for Sr. Both trace elements are considered environmental indicators, since a combination of <20 ppm Mn and >1300 ppm Sr is associated with marine environments, while the reverse relation of >20 ppm Mn and <1300 ppm are indicative of freshwater origins (Wehrmeister et al., 2007). However, the EDXRF analysis employed covered a 6.0 mm area of the surface (dependent on the collimator applied) and the penetration depth was on the order of a few microns, so it could not determine the chemistry deeper within the samples.

LA-ICP-MS is better suited to determine the elements deeper within a sample, although still limited to micron depths, yet the surface area tested is significantly smaller (Lu et al., 2011). LA-ICP-MS results identified both FW and SW signatures in different average spot compositions. The LA-ICP-MS depth profiles, obtained at the Max Planck Institute for Chemistry in Germany, revealed a trace element composition not previously observed for pearls: Several environment-indicative elements (namely B, Mg, Mn, Sr, and Ba) were found to vary in concentration, forming discrete layers of alternating FW-like and SW-like composition. In all spots, the patterns start at low Mn values of around 20 ppm that likely correspond to SW conditions and rise steadily to high values of over 1000 ppm, indicative of FW growth environments, for both pearls (figures 9B and 9D). The

FW conditions were found closer to the surface along the depth profile of pearl B at approximately 100 μm, compared to approximately 240 μm for pearl A. Peak concentrations decrease and rise in pearl B (figure 9D), creating a steady, alternating trend. These patterns imply that the pearls grew uninterruptedly within a single mollusk—and not in two separate mollusks—first within FW and later SW environments, which would have produced abrupt changes in their trace element characteristics. Such results would rule out the possibility that these pearls represent "atypical bead cultured pearls," which usually show clear boundaries marking the growth zones of the host (outer layers) and the inserted material (Hänni et al., 2010). It is worth noting that saltwater mollusks are routinely used as hosts, whereas atypical freshwater hosts are a rarity (Scarratt et al., 2017). The LA-ICP-MS craters were only drilled to a depth of around 270 μm since greater depths at some point hinder the rising evaporate and also increase the chance of element fractionation. However, it can be expected that the concentrations of Mn, Sr, and Mg continue to alternate toward the center of the pearl.

The alternating patterns between FW-like and SW-like compositions could result from growth in a river delta where the predominant water input is freshwater, with only occasional season-dependent saltwater input when the river carries little water (e.g., during summers in warm climates). While the authors are unaware of farms that operate in brackish waters, reports do exist of shells originating from around islands within the Mississippi Delta in North America (Moore, 1961), and farms are known to operate in river deltas in Vietnam (L.T.T. Huong, pers. comm., 2016), both underscoring this possibility. However, this does not aid in determining the natural or cultured nature of the pearls from this study. Although this hypothetical setting favors an overall FW-related origin, it does not satisfyingly answer the question of the bivalve species that produced these pearls, since little is known about the environmental tolerances of the Unionidae and Pteriidae families.

These changes in trace element composition are, however, too low to affect the major-element composition of the pearls and therefore cannot discriminate between marine and freshwater nacre in the μ-CT datasets. Instead, the μ-CT datasets show the density changes between organic material and nacre. The not fully enclosed organic layers could represent "pseudoannuli" growth rings (Jacob et al., 2011), which are characteristic of continuous growth within a mollusk, whereas the use of beads as nuclei for fur-

ther pearl growth would likely produce a prominent concentric layer of organic material, as often observed for bead cultured pearls (e.g., Karampelas et al., 2010; Krzemnicki et al., 2010; Otter et al., 2014b). These inner unenclosed growth rings also lead to questions about the intensity of the pearls' optical X-ray fluorescence, since most saltwater layers that cover freshwater layers/components (i.e., freshwater nuclei in most bead cultured pearls) mask the effects, producing weak to moderate fluorescence. This was not the case with these two samples, and the fluorescence was quite marked (again, see figure 8).

Average nacre deposition rates for marine environments range from 0.5 mm/year for akoya cultured pearls produced by *Pinctada imbricata fucata* in temperate climates (e.g., eastern Australia) to 2.0 mm/year for cultured pearls produced by *Pinctada maxima* in tropical climates in the South Seas (e.g., Strack, 2006; Otter et al., 2017). Lower deposition rates of akoya pearls are likely an effect of the colder climate compared to the warmer, near-equatorial distribution of *Pinctada maxima* (Strack, 2006). Freshwater species such as *Hyriopsis schlegelii* and *Hyriopsis cumingii* or their hybrids are known to have higher growth rates and can deposit up to 10 mm of nacre within six years, or approximately 1.5 mm/year (Akamatsu et al., 2001). Using the mean diameter of 10.5 mm for pearl A, we can assume a growth period of seven years (FW growth rate) or between 5 and 21 years (for tropic and temperate marine growth rates, respectively), depending on the mollusk species and environment used (the numbers for pearl B are in the same range). The shorter FW growth period of seven years would therefore still be in the timeframe of FW NBC pearls from China (Akamatsu et al., 2001). On the other hand, slower growth rates from a marine environment would point toward a natural origin, as the estimated SW growth period is up to 10 times longer. Since species of the *Pinctada* genus can reach ages of up to 40 years (Strack, 2006), a growth period of around 20 years does not seem impossible.

CONCLUSION
The identification of these two pearls presented challenges on many fronts. While the authors believe that their internal structures are more likely NBC, this is by no means definite. Hence, there is a chance they could be natural pearls with unusual structures. Pearl testing is relatively straightforward in most cases, yet there are plenty of instances where identification is subjective and opinions may differ, even within the same organization, let alone separate ones. Likewise, determination of the environment in which pearls form is almost always straightforward. Yet the pearls in this report prove that on very rare occasions it is possible to encounter trace element anomalies, thus leading to questions about the true environmental origin of the samples. The distinct fluorescence observed under X-rays as well as the pearls' general appearance led the authors to believe that they are more likely FW pearls, yet there is no clear explanation why either pearl (particularly A) should have reacted so markedly. Even if there are zones of freshwater material within the saltwater material, the freshwater reaction should in theory be masked to a greater extent, just as the reactions of freshwater bead nuclei in almost all commercial bead cultured pearls are when subjected to the same test.

As a consequence, these two factors also call into question the identity of the producing mollusk for laboratories, such as GIA, that routinely attempt to identify the species of mollusk in which a pearl formed. If either of the pearls could be identified as SW, they would likely have formed in a species from the Pteriidae family. If they were FW, however, they would have formed within a mussel species belonging to the Unionidae family, which inhabits rivers and lakes worldwide. The location would in many ways be influenced by whether they formed naturally or with human assistance, so again we come full circle to the subjectivity involved in evaluating all three factors from the data obtained during this study.

Although the final conclusions were not unanimous and questions still exist about the true identification, environment, and producing mollusk in which the pearls formed, the results obtained prove that there is always something new to discover when it comes to the analysis of gem materials, especially organic ones such as pearls. Further destructive work on the pearls, specifically cutting each in half to study their internal chemistry in greater detail and conducting deoxyribonucleic (DNA) analysis on powder samples extracted (Meyer et al., 2013; Saruwatari et al., 2018), might be necessary to reach a possible conclusion.

REFERENCES

Akamatsu S., Zansheng L.T., Moses T.M., Scarratt K. (2001) The current status of Chinese freshwater cultured pearls. *G&G*, Vol. 37, No. 2, pp. 96–113, http://dx.doi.org/10.5741/GEMS.37.2.96

Hänni H.A. (2012) Natural pearls and cultured pearls: a basic concept and its variations. *Australian Gemmologist*, Vol. 24, No. 11, pp. 256–266.

Hänni H.A., Kiefert L., Giese P. (2005) X-ray luminescence, a valuable test in pearl identification. *Journal of Gemmology*, Vol. 29, No. 5/6, pp. 325–329.

Hänni H.A., Krzemnicki M.S., Cartier L. (2010) Appearance of new bead material in cultured pearls. *Journal of Gemmology*, Vol. 32, No. 1/4, pp. 31–37.

Jacob D.E., Wirth R., Soldati A.L., Wehrmeister U., Schreiber A. (2011) Amorphous calcium carbonate in the shells of adult Unionoida. *Journal of Structural Biology*, Vol. 173, No. 2, pp. 241–249, http://dx.doi.org/10.1016/j.jsb.2010.09.011

Jochum K.P., Stoll B., Herwig K., Willbold M. (2007) Validation of LA-ICP-MS trace element analysis of geological glasses using a new solid-state 193 nm Nd:YAG laser and matrix-matched calibration. *Journal of Analytical Atomic Spectrometry*. Vol. 22, No. 2, pp. 112–121, http://dx.doi.org/10.1039/B609547J

Jochum K.P., Scholz D., Stoll B., Weis U., Wilson S.A., Yang Q., Schwalb A., Börner N., Jacob D.E., Andreae M.O. (2012) Accurate trace element analysis of speleothems and biogenic calcium carbonates by LA-ICP-MS. *Chemical Geology*, Vol. 318, pp. 31–44, http://dx.doi.org/10.1016/j.chemgeo.2012.05.009

Karampelas S., Michel J., Zheng-Cui M., Schwarz J.-O., Enzmann F., Fritsch E., Leu L., Krzemnicki M.S. (2010) X-ray computed microtomography applied to pearls: Methodology, advantages, and limitations. *G&G*, Vol. 46, No. 2, pp. 122–127, http://dx.doi.org/10.5741/GEMS.46.2.122

Karampelas S., Al-Alawi A.T., Al-Attawi A. (2017) Real-time microradiography of pearls: A comparison between detectors. *G&G*, Vol. 53, No. 4, pp. 452–456, http://dx.doi.org/10.5741/GEMS.53.4.452

Karampelas S., Mohamed F., Abdulla H., Almahmood F., Flamarzi L., Sangsawong S., Al-Alawi A. (2019) Chemical characteristics of freshwater and saltwater natural and cultured pearls from different bivalves. *Minerals*, Vol. 9, No. 6, Article 357, http://dx.doi.org/10.3390/min9060357

Kessrapong P., Lawanwong K., Sturman N. (2017) *Pinctada maculata* (Pipi) bead-cultured blister pearls attached to their shells. GIA Research News, April 25, https://www.gia.edu/gia-news-research/pinctada-maculata-bead-cultured-blister-pearls-shells

Krzemnicki M.S., Friess S.D., Chalus P., Hänni H.A., Karampelas S. (2010) X-ray computed microtomography: Distinguishing natural pearls from beaded and non-beaded cultured pearls. *G&G*, Vol. 46, No. 2, pp. 128–134, http://dx.doi.org/10.5741/GEMS.46.2.128

Lu R., Zhou C.H., Sturman N. (2011) Operational considerations of EDXRF, LA-ICP-MS, and photoluminescence techniques in the analysis of pearls. *G&G*, Vol. 47, No. 2, pp. 149–150.

Meyer J.B., Cartier L.E., Pinto-Figueroa E.A., Krzemnicki M.S., Hänni H.A., McDonald B.A. (2013) DNA fingerprinting of pearls to determine their origins. *PLOS One*, Vol. 8, No. 10, pp. 1–11, http://dx.doi.org/10.1371/journal.pone.0075606.

Moore D.R. (1961) The marine and brackish water mollusca of the state of Mississippi. *Gulf Research Reports*, Vol. 1, No. 1, pp. 1–58, http://dx.doi.org/10.18785/grr.0101.01. Retrieved from http://aquila.usm.edu/gcr/vol1/iss1/1

Otter L.M., Wehrmeister U., Enzmann F., Wolf M., Jacob D.E. (2014a) A look inside a remarkably large beaded South Sea cultured pearl. *G&G*, Vol. 50, No. 1, pp. 58–62, http://dx.doi.org/10.5741/GEMS.50.1.58

Otter L.M., Wehrmeister U., Enzmann F., Wolf M., Jacob D.E. (2014b) Einblicke in eine außergewöhnlich große Südseezuchtperle mittels Röntgen-Computertomographie. *Gemmologie: Zeitschrift der Deutschen Gemmologischen Gesellschaft*, Vol. 63, No. 3-4, pp. 73–84.

Otter L.M., Agbaje O.B., Huong L.T.T., Häger T., Jacob D.E. (2017) Akoya cultured pearl farming in eastern Australia. *G&G*, Vol. 53, No. 4, pp. 423–437, http://dx.doi.org/10.5741/GEMS.53.4.423

Saruwatari K., Suzuki M., Zhou C., Kessrapong P., Sturman N. (2018) DNA techniques applied to the identification of *Pinctada fucata* pearls from Uwajima, Ehime Prefecture, Japan. *G&G*, Vol. 54, No. 1, pp. 40–50, http://dx.doi.org/10.5741/GEMS.54.1.40.

Scarratt K., Sturman N., Tawfeeq A., Bracher P., Bracher M., Homkrajae A., Manustrong A., Somsa-ard N., Zhou C. (2017) Atypical "beading" in the production of cultured pearls from Australian *Pinctada maxima*. GIA Research News, Feb. 13, https://www.gia.edu/gia-news-research/atypical-beading-production-cultured-pearls-australian-pinctada-maxima

Strack E. (2006) *Pearls*. Rühle-Diebener-Verlag, Stuttgart, Germany.

Wada K., Fujinuki T. (1988) Factors controlling minor elements in pearls. *Journal of the Gemmological Society of Japan*, Vol. 13, pp. 2–12.

Wehrmeister U., Jacob D.E., Soldati A.L., Häger T., Hofmeister W. (2007) Vaterite in freshwater cultured pearls from China and Japan. *Journal of Gemmology*, Vol. 30, No. 7/8, pp. 399–412.

Wehrmeister U., Götz H., Jacob D.E., Soldati A., Xu W., Duschner H., Hofmeister W. (2008) Visualization of the internal structure of freshwater cultured pearls by computerized X-ray microtomography. *Journal of Gemmology*, Vol. 31, No. 1/2, pp. 15–21.

Zhou C., Yazawa E., Sturman N. (2016) New 3-D software expands GIA's pearl identification capabilities. GIA Research News, May 13, https://www.gia.edu/gia-news-research/3d-software-expands-pearl-identification-capabilities

Inclusions in Natural, Treated, Synthetic, and Imitation Opal

Nathan D. Renfro, John I. Koivula, Jonathan Muyal, Shane F. McClure, Kevin Schumacher, and James E. Shigley
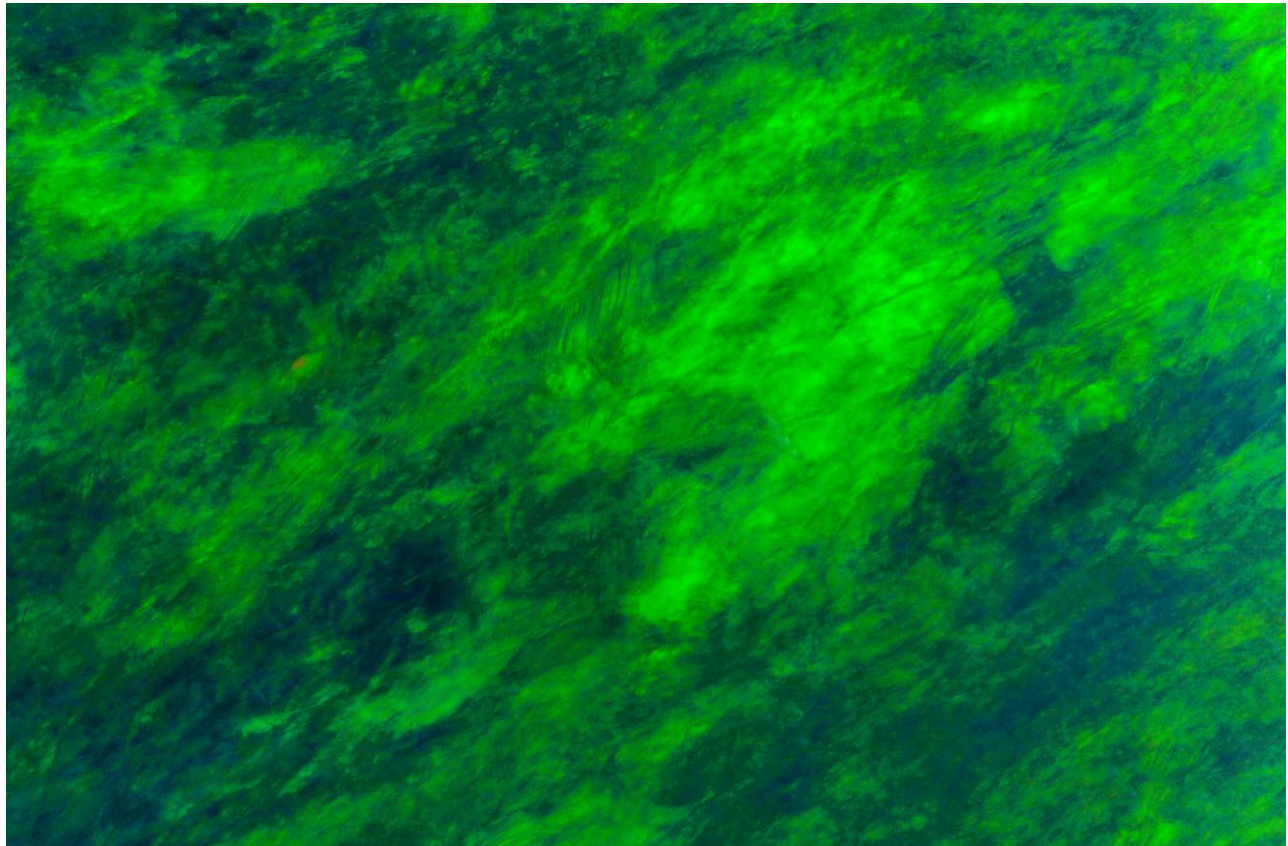
Figure 1. Play-of-color is the defining characteristic of gem opals. While play-of-color can be quite spectacular under magnification, as with the roiled green patterns seen in this crystal opal, other microscopic features are often found if one takes the time to look. Field of view 9.60 mm. Photomicrograph by Nathan Renfro.

When gemologists think of opals, play-of-color is almost certainly the first characteristic that comes to mind (figure 1). While play-of-color patterns can be extraordinarily beautiful under magnification, opals often contain a vast array of spectacular microscopic features in addition to this phenomenon. In continuing *G&G*'s series on inclusions, this chart will focus on natural, treated, synthetic, and imitation opals.

There have been significant developments in the opal industry in recent years with the discovery of opal from Wollo Province in Ethiopia (Rondeau et al., 2010). This deposit produces opals that contain a wide range of interesting inclusions such as fossilized plant material. Opals from Australia also have the potential to showcase spectacular inclusion scenes, from pyrite crystals to black plumes of manganese

oxide that stand out in high contrast to the play-of-color phenomenon. Other sources of natural opal that contain visually striking inclusions are Mexico, the United States, Honduras, and Peru.

Along with the new Ethiopian deposit came new treatments. The opal from this deposit was hydrophane, which meant it would readily absorb liquids. Soon gem treaters took advantage of this property and began to dye Ethiopian opal a myriad of colors, most notably purple (Renfro and McClure, 2011). This material also proved quite responsive to smoke treatment, which gives it a dark bodycolor (Williams and Williams, 2011). Other traditional opal treatments include color modification by sugar treatment and clarity enhancement by hiding fractures and cavities with resins or oils (Renfro and York, 2011).

One of the more prominent opal imitations was introduced in the early 1970s by John Slocum of Rochester, Michigan. In this imitation, thin sheets of metal foil were embedded in glass to produce thin-film interference colors resembling "play-of-color" in natural opal. In 1972, Pierre Gilson began to manufacture a true synthetic opal (Gübelin and Koivula, 2005) that did not require polymer impregnation. Synthetic and imitation opals have been produced over the years by other manufacturers including Kyocera, Almaztechnocrystal, and Openallday Pty. Ltd, but the most recent development is an opal-like plastic manufactured by Kyocera and others in Japan (Renfro and Shigley, 2017). This new material is 80% plastic and 20% silica. It can be produced in large sizes, giving rise to industrial applications such as use in eyeglass frames and watches.

While the images in the accompanying wall chart are by no means comprehensive, they do represent a wide variety of the micro-features one might encounter in natural, treated, synthetic, and imitation opals.

ABOUT THE AUTHORS
Mr. Renfro is manager of colored stones identification, Mr. Koivula is analytical microscopist, Mr. Muyal is a staff gemologist, Mr. McClure is global director of colored stone services, Mr. Schumacher is a photo and video producer for Gems & Gemology, *and Dr. Shigley is distinguished research fellow, at GIA in Carlsbad, California.*

REFERENCES

Gübelin E.J., Koivula J.I. (2005) *Photoatlas of Inclusions in Gemstones*, Vol. 2, Opinio Verlag, Basel, Switzerland, p. 486.

Renfro N.D., McClure S.F. (2011) Dyed purple hydrophane opal. *G&G*, Vol. 47, No. 4, pp. 260–270, http://dx.doi.org/10.5741/GEMS.47.4.260

Renfro N.D., Shigley J.E. (2018) Lab Notes: New plastic opal imitation from Kyocera. *G&G*, Vol. 54, No. 1, pp. 60–62.

Renfro N.D., York P. (2011) Lab Notes: Opal: Clarity-enhanced, with artificial matrix. *G&G*, Vol. 47, No. 4, pp. 312–313.

Rondeau B., Fritsch E., Mazzero F., Gauthier J.-P., Cenki-Tok B., Bekele E., Gaillou E. (2010) Play-of-color opal from Wegal Tena, Wollo Province, Ethiopia. *G&G*, Vol. 46, No. 2, pp. 90–105, http://dx.doi.org/10.5741/GEMS.46.2.90

Williams B., Williams C. (2011) Smoke treatment in Wollo opal. http://stonegrouplabs.com/wp/wp-content/uploads/2013/01/SmokeTreatmentinWolloOpal.pdf [date accessed: June 24, 2019].
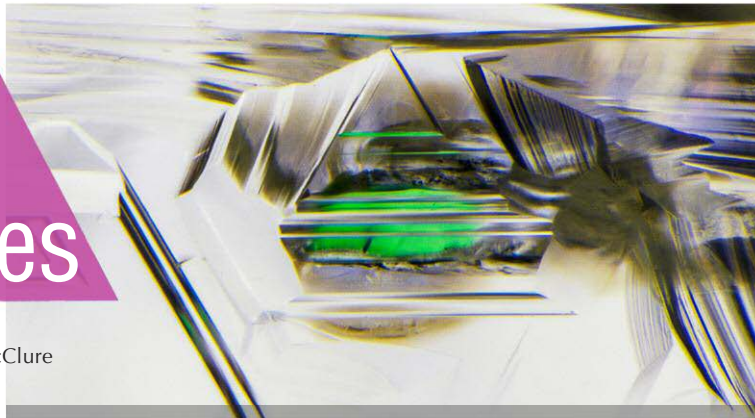
Additional Reading

For a list of references pertaining to inclusions in natural, synthetic, imitation, and treated opal, go to www.gia.edu/gems-gemology/summer-2019-suggested-reading-opal-chart or scan the QR code on the right.
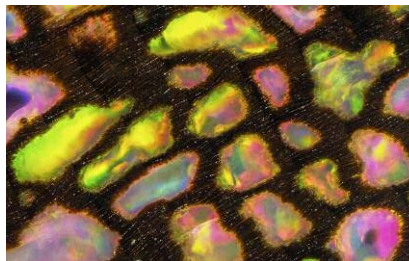
Lab Notes

Editors
Thomas M. Moses | Shane F. McClure

Resin-Coated and Clarity-Enhanced AQUAMARINE Pendant

The Carlsbad laboratory received a 34.24 ct light greenish blue free-form pendant (figure 1) measuring 33.40 × 25.75 × 6.40 mm. One side of the pendant was flat and polished, and the other side had a rough surface. Standard gemological testing gave a refractive index (RI) of 1.570–1.580. The pendant had the same reaction to long-wave and short-wave UV light: blue fluorescence in the center and green fluorescence around the edges of the stone. Examination with a standard gemological microscope revealed a blue and orange flash effect most clearly visible from the flat side (figure 2, left), which is diagnostic of clarity enhancement. Ultraviolet/visible/near-infrared (UV-Vis-NIR) spectra were consistent with natural aquamarine, with absorption peaks at 370 and 425 nm and an absorption band at ~830 nm (figure 2, right). Raman spectroscopy showed the presence of polymer on the rough side of the stone and aquamarine on the polished flat side. Although emeralds are the variety of beryl most commonly associated with clarity enhancement, filled aquamarine has previously been reported in the Chinese market (J. Li et al., "Polymer-filled aquamarine," Fall 2009 G&G, pp. 197–199).

Figure 1. This 34.24 ct light greenish blue free-form aquamarine pendant, measuring 33.40 × 25.75 × 6.40 mm, was seen in the Carlsbad laboratory. Stone courtesy of Stephen Challener.

Only one side, the rough side, was coated with polymer resin. Viewed in the microscope, this side appeared to have a thin transparent layer on the surface. Trapped air bubbles were visible with magnification (figure 3, left), and areas with the coating had a higher luster than the polished flat side. Fourier-transform infrared (FTIR) spectroscopy taken from the rough side revealed strong diagnostic peaks at ~3100–2850 cm⁻¹ (figure 3, right).

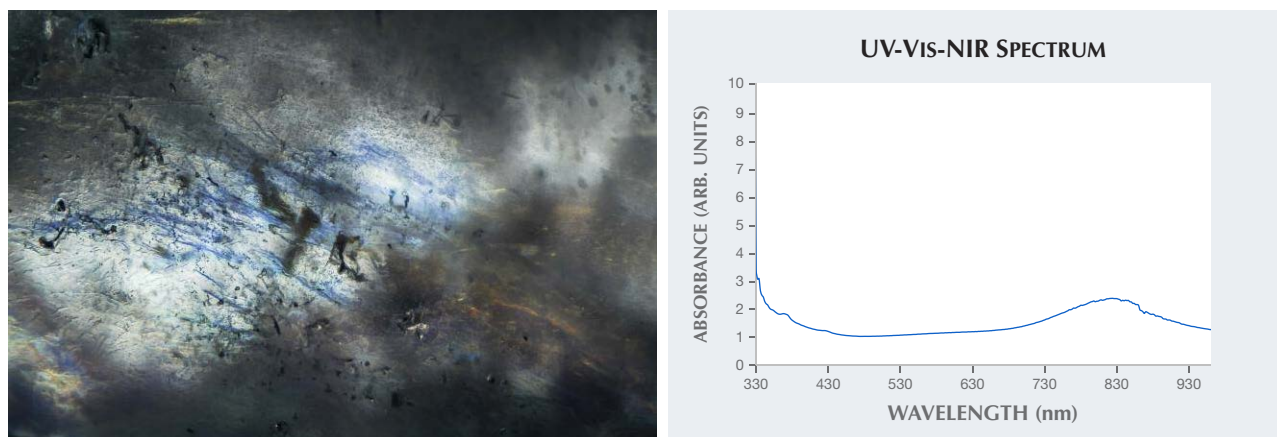Although clarity enhancement and coating of beryl gemstones are

Figure 2. Left: The orange and blue flash effect seen in a clarity-enhanced fracture of the aquamarine; field of view 4.24 mm. Right: The UV-Vis-NIR spectrum, with absorption peaks at 370 and 425 nm and an absorption band at ~830 nm, is consistent with natural aquamarine.

not uncommon, this material is rarely seen in a gemological laboratory. Both treatments are readily identified, but careful examination of every stone is important to identify them.

Michaela Stephan

Rough DIAMOND Crystal with an Unusual Coating of Fake Green "Radiation Stains"

Due to their rare occurrence and the environment required to create their color, natural green diamonds are some of the world's most beautiful and sought-after gems. Most diamonds acquire their color from impurities or defects incorporated into the

diamond lattice when the material is hundreds of kilometers deep in the earth's mantle. But most natural green diamonds are colored by radiation damage that occurs at very shallow depths in the earth's crust over long periods of time. Commonly accompanying this exposure to radioactive minerals and fluids are surface patches of green or brown color that gemologists call "radiation stains." These are simply areas of extreme damage to the diamond structure caused by alpha particle radiation. Initially green, they turn brown immediately after exposure to temperatures above 500°C. These surface features indicate that a diamond has been exposed to a source of natural

radiation; green stains are commonly associated with naturally colored green diamonds.

Recently, GIA's Carlsbad laboratory examined an interesting attempt to imitate a natural green diamond when a 6.49 ct green crystal was submitted for a Colored Diamond Grading Report (figure 4). The surfaces of the resorbed octahedron were covered by uneven patches of green color. Fourier-transform infrared (FTIR) analysis revealed a typical type Ia diamond with abundant nitrogen and hydrogen impurities. However, the ultraviolet-visible (UV-Vis) spectrum was very unusual and did not show any of the bands that are produced by radiation damage in diamond (e.g., the

Figure 3. Left: Gas bubbles and high luster on the aquamarine's resin-coated rough surface, shown near the drill hole. Field of view 7.19 mm. Right: The FTIR spectrum shows polymer peaks at ~3100–2850 cm⁻¹. The dotted line is the spectrum of an untreated aquamarine, shown for reference.
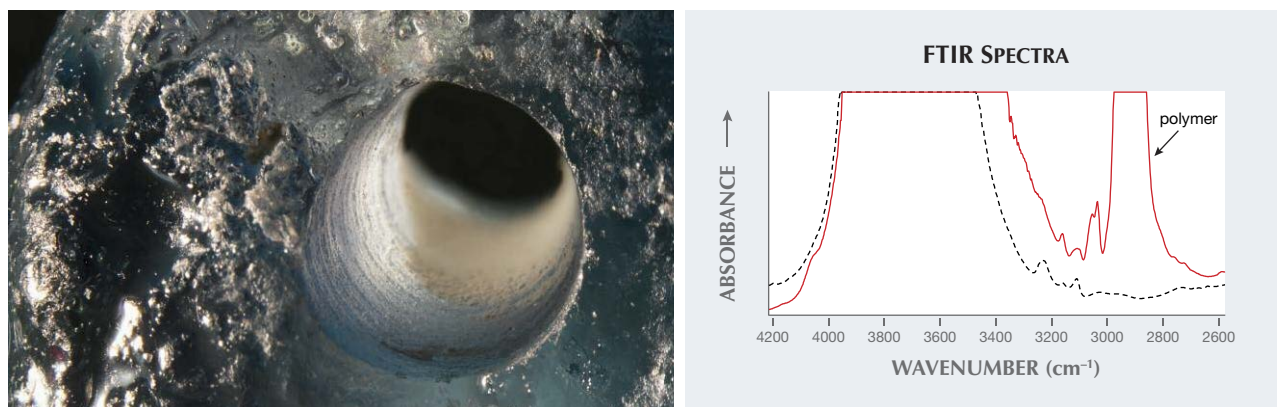
Figure 4. This 6.49 ct rough diamond with patchy green surface color was submitted to GIA's Carlsbad laboratory for a Colored Diamond Grading Report.

RAMAN SPECTRUM

Figure 6. The Raman spectrum (514 nm laser excitation) of the rough diamond's green coating shows clear peaks from chromium oxide (552 and 613 cm⁻¹) as well as the underlying diamond (1332 cm⁻¹). The specific positions of the chromium oxide peaks suggest the coating has been annealed to ~700°C (Mohammadtaheri et al., 2018).

GR1 defect). Careful examination under magnification found that the green color was not due to radiation stains, but instead to groupings of emerald-green platy crystals, ~40 μm in size, attached to the diamond surface (figure 5). Individual platy crystals could easily be flaked off using tweezers or a pointer probe, but they remained adhered to the surface under normal gem testing situations, including wiping the diamond with a stone cloth. X-ray fluorescence (XRF) analysis indicated high concentrations of chromium, and Raman analysis identified the green plates as chromium oxide (figure 6). The Raman peak positions correlated very well with chromium oxide powder that had been heated to ~700°C to produce a crystallized coating (M. Mohammadtaheri et al., "The effect of deposition parameters on the structure and mechanical properties of chromium oxide coatings deposited by reactive magnetron sputtering," *Coatings*, Vol. 8, No. 3, 2018, Article No. 111). A small H1b defect present in the diamond's FTIR spectrum supports this annealing temperature.

Most colored coatings encountered in the lab are on faceted stones and are pink, orange, red, or blue. The warmer hues are typically created by sputter-coating techniques involving metals and the colder hues by inks or other organic dyes. The use of chromium oxide powder to produce a green coating—along with annealing of the powder to produce crystallized plates that adhere to the rough surface to resemble radiation stains—represents a significant attempt to artificially reproduce the features seen on natural green diamonds. While the unique coating is easily discerned from natural green radiation stains under magnification, this stone is a strong reminder to carefully examine any green diamond,

Figure 5. The diamond's patchy green coloration is caused by interlocking platy crystals of chromium oxide, visible with magnification. Field of view 0.72 mm.
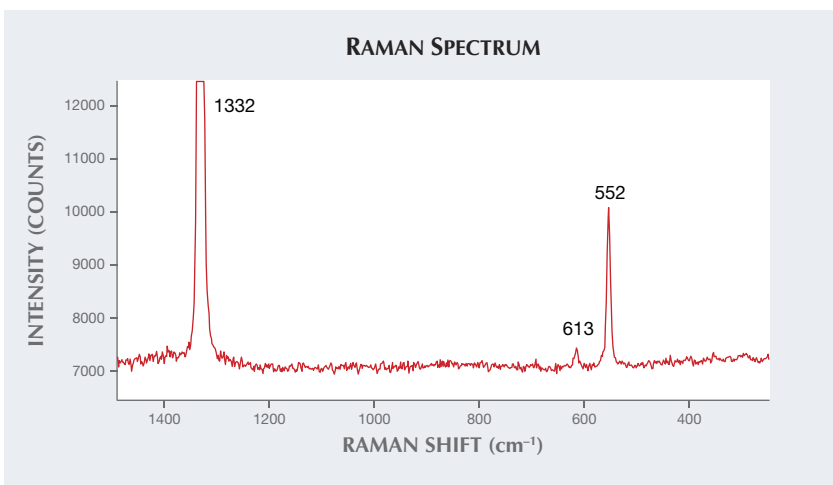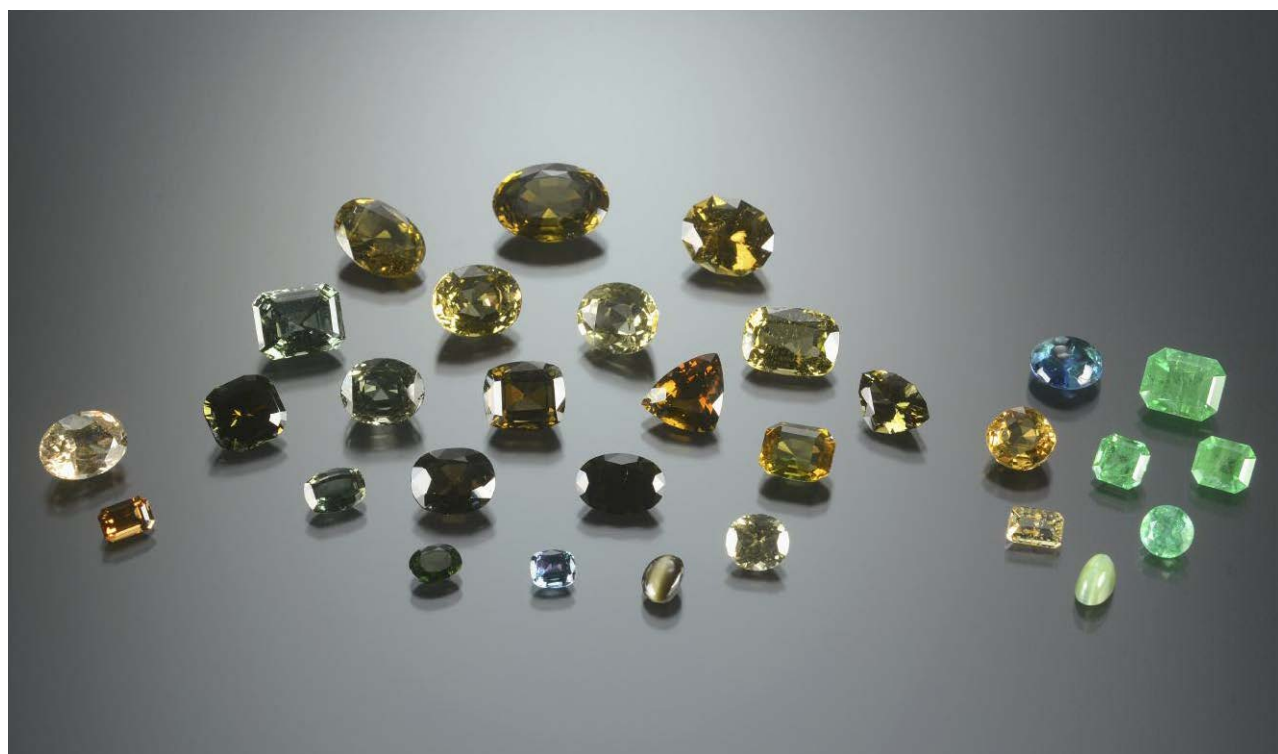
Figure 7. The two stones on the far left, corresponding to the blue analytical points in figure 8, were classified as kornerupine. The center 20 stones, corresponding to the yellow analytical points in figure 8, were classified as prismatine. For the eight stones on the right, corresponding to the red analytical points, the species could not be determined. The species classifications of all the stones were based on chemistry acquired by LA-ICP-MS. The largest stone is the 11.9 ct brown oval at the top of the center group. The smallest is the light blue cushion stone at the bottom of the center group, weighing 0.93 ct.

even rough crystals, in order to know exactly what you are buying.

Virginia A. Schwartz and
Christopher M. Breeding

Separation of KORNERUPINE and PRISMATINE

Kornerupine and prismatine form a solid solution series with a general chemical formula of $^X(\square,Mg,Fe)$ $^M(Al,Mg,Fe)_9 \, ^T(Si,Al,B)_5(O,OH,F)_{22}$ (X: cubic site; M: octahedral sites; T: tetrahedral sites). Chemically, they differ mainly in magnesium, iron, aluminum, and fluorine content, with boron content that ranges from 0 to 1 apfu (atoms per formula unit) in one of the tetrahedral sites. When the boron apfu is less than 0.5, the mineral is classified as kornerupine; above 0.5, it is classified as prismatine (E.S. Grew et al., "Prismatine: revalidation for boron-

rich compositions in the kornerupine group," *Mineralogical Magazine*, Vol. 60, No. 400, 1996, pp. 483–491).

GIA laboratories have recently implemented a method using laser ablation–inductively coupled plasma–mass spectrometry (LA-ICP-MS) to quantify boron concentration in kornerupine and prismatine in order to distinguish the two. The 30 stones shown in figure 7—all thought to be kornerupine—were borrowed from the GIA Museum and tested using a Thermo Fisher iCAP Qc ICP-MS, coupled with an Elemental Scientific Lasers NWR213 laser ablation system. GSD-1G and GSE-1G (U.S. Geological Survey) and NIST 610 were used as external standards. ^{29}Si was used as an internal standard. Three 55 µm circular spots were ablated on the girdle of each stone. The data reduction was a modified version of that used at GIA for tourmaline (Z. Sun et al., "A new method for deter-

mining gem tourmaline species by LA-ICP-MS," Spring 2019 *G&G*, pp. 2–17). As a result, we have slightly modified the criteria for separating the two to account for analytical error. If the boron apfu is between 0 and 0.45, the stone is classified as kornerupine. Between 0.45 and 0.55 apfu, the species cannot be determined by this method. If the boron apfu is between 0.55 and 1, the stone is classified as prismatine. For three spot analyses, if one spot has a boron apfu between 0.45 and 0.55, the species is undetermined.

All analytical points were plotted in figure 8 (full chemical results are in appendix 1 at www.gia.edu/gems-gemology/summer-2019-labnotes-separation-kornerupine-prismatine-appendix1.pdf). There were 2 kornerupine, 20 prismatine, and 8 undetermined species, for a total of 30 tested stones. This result suggests that, contrary to popular belief, prismatine may
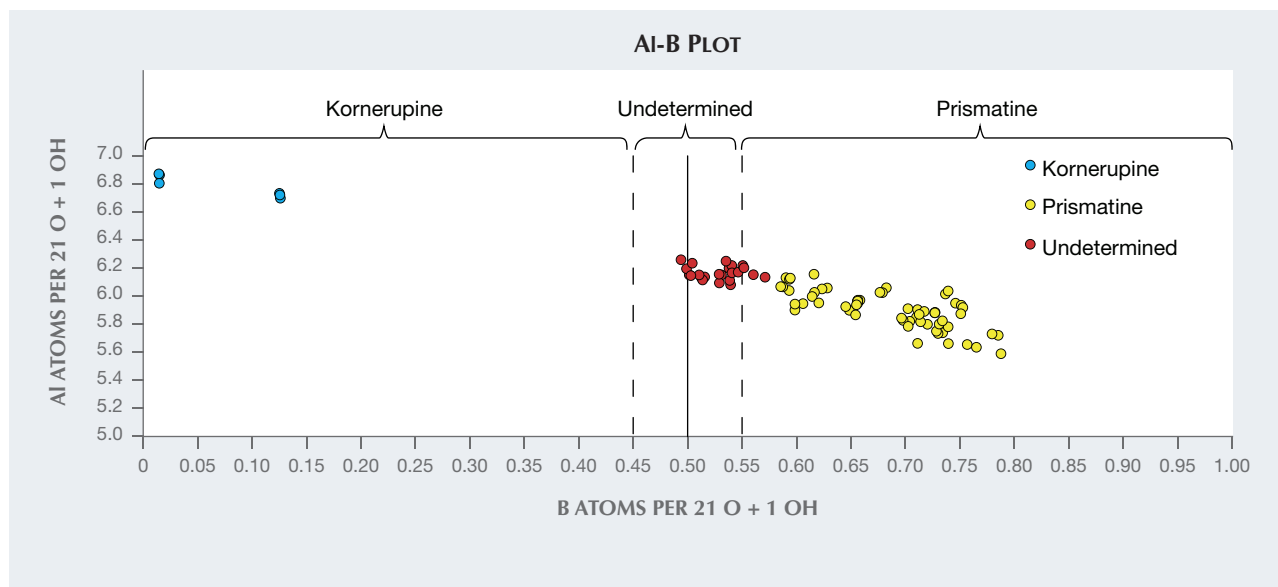
AL-B PLOT

Figure 8. The Al-B plot shows three sections. When the B (apfu) is between 0 and 0.45, stones are classified as kor-nerupine (blue spots). When the B (apfu) is between 0.45 and 0.55, the species for the stones (red spots) cannot be de-termined. When the B (apfu) is between 0.55 and 1.00, stones (yellow spots) are classified as prismatine. For three spot analyses, if one spot has a B (apfu) between 0.45 and 0.55, the species is considered undetermined.

be a far more common gem species than kornerupine, which is also supported by the analyzed boron concentration of many production stones submitted to GIA laboratories. Interestingly, for the five green stones tested here the species could not be determined, although they slightly favor prismatine chemistry (some of the red spots in figure 8). Aluminum apfu is also a good indicator for separating kornerupine from prismatine. Boron-rich prismatine has an Al apfu around 5.8 to 6.0, compared to boron-poor kornerupine with an Al apfu around 6.6 to 6.8. Extra Al in kornerupine functions as a substitute for B in one of the tetrahedral sites in the crystal lattice.

Kornerupine is an appropriate group name for kornerupine-structure minerals of an unknown boron content or for cases where the species cannot be determined. For extreme cases, such as when boron apfu is close to 0 or 1, Raman spectroscopy could be sufficient to separate kornerupine from prismatine (B. Wopenka et al., "Raman spectroscopic identification of B-free and B-rich kornerupine (prismatine)," *American Mineralogist*, Vol. 84, No. 4, 1999, pp. 550–554). However, the more accurate separation for

the two is determined by LA-ICP-MS analysis because the species definition is based on concentration of a chemical element, boron.

Ziyin Sun, Jonathan Muyal,
Nathan D. Renfro, Shane F. McClure,
and Aaron C. Palke

Faceted MILARITE

Recently the Carlsbad lab received a light yellow 2.07 ct unknown gemstone (figure 9). The measured refractive index was 1.548–1.550 with a birefringence of 0.002. The specific gravity, measured hydrostatically, was

Figure 9. This 2.07 ct oval brilliant is the first faceted milarite examined by the Carlsbad lab.
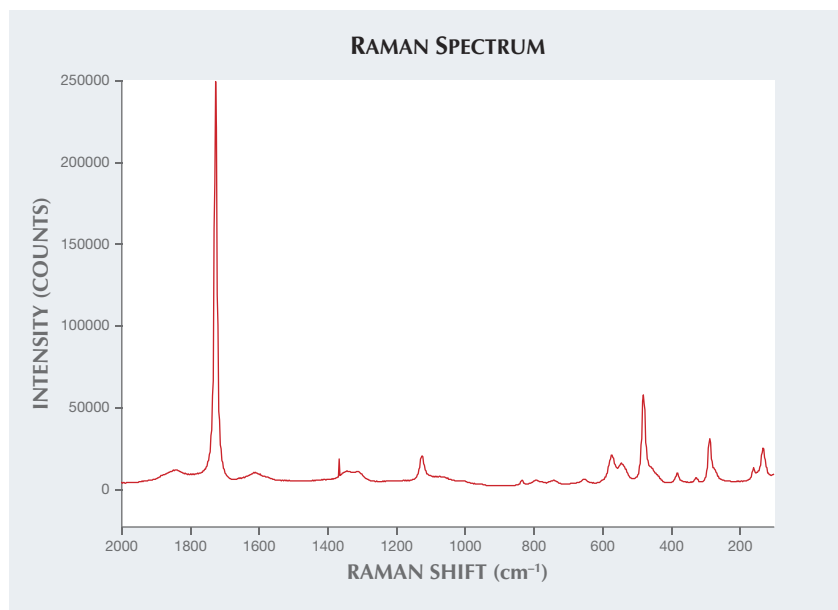
RAMAN SPECTRUM

Figure 10. Raman spectroscopy confirmed the gem to be milarite.

2.52. These properties were consistent with the mineral milarite, which was confirmed by Raman spectroscopy (figure 10). The stone showed planar/patterned liquid inclusions resembling a honeycomb pattern and also contained needle-like inclusions.

Milarite is fairly rare but gives its name to a somewhat large group of silicates, namely the milarite-osumilite group. This group is composed of similar cyclosilicate minerals that are very rare and obscure. Crystals are generally small and often have a muted green or yellow color, and they occur as well-formed prismatic hexagonal crystals. Milarite is a hexagonal-dihexagonal dipyramidal mineral with a composition of $K_2Ca_4Al_2Be_4Si_{24}O_{60}\cdot H_2O$. It forms as a primary mineral in granitic pegmatite, low-temperature hydrothermal veins, and alpine clefts.

The mineral was named by Gustav Kenngott (1870) after he mistakenly identified its provenance as Val Milar, located in eastern Switzerland. The original specimens actually came from neighboring Val Giuf. Even though milarite was the first newly described mineral from a Swiss Alpine fissure, it took more than 60 years to identify the mineral's true chemical nature, in particular its Be content. Milarite was originally known as a green mineral, until fine yellow crystals were discovered in Mexico in 1968. Larger Mexican crystals with transparent areas have occasionally been faceted into small gems with a pleasing appearance, but these are exceedingly rare.

Outside of Switzerland, notable occurrences have been recorded in Brazil, Mexico, Germany, Russia, Canada, Italy, Norway, and the Czech Republic. Nevertheless, this is the first example of faceted milarite ever examined by the Carlsbad laboratory.

Forozan Zandi

A "Hollow" PEARL Filled with Foreign Materials

The interior structures of pearls are always of interest, as they are never revealed until the analysis begins. External appearance may provide experienced pearl testers with some clues on what to expect when microradiography commences, but sometimes the structure revealed is beyond expectation (Spring 2014 Lab Notes, pp. 66–67; Winter 2015 Lab Notes, pp. 434–436).

In early 2019, a semi-baroque white and cream pearl, weighing 28.49 ct and measuring 19.23 × 16.44 × 15.05 mm (figure 11), was submitted to GIA's Bangkok laboratory. Its external appearance and size gave no obvious preliminary clues about its identity. A fairly small oval area on the base measuring approximately 5.20 × 3.10 mm differed in appearance from the rest of the pearl. Initial examination with a loupe and micro-

Figure 11. The submitted 28.49 ct pearl, alongside a Thai one-baht coin.

scope revealed that the pearl's surface had been worked and heavily polished, producing a lustrous appearance. Many surface areas had been modified, including the small oval area already mentioned. More detailed observation using a stereomicroscope revealed foreign materials within the yellow-brown area on the base (figure 12), including a piece of shell-like material (figure 12B and 12C, red arrows) together with other random fragments within a transparent light yellow substance enclosing several gas bubbles (figure 12D, blue arrows). Similar features were observed in the filler material used in natural blisters previously submitted to GIA (Summer 2016 Lab Notes, pp. 192–194). Although the surface structure indicated that the pearl was most likely filled with foreign materials, such an assumption could only be proved after more detailed study.

Real-time microradiography (RTX) and X-ray computed microtomography (μ-CT) revealed the pearl's internal structure, including a large dark and fairly irregular outline that indicates the pearl was hollow at one time. RTX analysis (figure 13A)
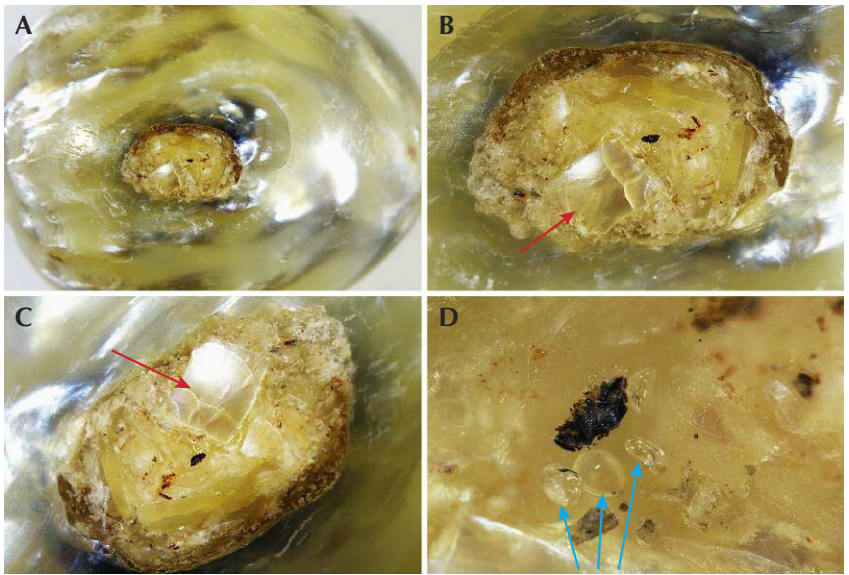

Figure 12. The pearl's base showing the filler (yellow-brown area) exposed at the surface (A). Field of view 19.20 mm. A magnified view of the filled area showing the largest shell-like material (B and C, red arrows) with other fragments within the transparent light yellow host filler. Field of view 7.20 mm. The gas bubbles in the filler are easily visible in this magnified view (D, blue arrows). Field of view 1.44 mm.

showed that some parts of the structure clearly reached the surface at the base. After RTX examination in a number of different orientations, however, it was very apparent that the structure was no longer hollow. In-
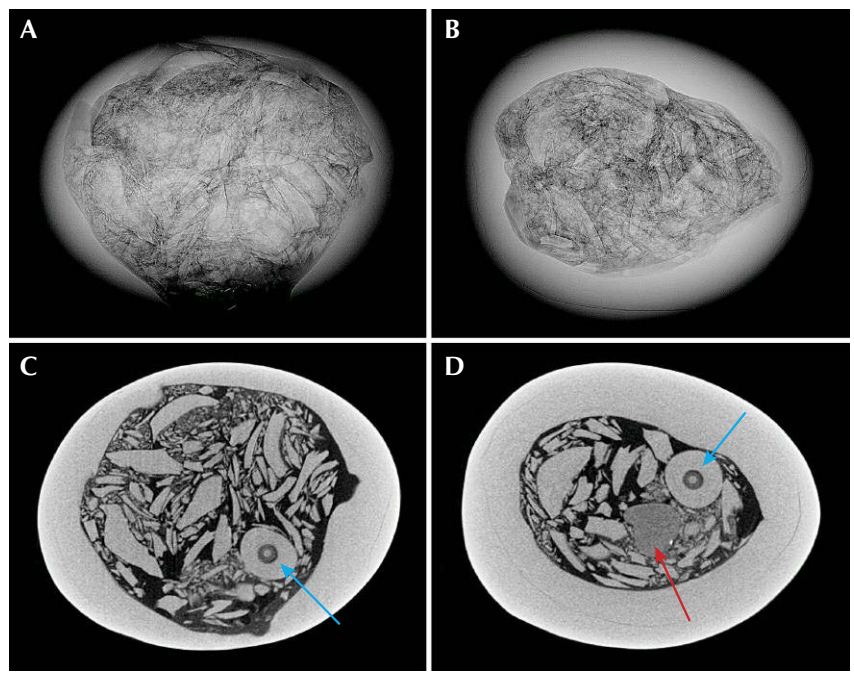
Figure 13. Top: Two RTX images reveal the complex internal structure observed in two different directions. Field of view ~21.19 mm. Bottom: Two μ-CT images reveal the structures in more detail. Field of view ~21.07 mm. The off-round features with a dark organic ring toward the center and a white core could be a natural seed pearl (C and D, blue arrows), while most of the other pieces seem to be fragments of shell. The identity of the more radio-translucent object (D, red arrow) with part of an additional white radio-opaque impurity within the filler is unknown and can only be solved through destructive testing.

stead, it was completely filled with foreign materials, displayed as an array of disorderly fragments (figures 13A and 13B). The μ-CT images revealed clearer structures, with the outlines of fragments in various sizes apparently suspended in the former void. The μ-CT results also showed a degree of structural variance in the materials present within the filler. One off-round feature displayed an organic-rich ring at its center, with a very small white core possibly indicating the presence of a small natural seed pearl (figure 13C and 13D, blue arrows). Other irregular features with a similar radio-opacity seemed to be related to pieces of shell (as seen with the microscope at the surface of the filled area on the base), while an unidentified, more radio-translucent feature was also noted (figure 13D, red arrow). An additional small radio-opaque white impurity (likely a metal fragment) was observed in association with the latter and may be seen with all the other components in the supplemental μ-CT videos (www.gia.edu/gems-gemology/summer-2019-lab-notes-hollow-pearl-filled-with-foreign-material).

The "hollow" form bears some similarity to previous cases, such as a natural hollow pearl (N. Sturman, "Pearls with unpleasant odors," GIA Laboratory, Bangkok, 2009, www.gia thai.net/pdf/Pearls_with_unpleasant_odours.pdf) or the voids seen in some non-bead cultured pearls (N. Sturman et al., "X-ray computed microtomography (μ-CT) structures of known natural and non-bead cultured *Pinctada maxima* pearls," *Proceedings of the 34th International Gemmological Conference*, 2015, pp. 121–124). Nevertheless, we cannot be certain why this void was filled with a variety of materials. The most plausible reasons are that (A) the feature needed to be filled so the pearl could be used in jewelry, and a selection of natural "shell-related" materials were mixed with adhesive to achieve this goal, or (B) the process was carried out to add weight to the pearl so it could be sold for a higher price, or both.
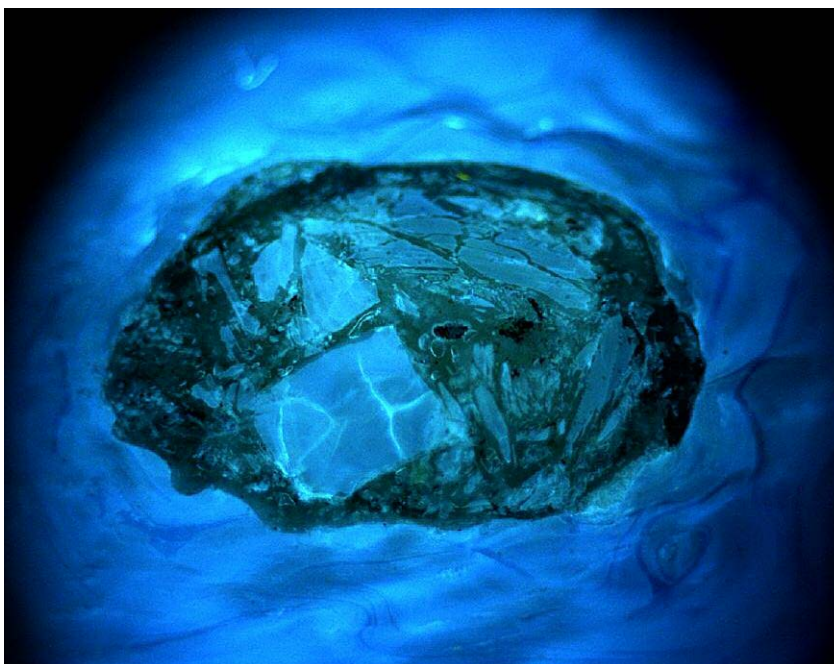

Figure 14. A strong blue fluorescence was visible on the pearl's surface under the DiamondView; the largest piece of shell and some of the smaller pieces with a matching appearance within the filler reacted in a similar manner. The other pieces in the filler exhibited slightly weaker reactions; the surrounding transparent filler showed a yellow-green color.

The pearl's fluorescence in the DiamondView was a strong blue, typical of many previously examined pearls. However, there was a degree of inhomogeneity that might be due to the surface condition (figure 14). The main reason to expose the pearl to the radiation of the DiamondView was to see how the materials in the filled area reacted. The results showed that the largest fragment and the pearl's surface produced a similar reaction, which supports the possible presence of shell pieces. Other smaller constituents showed weaker reactions, and the surrounding transparent host exhibited a yellow-green reaction.

Raman spectroscopic analysis of the filler confirmed the presence of shell based on a match with aragonite spectra, which is characteristic of many mollusks and pearls. The transparent filler material produced spectra that closely matched with a polymer. The chemistry of the largest piece of shell visible at the filler's surface was checked by energy-dispersive X-ray fluorescence (EDXRF) spectrometry and showed manganese (Mn) and strontium (Sr) levels characteristic of a saltwater environment.

Since the void within the pearl had been completely filled with foreign materials, it was unclear exactly what its original structure was prior to the work undertaken. Several scenarios are possible:

1. The pearl contained natural organic matter and formed naturally.

2. It had a large void with some organic matter in it, typical of some non-bead cultured pearls.

3. The large void contained a bead nucleus that was intentionally broken and mixed with bonding material and other components to fill the void and mask the identity, or the pieces of broken bead were removed before the void was filled with shell and other materials.

Figure 15. These two beads, 6.96 ct (left) and 2.25 ct (right), were identified as dyed serpentine.

Where doubt about the actual identity exists and each possibility has merit, it is unfair to the client to simply make an educated guess. After explaining the situation to the client, we left the identity of this pearl as "filled" but of an "undetermined" origin (natural, bead cultured, or non-bead cultured). Accordingly, a report was not issued.

Nanthaporn Nilpetploy

Dyed SERPENTINE Imitating Sugilite
The Carlsbad laboratory recently received a parcel of mottled purple beads (figure 15). A 2.25 ct translucent reddish purple broken bead from this parcel (shown on the right in figure 15) was examined for an identification report. At first glance, based on the color and structure, the sample resembled sugilite. Standard gemologi-

cal testing revealed a refractive index of 1.56, a specific gravity of 2.71, weak orange fluorescence in both long-wave and short-wave UV, and a dye band with a handheld spectroscope. Sugilite has an RI of 1.607–1.610 and an SG of 2.74, and may show a concentrated band at 600 nm that can be confused with a dye band. The bead showed uneven color and a fibrous structure under the microscope (figure 16). There were no obvious dye concentrations, but the orange fluorescence and dye band in the spectroscope indicated the presence of dye. By performing a simple acetone test, we were able to prove that the material had been dyed. A light pink streak was examined after rubbing the test sample on a tissue soaked with acetone. The specimen's infrared spectrum was not consistent with sugilite but ended up matching well with serpentine. Chemistry collected via laser ablation–inductively coupled plasma–mass spectrometry (LA-ICP-MS) was consistent with serpentine, ruling out the possibility of sugilite.

Without advanced testing, it would have been difficult to conclusively identify this material as serpentine. This is the first time reddish purple dyed serpentine imitating sugilite has been examined in the Carlsbad laboratory, and gemologists should be aware of this imitation when examining sugilite.

Jessa Rizzo

Figure 16. The fibrous internal structure of the specimen resembling sugilite was actually consistent with serpentine. Field of view 4.11 mm.

Color-Change SPESSARTINE Garnet: A First Report
GIA's Carlsbad laboratory recently examined a 2.11 ct faceted stone (figure 17) that showed strong color change from dark green under daylight-equivalent lighting to dark red under incandescent illumination. Standard gemological testing revealed a refractive index that was over the 1.80 RI limit of the GIA desktop refractometer. This was the first example of a color-change garnet with an over-the-limit RI reading examined by GIA. Fluorescence was inert to long-wave and short-wave

Figure 17. Color-change phenomenon was observed in this 2.11 ct octagonal mixed-cut spessartine. The left image, with a dark green color, was taken using an LED light source with 6500K color temperature (a daylight-equivalent light simulator). The right image, showing a dark red color, was taken with an LED light source with 2700K color temperature (an incandescent light simulator).

UV light. The stone did not show any pleochroism with the dichroscope. Using a handheld spectroscope, we observed a cutoff at about 460 nm and a broad band centered at about 575 nm. Microscopic examination revealed only a small fracture and strong internal strain. High-order interference colors were observed in cross-polarized light from the strain along grain boundaries.

Laser ablation–inductively coupled plasma–mass spectrometry (LA-ICP-MS) results showed that the stone was composed predominantly of spessartine (80.37 mol.%), with minor contributions from other end members of the garnet species (see table 1 at www.gia.edu/gems-gemology/summer-2019-labnotes-color-change-spessartine-garnet-icp-table1.pdf). It is classified as a spessartine garnet based on the criteria in the pyrope-spessartine-almandine ternary diagram (figure 18, left) modified from Stockton and Manson ("A proposed new classification for gem-quality garnets," Winter 1985 *G&G*, pp. 205–218). The RI and SG could also be calculated based on chemical composition (W.A. Deer et al., *Rock-Forming Minerals: Orthosilicates*, Vol. 1A, Geological Society of London, 1982, pp. 485–488).

Figure 18. Left: Three LA-ICP-MS data points, calculated based on molecular percentages for pyralspite garnet, were plotted in a pyrope-spessartine-almandine ternary diagram (modified after Stockton and Manson, 1985). Refractive index and spectral boundaries were used to distinguish among the six proposed garnet gem species labeled in the diagram. Right: The same data points were further plotted in the pyrope-spessartine-almandine RI-SG diagram (modified after Deer et al., 1982) to validate the measured over-the-limits RI.
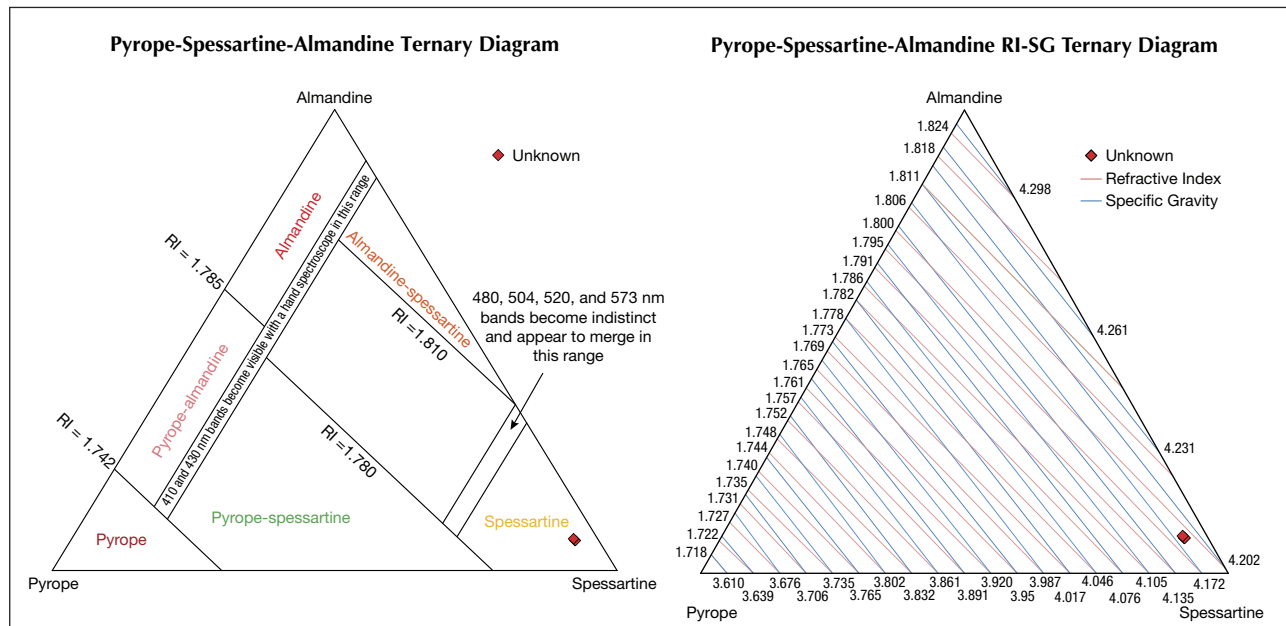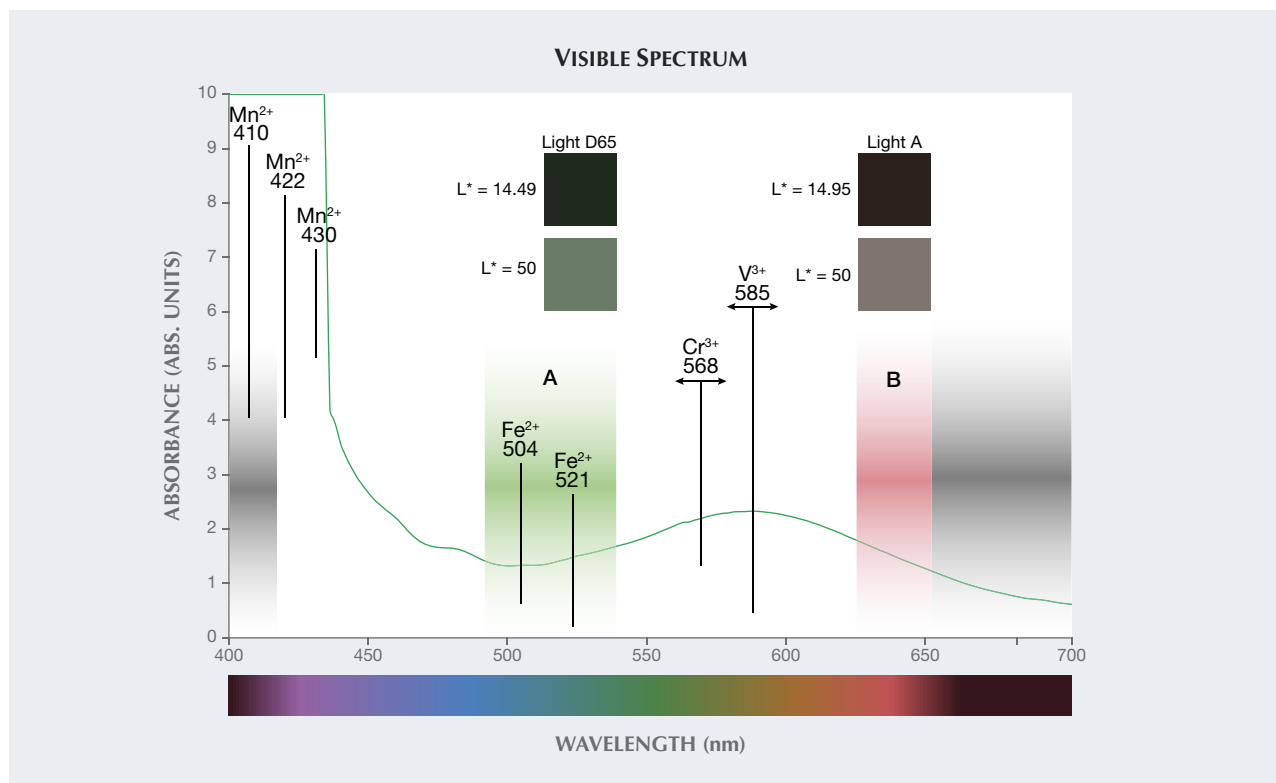
VISIBLE SPECTRUM

Figure 19. In the visible absorption spectrum of the stone, transmission window A is centered at 510 nm, while transmission window B is between 630 and 650 nm. The strong absorption below 450 nm is caused by Mn^{2+}; a wide absorption band between 550 and 650 nm is caused mainly by V^{3+}. The stone had so much Mn that the detector of the instrument was saturated below 440 nm. Calculated color pairs, representing the color of the stone seen under CIE D65 illumination and CIE A illumination, are shown above the two transmission windows. The human eye is not color sensitive above 650 nm or below 420 nm (both represented in the graph by the gray color zoning). The transmission in these wavelength ranges cannot be perceived effectively.

The calculated RI and SG—plotted in figure 18, right—were 1.797 and 4.182, respectively. The calculated RI value was consistent with the measured RI value. In 2001, Krzemnicki et al. reported a garnet composed of 76.9 mol.% spessartine and 4.2 mol.% goldmanite with a color change from orange-yellow under daylight-equivalent lighting to reddish orange under incandescent illumination based on the colorimetric data in the article, although color change from brownish green to brownish was observed visually ("Colour-change garnets from Madagascar: Comparison of colorimetric with chemical data," *Journal of Gemmology*, 2001, Vol. 27, No. 7, pp. 395–408). The high spessartine and goldmanite composition of the stone is similar to our stone reported here, but with much weaker color change.

To understand why this spessartine garnet showed a color-change phenomenon, we collected an ultraviolet/visible/near-infrared (UV-Vis-NIR) spectrum (the visible portion of the spectrum is shown in figure 19), which was then used to quantitatively calculate the stone's colorimetric coordinates (L*, a*, and b*; see table 2 at www.gia.edu/gems-gemology/summer-2019-labnotes-color-change-spessartine-garnet-icp-table2.pdf) under different lighting conditions. The strong absorption below 450 nm is caused by Mn^{2+} (R.K. Moore and W.B. White, "Electronic spectra of transition metal ions in silicate garnets," *Canadian Mineralogist*, Vol. 11, No. 4, 1972, pp. 791–811). A wide absorption band centered at about 585 nm is caused mainly by V^{3+} (C.A. Geiger et al., "Single-crystal IR- and

UV/VIS-spectroscopic measurements on transition-metal-bearing pyrope: the incorporation of hydroxide in garnet," *European Journal of Mineralogy*, Vol. 12, No. 2, 2000, pp. 259–271), which produced two transmission windows: one in the blue-green part of the spectrum (figure 19, window A) and the other in the red (figure 19, window B). This was the cause of the color change in this spessartine garnet, as incandescent illumination highlighted the red transmission window and daylight-equivalent lighting highlighted the blue-green window. Color pairs under CIE D65 illumination (representing daylight-equivalent lighting) and CIE A illumination (representing incandescent illumination) were calculated and are shown in figure 19, above transmission window A and B. The darker color pair (top row), di-

Colorimetric Parameters of Color-Change Spessartine in CIE Standard Illuminant A and D65 in the CIELAB 1976 Color Circle
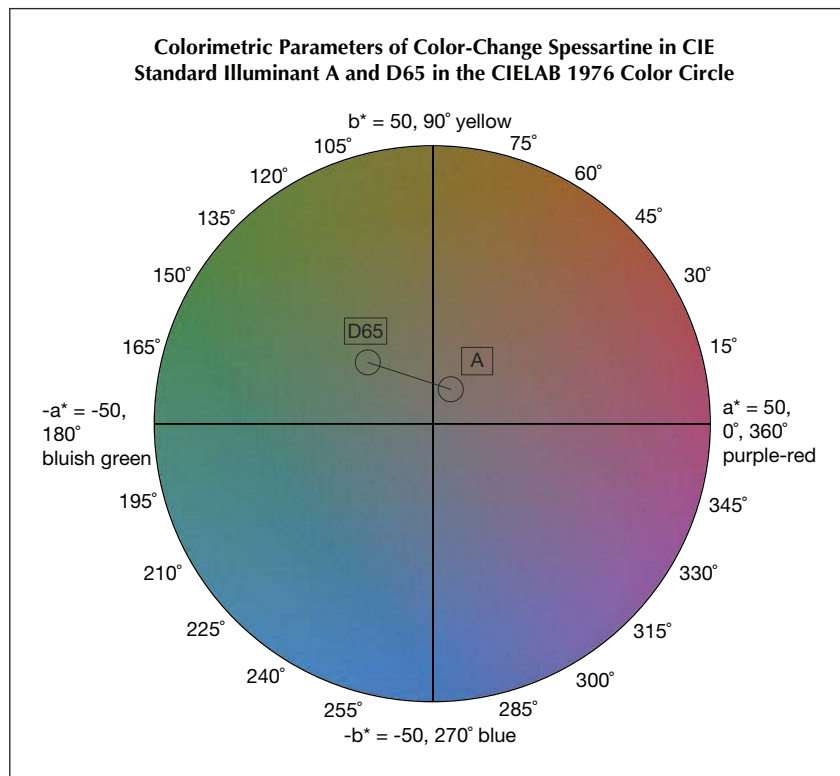

Figure 20. In the CIELAB 1976 color circle, the color of the stone changes from medium saturated green under CIE D65 illumination to low saturated orangy red under CIE A illumination, with a hue angle difference of 79.11°, a chroma difference of 9.25, and a color difference of 15.82. Full sets of L*, a*, b* and RGB color coordinates are shown in table 2.

rectly calculated from the measured UV-Vis-NIR spectrum, closely matched the dark appearance of the stone (again, see figure 17) with L* (lightness) around 14.5. It was the strong absorption generated by very high Mn and V concentration, along with the stone's relatively large size, that produced a long light path length. To better observe the saturation and hue of the color pair, the authors changed the L* to 50 and reproduced the color pair with the same a* and b* values (bottom row). The hue difference of the color pair is easier to see with increased lightness.

One way to judge the quality of a color-change stone is to plot the color pair in the CIELAB 1976 color circle. Good color-change pairings show a large hue angle difference, small chroma difference, and large chroma

values (Z. Sun et al., "How to facet gem-quality chrysoberyl: Clues from the relationship between color and pleochroism, with spectroscopic analysis and colorimetric parameters," *American Mineralogist*, Vol. 102, No. 8, 2017, pp. 1747–1758). The color coordinates L*, a*, and b* (again, see table 2) of the stone under CIE D65 illumination and CIE A illumination were plotted in the CIELAB 1976 color circle in figure 20. The spessartine showed a low saturation under CIE A illumination.

Color change has been reported previously in pyrope-spessartine (K. Schmetzer et al., "Color-change garnets from Madagascar: Variation of chemical, spectroscopic and colorimetric properties," *Journal of Gemmology*, Vol. 31, No. 5-8, 2009, pp. 235–282), in pyrope (Z. Sun et al.,

"Vanadium- and chromium-bearing pink pyrope garnet: characterization and quantitative colorimetric analysis," Winter 2015 *G&G*, pp. 348–369), and in grossular (Spring 2018 GNI, pp. 233–236). To the authors' knowledge, this was the first color-change spessartine reported.

Heidi Breitzmann, Ziyin Sun, and Aaron C. Palke

SPURRITE

Recently, a 19.68 ct gray-purple stone (figure 21) was submitted to the Carlsbad laboratory for identification. The square cabochon was semitranslucent and had wispy white features throughout.

It had a refractive index of 1.68–1.64 and a hydrostatic specific gravity of 3.00. Raman spectroscopy identified it as spurrite (figure 22), which aligned with the gemological properties already measured. Spurrite is a nesosilicate with a chemical composition of $Ca_5(SiO_4)_2CO_3$ (J.W. Anthony et al., *Handbook of Mineralogy*, Vol. 2, Mineral Data Publishing, 1995). Analysis by energy-dispersive X-ray fluorescence (EDXRF) showed high amounts of calcium and silicon.

Figure 21. A 19.68 ct gray-purple spurrite that was submitted to GIA's Carlsbad lab.
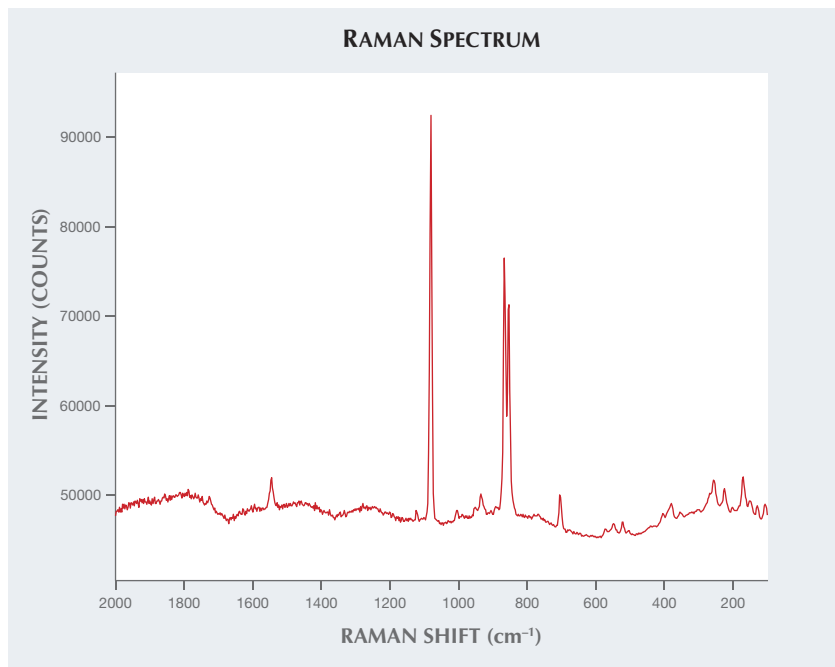
RAMAN SPECTRUM

Figure 22. Raman spectroscopy identified the gray-purple stone as spurrite.

Spurrite occurs in high-temperature thermal metamorphism along the contact between carbonate rock and mafic magma (Anthony et al., 1995). A common inclusion found within spurrite is black metallic mag-

Figure 24. Raman spectroscopy identified the inclusion in the spurrite as magnetite.
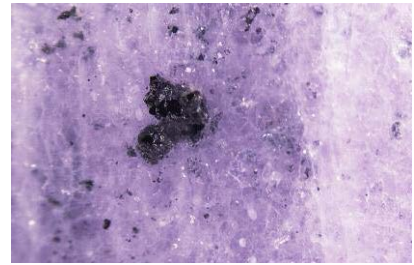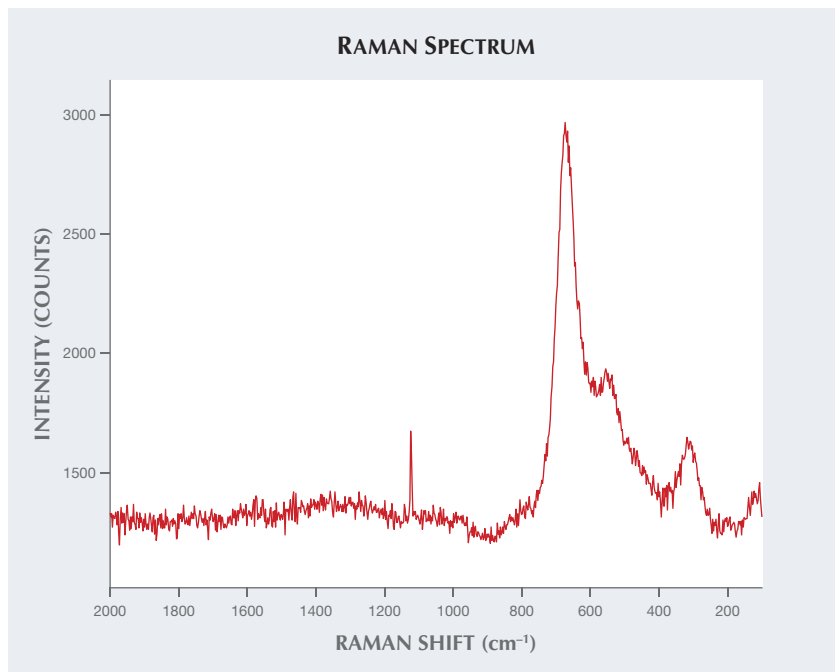
RAMAN SPECTRUM

Figure 23. Magnetite, identified using Raman spectroscopy, breaks the surface of the spurrite. Field of view 4.79 mm.

netite crystals. Raman spectroscopy identified the metallic opaque inclusions that broke the surface (figure 23) as magnetite (figure 24), further evidence that this stone was a spurrite.

Encountering stones that require more research and a little detective work, such as this spurrite, can enhance one's curiosity about gemology.

Nicole Ahline

Exsolved Particles with Natural Appearance Within Flux-Grown Pink SYNTHETIC SAPPHIRE

The Carlsbad laboratory recently examined unusual exsolved flux particles in a flux-grown pink synthetic sapphire. The specimen, mounted in a ring, had an estimated weight of 13.07 ct and a refractive index of 1.760–1.770. It displayed a typical pink sapphire spectrum with a hand-held spectroscope. Strong red fluorescence was seen under both long-wave and short-wave UV. Laser ablation–inductively coupled plasma–mass spectrometry (LA-ICP-MS) detected high levels of platinum; the concentrations of iron, beryllium, titanium, vanadium, and gallium were either below the detection or quantification limit.

Microscopic examination revealed further evidence of a synthetic origin: a single reflective platinum platelet with negative hexagonal growth through the center (figure 25, left). Also observed were interconnected channels of exsolved flux creating fingerprints (figure 25, right).
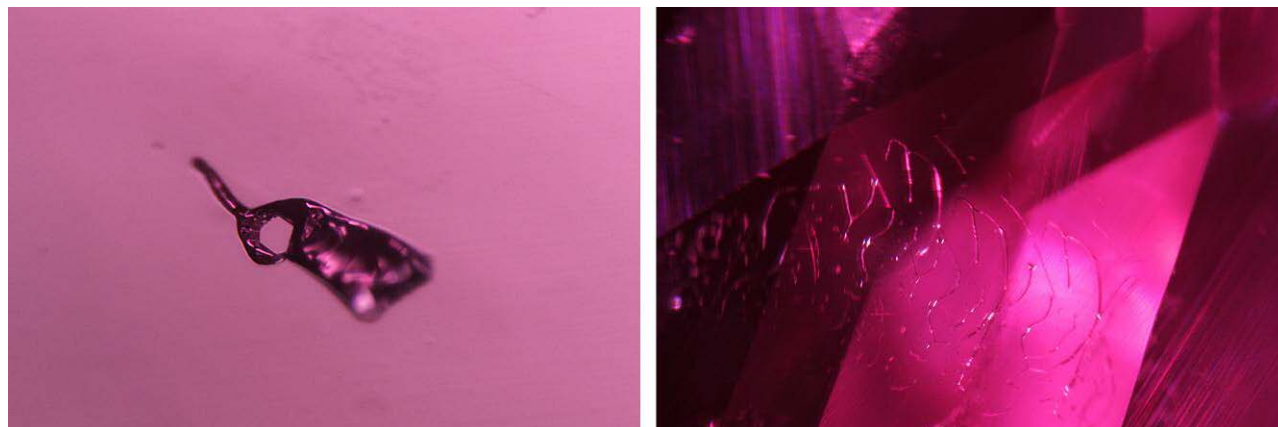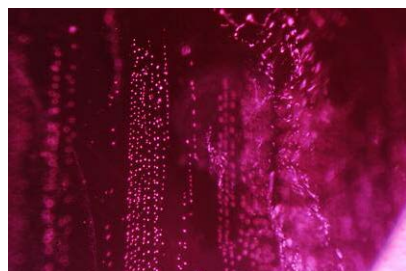
Figure 25. Left: Reflective platinum platelet with negative hexagonal growth within a flux-grown pink synthetic sapphire; field of view 2.34 mm. Right: Channels of exsolved interconnected flux; field of view 4.79 mm.

A potentially challenging inclusion was seen in the form of minute rounded flux particles aligned in organized linear rows (figure 26), which displayed a striking resemblance to fingerprints and silk clouds commonly seen within natural corundum. These particles were observed in relative abundance at varying depths. Grid-like exsolved solid inclusions have been mentioned in the literature as possible properties of synthetic corundum (R.W. Hughes et al., *Ruby & Sapphire: A Gemologist's Guide*, Lotus RWH Publishing, Bangkok, 2017). It has not been stated how abundant these natural-looking fingerprints are within flux-grown synthetic material, but this type of inclusion is rarely seen at the Carlsbad laboratory. Identifying the natural or synthetic origin of a stone with this type of natural-looking inclusion can be challenging. If a gem material is suspected of being synthetic, it is advisable to submit it to a gemological laboratory.

Britni LeCroy

Figure 26. Fine rounded flux particles aligned into linear stringers resembling fingerprints and silk clouds seen within natural corundum; field of view 1.73 mm.

For More on Lab Notes

X-ray computed microtomography (μ-CT) imaging reveals a hollow pearl filled with foreign material. View the videos at www.gia.edu/gems-gemology/summer-2019-labnotes-hollow-pearl-filled-with-foreign-material

Intergrown Emerald Specimen from Chivor

Colombia's Chivor emerald mines are located in the eastern zone of the Eastern Cordillera range of the Andes Mountains. *Chivor* translates to "green and rich land" in Chibcha, the language of the indigenous people who were already mining emerald more than 500 years ago, before the arrival of the Spanish conquistadors (D. Fortaleché et al., "The Colombian emerald industry: Winds of change," Fall 2017 *G&G*, pp. 332–358). Chivor emeralds exhibit a bright green color with a tint of blue; they have relatively high clarity and fewer inclusions than emeralds found in Colombia's western belt.

The authors recently examined a rough emerald crystal specimen (figure 1), measuring 18.35 × 10.69 × 9.79 mm, reportedly from Chivor. This crystal weighed 3.22 g (16.10 ct) and had a prismatic hexagonal crystal shape. Standard gemological examination confirmed the gemstone to be emerald, and ultraviolet/visible/near-infrared (UV-Vis-NIR) spectroscopy showed a classic Colombian emerald absorption spectrum. The crystal's color was typical of Chivor emeralds, a medium dark green showing a blue tint. The emerald, which hosted jagged three-phase inclusions that are typically observed in Colombian material, showed no signs of clarity enhancement.

The emerald specimen hosted a large, unique inclusion of emerald almost perpendicular to the c-axis, measuring approximately 2.67 × 2.71 × 5.43 mm. The inclusion's iden-

tity was confirmed by Raman spectroscopy. The inclusion exhibited a well-formed hexagonal prismatic shape with pyramid-like termination (figure 2). Although intergrowth emerald crystals have been described and documented in the literature several times (G. Grundmann and G. Giuliani, "Emeralds of the world," in G. Giuliani et al., Eds., *Emeralds of the World*, extraLapis English, No. 2, 2002, pp.

Figure 1. An emerald crystal inclusion measuring ~2.67 × 2.71 × 5.43 mm is found inside this large emerald specimen (18.35 × 10.69 × 9.79 mm) from Colombia's Chivor mine. Photo by John Jairo Zamora.
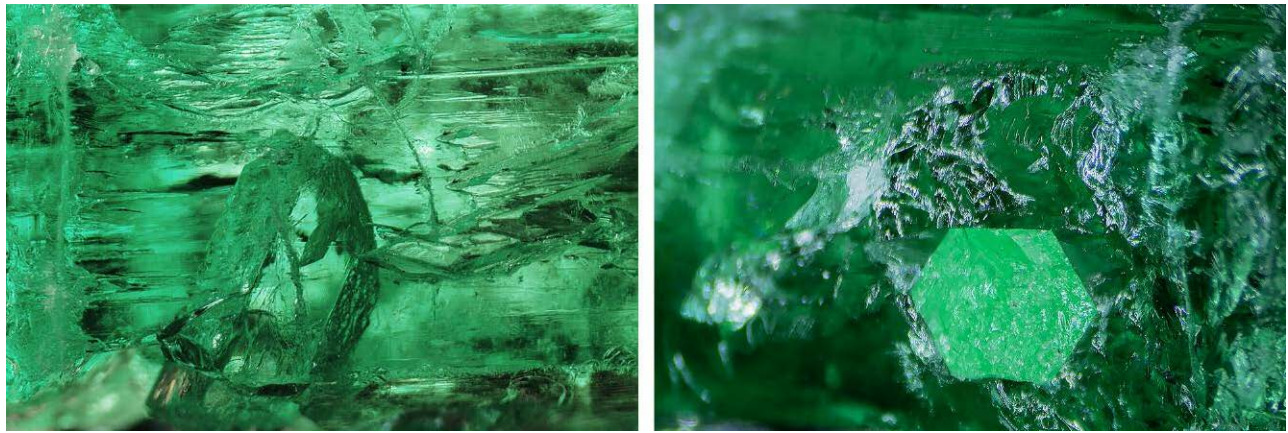

Figure 2. Left: A well-formed emerald inclusion, showing a hexagonal prismatic shape with pyramidal termination. Right: The view from below shows a perfect hexagonal crystal outline. Photomicrographs by John Jairo Zamora; field of view 12 mm.

24–35; I. Sunagawa, *Crystals: Growth, Morphology and Perfection*, Cambridge University Press, 2005, pp. 127–149), it is always a spectacular feature to observe, making this emerald rough crystal from Chivor with an emerald crystal inclusion a unique collector's specimen.

Luis Gabriel Angarita and John Jairo Zamora
CDTEC, Bogotá

Jonathan Muyal
GIA, Carlsbad

Purple Fluorite Inclusion in Emerald from Russia

Fluorite inclusions in emeralds from various localities have been reported extensively in the literature. They have been described as "whitish-colorless, octahedral-cube and/or corroded rounded shapes" (E.J. Gübelin and J.I. Koivula, *Photoatlas of Inclusions in Gemstones*, Vol. 3, Opinio Publishers, Basel, Switzerland, 2008). However, purple fluorite in an emerald host is rare.

Author CM previously documented a purple banded fluorite inclusion in an emerald submitted to GIA for identification (Fall 2016 Lab Notes, pp. 302–303). This was noted as "an interesting and unexpected addition to an otherwise typical (emerald) inclusion scene." Surprisingly, the current authors recently found another purple fluorite inclusion in an emerald (figure 3) from GIA's research reference collection. Purchased from Alexey Burlakov (Tsarina Jewels, JTC, Bangkok), it was reportedly from the Maly-

Figure 3. A Russian emerald hosts a crystal inclusion—identified by laser Raman microspectrometry analysis as fluorite—that exhibits a distinct purple color. Photomicrograph by Jonathan Muyal; field of view 1.44 mm.
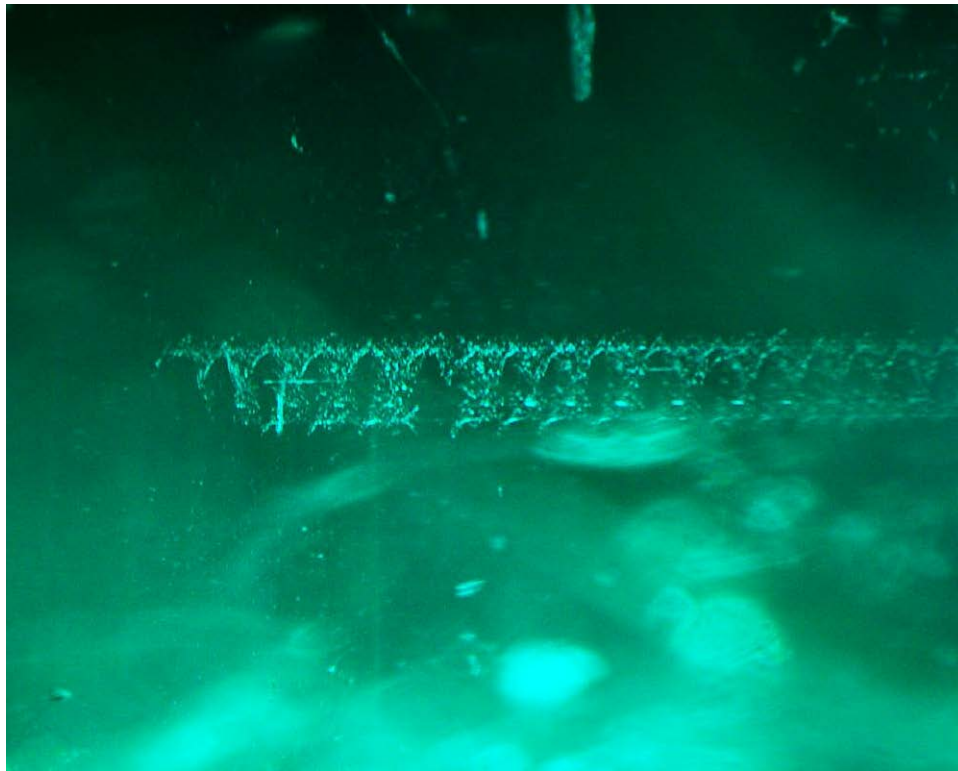
Figure 4. A three-dimensional helical inclusion in emerald. Photomicrograph by Taku Okada; field of view 2.93 mm.

sheva mine, located a few kilometers northeast of Yekaterinburg, Russia.

Closer examination of the inclusion revealed a large, distinct purple zone, as well as a purple band and a subhedral crystal form. The inclusion proved to be singly refractive when viewed between crossed polarizers. Laser Raman microspectrometry confirmed that the inclusion was fluorite. Trace-element chemistry of the host emerald collected via laser ablation–inductively coupled plasma–mass spectrometry (LA-ICP-MS) matched well with GIA's Russian emerald chemistry reference data.

Raman analysis and microscopic observation conclusively identified the inclusion as fluorite. This strongly suggests that the unusual purple inclusion observed by author CM in 2016 was indeed fluorite; in that case, the inclusion was too deep in the stone to analyze with Raman. It is possible that purple fluorite is an unusual internal feature found only in Russian emerald, since that is the only known source from which we have observed this inclusion.

Jonathan Muyal and Claire Malaquias
GIA, Carlsbad

Helical Inclusion in Colombian Emerald

GIA's Tokyo laboratory recently examined a 7.54 ct natural emerald containing a 3D helical inclusion (figure 4) resembling a DNA double helix or fish bone. This helix, consisting of whitish grains, reached the emerald's surface. The other associated inclusions were jagged three-phase finger-

prints, growth tubes, and the *gota de aceite* optical effect (R. Ringsrud, "*Gota de aceite*: Nomenclature for the finest Colombian emeralds," Fall 2008 *G&G*, pp. 242–245). All these features supported a Colombian origin. To date, three emeralds examined in GIA's Tokyo laboratory that were reportedly Colombian have exhibited similar inclusions. This helical inclusion may therefore be a characteristic of Colombian emeralds. Such a discovery within a stone is always pleasing.

Taku Okada
GIA, Tokyo
Piradee Siritheerakul
GIA, Bangkok

Mexican Opal with Large Fluid Inclusion

Although opals generally contain water in their structure, fluid inclusions large enough to be resolved with the microscope are rare; those that can be seen with the unaided eye are exceedingly rare. While at the JCK Show in Las Vegas, the author examined a most unusual common opal with a very large eye-visible fluid inclusion (figure 5). The fluid cavity was approximately 14 mm in diameter, and most of the space inside was occupied by a large gas bubble. An aqueous liquid could clearly be observed wetting the walls of the cavity, along with some unknown solid particles (figure 6). Since this fluid inclusion contained solid, liquid, and gaseous phases, it is appropriately described as a three-phase inclusion. According to

Figure 5. This 19.94 ct polished freeform opal contained a large, eye-visible three-phase fluid inclusion. Photo by Jian Xin (Jae) Liao; courtesy of Javier Lopez Ávila.

Javier Lopez Ávila, the stone's owner, this rare opal specimen was mined from the San Simon mine in Jalisco, Mexico, by Opalos de México. It is the first opal with a large fluid inclusion that he has observed from this deposit. This rare inclusion in Mexican opal is an interesting gemological oddity that any collector can appreciate.

Nathan Renfro
GIA, Carlsbad

Figure 6. This eye-visible three-phase fluid inclusion in a Mexican opal was just over 14 mm in diameter and contained solid, liquid, and gaseous phases. Photomicrograph by Nathan Renfro.
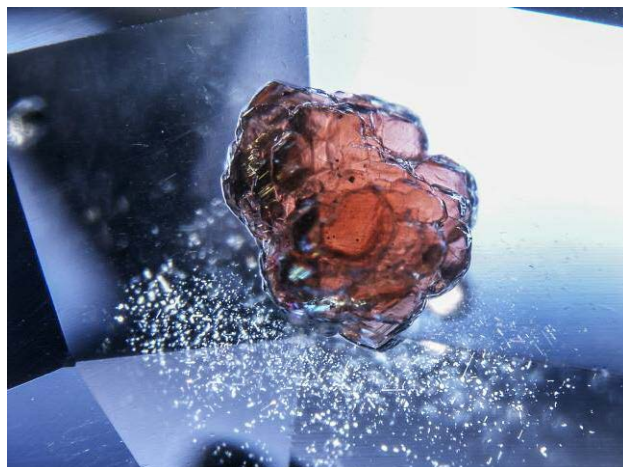

Figure 7. A protogenetic crystal of pyrope-almandine garnet with reflective needles in a greenish blue sapphire. Photomicrograph by Nattida Ng-Pooresatien; field of view 2.70 mm.

Pyrope-Almandine Garnet in Sapphire Host

In gemology, garnet occurs in a wide variety of colors, including red, orange, yellow, and green. Garnet is also found as inclusions in diamond, quartz, topaz, aquamarine, and zircon (E.J. Gübelin and J.I. Koivula, *Photoatlas of Inclusions in Gemstones*, Vol. 1, ABC Edition, Zurich, 1986, pp. 158–160).

GIA's Bangkok laboratory recently received a 3.97 ct transparent greenish blue sapphire for a colored stone identification report. Standard gemological testing and advanced analysis revealed properties consistent with natural sapphire. Interestingly, microscopic examination with a combination of darkfield and oblique fiber-optic illumination revealed a well-formed brownish orange crystal cluster with reflective needles (figure 7). The crystal was singly refractive, and Raman spectrometry matched it with pyrope-almandine garnet. Sapphires with garnet inclusions are rarely seen in laboratory examination, although they are occasionally found in samples from Tanzania and the state of Montana (E.J. Gübelin and J.I. Koivula, *Photoatlas of Inclusions in Gemstones*, Vol. 3, Opinio Publishers, Basel, Switzerland, 2008, pp. 228–242).

Nattida Ng-Pooresatien
GIA, Bangkok

Euhedral Phantom Sapphire in Sapphire

A phantom sapphire crystal within a host sapphire crystal was recently examined at GIA's Carlsbad laboratory. The inclusion showed euhedral morphology as one half of a partially tapered bipyramid. The visible boundaries of the included crystal were composed of unaltered fingerprints with geometric patterns and fine linear rows. The crystal's
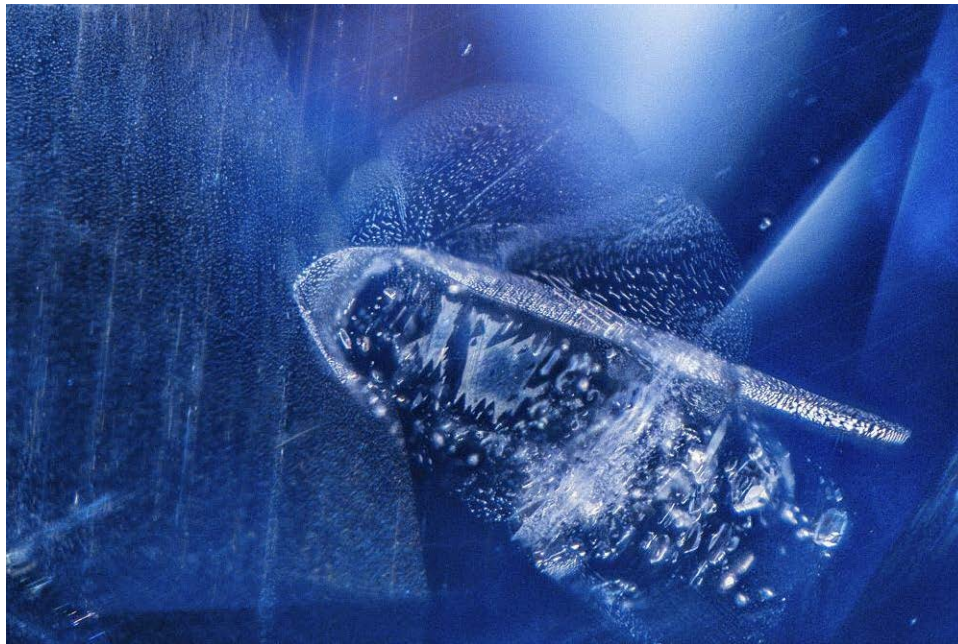
Figure 8. A partially tapered bipyramid sapphire inclusion within a sapphire. Photomicrograph by Britni LeCroy; field of view 2.90 mm.

surface also showed moderate-order birefringence colors; these represented the shared interface between the host's crystal lattice and the inclusion's crystal lattice (figure 8). External local fingerprints also terminated around the crystal's end point. Negative crystals within the inclusion showed tabular hexagonal habit (figure 9, left). When the host sapphire was exposed to temperatures below the freezing point of water, a CO_2 bubble was seen within the largest negative crystal (figure 9, right). A sapphire with this inclusion combination is rarely seen.

Britni LeCroy
GIA, Carlsbad

Curved Banding in Flame-Fusion Synthetic Sapphires

Most synthetic ruby and sapphire on the market is grown by Verneuil flame fusion. It can usually be separated from natural corundum by its distinctive curved banding, in contrast to the angular zoning seen in natural stones. Gemologists may see these features in the microscope when using darkfield or brightfield illumination. This zoning can also be seen with use of a short-wave fluorescent light, as noted in *Ruby & Sapphire: A Gemologist's Guide* (R.W. Hughes et al., Lotus Publishing, Bangkok, 2017).

Figure 9. Left: Negative crystals with tabular hexagonal habit within a euhedral sapphire inclusion. Right: A CO_2 bubble appears within the largest negative crystal (see arrow) after the stone was exposed to temperatures below the freezing point of water. Photomicrographs by Britni LeCroy; field of view 1.76 mm.
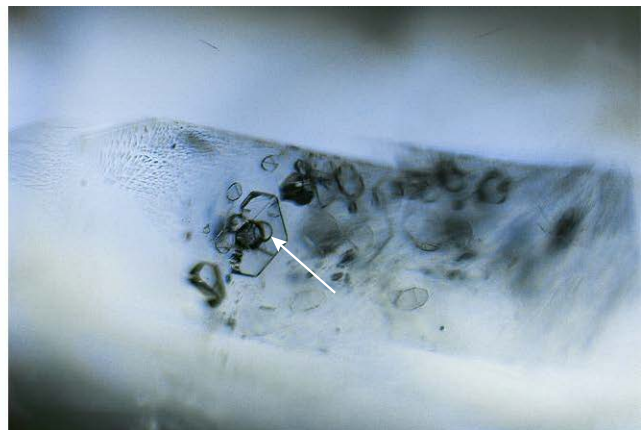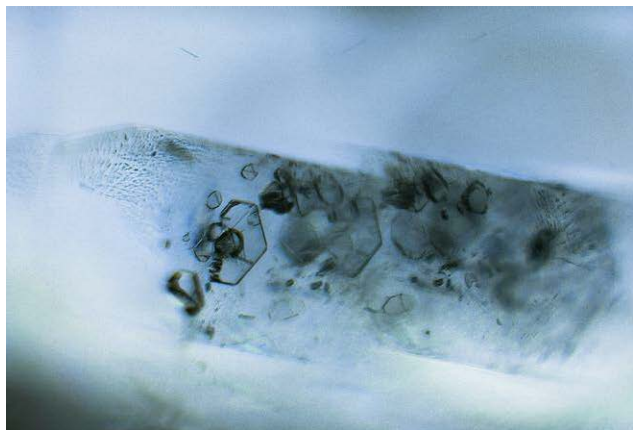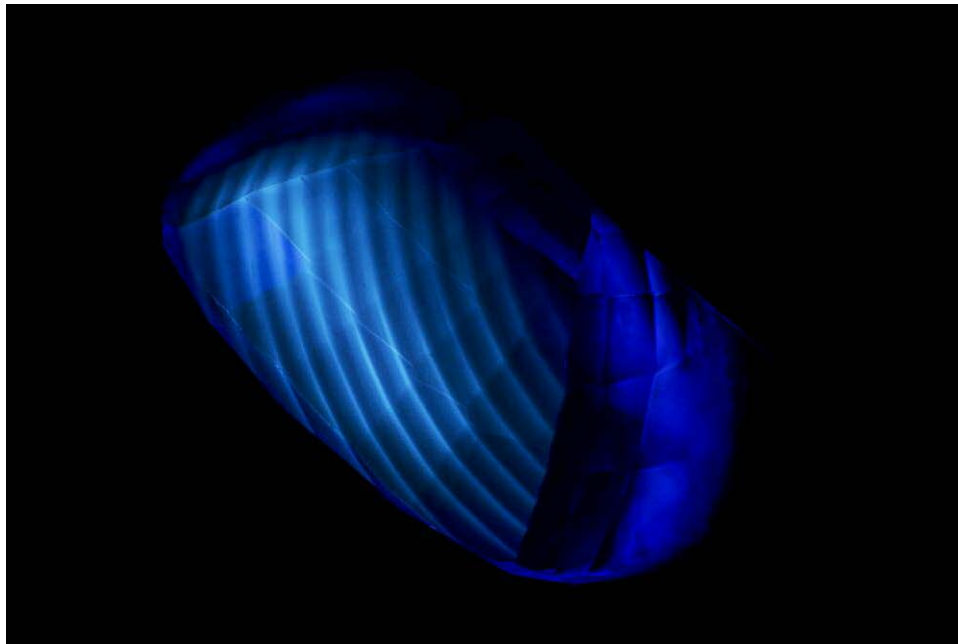
Figure 10. Curved banding is easily spotted in this flame-fusion blue synthetic sapphire when illuminated with the Magilabs deep-UV fluorescence system, a short-wave UV source. Photomicrograph by E. Billie Hughes; field of view ~13 mm.

Recently the author noticed two excellent examples. When viewed with the Magilabs deep-UV fluorescence system (a proprietary short-wave UV source), the curved banding in the synthetics was clear (figures 10 and 11), allowing them to be easily separated from natural corundum. Gemologists using a DiamondView may see the same reaction.

E. Billie Hughes
Lotus Gemology, Bangkok

Iridescent Tabasco Geode

Tabasco geodes are a small geode variety named for the area where they are mined in the Mexican state of Zacatecas, near the city of Tabasco. Typically, these geodes are lined with water-clear drusy quartz, but the author recently examined one that was filled with greenish blue botryoidal chalcedony that also showed iridescent colors (figure 12). The cause of the colors was not immediately
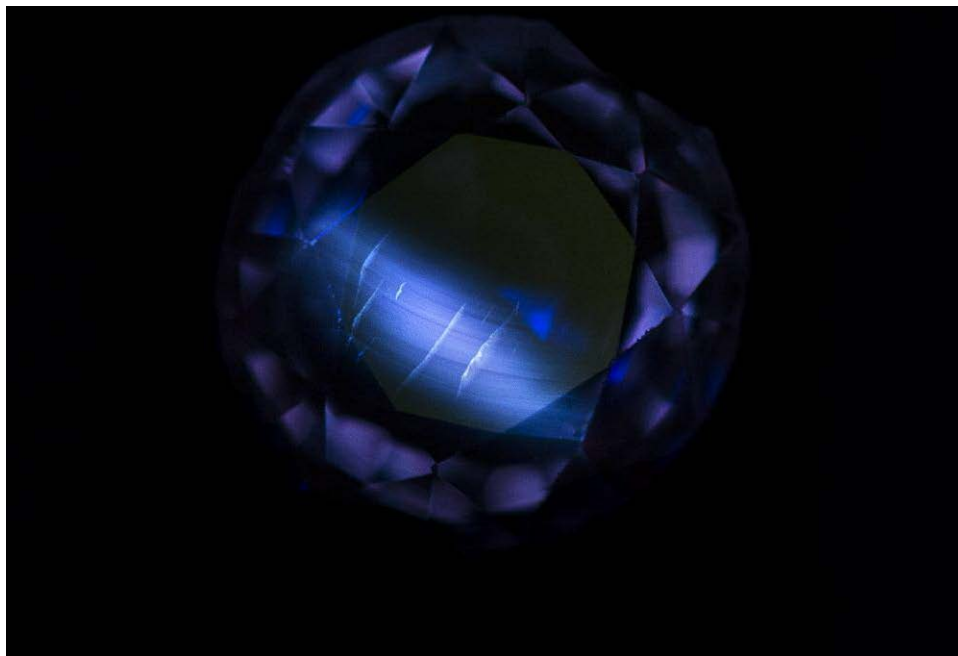

Figure 11. Observed with a short-wave UV light source, the sample displays curved banding, a telltale sign of a flame-fusion synthetic sapphire. Photomicrograph by E. Billie Hughes; field of view ~24.5 mm.

Figure 12. This unique Tabasco geode from Mexico's Zacatecas State, containing greenish blue botryoidal chalcedony, measures 24 mm in the longest dimension. Photo by Diego Sanchez; courtesy of Marquez Mining.

apparent, but microscopic examination revealed clues. The outermost layer of chalcedony had not firmly adhered to the underlying botryoidal mass. This delamination allowed an air gap along the interface of the thin outermost layer of chalcedony and the botryoidal mass of greenish blue chalcedony underneath. This air gap, in addition to the transparent nature of the very thin chalcedony shell, created thin-film interference colors along the interface of the chalcedony shell and substrate (figure 13). This explanation was supported by the observation that where areas of the delicate shell were damaged, the

iridescence was not present. This Tabasco geode is one of the most visually interesting geodes examined by the author.

Nathan Renfro

Inclusion-Rich Black Topaz from the Thomas Mountains, Utah

Topaz is an important gemstone that occurs in various colors. The authors had the opportunity to examine some unusual black topaz crystals and crystal fragments whose

Figure 13. The Tabasco geode hosts greenish blue chalcedony, with a thin chalcedony shell that was responsible for the iridescent thin-film interference colors. Photomicrograph by Nathan Renfro; field of view 1.83 mm.
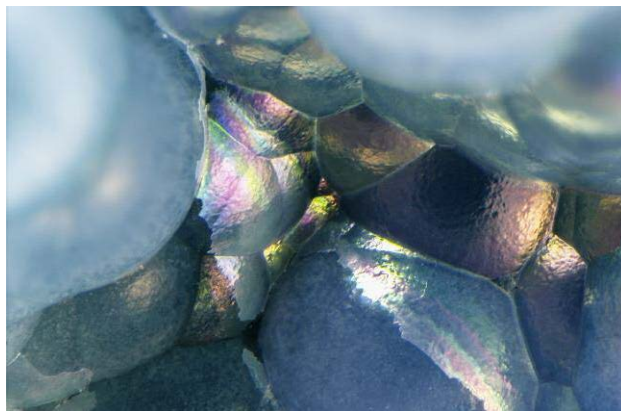
Figure 14. The black appearance of a topaz was due to these small dark mineral inclusions. Photomicrograph by Jonathan Muyal; field of view 1.44 mm.
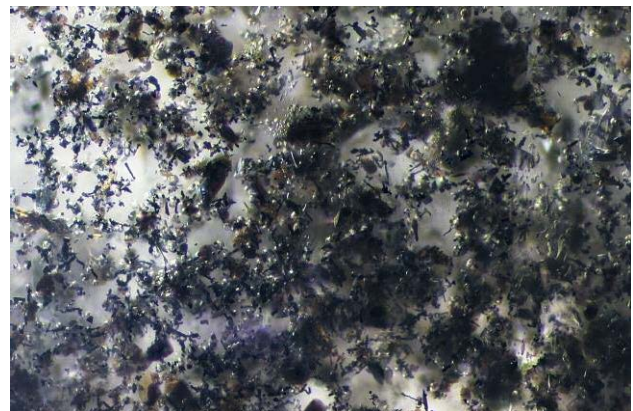
Figure 15. A black topaz crystal specimen from the Thomas Mountains in Utah (24.8 × 17.92 × 12.29 mm). Photo by Kevin Schumacher.

appearance was the result of numerous small dark mineral inclusions (figures 14 and 15). The topaz originated from an undisclosed locality in the Thomas Mountains in Juab County, Utah. They were provided by Shaun Rasmussen and Krisann Morrill (SK Star Claims, Provo, Utah), who discovered the occurrence. Careful microscopic examina-

Figure 16. Top: Inclusions seen in this photomicrograph include black magnetite, colorless fluorite, and brown annite/phlogopite. Bottom: Clusters of tabular wolframoixiolite crystals along with fluorite and mica inclusions. Photomicrographs by Jonathan Muyal; fields of view 0.288 mm (top) and 0.36 mm (bottom).

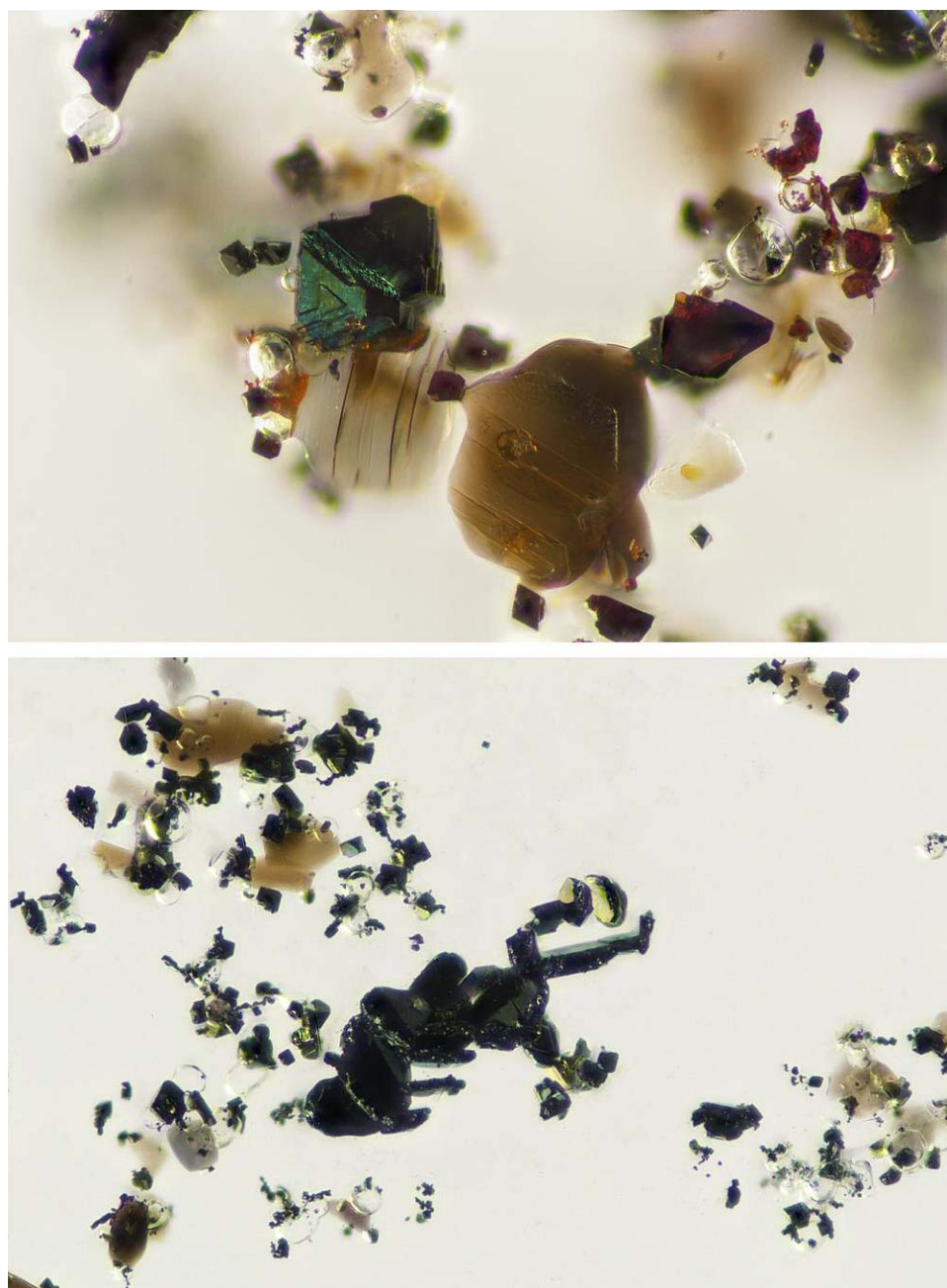tion revealed the presence of several inclusion minerals (figure 16, top). Among these were thin, translucent brownish plates of annite/phlogopite mica; transparent colorless, spherical crystals of fluorite; and opaque black octahedral crystals of magnetite. These minerals, which are well-known inclusions in topaz, were confirmed by Raman microspectrometry.

The most abundant inclusions—and apparently the principal cause of the black appearance—were numerous opaque flattened or stubby crystals of wolframoixiolite (figure 16, bottom), a rare complex oxide mineral with the ideal formula $(Nb,W,Ta,Fe,Mn,Nb)_2O_4$ (N. Ray, "Mineralogy and geochemistry of unusual localized W-Nb included black topaz from the Thomas Mountain Range, UT," unpublished and undated manuscript, provided by SK Star Claims to the authors). Quantitative chemical analysis by LA-ICP-MS revealed a composition of 1.66 wt.% CaO, 2.28 wt.% TiO_2, 5.52 wt.% MnO, 19.93 wt.% Fe_2O_3, 1.94 wt.% ZrO_2, 24.66 wt.% Nb_2O_5, 1.17 wt.% MoO_3, 1.17 wt.% Ta_2O_5, 40.15 wt.% WO_3, and 1.53 wt.% other elements. This gave a calculated chemical formula of $(Ca_{0.074}, Ti_{0.071}, Mn_{0.193}, Fe^{3+}_{0.620}, Zr_{0.039}, Nb_{0.461}, Mo_{0.020}, Ta_{0.013}, W_{0.430}, others_{0.026})_{1.948}O_4$,

Figure 17. Measuring 25.28 × 17.51 × 7.67 mm and weighing 15.65 ct, this colorless quartz crystal from Namibia hosts numerous transparent blue-green inclusions of dioptase. Photo by Diego Sanchez.

which is consistent with the chemistry of this uncommon mineral.

The presence of both magnetite and wolframoixiolite inclusions in the topaz resulted in a slight magnetic behavior. The corroded and sometimes altered appearance of both dark inclusion phases suggests that they represent protogenetic inclusions that formed during an earlier stage of mineral crystallization in the growth environment and were subsequently incorporated within the topaz. In spite of their abundance, these different inclusion minerals did not create any optical phenomena.

We thank those who provided these samples, which represent the first black-appearing topaz we have examined.

Jonathan Muyal, Ziyin Sun, and James Shigley
GIA, Carlsbad

Figure 18. Trigonal blue-green crystals in and on the surface of this colorless quartz were identified by Raman analysis as dioptase. Photomicrograph by Nathan Renfro; field of view 11.75 mm.

Quarterly Crystal: Dioptase in and on Quartz

Crystals of transparent colorless rock crystal quartz play host to a wide variety of mineral inclusions, some of which are highly attractive. Due to its transparency and bright blue-green color, one of the most visually striking inclusions occasionally found in quartz is dioptase. Occurring in the oxidized zones of some copper deposits, dioptase gets its vibrant color from copper, the chemical formula of dioptase being $Cu_6Si_6O_{18} \cdot 6H_2O$.

Recently we had the opportunity to examine an unusual arrowhead-shaped, fully terminated colorless quartz crystal that was decorated on one side with a crust of numerous trigonal transparent dioptase crystals that were both in and on their host. The geographic source for the crystal shown in figure 17 is Kaokoveld, Namibia. Weighing 15.65 ct and measuring 25.28 × 17.51 × 7.67 mm, this unusual example of rock crystal plays host to numerous near-surface trigonal crystals (figure 18) up to 3.0 mm in length.

The visual characteristics of the features—the trigonal micromorphology, degree of transparency, and color of the numerous inclusions—suggested dioptase; this was confirmed using laser Raman microspectrometry. The euhedral dioptase inclusions were situated on only one side of the quartz, which illustrates that they developed through directional deposition late in the quartz growth cycle.

John I. Koivula and Nathan Renfro
GIA, Carlsbad

Kimberlites: Earth's Diamond Delivery System

Diamonds are the most amazing of gems. Just as amazing, however, is how natural diamonds reach Earth's surface. Diamonds are formed 150 to 700 km deep in Earth, and are then carried upward in a rare volcanic eruption of a kimberlite magma. Man has never witnessed such an event, and the eruption of this magma is thought to be the most rapid and violent type of volcanic eruption on Earth. Luckily, since diamond is the hardest mineral, it can usually survive such rough handling. This delivery system in the form of volcanic transport only adds to the mystique and value of natural diamond.

There are two main magma types that carry natural diamonds to the surface. These magmas crystallize on cooling into volcanic rocks known as kimberlite and lamproite (see box A). Kimberlite is by far the dominant type of eruption to bring diamonds to Earth's surface (figure 1). Although diamond is only an accidental passenger and not actually created by the kimberlite, a basic understanding of kimberlites helps us understand the setting for most natural diamond formation in the mantle.

The Relationship Between Kimberlite and Diamond

Prior to the discovery of kimberlites, diamonds were all mined from secondary alluvial sources: river environments where diamonds had been eroded from their primary source. Historical diamonds from India were predominately recovered along the Krishna River in Madhya Pradesh. Today, secondary diamond mining still occurs in many areas of Sierra Leone, Brazil, Angola, Namibia, and even along the seafloor where rivers drain into the oceans.

The common occurrence of shale pieces in the first discovered kimberlite confused early geologists (see box B). Shale was a piece of the surrounding rock that had been picked up by the kimberlite as it traveled through the crust before eruption. Since shale is often very carbon rich, some geologists reasoned that diamonds might have formed by reaction between the magma and the shale (Lewis, 1887b). At the time, some 30 years before the discovery of radioactivity, there was no way to accurately determine the absolute age of a diamond (see Spring 2019 Diamonds from the Deep), the kimberlite, or the shale.

It took experiments and geochemical analysis to show that diamonds do not form as a result of kimberlite reaction with shale. But it would take more than 100 years after the discovery of kimberlite to prove that diamonds do not crystallize out of the kimberlite magma.

The first step in our knowledge about the relationship between diamonds and kimberlites comes from early work on how diamond crystallizes. Experiments in the laboratory showed that the transformation of graphite to diamond occurred at high pressure and temperature deep within the mantle, although we now know most diamond forms by other reactions (see Winter 2018 Diamonds from the Deep). Subsequently, geoscientists obtained pressure and temperature constraints for diamond formation (from diamond host rocks and their mineral inclusions), bolstering the high-pressure origin for natural diamonds (e.g., Bundy et al., 1961; Mitchell and Crocket, 1971). Evidence of their high-pressure origin meant that diamonds clearly had to have formed before any interaction between kimberlite and crustal rocks such as shale (again, see box B). However, it was still thought that diamonds could crystallize from the kimberlite magma at depth in the mantle before the eruption to Earth's surface took place, or that diamonds grew under metastable conditions during kimberlite ascent (Mitchell and Crocket, 1971).

In the 1970s, scientists used isotopic dating of kimberlitic minerals to determine the first ages of kimberlite eruptions. Using Rb-Sr geochronology of kimberlitic micas, geoscientists at the University of the Witwatersrand determined that kimberlites from the Kimberley area erupted about 86 million years ago (Allsopp and Barrett, 1975). Around the same time, U-Pb geochronology on kimberlitic zircons of these same kimberlites showed similar results, that they erupted around 90 million years ago (Davis et al., 1976). Later analytical work refined these ages (e.g., Allsopp and Kramers, 1977; Davis, 1977, 1978; Clement et al., 1979; Kramers and Smith, 1983; Smith, 1983). We now know that the majority of Earth's kimberlites erupted relatively recently (geologically speaking) between 250 and 50 million years ago (see compilations in Heaman et al., 2003; Jelsma et al., 2009; Tappe et al., 2018).

In the 1980s, Stephen H. Richardson and colleagues at MIT, working on diamonds from the Kimberley mines, found that the diamonds range in age from a billion years to more than three billion years old and that they originated in the lithospheric mantle region below the Kaapvaal craton (Richardson et al., 1984). Since the Kimberley kimberlites

Figure 1. Open-pit diamond mines in kimberlite rock. Mining operations remove as much kimberlite as possible and leave deep pits that outline the shape of a "kimberlite pipe." A: The Cullinan mine started as an open-pit operation and transitioned to underground mining in 1946. Photo by DeAgostini/Getty Images. B: Active mining in one of the kimberlite pipes at the Letšeng mine. Photo by Karen Smit/GIA. C: The Kimberley mine "Big Hole," where mining was completed in 1914. Photo by The Print Collector/Getty Images. D: The bottom of the open pit in the Diavik mine. Photo by Ben Nelms/Bloomberg via Getty Images. E: The "Big Hole" of the Kimberley mine today. Photo by Karen Smit/GIA.

erupted only 84 million years ago (Clement et al., 1979), the Richardson et al. study showed definitively that the diamonds had no genetic relationship to the kimberlite. This basic age relationship holds for all other diamondiferous kimberlites. Kimberlite eruptions, then, are just the way that diamonds make their way from depth in the mantle to Earth's surface. Diamonds are simply the passenger, and kimberlites are their transport.

Why Do Diamonds Survive in Kimberlite During Eruption?

Another wonderful feature of the way kimberlites transport diamonds from great depth is that the diamonds manage to survive. Rough diamonds are often resorbed from their primary octahedral shapes into secondary shapes called dodecahedrons. This is because kimberlites are in the process of dissolving the diamond—it's just that this process has not gone to completion. Nearly all other magmas on Earth, such as basalts and andesites, would completely dissolve diamond, so it is a gift of nature that kimberlites allow diamonds to survive.

Successful diamond transport and delivery also occurs because kimberlites erupt faster and are less oxidizing than other magmas on Earth. Diamonds may also be shielded in pieces of their host rocks during much of their transport. Speed is of the essence here: A low-viscosity kimberlite is estimated to travel at speeds around 8 to 40 miles per hour

(Sparks et al., 2006), whereas a normal-viscosity basaltic magma moves at a fraction of this pace. Chemical composition of the kimberlite and its volatile components are also thought to be important factors.

Kimberlite Eruptions in Earth's History

From field observations made at the site of emplaced kimberlites, kimberlites are more explosive than the eruptions we see today in places like Hawaii, Iceland, Indonesia, and Mount St. Helens. Evidence for crystal granulation, xenolith rounding, and fragmentation (see box A, figure A-1) leads geologists to conclude that kimberlite eruptions are much more violent and breach the surface with the highest velocities of any volcano.

The last known kimberlite eruptions were the circa 10,000-year-old Igwisi Hills kimberlites (Brown et al., 2012) in Tanzania, although there is some debate about whether these constitute true kimberlite. Furthermore, these kimberlites are not diamond-bearing. The next youngest African kimberlites are the 32-million-year-old Kundelungu kimberlites in the Democratic Republic of Congo (Batumike et al., 2008). The most recent *diamond-bearing* kimberlite-like eruptions were the West Kimberley lamproites (box A), which erupted 24 to 19 million years ago (Allsopp et al., 1985). Around 45% of these lamproites are diamond-bearing, although only two have been mined for their diamonds.

Rocks, like minerals, have their own names given by the international community of geologists when they are recognized for what they are. In the case of rocks, these names are based on chemical composition, texture (figure A-1), color, mineral content, and the way they form. Once a rock name such as *kimberlite* has been defined and accepted, that becomes shorthand for all its features—including those that are observable by the field geologist in outcrop and those that relate to its actual origin deep within Earth by plate tectonic processes. Rock names are useful because they embody all these important ideas.

Kimberlite is the name given to a silica-poor and magnesium-rich extrusive igneous rock (e.g., a volcanic rock) that contains major amounts of olivine, often serpentinized. It is a highly variable mixture of melt, minerals crystallizing from the melt, and foreign crystals and rock pieces. Kimberlite may occur in the field as dikes or pipes that crystallize near but below the surface (*hypabyssal* kimberlite) or as magmas that erupt volcanically (*volcaniclastic* kimberlite).

Lamproite is the rock name given to a crystallized extrusive igneous rock that is rich in potassium and magnesium and missing the common crustal mineral feldspar. While lamproites are much more common than kimberlites, those that carry diamonds are much rarer than kimberlites. In fact, we only know of around four or five diamondiferous lamproites on Earth.
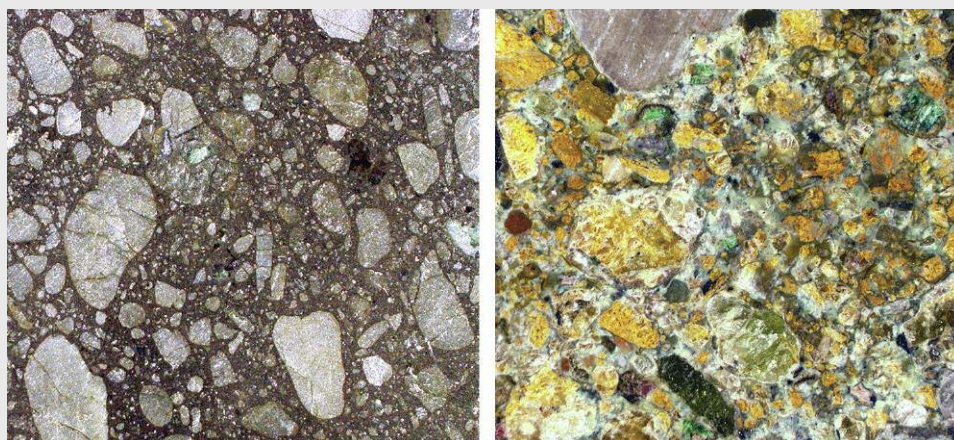

Figure A-1. Images of kimberlite textures. Left: Hypabyssal kimberlite from the Grizzly 3 kimberlite, Canada (field of view 7.62 cm). Right: Volcaniclastic kimberlite from the Victor North kimberlite, Canada (field of view 7.62 cm). Photos by Steve Shirey.

Kimberlites have been erupting since at least the Archean, and the oldest ones discovered so far are the Mitzic kimberlites in Gabon (West Africa), which erupted around 2.8 billion years ago (de Wit et al., 2016). However, kimberlites have not been continuously erupting since that time, and globally there have been several time periods when kimberlites erupted more frequently (Heaman et al., 2003; Jelsma et al., 2009):

Time period (millions of years ago)	1200–1075	600–500	400–350	250–50
% of global kimberlites	9.4%	7.4%	5%	62.5%

(from Tappe et al., 2018)

How and Why Do Kimberlites Form?

Melt Composition. The primary (or original) melt composition of kimberlite is poorly known because the rock we see today is such a variable, complicated physical mixture. Kimberlite contains magma that has been mixed with many components picked up along the >150 km path to the surface. At the surface, kimberlite contains fine-grained matrix material and minerals known as phenocrysts, foreign minerals known as xenocrysts (diamond being the xenocryst that we want!), and foreign rocks known as xenoliths. In other words, kimberlite is considered a "hybrid" rock. Xenoliths themselves are very interesting to geologists because they are samples of the rock through which the kimberlite has passed.

The predominant mineral in kimberlite is olivine, which could be either phenocrystic (from the kimberlite itself) or xenocrystic (from the mantle and broken off and sampled by the eruption). Making the distinction between these two populations of olivine is not always clear. Olivine is easily altered to a mineral called serpentine, and this alteration also makes estimation of the original magma composition difficult.

There are many different ways to try to determine the primary melt composition: conducting experiments at high pressures and temperatures, looking at melt inclusions found in kimberlite minerals, and performing mass balance calculations where the xenocryst and alteration material are subtracted to arrive at the remaining kimberlite material. All these different approaches now seem to suggest that kimberlite magmas form as melts that are rich in carbonate in the asthenospheric mantle (Stone and

Figure B-1. Image of the haphazard mining operations at the Kimberley "Big Hole" before the consolidation of mining operations by Cecil Rhodes and Barney Barnato, and the founding of the De Beers Consolidated Mines in 1888. Each miner owned a small claim of land and sent diggings to the surface by winch and rope. They worked at different rates and left a highly irregular and dangerous surface. See also figure 1C.

Between 1866 and 1869, the first South African diamonds were discovered along the Vaal and Orange River beds (known as "alluvial" diamonds). This was followed by the first discoveries of diamonds in their primary source rock at Jagersfontein, Koffiefontein, and the Kimberley area in 1870. Figure B-1 shows early mining operations at Kimberley.

Ernest Cohen first recognized this new source rock as igneous (Janse, 1985), and Henry Lewis (1887a) proposed to call the rock "kimberlite." It was named after the town of Kimberley, which in turn was named after Lord Kimberley, the British Secretary of State (Field et al., 2008, and references therein). The observations of Lewis (1887b), extracted below, provide an interesting glimpse into the dawning understanding of the geologic conditions of diamond occurrences more than 130 years ago:

In 1870, at which time some ten thousand persons had gathered along the banks of the Vaal, the news came of the discovery of diamonds at a point some fifteen miles away from the river, where the town of Kimberley now stands. These were the so-called "dry diggings," at first thought to be alluvial deposits, but now proved to be volcanic pipes of a highly interesting character. Four of these pipes or necks, all rich in diamonds, and of similar geo-

logical structure, were found close together. They have been proved to go down vertically to an unknown depth, penetrating the surrounding strata. The diamond-bearing material at first excavated was a crumbling yellowish earth, which at a depth of about 50 feet became harder and darker, finally acquiring a slaty blue or dark green colour and a greasy feel, resembling certain varieties of serpentine. This is the well-known "blue ground" of the diamond miners.

It is exposed to the sun for a short time, when it readily disintegrates, and is then washed for its diamonds. This "blue ground" has now been penetrated to a depth of 600 feet, and is found to become harder and more rock-like as the depth increases.

The diamond-bearing portions often contain so many inclusions of shale as to resemble a breccia, and thus the lava passes by degrees into tuff or volcanic ash, which is also rich in diamonds, and is more readily decomposable than the denser lava.

It seems evident that the diamond-bearing pipes are true volcanic necks, composed of a very basic lava associated with a volcanic breccia and with tuff, and that the diamonds are secondary minerals produced by the reaction of this lava, with heat and pressure, on the carbonaceous shales in contact with and enveloped by it.

Luth, 2016; Bussweiler et al., 2016; Stamm and Schmidt, 2017; Soltys et al., 2018; Howarth and Buttner, 2019). Kimberlite magma forms after low amounts of melting of peridotite (see Winter 2018 Diamonds from the Deep for more information on peridotite), at depths around 200–300 km, and contains high amounts of carbon dioxide and water. The presence of these so-called volatile compo-

nents in the kimberlite magma is one reason why kimberlite eruptions are thought to be particularly explosive.

Why Did Melting Start? We know now roughly where in Earth kimberlite magmas originated, but why did melting actually start? The "triggers" for deep Earth melting that precede kimberlite eruption are not the same for all kim-
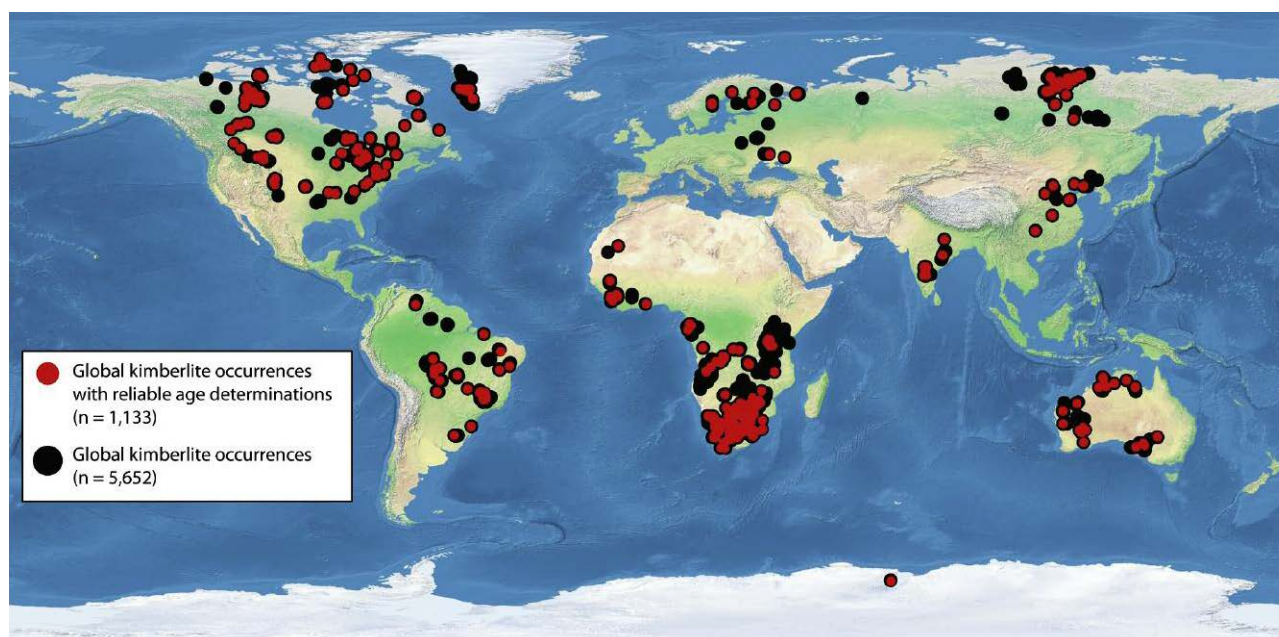
Figure 2. Map showing the known occurrences of kimberlites worldwide and their restriction to the oldest parts of the world's continents. From Tappe et al. (2018), used with permission.

berlites, and there are three main large-scale geologic scenarios that geologists typically consider:

1. mantle plumes rising up from the deep in the mantle and interacting with the cratonic lithosphere
2. subduction of oceanic crust and associated collisional processes during supercontinent formation
3. tectonothermal events associated with supercontinent breakup (e.g., Heaman and Kjarsgaard, 2000; Heaman et al., 2004; Jelsma et al., 2009; Kjarsgaard et al., 2017)

In particular, rifting of continents and supercontinent breakup—with associated fracturing and brittle deformation in the lithosphere—provide the pathways for kimberlite magmas to reach the surface (e.g., Jelsma et al., 2009). But underlying all these processes of magma generation and the resulting kimberlite eruption is the relationship to the process of plate tectonics. Without plate tectonics to recycle carbonate and volatiles into the mantle, there would be no kimberlites.

Where Do Kimberlites Occur?

Kimberlites do not erupt in all areas of Earth. Globally, kimberlites all occur below the oldest parts of continents, known as *cratons* (figure 2) (Clifford, 1966; Shirey and Shigley, 2013). Cratons have thick lithospheric roots that extend down to at least 150–200 km, and kimberlite generation in the mantle is probably associated with the physical barrier to mantle upwelling provided by these deep continental roots. Regardless of how kimberlites form, the association of these eruptions with deep continental roots is another of the wonderful mysteries about how kimber-

lites deliver diamonds. These deep continental roots are Earth's diamond storehouse.

Ongoing Research

There is still much to learn about kimberlites and the relationship between kimberlite magmas and the diamonds that they carry: Why exactly does diamond survive in a kimberlite eruption? What surface features on a diamond are related to the effects of the kimberlite magma versus those that might be caused by fluids deep within the mantle where the diamonds reside (e.g., Fedortchouk, 2019)?

While each kimberlite is unique, general eruption and emplacement models (see box C) are needed to help understand why many kimberlites are devoid of diamonds—is this simply because they did not erupt through diamond-bearing mantle? Or is the lack of diamonds somehow related to dissolution and/or eruption mechanisms? Information such as this is important during exploration and evaluation of new diamond occurrences.

Ultimately there are reasons to care about kimberlites that do not directly relate to their sampling of diamonds but rather to the large-scale view of the solid Earth's deepest geochemical cycles. Kimberlite magma is an extreme end member for small amounts of mantle melting and high volatile (including water and carbon dioxide) content. How do such melts form and migrate at such high pressures and temperatures? What does the high percentage of young kimberlites reveal about plate tectonics and deep recycling of volatiles? What can kimberlites tell us about the connection between the dynamics of the solid Earth and our major atmospheric greenhouse gas, carbon dioxide?

BOX C: KIMBERLITE ERUPTION

Kimberlites all have feeder "magmatic plumbing" systems at depth that can be composed of a cylindrical (pipe), a planar vertical (dike), and/or a planar horizontal (sill) shape at depth. It is only close to the surface that the high volatile content of the magma causes an eruptive "blowout" that results in a volcanic crater; this is the *magmatic model* (Sparks et al., 2006). Another eruption model is the *phreatomagmatic model* (Lorenz et al., 2003), which proposes that it is the reaction of magma with surface water that drives the eruption, rather than the gases and volatiles in the magma. The phreatomagmatic model was proposed for the Argyle lamproite eruption (Rayner et al., 2018) and some eruptive phases at Fort à la Corne (Kjarsgaard et al., 2009). Both the magmatic and phreatomagmatic eruptive phases are shown in figure C-1.
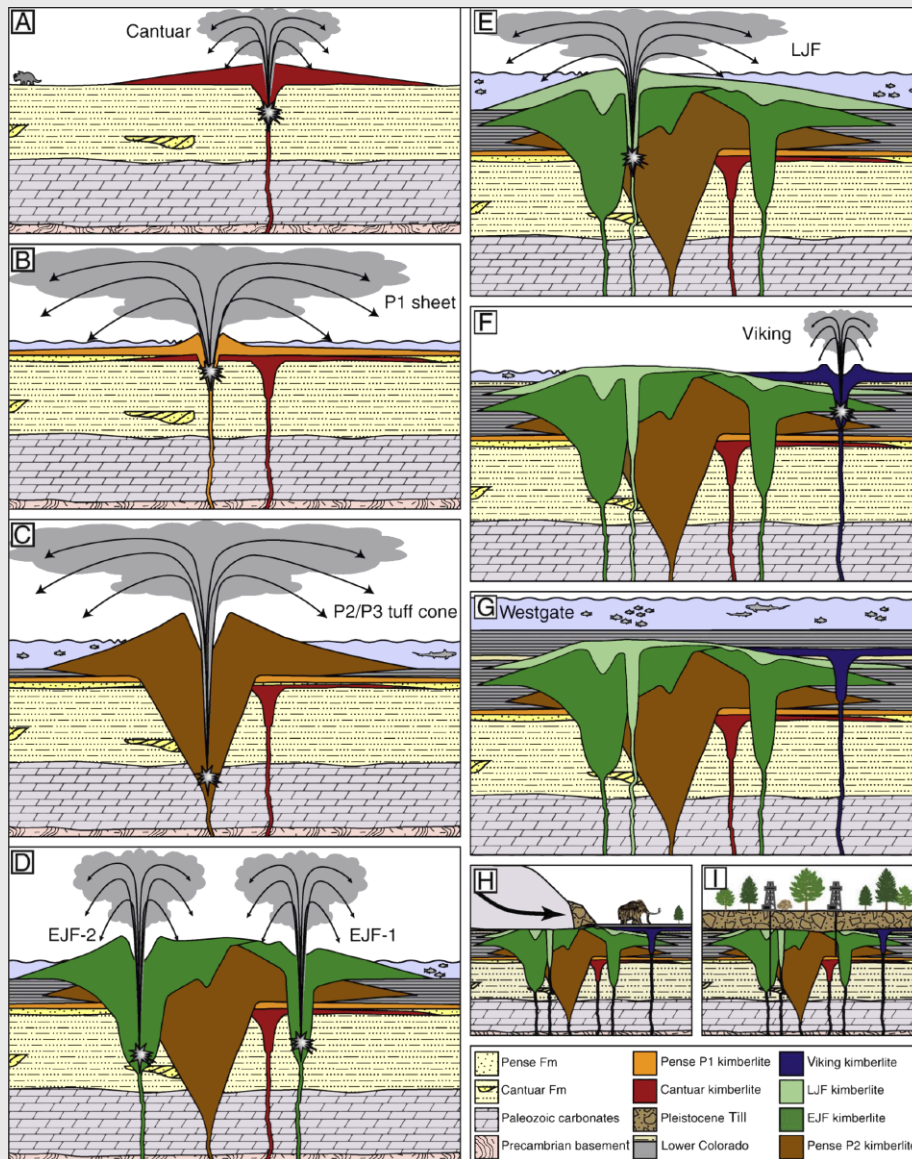

Figure C-1. Many kimberlite complexes globally developed through multiple stages of eruption that could have taken place over millions of years. Here is one example from the Orion South kimberlite in Saskatchewan, Canada, where several eruption events occurred between 106 and 95 million years ago (Heaman et al., 2004; Kjarsgaard et al., 2009, 2017). They even had varying eruption styles: both magmatic and phreatomagmatic. Solid colors in the key are for different kimberlite eruption phases (LJF, EJF, Viking, etc.), while textured colors are for non-kimberlite geological units that the kimberlite erupted through (Precambrian basement, Pense formation, etc.). From Kjarsgaard et al. (2009), used with permission.

We have highlighted the basic geological, historical, and practical features of kimberlites. What's exceptional is that in the end, when a natural diamond is purchased, we have a kimberlite to thank for bringing it to us.

REFERENCES

Allsopp H., Kramers J. (1977) Rb-Sr and U-Pb age determinations on southern African kimberlite pipes. *International Kimberlite Conference: Extended Abstracts*, Vol. 2, pp. 8–10, http://dx.doi.org/10.29173/ikc924

Allsopp H.L., Bristow J.W., Skinner E.M.W., Scott-Smith B.H., Danchin R.V. (1985) Rb-Sr geochronology of some Miocene West Australian lamproites. *Transactions of the Geological Society of South Africa*, Vol. 88, No. 2, pp. 341–345.

Batumike J.M., et al. (2008) LAM-ICPMS U–Pb dating of kimberlitic perovskite: Eocene–Oligocene kimberlites from the Kundelungu Plateau, D.R. Congo. *Earth and Planetary Science Letters*, Vol. 267, pp. 609–619, http://dx.doi.org/10.1016/j.epsl.2007.12.013

Brown R.J., et al. (2012) Eruption of kimberlite magmas: Physical volcanology, geomorphology and age of the youngest kimberlitic volcanoes known on Earth (the Upper Pleistocene/Holocene Igwisi Hills volcanoes, Tanzania). *Bulletin of Volcanology*, Vol. 74, No. 7, pp. 1621–1643, http://dx.doi.org/10.1007/s00445-012-0619-8

Bundy F.P., Bovenkerk H.P., Strong H.M., Wentorf R.H. (1961) Diamond-graphite equilibrium line from growth and graphitization of diamond. *The Journal of Chemical Physics*, Vol. 35, No. 2, pp. 383, http://dx.doi.org/10.1063/1.1731938

Bussweiler Y., et al. (2016) The evolution of calcite-bearing kimberlites by melt-rock reaction: Evidence from polymineralic inclusions within clinopyroxene and garnet megacrysts from Lac de Gras kimberlites, Canada. *Contributions to Mineralogy and Petrology*, Vol. 171, No. 7, p. 65, http://dx.doi.org/10.1007/s00410-016-1275-3

Clement C.R., et al. (1979) Precambrian ultramafic dykes with kimberlite affinities in the Kimberley area. In H.O.A. Meyer and F.R. Boyd, Eds., *Kimberlites, Diatremes, and Diamonds: Their Geology, Petrology, and Geochemistry*. Proceedings of the Second International Kimberlite Conference, Vol. 1, pp. 101–110. American Geophys. Union, Washington DC, http://dx.doi.org/10.1029/SP015p0101

Clifford T.N. (1966) Tectono-metallogenic units and metallogenic provinces of Africa. *Earth and Planetary Science Letters*, Vol. 1, pp. 421–434, http://dx.doi.org/doi.org/10.1016/0012-821x(66)90039-2

Davis G.L. (1977) The ages and uranium contents of zircons from kimberlites and associated rocks. *Carnegie Institution of Washington Yearbook 1976*, pp. 631–635.

Davis G.L. (1978) USGS Open File Report 78-701, pp. 81–93.

Fedortchouk Y. (2019) A new approach to understanding diamond surface features based on a review of experimental and natural diamond studies. *Earth-Science Reviews*, Vol. 193, pp. 45–65, http://dx.doi.org/10.1016/j.earscirev.2019.02.013

Field M., Stiefenhofer J., Robey J., Kurszlaukis S. (2008) Kimberlite-hosted diamond deposits of southern Africa: A review. *Ore Geology Reviews*, Vol. 34, No. 1–2, pp. 33–75, http://dx.doi.org/10.1016/j.oregeorev.2007.11.002

Heaman L.M., Kjarsgaard B.A. (2000) Timing of eastern North American kimberlite magmatism: Continental extension of the Great Meteor hotspot track? *Earth and Planetary Science Letters*, Vol. 178, pp. 253–268, http://dx.doi.org/10.1016/S0012-821X(00)00079-0

Heaman L.M., Kjarsgaard B.A., Creaser R.A. (2003) The timing of kimberlite magmatism in North America: Implications for global kimberlite genesis and diamond exploration. *Lithos*, Vol. 71, pp. 153–184, http://dx.doi.org/10.1016/j.lithos.2003.07.005

Heaman L.M., Kjarsgaard B.A., Creaser R.A. (2004) The temporal evolution of North American kimberlites. *Lithos*, Vol. 76, No. 1–4, pp. 377–397, http://dx.doi.org/10.1016/j.lithos.2004.03.047

Howarth G.H., Buttner S.H. (2019) New constraints on archetypal South African kimberlite petrogenesis from quenched glass-rich melt inclusions in olivine megacrysts. *Gondwana Research*, Vol. 68, pp. 116–126, http://dx.doi.org/10.1016/j.gr.2018.11.009

Janse A.J.A. (1985) Kimberlites—where and when. In J.E. Glover and P.G. Harris, Eds., *Kimberlite, Occurrence and Origin: A Basis for Conceptual Models*. University of Western Australia Press, pp. 19–61.

Jelsma H., Barnett W., Richards S., Lister G. (2009) Tectonic setting of kimberlites. *Lithos*, Vol. 112, pp. 155–165, http://dx.doi.org/10.1016/j.lithos.2009.06.030

Kjarsgaard B.A., Harvey S., McClintock M., Zonneveld J.P., Du Plessis P., McNeil D., Heaman L. (2009) Geology of the Orion South kimberlite, Fort à la Corne, Canada. *Lithos*, Vol. 112, pp. 600–617, http://dx.doi.org/10.1016/j.lithos.2009.05.039

Kjarsgaard B.A., Heaman L.M., Sarkar C., Pearson D.G. (2017) The North America mid-Cretaceous kimberlite corridor: Wet, edge-driven decompression melting on an OIB-type deep mantle source. *Geochemistry, Geophysics, Geosystems*, Vol. 18, No. 7, pp. 2727–2747, http://dx.doi.org/10.1002/2016GC006761

Kramers J.D., Smith C.B. (1983) A feasibility study of U–Pb and Pb-Pb dating of kimberlites using groundmass mineral fractions and whole-rock samples. *Chemical Geology*, Vol. 41, pp. 23–38, http://dx.doi.org/10.1016/S0009-2541(83)80003-5

Lewis H.C. (1887a) The matrix of diamond. *Fifty-Seventh Meeting of the British Association for the Advancement of Science*, Manchester, https://archive.org/stream/reportofbritisha88brit/reportofbritisha88brit_djvu.txt

Lewis H.C. (1887b) On a diamantiferous peridotite and the genesis of the diamond. *Geological Magazine*, Vol. 4, No. 1, pp. 22–24, http://dx.doi.org/10.1017/S0016756800188399

Lorenz V. (2003) Maar-diatreme volcanoes, their formation, and their setting in hard-rock or soft-rock environments. *GeoLines*, Vol. 15, pp. 72–83.

Mitchell R.H., Crocket J.H. (1971) Diamond genesis – A synthesis of opposing views. *Mineralium Deposita*, Vol. 6, No. 4, pp. 392–403, http://dx.doi.org/10.1007/BF00201895

Rayner M.J., et al. (2018) The geology of the Argyle (AK1) diamond deposit, Western Australia. *Society of Economic Geologists - Special Publication*, No. 20, pp. 89–117.

Richardson S.H., Gurney J.J., Erlank A.J., Harris J.W. (1984) Origin of diamonds in old enriched mantle. *Nature*, Vol. 310, pp. 198–202, http://dx.doi.org/10.1038/310198a0

Shirey S.B., Shigley J.E. (2013) Recent advances in understanding the geology of diamonds. *G&G*, Vol. 49, No. 4, pp. 188–222, http://dx.doi.org/10.5741/GEMS.49.4.188

Smith C.B. (1983) Pb, Sr and Nd isotopic evidence for sources of southern African Cretaceous kimberlites. *Nature*, Vol. 304, No. 5921, pp. 5–54, http://dx.doi.org/10.1038/304051a0

Soltys A., Giuliani A., Phillips D. (2018) A new approach to reconstructing the composition and evolution of kimberlite melts: A case study of the archetypal Bultfontein kimberlite (Kimberley, South Africa). *Lithos*, Vols. 304–307, pp. 1–15, http://dx.doi.org/10.1016/j.lithos.2018.01.027

Sparks R.S.J., et al. (2006) Dynamical constraints on kimberlite volcanism. *Journal of Volcanology and Geothermal Research*, Vol. 155, pp. 18–48, http://dx.doi.org/10.1016/j.jvolgeores.2006.02.010

Stamm N., Schmidt M.W. (2017) Asthenospheric kimberlites: Volatile contents and bulk compositions at 7 GPa. *Earth and Planetary Science Letters*, Vol. 474, pp. 309–321, http://dx.doi.org/10.1016/j.epsl.2017.06.037

Stone R.S., Luth R.W. (2016) Orthopyroxene survival in deep carbonatite melts: Implications for kimberlites. *Contributions to Mineralogy and Petrology*, Vol. 171, p. 63, http://dx.doi.org/10.1007/s00410-016-1276-2

Tappe S., Smart K.A., Torsvik T., Massuyeau M., de Wit M. (2018) Geodynamics of kimberlites on a cooling Earth: Clues to plate tectonic evolution and deep volatile cycles. *Earth and Planetary Science Letters*, Vol. 484, 1–14, http://dx.doi.org/10.1016/j.epsl.2017.12.013

de Wit M., et al. (2016) Overview of diamond resources in Africa. *Episodes*, Vol. 39, No. 2, pp. 199–237, http://dx.doi.org/10.18814/epiiugs/2016/v39i2/95776
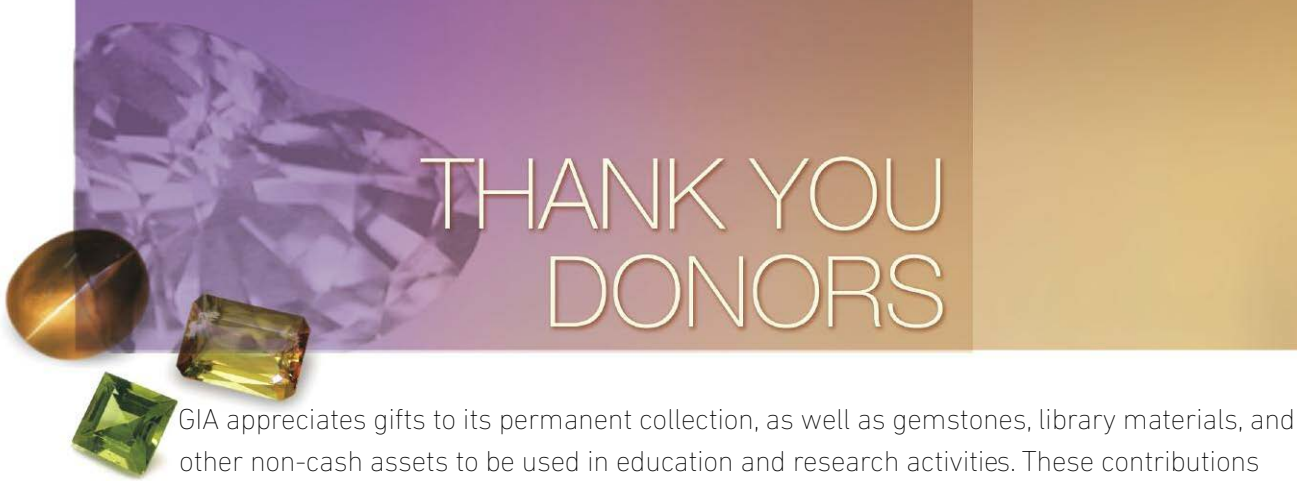
THANK YOU DONORS

GIA appreciates gifts to its permanent collection, as well as gemstones, library materials, and other non-cash assets to be used in education and research activities. These contributions help GIA further its public service mission while offering donors philanthropic benefits. We extend sincere thanks to all 2018 contributors.

CIRCLE OF HONOR*

$100,000 and higher
Dr. J.K. Agrawal
Dr. Suman Agrawal
Robert and Marlene Anderson
K.C. Bell
Thomas Cacek
In Memory of Nicholas Scott Golden

Hauser Family In Memory of Joel and Barbara Hauser
Dr. James Y. Hung
Kazanjian Beverly Hills
Bill Larson
Thomas M. Schneider
Dr. Geoffrey A. Smith

2018 DONORS

$100,000 to $149,999
In Memory of Nicholas Scott Golden

$50,000 to $99,999
Dr. J.K. Agrawal
Dr. Suman Agrawal

$10,000 to $49,999
Thomas M. Schneider

$2,500 to $4,999
David M. Baker
Dr. James Y. Hung
Maximilian Art Foundation
Michal & Company
Stephen and Betty Lou Neely
Mark Prus
Ken and Elaine Roberts
Dr. Clark Scovel

Under $500
Cos Altobelli
Garland Jewelers
Gianmaria Buccellati Foundation
Larry D. and Carol A. Greenfield
In Memory of William "Bill" Junkin
K. Brunini Jewels
Renee Newman
In Honor of Paspaley
Pearl Paradise
Shaun Rassmussen
Woolley and Wallis Auctioneers

Gem News International

Contributing Editors

Emmanuel Fritsch, *University of Nantes, CNRS, Team 6502, Institut des Matériaux Jean Rouxel (IMN), Nantes, France* (fritsch@cnrs-imn.fr)

Gagan Choudhary, *Gem Testing Laboratory, Jaipur, India* (gagan@gjepcindia.com)

Christopher M. Breeding, *GIA, Carlsbad* (christopher.breeding@gia.edu)

COLORED STONES AND ORGANIC MATERIALS

Plume agate from Iran. Iran has long had a reputation as a source of quality agate, principally derived from extensive volcanic deposits throughout the country. Archaeological research on ancient tombs and finds in early human settlement sites there show that agate, chalcedony, and jasper were used not only for arrowheads and other stony instruments but also for ornamental beads and pendants.

Today, Iranian agates are primarily traded in the city of Mashhad, the largest holy city of Iran and the capital of the northwest province of Khorasan. Several varieties can be found in the market, but plume agates are the most colorful and most sought after. The samples of Iranian agate examined by the authors contained numerous plume structures in a variety of colors including green, yellow, red, white, and orange (figure 1). These plume structures are characterized by elongate billowy inclusions that can resemble clouds of smoke or feathers. The material with predominantly green, white, and orange inclusions is sold as "Bahary" (spring) agate (figure 2). The material that is principally green, yellow, and red is sold as "Paaeasy" (autumn) agate (figure 3).

The samples examined were acquired in Iran by author MMS from Dr. Hamid Mir-Blukey, who has a private mining claim in the Ferdows agate field in the southern region of Khorasan (figure 4). Mining there is done mainly with primitive hand tools at or near the surface, where veins of agate are exposed as they weather out of their volcanic host rock.

Figure 1. Iranian plume agate (22.45–82.03 ct) from the Ferdows agate field comes in two main varieties. The material on the left with white, green, and orange inclusions is known as "spring agate." The stones on the right with red, yellow, and green inclusions are called "autumn agate." Photo by Diego Sanchez.

While most material from this region is locally traded, the area could become an important global source for plume agate.

Maryam Mastery Salimi and Nathan Renfro
GIA, Carlsbad

Ornamental jadeites from the Levoketchpel deposit in the Polar Urals of Russia. Although most jadeites on the mar-
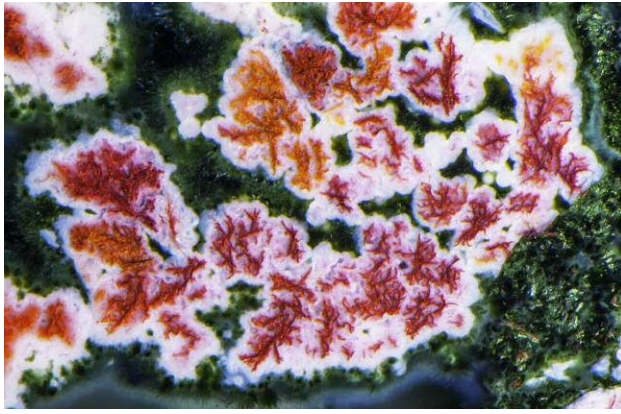
Figure 2. Iranian "spring agate" showcases inclusions that are typically green, white, and orange. Photomicrograph by Nathan Renfro; field of view 3.78 mm.
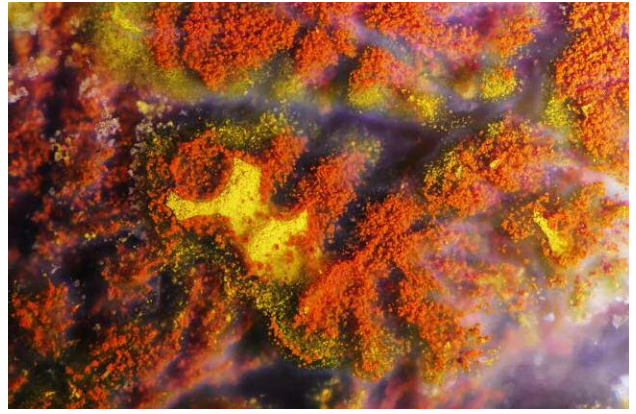

Figure 3. A display of orangy red, green, and yellow inclusions seen in "autumn agate" from Iran. Photomicrograph by Nathan Renfro; field of view 6.00 mm.

ket are from Myanmar, other sources include Guatemala, Japan, Kazakhstan, and Russia. Russian jadeites have been studied using geological and petrological approaches (e.g., A.M. Fishman, *Gems in the North Ural and Timan*, Geoprint, Syktyvkar, 2006, pp. 1–88; F. Meng et al., "Jadeitite in the Syum-Keu ultramafic complex from Polar Urals, Russia: insights into fluid activity in subduction zones," *European Journal of Mineralogy*, Vol. 28, No. 6, 2016, pp. 1079–1097), but their gemological characteristics are still unclear. To date, several jadeite deposits have been found within some ultramafic complexes at the Polar Urals (Fish-

man, 2006). In August 2013, the authors visited a closed jadeite mine at the Levoketchpel deposit in the Voykar-Syninsky ultramafic complex of the Polar Urals to collect samples (figure 5). Here we describe the gemological and trace element chemistry of these jadeites.

The jadeites were found as dikes within serpentinized peridotite (figure 6A). The Levoketchpel deposit was reportedly discovered in 1959 (V.F. Morkovkina, "Jadeites in the hyperbasites of the Polar Urals," *Izvestiya Akademii Nauk SSSR* (Seriya Geologicheskaya), 1960, Vol. 4, pp. 103–108). Mining at this area was done on a small scale, and the quality was low. In the outcrop, the jadeite dike is surrounded by phlogopite-rich rock (figure 6B) and peridotite. The Levoketchpel jadeites are translucent to opaque, and whitish to pale green and vivid green with a mottled color distribution. The samples showed a mosaic to fibrous aggregate

Figure 4. An agate sample collected at the Aysak area in the Ferdows agate field in the southern region of Iran's Khorasan Province. Photo by Hamid Mir-Blukey.

Figure 5. Five of the 10 jadeite samples from the Levoketchpel deposit (back row) and four jadeites reportedly from the Polar Urals (front row). Photo by Shunsuke Nagai.
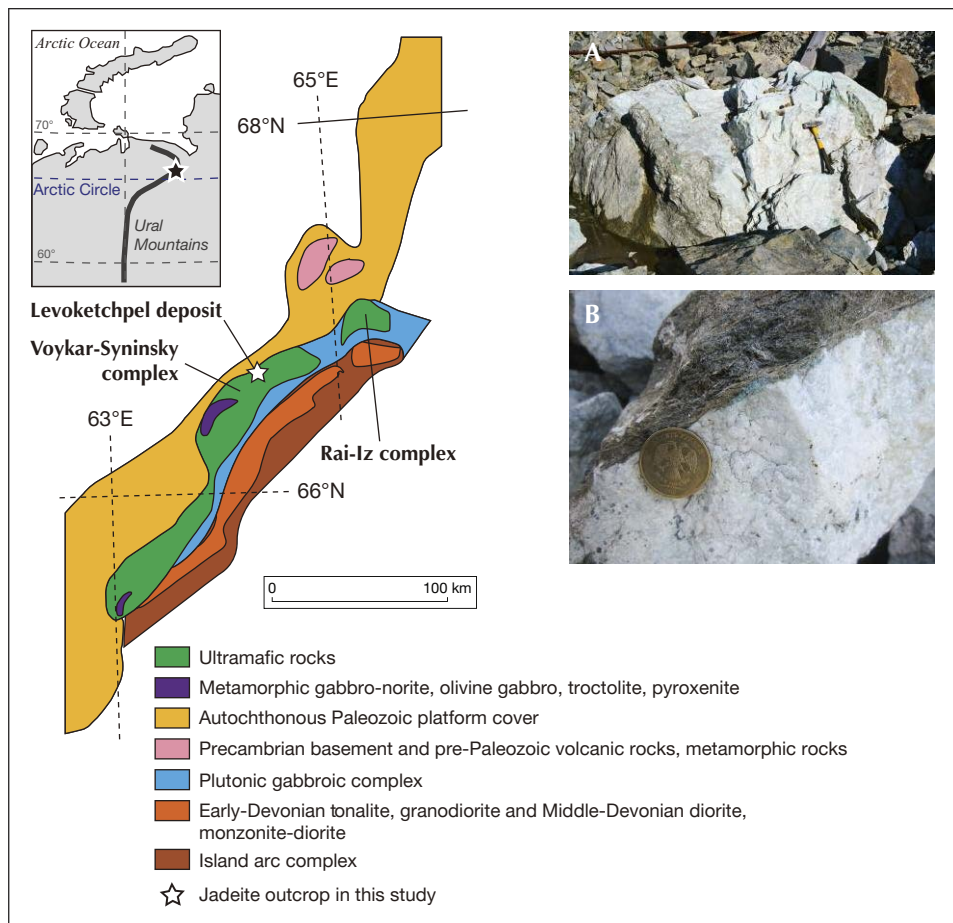
Figure 6. Left: A geological map of the Voykar-Syninsky ultramafic complex in the Polar Urals. Modified from Meng et al. (2011). A: A whitish jadeite dike within serpentinized peridotite at the Levoketchpel area. The hammer is 40 cm long. Photo by Dimitri Kuznetsov. B: A jadeite boulder with surrounding phlogopite-rich rock. Photo by Makoto Miura.

structure. We collected 10 samples from the jadeite dike (five of these are shown in figure 5) and rubbles produced during mining. For the gemological observation, advanced testing, and quantitative laser ablation–inductively coupled plasma–mass spectrometry (LA-ICP-MS) analysis of trace elements, we prepared wafers and thin sections (figure 7). Standard gemological testing revealed RI values of 1.66 to 1.67 and hydrostatic SG values of 3.2 to 3.4. In a handheld spectroscope, the whitish and pale green zones in the samples showed fine chrome lines at 630, 655, and 691 nm, and the diagnostic 437 nm line. These results strongly suggested that the samples were all jadeite.

EDXRF testing also indicated that the samples were composed mainly of jadeites. The pale green jadeites were characterized by a low CaO/Na_2O ratio of 0.20 to 0.26, and a relatively high Al_2O_3/Fe_2O_3 ratio of 11.03 to 20.14. The vivid green parts tended to be slightly rich in Ca (CaO/Na_2O ratio, 0.32 to 0.34), and the compositional ranges are suited for jadeite (Al_2O_3/Fe_2O_3 ratio of 10.73 to 20.14). Vivid green zones were slightly higher in Cr_2O_3, 0.06 to 0.16 wt.%, than the whitish and pale green samples (Cr_2O_3 up to 0.01 wt.%).

Careful observation and Raman spectroscopic analysis suggested that the samples were mainly composed of fine jadeite grains with minor amounts of omphacite, natrolite,

feldspar, phlogopite, zircon, and chromite. Natrolite was found as the interstitial phase between jadeite grains. Jadeite crystals surrounding chromite crystals tended to be rich in green color. This green color concentration around chromite crystals is probably due to chromium diffusion from chromite during the jadeite's formation. The coexist-

Figure 7. Two jadeite samples from the Levoketchpel deposit, measuring 3.4 cm and 1.8 cm wide. Photo by Shunsuke Nagai.
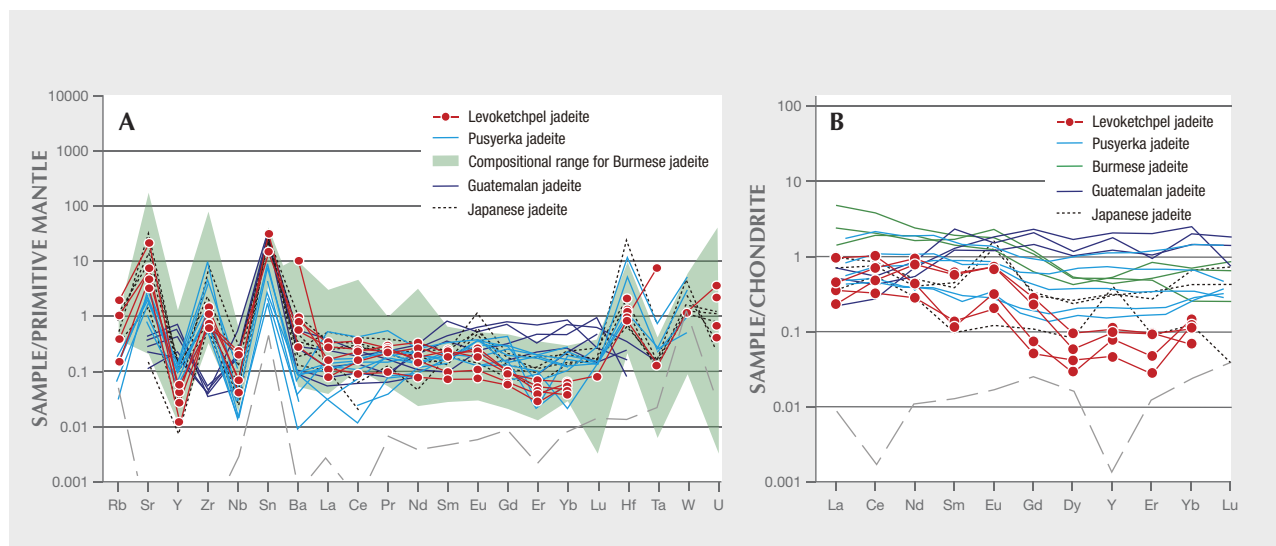
Figure 8. Trace element characteristics of the Levoketchpel jadeites. (A) Primitive mantle–normalized trace element patterns for green jadeites. (B) Chondrite-normalized rare earth element (REE) patterns for green jadeites. The detection limit is shown by the gray dashed line. Samples in this study are shown in red and compared with jadeites from the Pusyerka deposit at the Syum-Keu complex, the Polar Urals (Meng et al., 2016), Myanmar, Guatemala, and Japan (Abduriyim et al., 2017; Abduriyim et al., unpublished data). Primitive mantle and chondrite values for normalizing are from Sun and McDonough (1989).

ing mineral assemblage observed is consistent with previous petrological studies (e.g., G.E. Harlow and S.S. Sorensen, "Jade (nephrite and jadeite) and serpentinite: metasomatic connections," *International Geological Review*, Vol. 12, 2005, pp. 49–68). In UV-Vis spectra, vivid green regions of the jadeites from Levoketchpel show an Fe^{3+} band and strong chromium bands in the 550–700 nm range. Similar results were also reported from jadeites from the Polar Urals (A. Abduriyim et al., "Japanese jadeite: History, characteristics, and comparison with other sources," Spring 2017 *G&G*, pp. 48–67).

Trace element compositions (Rb, Sr, Y, Zr, Nb, Ba, and the rare earth elements Hf, Ta, W, and U) were analyzed by LA-ICP-MS for 10 samples (70 spots total). Four of the samples had both whitish to pale green and vivid green zones. Chemical analyses were conducted on five spots for each of these zones. The whitish to pale green jadeites were depleted in REEs, while the vivid green zones tended to be richer in REEs. We calculated the primitive mantle–normalized trace element patterns and the chondrite-normalized REE patterns (figure 8) of the vivid green Levoketchpel jadeites (W.F. McDonough and S.-S. Sun, "The composition of the earth," *Chemical Geology*, Vol. 120, 1995, pp. 223–253) and compared them to jadeites with similar color ranges from another jadeite locality in the Polar Urals (the Pusyerka deposit in the Syum-Keu ultramafic complex; Meng et al., 2016), Myanmar, Guatemala, and Japan (Abduriyim et al., 2017; Abduriyim et al., unpublished data). The primitive mantle–normalized trace element patterns of the Lavoketchpel jadeites reveal strong positive anomalies of Sr, Zr, and Nb (figure 8A).

Such enrichment of the large-ion lithophile elements (LILE) and the high field strength elements (HFSE) in jadeites have been reported previously in jadeites from other localities (e.g., G.E. Harlow et al., "Jadeites and plate tectonics," *Annual Review of Earth and Planetary Sciences*, Vol. 43, 2015, pp. 105–138). In these patterns, green jadeites from each locality show a very close overlap. In the chondrite-normalized patterns, the Levoketchpel jadeites show a right-downward slope: the light rare earth element (LREE) La, Ce, Nd, and Sm concentrations tended to be higher than the heavy rare earth element (HREE) Eu, Gd, Dy, Y, Er, Yb, and Lu contents (figure 8B). The Levoketchpel jadeites are depleted in HREE relative to the Pusyerka jadeites. Jadeites from Myanmar and Guatemala have higher total REE concentrations than the Polar Ural and Japanese jadeites (figure 8B). Burmese jadeite patterns show a gentle right-downward slope from La to Lu, and Guatemalan jadeites tend to be enriched in HREE. The Levoketchpel jadeites and some Japanese jadeites display a similar slope in REE concentration, although the former tend to be relatively depleted in HREE.

Makoto Miura
GIA, Tokyo

Shoji Arai
Kanazawa University, Kanazawa, Japan

Satoko Ishimaru
Kumamoto University, Kumamoto, Japan

Vladimir R. Shmelev
Ural Branch, Russian Academy of Sciences,
Ekaterinburg, Russia

*Figure 9. The natural freshwater pearls of various shapes and colors collected from the Mississippi River system, together with heelsplitter (*Potamilus alatus, *left), purple wartyback or purple pimpleback (*Cyclonaias tuberculate, *center), and bankclimber (*Plectomerus dombeyanus, *right) mussel shells. Photo by Diego Sanchez.*

Gemological and chemical characteristics of natural freshwater pearls from the Mississippi River system. The Carlsbad laboratory received 854 natural freshwater pearls from Kari Anderson (Kari Pearls, Muscatine, Iowa), who stated that they were collected from the Mississippi River system (figure 9). Although the time and location of recovery and the mollusk species were not recorded, we were informed that all were recovered as a byproduct of the shelling business in the past couple of years. The samples ranged from 0.013 to 3.59 ct and measured from 1.63 × 1.19 mm to 9.87 × 8.52 × 5.89 mm. The shapes varied from baroque (the majority) to near-round, button, and oval. Many of the baroque pearls exhibited the unique "wing" or "feather" form (Anderson mentioned that the divers refer to these as "spike"

pearls) typically associated with American natural freshwater pearls (J.L. Sweaney and J.R. Latendresse, "Freshwater pearls of North America," Fall 1984 *G&G*, pp. 125–140). The wing pearls are elongated, with a roughly triangular shape, and usually taper to more pointed ends. Most possessed an uneven rippled surface along their lengths. The surface texture and shape of the wing pearls are identical to the lateral "teeth" areas found on the mussel shells that host these organic gems (figure 10, left).

The pearl colors also varied widely in hue, tone, and saturation. The range of hues included very light pink, purplish pink, orangy pink, brownish orange, and brownish purple to brown. Many displayed a pronounced orient effect (iridescence or multiple colors on or below the surfaces),

Figure 10. Left: A mussel shell and pearl showing a strikingly similar appearance. The elongated wing pearl's shape resembles the shape of the lateral "teeth" on the shell. Right: Iridescent rainbow surface colors, or orient, creating a beautiful shimmering appearance; field of view 7.19 mm. Photos by Diego Sanchez (left) and Artitaya Homkrajae (right).
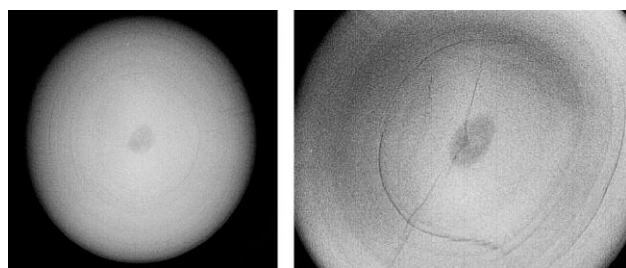
Figure 11. RTX images of a 0.27 ct oval pearl showing a growth ring with an ovoid feature in the center. Void structures may be encountered in natural and non-bead cultured (NBC) pearls, but this small void is unlike the twisted void-like structures typically observed in freshwater NBC pearls.

TABLE 1. LA-ICP-MS chemical composition values of pearls from the Mississippi River system. All values are shown in ppmw.

Element	Maximum	Minimum[a]	Average[b]	Detection limits
^{7}Li	20.9	bdl	0.045	0.024–1.08
^{11}B	16.9	bdl	0.20	0.092–0.51
^{23}Na	**2410**	**695**	**1790**	**0.57–1.86**
^{24}Mg	1940	11.7	54.4	0.006–0.68
^{31}P	389	25.0	206	0.65–0.91
^{39}K	71.2	bdl	4.95	0.25–1.00
^{43}Ca	427000	374000	406000	25.1–122
^{47}Ti	1.48	bdl	0.007	0.069–5.86
^{53}Cr	27.7	bdl	0.076	0.084–0.73
^{55}Mn	**4210**	**64.2**	**887**	**0.060–0.19**
^{57}Fe	504	248	334	0.54–2.21
^{59}Co	9.30	bdl	0.17	0.008–0.60
^{60}Ni	1.10	bdl	0.52	0.017–0.21
^{63}Cu	13.6	bdl	0.59	0.018–0.28
^{66}Zn	10.2	bdl	0.31	0.045–0.31
^{69}Ga	15.6	bdl	2.44	0.005–0.78
^{88}Sr	**737**	**105**	**308**	**0.011–0.049**
^{89}Y	0.027	bdl	0.001	0.001–0.003
^{95}Mo	0.80	bdl	0.017	0.002–0.11
^{137}Ba	**515**	**17.2**	**84.3**	**0.006–0.033**
^{139}La	0.022	bdl	0.0003	<0.005
^{208}Pb	0.12	bdl	0.0006	0.002–0.15

[a]bdl = below detection limits
[b]Data below detection limits is treated as zero when calculating average values.

creating a beautiful shimmering appearance (figure 10, right). Moreover, some exhibited high metallic-like surface reflections that resulted in excellent luster. Classifying the colors was often quite complex, as the overtone and orient were strong enough to affect the actual bodycolor and the combinations produced different colors when viewed from different angles. Experience has shown that in most cases a pearl's color is directly related to the mussel species and the color of the shell's interior, though water environment and the nutrients available during formation also play an important role. The heelsplitter (*Potamilus alatus*), purple wartyback or purple pimpleback (*Cyclonaias tuberculate*), and bankclimber (*Plectomerus dombeyanus*) mussel species shown in figure 9 possess pink and purple interior surfaces. All have been known to produce pearls with desirable color.

The lightly colored samples exhibited moderate to strong yellow or bluish yellow fluorescence when exposed to long-wave ultraviolet radiation (365 nm), while the darker samples exhibited the same colors with weaker intensities. X-ray fluorescence imaging was used to help check the growth environment. The majority of the samples fluoresced weak to strong greenish yellow due to manganese content, thus confirming their freshwater origin. As with the long-wave UV reactions, the darker samples displayed weaker reactions, and this fluorescence quenching is related to the concentration of coloring pigments present (H. Hänni et al., "X-ray luminescence, a valuable test in pearl identification," *Journal of Gemmology*, Vol. 29, No. 5/6, 2005, pp. 325–329). A few of the samples also exhibited a moderate to strong orangy reaction in some surface areas.

One hundred samples encompassing a broad range of colors, shapes, surface qualities, and sizes were selected in order to study their internal structures and trace element concentrations using real-time microradiography (RTX) and laser ablation–inductively coupled plasma–mass spectrometry (LA-ICP-MS), respectively. The baroque pearls showed growth structures that followed their shapes. The number and visibility of these structures varied from pearl to pearl. In certain orientations the growth structures resembled "linear features" in some wing pearls. Dark or-

ganic-rich and void centers were observed in some of the symmetrically shaped samples (i.e., button and oval). Although void structures could be considered characteristic of non-bead cultured (NBC) pearls, the voids in these samples appeared ovoid and relatively small (e.g., figure 11) and unlike the "twisted" void-like structures typically encountered within freshwater NBC pearls.

Chemical compositions were analyzed using the same parameters published in a recent study (A. Homkrajae et al., "Provenance discrimination of freshwater pearls by LA-ICP-MS and linear discriminant analysis (LDA)," Spring 2019 *G&G*, pp. 47–60). Three ablation spots were tested on each sample, and results for the 22 elements selected are shown in table 1. The majority contained high Mn content, as expected for freshwater pearls and corresponding with the X-ray fluorescence results seen from the majority. Only one sample showed Mn levels below 100 ppmw in two spots at 89.7 and 64.2 ppmw, which is unusual for this pearl type. Yet both spots matched positions for freshwater pearls in the ternary diagram of Ba, Mg, and Mn (see Homkrajae et al., 2019), indicating a likely freshwater origin. Chemical data for the analyzed spots, especially the four discriminator elements Na, Mn, Sr, and Ba (bolded in table 1), showed results comparable with those of the American natural (USA-NAT) pearls group previously re-
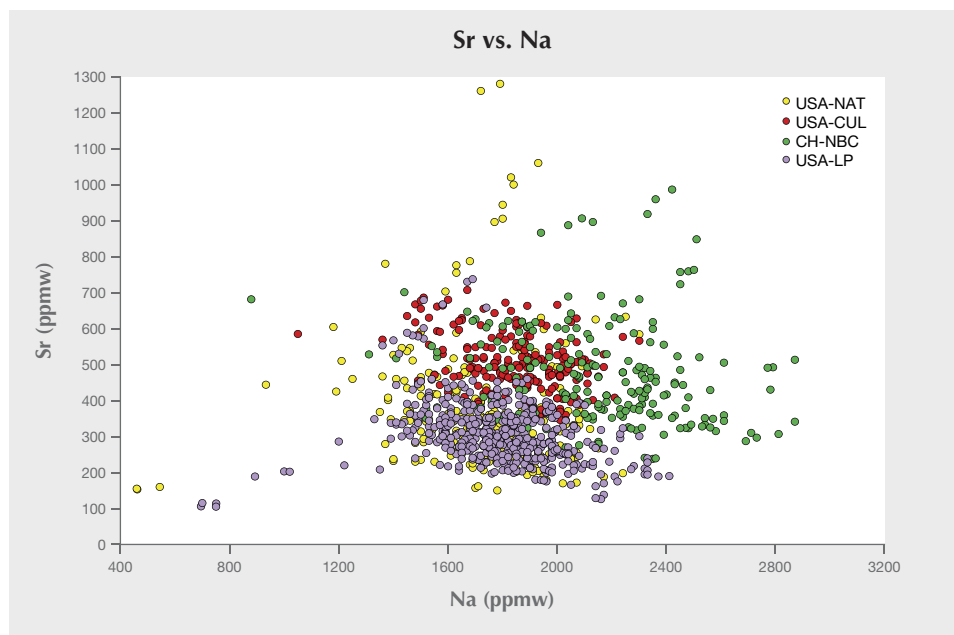
Figure 12. The majority of the analyzed spots (USA-LP) fell within the same region as those from American natural (USA-NAT) pearls in the chemical plotting of Sr and Na content reported in Homkrajae et al. (2019). Red spots represent results for American cultured (USA-CUL) pearls and green spots equate to Chinese NBC (CH-NBC) pearl samples.

ported. The majority of the analyzed spots fell within the same region as the USA-NAT group in the Sr and Na content plot (figure 12). Furthermore, the linear discriminant analysis (LDA) method developed during the previous study discriminated 70% of these samples as USA-NAT.

Pearls exhibiting six different colors—pink, purplish pink, orangy pink, pinkish purple, brownish orange, and orangy brown—were selected in order to study their spectroscopic characteristics. Apart from the brownish orange sample, each possessed orient. The analysis was conducted on the most homogeneously colored area of each

sample. Raman spectroscopic analysis with a 514 nm argon-ion laser revealed aragonite peaks at 701, 703, and 1085 cm^{-1} along with strong polyene peaks between the approximate ranges 1119–1126 and 1503–1508 cm^{-1}. UV-Vis reflectance spectra were recorded from 250 to 800 nm, and each spectrum revealed a clear absorption feature at about 280 nm, possibly associated with the protein conchiolin and usually observed in nacreous pearls (figure 13). The reflectance patterns of the pearls are associated with the bodycolors, and the reflectance levels decreased as the sample color became more saturated. The samples with a
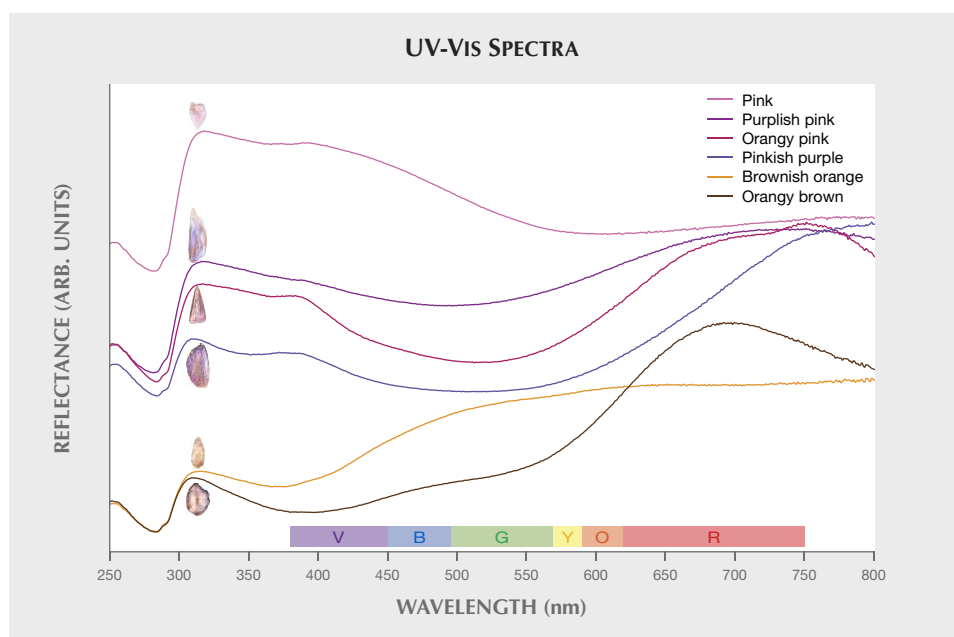
Figure 13. UV-Vis reflectance spectra of six representative pearls revealed a clear absorption feature at approximately 280 nm that is likely associated with the protein conchiolin. Each spectrum showed absorption features in the visible region related to the pearl's bodycolor. The samples with pink component revealed a similar absorption feature from blue to yellow range and centered around 506 nm. The intensity of the absorption increase is related to saturation of the colors. The spectra are vertically offset for clarity.

pink component showed reflection minima in the blue to yellow range corresponding to their bodycolors, with a reflection minimum centered around 506 nm. The results corresponded with previous findings on natural-color freshwater cultured pearls from *Hyriopsis* species (S. Karampelas et al., "Role of polyenes in the coloration of cultured freshwater pearls," *European Journal of Mineralogy*, Vol. 21, No. 1, 2009, pp. 85–97; A. Abduriyim, "Cultured pearls from Lake Kasumigaura: Production and gemological characteristics," Summer 2018 *G&G*, pp. 166–183). Surface observations and spectroscopic studies did not reveal any sign of color treatment, which indicates the pearls' natural color origin.

The Mississippi River and its tributaries are renowned for the diversity of native American mussels found in their waters. The extensive variety of species from the Unionidae family continues to produce a variety of colored natural pearls. This was a great opportunity to study and document the gemological and chemical characteristics of these unique freshwater natural pearls. The data collected enlarges GIA's pearl identification database and will provide useful reference material in the years to come.

Artitaya Homkrajae and Ziyin Sun
GIA, Carlsbad

Sally Chan Shih
GIA, New York

A special type of trapiche quartz. Recently, the National Gem and Gold-Silver Jewelry Testing Center at Zhengzhou examined a light yellow hexagonal piece of quartz (figure 14) weighing 22.18 g and measuring approximately 42.4 × 34.5 × 10.3 mm, which the buyer said was purchased from the Inner Mongolia autonomous region of northern China. Standard gemological testing gave a spot refractive index of 1.54 and a hydrostatic specific gravity of approximately 2.65. The sample was inert to both long-wave and short-wave UV.

Figure 14. This 22.18 g hexagonal quartz piece was unusual for its texture under transmitted light. Small crystals are seen on the side. Photo by Xiaodi Wang.
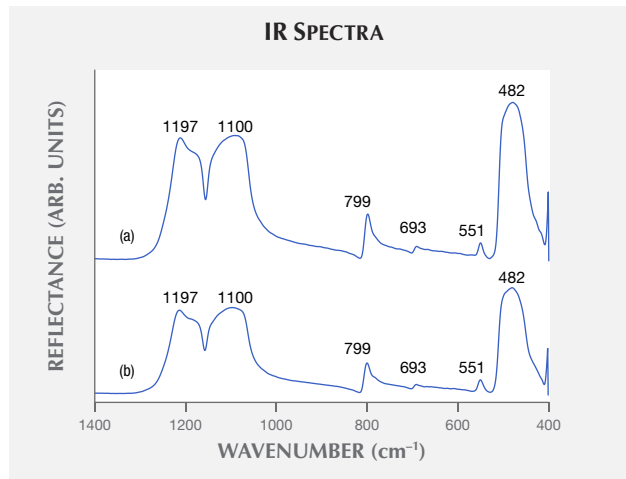
Figure 15. Major mineral composition at the star lines (a) and the area between the star lines (b) was quartz, with characteristic peaks at 1197, 1100, 799, 693, 551, and 482 cm^{-1}. The spectra are offset for clarity.

This special sample was made up of three incomplete trapiche quartz. All growth reached prism faces in both of the tabular crystals, as well as those faces on the secondary growth crystals. The sample exhibited the tabular prismatic habit characteristic of the species, but with six-spoke trapiche structure that was clearly visible in both reflected and transmitted light.

The infrared reflectance spectra (figure 15) of the translucent star lines and other areas both indicated quartz, with characteristic peaks at 1197, 1100, 799, 693, 551, and 482 cm^{-1}. Raman spectra of the star lines and other areas (e.g., figure 16) were obtained using 785 and 532 nm laser excitation, respectively. Peaks at about 466, 205, 353, and 396

Figure 16. The sample's Raman spectrum further confirmed quartz, with characteristic peaks at 466, 205, 353, and 396 cm^{-1}.
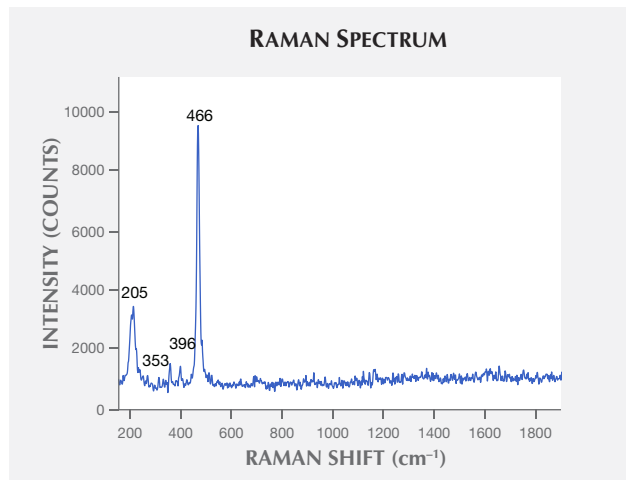
cm⁻¹ further confirmed quartz. This phenomenon may be caused by different growth rates and growth conditions. The origin of the special structure observed here is uncertain, but it is strong evidence of nature's ability to produce rarities.

Xiaodi Wang
Henan Institute of Product Quality
Inspection and Supervision
National Gem and Gold-Silver Jewelry Testing Center
at Zhengzhou
Henan, China

Yanjun Song
College of Gemstone and Material Technology, Hebei
GEO University
Shijiazhuang, China

Rubies from Rock Creek, Montana. North America has several productive colored stone deposits, from gem tourmaline in Maine and California, to emerald in North Carolina, to peridot, turquoise, and opal in the Western states. One gap in all of this gemological wealth is the virtual lack of any American ruby sources, with the exception of a minor deposit in North Carolina (G.F. Kunz, *Gems & Precious Stones of North America,* Dover Publishing, Mineola, New York, 1968, 367 pp.). This is surprising given the number of geographic locales in the American West named after the red variety of corundum (i.e., the Ruby Mountains of Nevada and the "Ruby Peaks" found in several states). In his epic tome *Yogo: The Great American Sapphire* (1987), Stephen M. Voynick provides an explanation for this apparent geographic contradiction. He proposes that early prospectors named these sites after stumbling upon garnets and mistaking them for rubies. Their vision also may have been clouded by dreams of wealth and hopes of striking a rich gem deposit. But what if there is some shred of truth to the old prospectors' tales?

This journal recently described a ruby submitted to GIA with gemological properties that clearly indicated a Montana origin (Winter 2019 Lab Notes, pp. 434–435). Additionally, Palke et al. (2018) noted the occurrence of rare rubies and violet sapphires from Yogo Gulch ("A common origin for Thai/Cambodian rubies and blue and violet sapphires from Yogo Gulch, Montana, USA?" *American Mineralogist*, Vol. 103, No. 3, 2018, pp. 469–479). Over the course of several years, Jeffrey R. Hapeman (Earth's Treasury, Westtown, Pennsylvania) has amassed a unique collection of true rubies from Potentate Mining's operation at Montana's Rock Creek deposit. According to Hapeman and Potentate's Warren Boyd, rubies were only recovered when the miners were asked to put aside anything that resembled a garnet so they could be examined more carefully. Presumably, many rubies had been discarded as garnets in years past. Regardless, rubies from this deposit are extremely rare. To date, only 29 rubies—just over 6 grams— have been found in more than 400 kilograms of mine production.

Nine faceted Montana rubies from 0.172 to 0.578 ct (figure 17) and seven rough rubies from 0.11 to 0.34 grams, supplied by Mr. Hapeman, were included in this study. Additionally, 10 pink, blue, and green sapphires from Hapeman and 15 from GIA's reference collection, gathered onsite at the Potentate mine, were used for comparison with the rubies. Standard gemological testing of several of the rubies with a handheld spectroscope yielded chromium spectra. The stones displayed weak to moderate red fluorescence

Figure 17. A suite of nine rubies from the Rock Creek sapphire deposit in Montana. The stones range in weight from 0.172 to 0.578 ct. Photo by Kevin Schumacher, courtesy of Jeffrey R. Hapeman, Earth's Treasury.

Figure 18. Inclusion scenes in Montana rubies. Left: A decrepitation halo surrounding an inclusion. Field of view 2.23 mm. Center: Angular bands composed of loosely to densely packed particles and short to long needles. Field of view 3.57 mm. Right: Oriented needles and platelets. Field of view 1.26 mm. Photomicrographs by Aaron Palke (left and right) and Tyler Smith (center).

in long-wave UV and no fluorescence under short-wave UV. Microscopic examination showed inclusion scenes resembling those of typical Montana sapphires, including crystalline or glassy melt inclusions surrounded by decrepitation halos (figure 18, left). Also common were angular particulate bands, often arranged in partial hexagonal patterns following the crystallographic orientation of the host corundum (figure 18, center). These bands are composed of loosely to densely spaced particles, short to long needles, and/or reflective platelets (figure 18, right). These features are consistent with material from the secondary Montana sapphire deposits at Rock Creek and the Missouri River. Similar inclusion scenes were also observed in the blue, green, pink, and purple sapphires from this study (figure 19).

The rubies were analyzed by laser ablation–inductively coupled plasma–mass spectrometry (LA-ICP-MS) to uncover their trace element patterns for comparison with the blue, green, pink, and purple sapphires from Montana also studied here. Generally, the rubies had trace element profiles of 13–38 ppma Mg, 16–81 ppma Ti, 1–27 ppma V, 408–2400 ppma Cr, 1106–2958 ppma Fe, and 11–20 ppma Ga with averages of 24 ppma Mg, 31

ppma Ti, 8 ppma V, 979 ppma Cr, 2123 ppma Fe, and 15 ppma Ga. Except for Cr, these values are consistent with the general ranges of pink/purple and blue/green Montana sapphires shown in the supplementary table 1 (available online at www.gia.edu/gems-gemology/summer-2019-gemnews-rubies-rock-creek-montana-icp-table1.pdf). This is seen more easily in a Cr vs. Ga plot, which exhibits a continuous and seamless transition in Cr values increasing from the blue/green sapphires through the pink/purple sapphires to the true red rubies (figure 20). Additionally, plots not involving Cr tend to show similarities in the trace element chemistry of all other elements between Montana rubies and pink/purple and blue/green Montana sapphires. Figure 21 shows this similarity; it also compares these data against sapphires from a select number of globally important sapphire deposits. Figure 21 suggests that, except for Cr, the trace element profiles of Montana rubies and sapphires are the same, especially in comparison to other global sources of gem corundum. The rubies and pink/purple sapphires have a slight tendency toward lower Mg values, although it is unclear if this is statistically valid or a result of the small sample size. The trace

Figure 19. Left: An inclusion with a partially healed decrepitation halo surrounded by angular particulate bands in a pink Montana sapphire. Right: A typical inclusion scene in a blue Montana sapphire composed of partial hexagonal particulate bands, loosely packed short to long needles, and reflective platelets. Photomicrographs by Aaron Palke; fields of view 2.34 mm (left) and 4.08 mm (right).
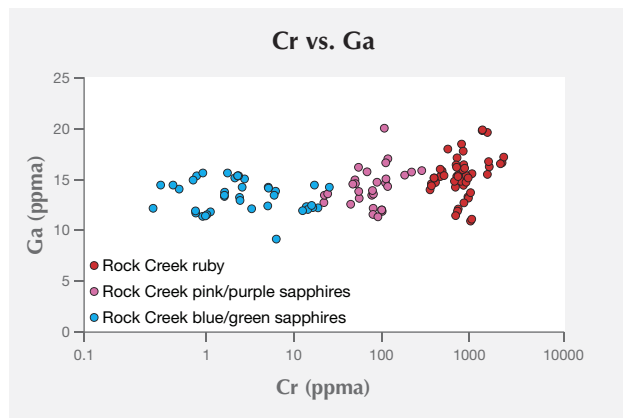
Figure 20. A Cr vs. Ga plot for blue/green sapphires, pink/purple sapphires, and rubies from the secondary Montana sapphire deposits (Rock Creek and Missouri River).

element Cr appears to operate independently of most of the other trace elements and can vary more than four orders of magnitude, which is unheard of for the other trace elements in Montana sapphires. While further research may elucidate these geochemical mysteries, these unusual stones are a testament to the unique corundum produced at Rock Creek.

Aaron C. Palke
GIA, Carlsbad

Jeffrey R. Hapeman
Earth's Treasury LLC
Westtown, Pennsylvania

SYNTHETICS AND SIMULANTS

Glass-filled *polki*-cut CVD synthetic diamonds. The term *polki* refers to a flat-cut diamond that is a simple and ancient form of today's "rose cut" and has been popular in traditional Indian *kundan-meena* jewelry. Since most commercial-quality polkis are fashioned from flat rough crystals (macles, for example) or chips derived from the cutting of larger crystals, they often contain cleavages or fissures opening on the surface, making them even more delicate. In the past decade, the trade has been flooded with polkis filled with high-RI glass to improve their clarity as well as durability, and these have been widely used in kundan-meena jewelry.

Recently, the Gem Testing Laboratory (GJEPC) in Jaipur received three light gray to brown polki-cut diamonds (figure 22) with square profiles for identification. They weighed 0.27–0.29 ct and measured 6.86–7.41 mm long and 0.36–0.41 mm thick. The client informed us that the polkis were natural but wanted to know if they were glass-filled. On initial examination under a microscope, glass filling in all three was evidenced by color flashes (figure 23), typically blue, violet, and pink, along with some crackling effects within the fissures and cleavage planes in two directions, intersecting each other at almost 90° (octahedral cleavage in diamond). The presence of glass (containing lead and bromine) was further confirmed by energy-dispersive X-ray fluorescence (EDXRF) analyses. These polkis also displayed a few dark brown grains, some of which were associated with stress cracks. No attempt was made to identify the nature of these grains.
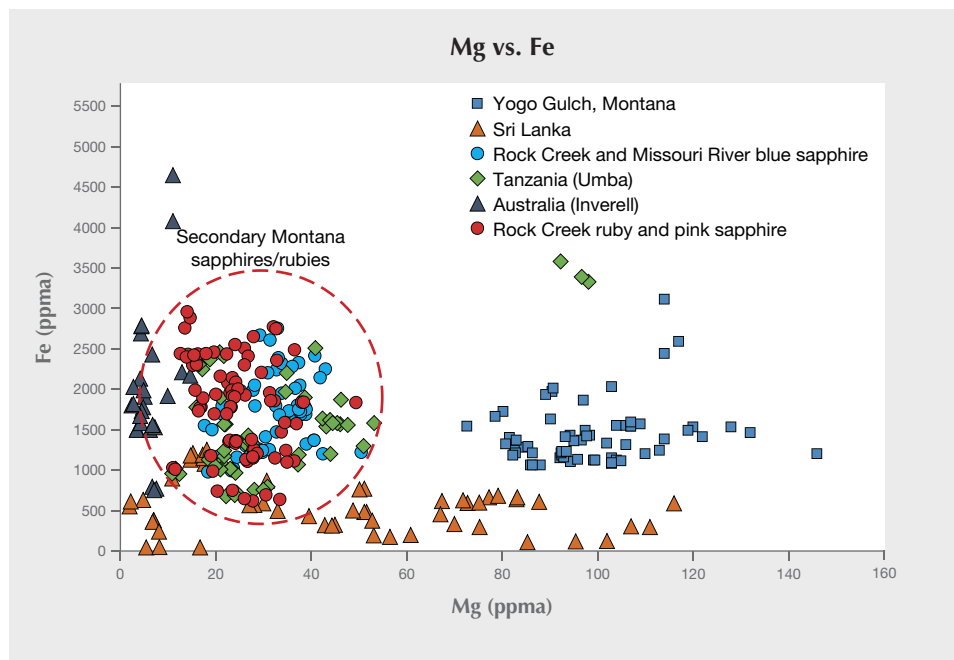
Figure 21. A Mg vs. Fe plot for sapphires and rubies compares material from Rock Creek and Missouri River with a small sampling of data from other important sapphire localities.

Figure 22. These "polkis" exhibiting a square profile, (0.27–0.29 ct) were identified as glass-filled CVD synthetic diamonds. Photo by Gagan Choudhary.
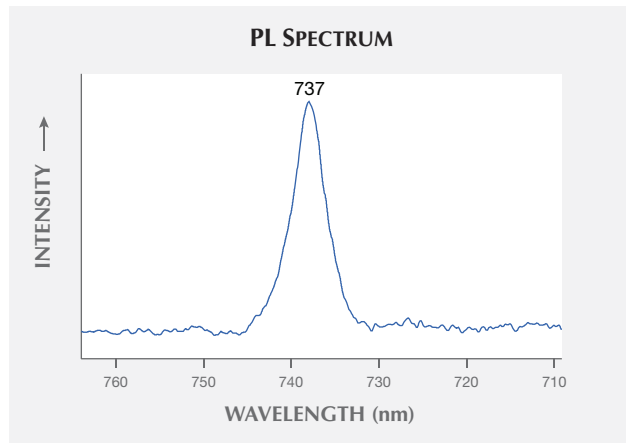

Figure 24. The room-temperature photoluminescence spectrum of each polki sample, with 532 nm laser excitation, revealed a strong silicon-vacancy related feature at ~737 nm.

Considering our past experiences with polkis having square profiles, further tests were performed to determine a natural or synthetic origin. When viewed under crossed polarizers, all three polkis displayed a checkerboard strain pattern from the top and sub-parallel columnar patterns from the sides. Infrared spectra confirmed all three specimens as type IIa; DiamondView imaging displayed orange fluorescence, but no distinct growth patterns could be resolved. No phosphorescence was detected in any of the samples. Such growth patterns (under crossed polarizers) and fluorescence have been observed previously in CVD-grown synthetic diamonds by this author, as well as reported in the literature (e.g., P.M. Martineau et al., "Identification of synthetic diamond grown using chemical vapor deposition (CVD)," Spring 2004 *G&G*, pp. 2–25). Fur-

thermore, photoluminescence spectra using 532 nm laser excitation revealed a distinct silicon vacancy–related peak at ~737 nm, even at room temperature (figure 24). This feature is widely used by gemological laboratories to identify synthetic diamonds (both CVD- and HPHT-grown).

In the past we have seen numerous examples of polki-cut diamonds with glass filling, as well as many CVD synthetic diamonds fashioned as polkis. This was the first time we had encountered glass-filled CVD synthetic diamond polkis, though their market penetration is unknown. Although glass filling is not challenging to identify, encountering it in synthetic diamonds could lead to a misidentification as natural, especially among the trade. Since diamond polkis are usually fashioned from flat rough or chips derived during cutting larger crystals, they often

Figure 23. Glass filling in the three polkis from figure 22 was indicated by color flashes along cleavages and fissures (left and right). Also note multiple parallel incipient and intersecting cleavage planes in the left image. Photomicrographs by Gagan Choudhary; fields of view 6.35 mm (left) and 5.08 mm (right).
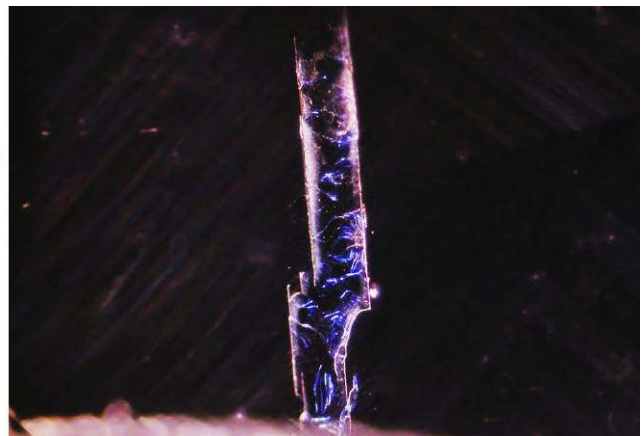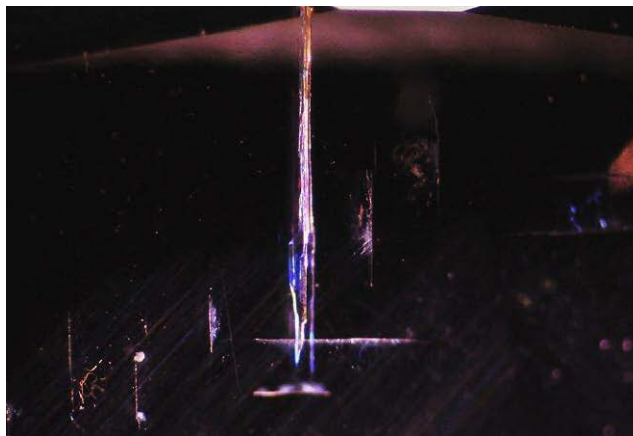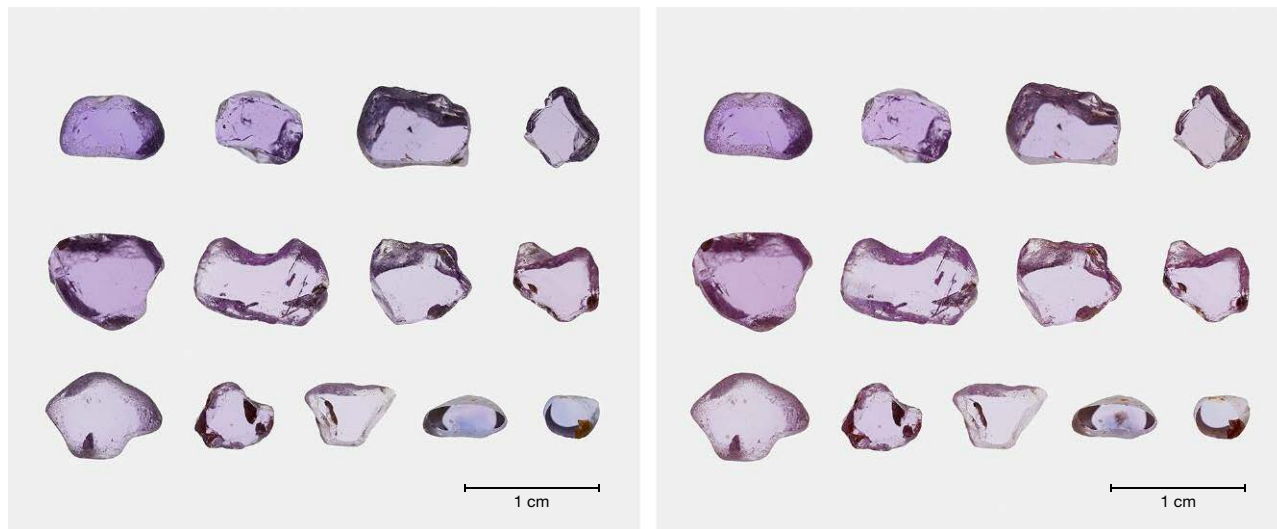
Figure 25. Color-calibrated photos of samples before (left) and after (right) heat treatment in air at 800°C for 160 minutes. Photos by Sasithorn Engniwat.

display triangular or irregular profiles, while the polkis described here had a square profile. In view of this, square-shaped polkis offer the best yield for crystals with square profiles, such as natural cubic crystal or synthetic diamond crystals grown by the CVD process, which display a square and tabular habit. Therefore, this feature is quite useful in raising doubts, especially when mixed in parcels of polki-cut natural diamond.

Gagan Choudhary (gagan@gjepcindia.com)
Gem Testing Laboratory (GJEPC), Jaipur, India

TREATMENTS

The effect of low-temperature heat treatment on pink sapphire. GIA has been studying low-temperature heat treatment on sapphires and rubies for the last five years. This report presents preliminary results of low-temperature heat treatment on pink sapphires, a procedure commonly used to reduce blue color components or zones. In this study, we selected 11 samples from Ilakaka, Madagascar, and one sample from Ratnapura, Sri Lanka, that were suitable for heat experiments—in other words, samples showing a 3309 cm^{-1} peak in FTIR with an absorption coefficient intensity of at least 0.04 cm^{-1} before heat treatment and fewer inclusions or fractures. From previous studies (S. Saeseaw et al., "Update on 'low-temperature' heat treatment of Mozambican ruby: A focus on inclusions and FTIR spectroscopy," GIA Research & News, April 30, 2018), we know that when the 3309 cm^{-1} peak is high enough, the 3309 series will develop after heat treatment. While the samples' bodycolor was predominantly pink, they all had a blue or purple modifier, as seen in figure 25 (left). Their

fluorescence under UV radiation was pink, with a stronger reaction in long-wave UV than short-wave. The sapphires from Madagascar contained abundant zircon (both as single crystals and clusters), stringers of particles, short needles, growth tubes, and other minerals such as monazite. The Sri Lankan stones revealed short and long needles, fingerprints, and some single zircon crystals with tension halos.

In this experiment, the samples were heated in air at 800°C for 160 minutes. These are the minimal heating conditions for significantly reducing blue color in Mozambique rubies (Saeseaw et al., 2018). After heating, the blue component was reduced and the samples were a purer pink (figure 25, right). Their fluorescence reactions remained the same, and no chalky fluorescence was observed under short-wave UV. Most of the zircon inclusions remained unaltered, but in a few cases some small discoid fractures developed. Some of the other crystals showed tension fractures, but we noticed that only some of the mica or monazite crystals were affected by low-temperature treatment. Thus, not every stone will show clear signs of heat treatment, especially when heated only at low temperature. As reported previously, advanced techniques such as FTIR are useful in detecting heat treatment, and we applied it to these samples.

Before heating, all 12 samples exhibited a single peak at 3309 cm^{-1}. After heat treatment, they showed a decreased 3309 cm^{-1} peak, while eight Madagascan and one Sri Lankan sample had developed a peak at 3232 cm^{-1}. No 3185 cm^{-1} peak was detected in this experiment (see figure 26). The intensity of the peaks at 3309 and 3232 cm^{-1} was quite low after heat treatment; maximum intensity was only about 0.04 and 0.01 cm^{-1}, respectively. In addition, we collected FTIR spectra on 120 unheated pink sapphires
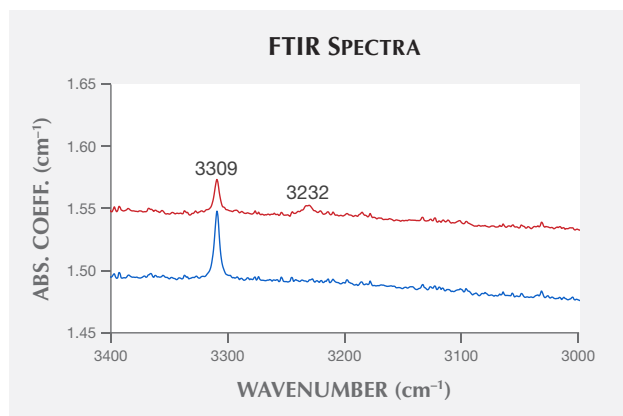
Figure 26. Comparison of FTIR spectra before (blue) and after (red) heat treatment on an unoriented pink sapphire from Madagascar.

from Madagascar and 80 samples from Sri Lanka, and no 3232 cm^{-1} peak was detected. We concluded that the 3232 cm^{-1} peak is only found in heated pink sapphires.

Sudarat Saeseaw and Charuwan Khowpong
GIA, Bangkok

RESPONSIBLE PRACTICES

Tagua nut as a sustainable botanical alternative for ivory. Award-winning haute couture jewelry designer Alexandra Mor considers sustainability a way of life. When designing her one-of-a-kind pieces, she is mindful of her client's lifestyle and interests while also thinking of the environment and of the culture and well-being of the artisans who bring each object to completion. It is in this spirit that she created the Tagua Collection, which uses the endosperm of the ivory palm tree—also known as the tagua nut or tagua seed—as an elephant ivory substitute. Now she is expanding into 3D printing using tagua nut specimens.

Mor, who believes that "designers are the new activists," is not new to ethical or sustainable jewelry design. In 2013, she created a ring (later modeled by actress Mila Kunis) using ethically sourced emeralds, the same year she won the Fashion Group International Rising Star Award. But Mor wished to create a more meaningful, spiritual, and eco-conscious practice of her own. Concerned about the plight of elephants and the continued use of ivory in jewelry, she was inspired to use the tagua nut as a botanical alternative. Mor, who was influenced by Balinese philosophy, chose to ethically source the tagua nuts from Ecuador and Colombia and create the collection in Bali. She worked for 10 months with carvers and master goldsmiths to create the pieces, which are rich in local cultural motifs and Buddhist symbolism. Balinese designs found in this collection include the vines, leaves, and tendrils seen in the gold work of the tagua seed, wood, and diamond earrings (figure 27); these are often seen on the island's temples. The *kay-*

Figure 27. These teardrop earrings show the kayonan, or tree of life, carved into the tagua nut and the lotus flower in sawo wood. Two brilliant-cut diamonds totaling 0.11 carats are at the center of the earrings. The gold work shows designs usually seen on Balinese temples. Photo by Russell Starr, courtesy of Alexandra Mor.

onan, or tree of life, motif is carved into the tagua nut sections of the earrings in figure 28.

Figure 28. These hoop earrings measure 57 × 42 mm, and once again show the kayonan *motif carved into the tagua seed surface. The areng ebony wood rim shows off the tagua's color. The earrings are set on 22K gold. Photo by Russell Starr, courtesy of Alexandra Mor.*

Figure 29. This one-of-a-kind ring is part of a collaboration between Mor and Colombia's Muzo emerald mine. The ethically sourced emerald beads, weighing a total of 18.15 carats, are set with a 16.80 ct wild tagua seed bead. The 1.15 carats of diamond melee are in platinum set on 18K yellow gold. Photo by Russell Starr, courtesy of Alexandra Mor.

The Tagua Collection has been well received among collectors and in the trade. The introduction of a new and sustainable fine jewelry material, at a time when clients seek out such goods, has been an inspiration to others, and Mor was named *Town & Country*'s Fine Jewelry Innovator of the Year for 2018. Since 2016 she has directed *Vogue Italia*'s The Protagonist at Christie's New York, a competition in which 14 designers use sustainable materials such as reclaimed gold and wood, vegetable leather, and responsibly mined gemstones alongside the tagua nut. Mor's work has also drawn attention outside the industry, allowing opportunities to expand her work. At the 2018 Gem & Jewellery Export Promotion Council (GJEPC) meeting in Mumbai, she met Kamlesh Parekh of Imaginarium, India's largest 3D printing company. After touring their facilities with Parekh, Mor believed she had found a way to overcome the small size of the tagua seed, a major limitation. She gave Parekh three seeds to test, and Imaginarium has produced the first 3D-printed tagua nut. Such production will allow for larger, more plentiful tagua pieces in the future.

Mor's next collections will continue to use tagua seeds, as well as sustainably sourced precious metals and conflict-free diamonds, and she will continue to collaborate with Colombia's Muzo mine due to their social and environmental commitment (figure 29). She supports Space for Giants,

a conservation organization dedicated to protecting elephant habitats. She has also launched the Tagua Foundation, which is dedicated to inspiring young designers and leaders, as well as students of all ages, to create sustainable jewelry.

Mor explained, "As designers, we have a responsibility to what materials we are using, and as collectors of fine jewelry, we have a voice and can make a difference in how we purchase. I have decided to use my voice to lead and inspire the fine jewelry industry to take the necessary steps to care for our planet and its people through grace and education. It doesn't matter what we choose to do, what matters is that what we choose will make a difference."

Jennifer-Lynn Archuleta
GIA, Carlsbad

ANNOUNCEMENT

Nathan Renfro wins Royal Microscopical Society award. GIA Carlsbad manager of colored stones identification and *G&G* regular contributor Nathan Renfro took second place in the Light Microscopy–Physical Sciences division of the Royal Microscopical Society's biennial Scientific Imaging Competition. The award-winning image (figure 30) shows a rutile star in smoky quartz.

ERRATUM

The Spring 2019 lab note on a large faceted gahnospinel (pp. 92–93) referred to the specific gravity of spinel as 3.06. The correct SG is 3.60. We thank reader Tinh Nguyen Xuan for noticing this error.

Figure 30. A six-rayed star of golden rutile needles radiates from a black ilmenite core beautifully preserved in smoky quartz. Photomicrograph by Nathan Renfro; field of view 18 mm. Stone courtesy of the John Koivula Inclusion Collection.
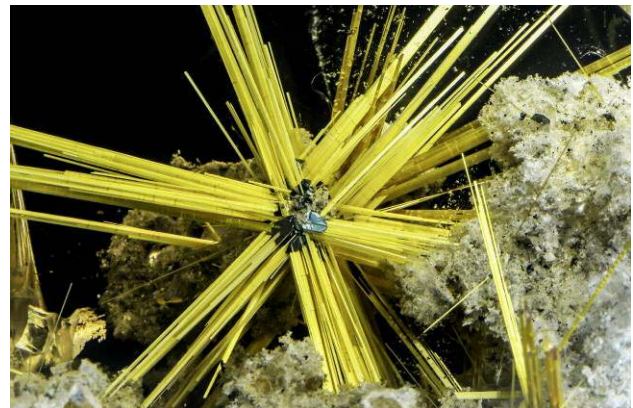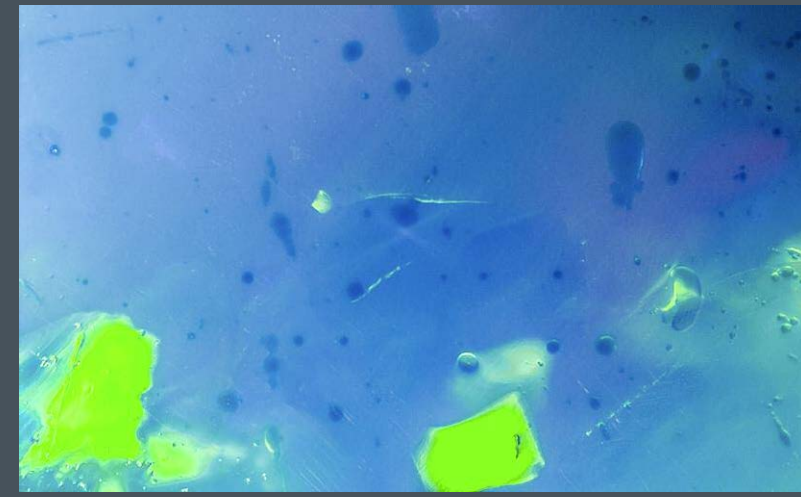
# MICRO-FEATURES OF OPAL

Treated

Some opals are prone to crazing or cracking, which can be hidden by filling the cracks with oil or resin. Trapped bubbles in the cracks of this opal reveal the treatment. Field of view 2.15 mm.


Hydrophane opal from Wollo, Ethiopia, is commonly dyed. Spotty color concentrations near the surface are often present. Field of view 2.34 mm.

This Honduran opal formed in a natural porous volcanic rock that has been infilled with precious opal by a secondary process. Although the black bodycolor is natural, this stone is polymer impregnated to fill in surface voids and pits. Field of view 2.79 mm.
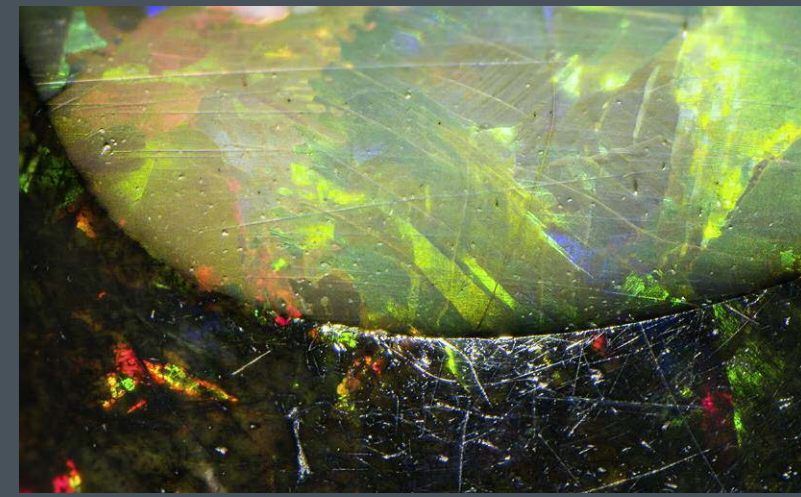
This porous white opal from Jalisco, Mexico, shows a dark rind of brown to black color induced by exposure to carbon-rich smoke. One end of the stone has been polished away to show the shallow color. Field of view 5.74 mm.
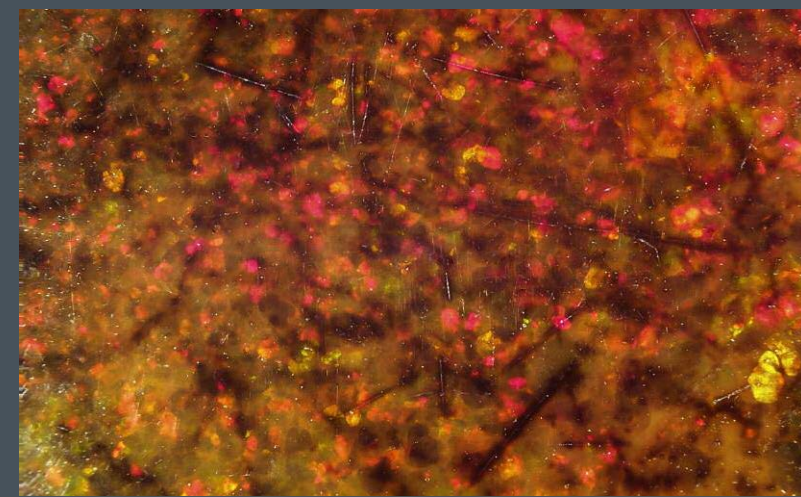
Smoke treatment in Ethiopian hydrophane opal is readily detectable by the pronounced color concentrations left along pits and scratches. Field of view 9.00 mm.

Natural
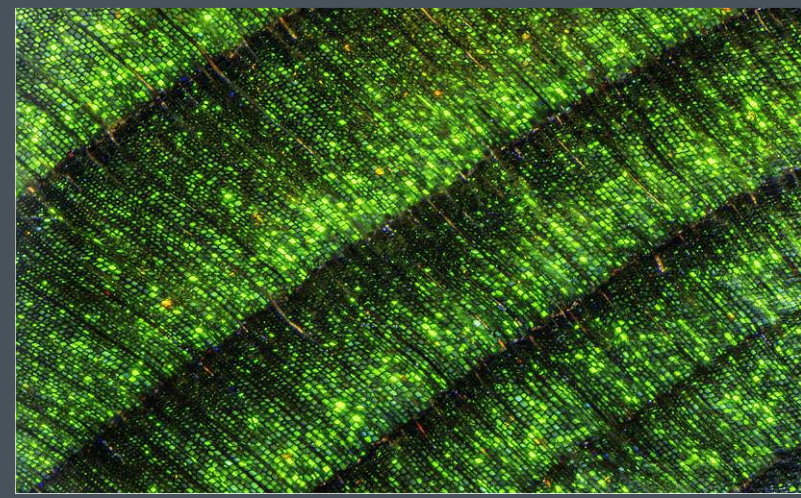
Viewed perpendicular to the grain of this opalized wood from Virgin Valley, Nevada, the cellular structure of the wood shows up as distinct linear strings of play-of-color spots. Field of view 4.87 mm.
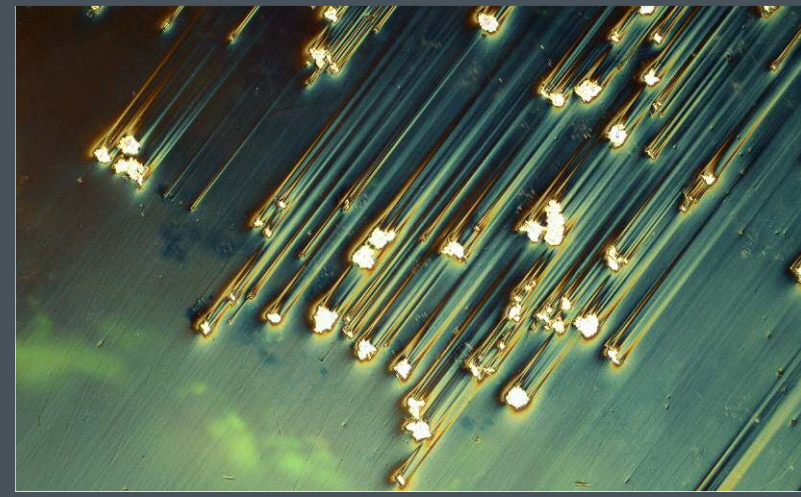
This Australian opal is host to a multitude of surface-breaking pyrite crystals. Examined using differential interference contrast, drag lines are clearly resolved. Field of view 1.24 mm.
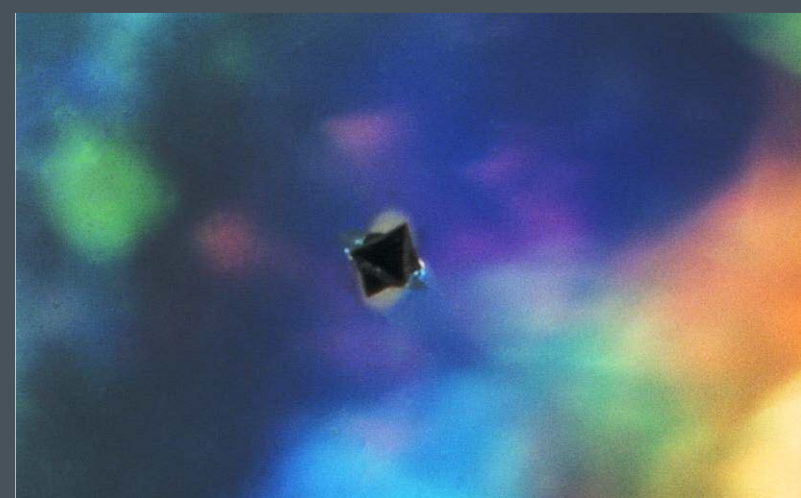
Modified octahedrons of the iron sulfide mineral pyrite are common in opal from Wollo, Ethiopia. Field of view 0.86 mm.
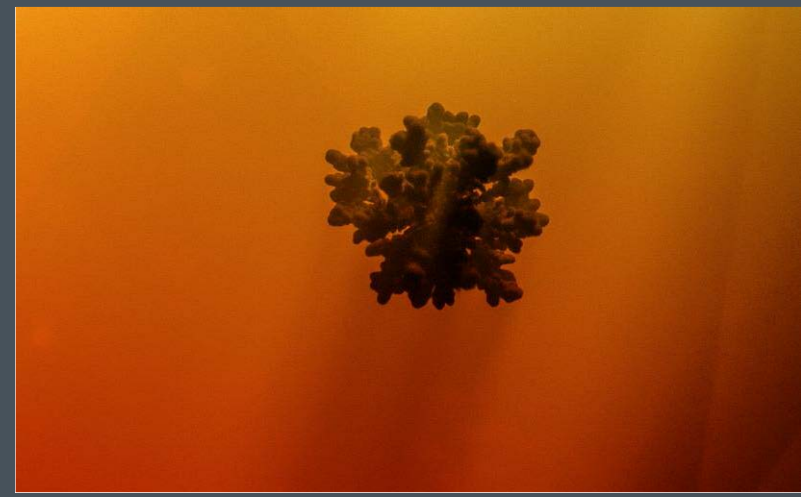
This orange fire opal from Oregon contains a free-floating dendritic mass of iron oxide (hematite). Field of view 4.36 mm.

This opal from Yita, Ethiopia, contains numerous tendrils of kaolinite and pyrite. Field of view 2.46 mm.
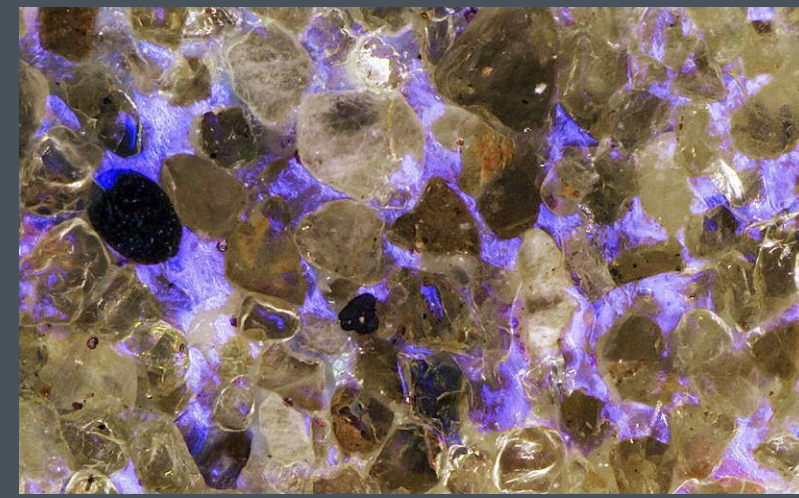

Louisiana sandstone opal is composed of quartz sand grains cemented together with precious opal. Field of view 5.76 mm.
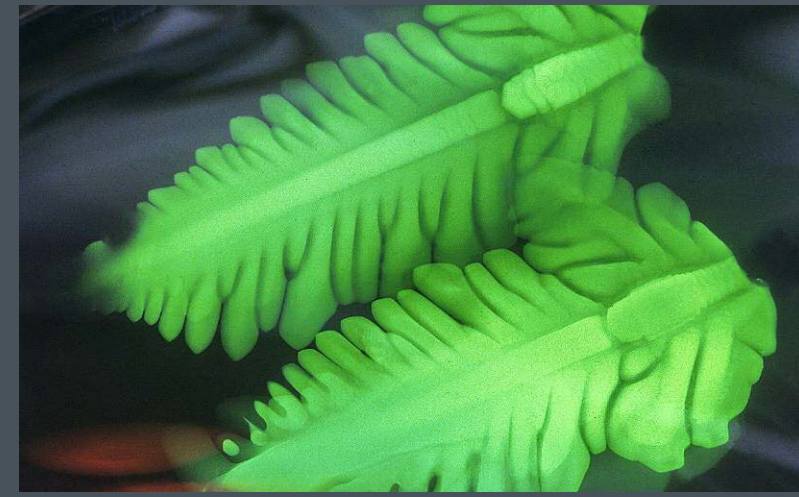

This opal from Virgin Valley, Nevada, contains a pair of fern-shaped holographic play-of-color patterns. Field of view 13.50 mm.
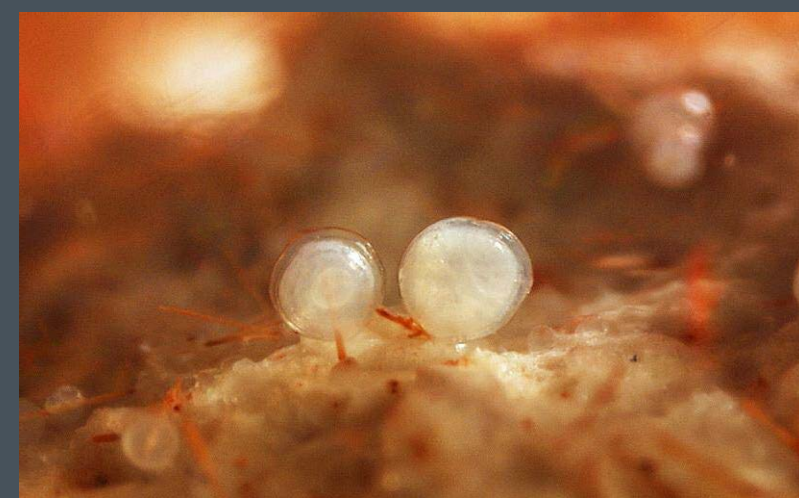

Mexican opals are host to a wide variety of interesting inclusions, such as these chalcedony spherules perched on amphibole needles. Field of view 2.15 mm.
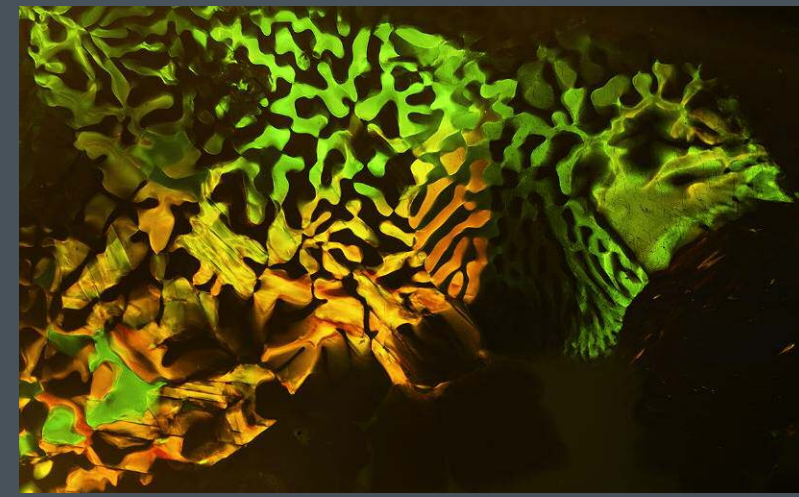
Ethiopian opals often show interesting patterns in their play-of-color, and this dendritic example is no exception. Field of view 5.78 mm.
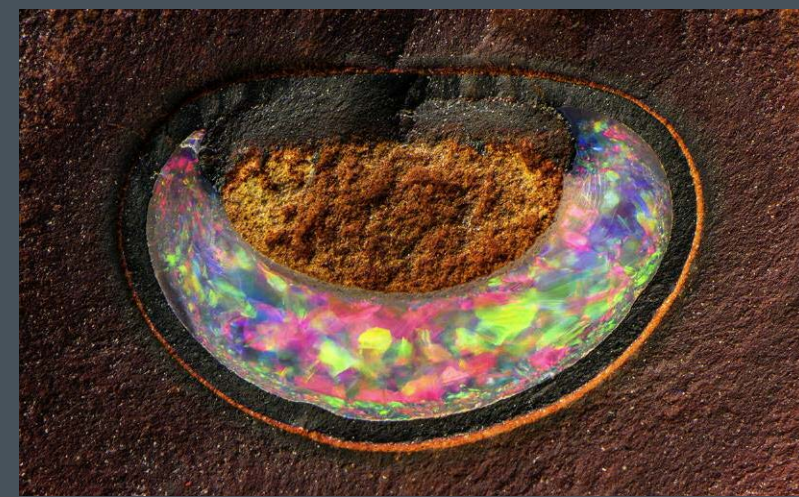

This Yowah Nut opal contains a crescent-moon-shaped pocket of precious opal in ironstone matrix. Field of view 12.00 mm.
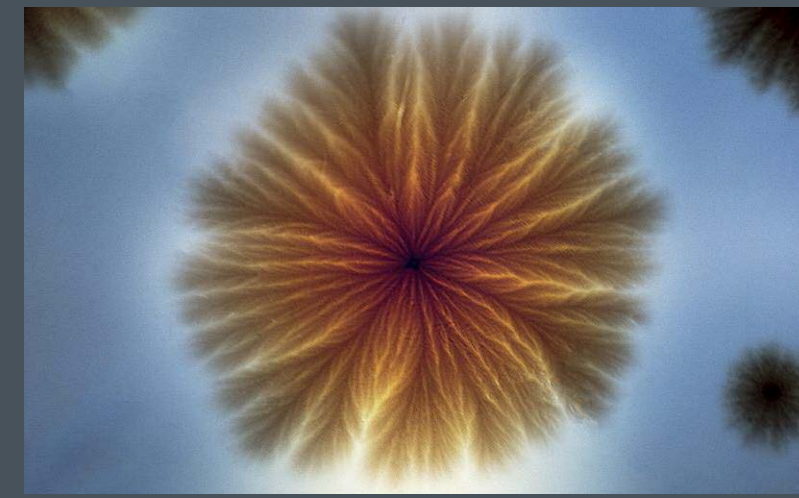

This manganese oxide "flower" lies just under the surface of an opal from Wollo, Ethiopia. Field of view 2.47 mm.

This green opal from Tanzania, colored by nickel, contains fragments of matrix trapped within the stone. The opal resembles an aerial view of a coastline. Field of view 15.16 mm.
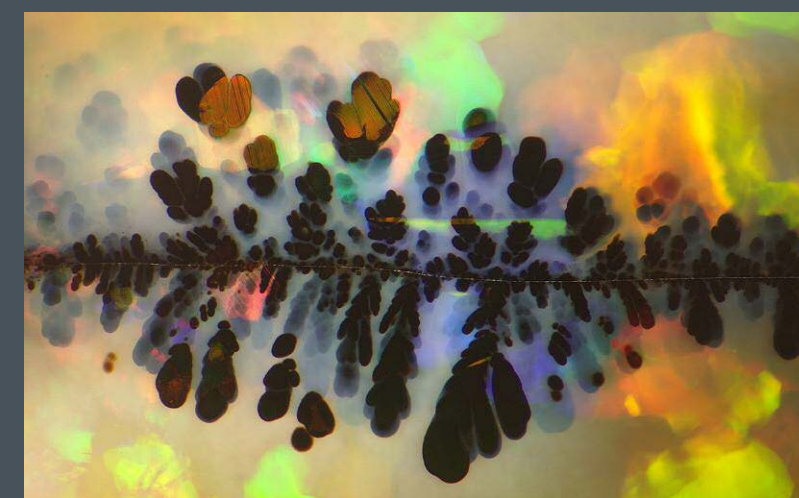

Black manganese oxide plumes stand out in sharp contrast in this Australian opal. Field of view 5.85 mm.
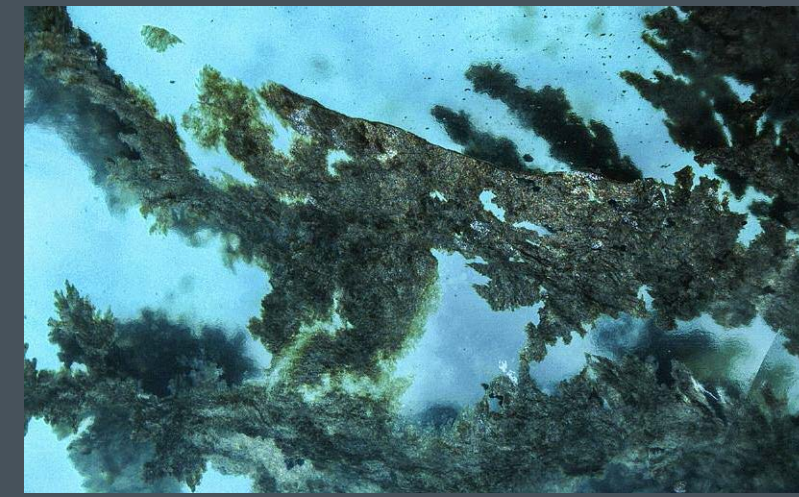

The Acari and Lily mines, both located in the Peruvian Andes, produce blue opal that is colored by copper. This sample also contains numerous dark dendritic inclusions of manganese oxide. Field of view 5.78 mm.

Sold in the trade as "Morado Opal" or "Opal Royale," this common opal from Mexico is naturally colored by purple fluorite inclusions. Field of view 3.91 mm.
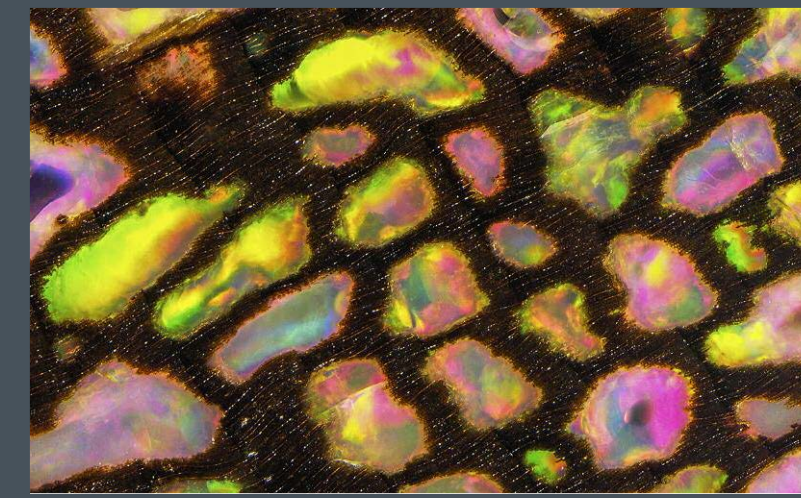

This rare conk opal from Virgin Valley, Nevada, results when diseased wood containing large pores is filled with precious opal. Field of view 11.52 mm.
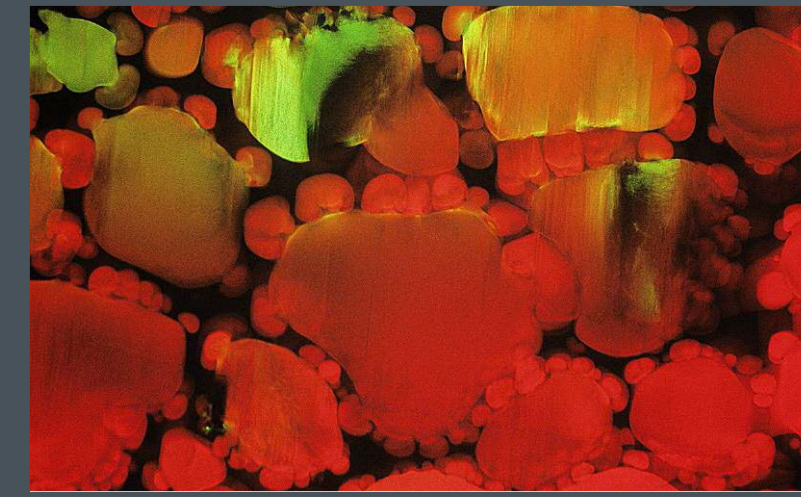

The cellular structures in this Ethiopian opal show evidence of pressurization causing the cells to rupture and spill their contents into the veins of non-phenomenal secondarily deposited common opal. Field of view 6.11 mm.

Inclusions of wood are sometimes present in opals from Virgin Valley, Nevada. Field of view 5.63 mm.
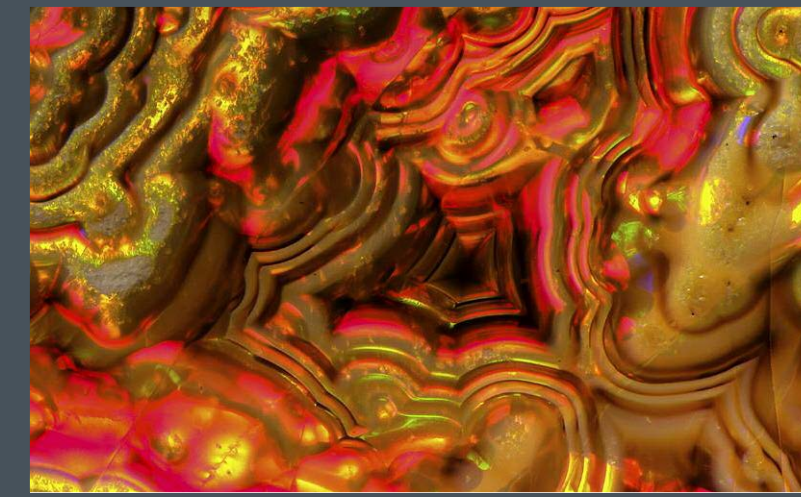
This opal from the Shewa deposit in Ethiopia shows a peculiar banding pattern that resembles the fortification patterns seen in agates. Field of view 3.89 mm.
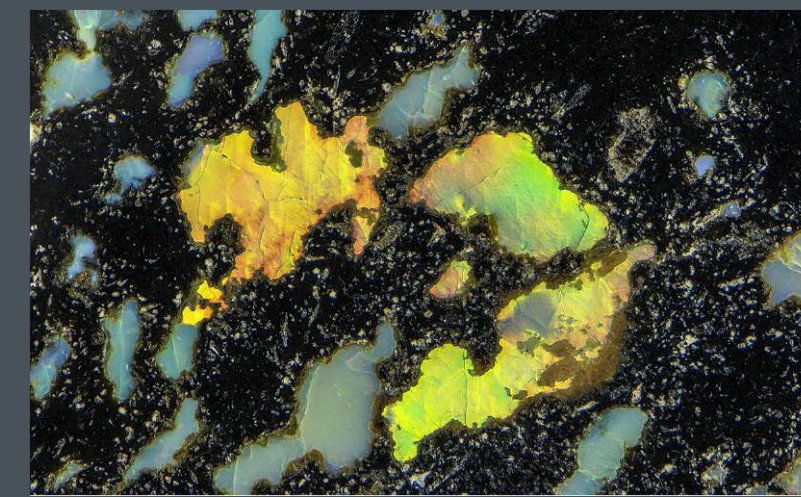

Vesicles in this black basalt rock from Hidalgo, Mexico, have been filled with precious opal. This material is known as "Leopard Opal." Field of view 5.71 mm.
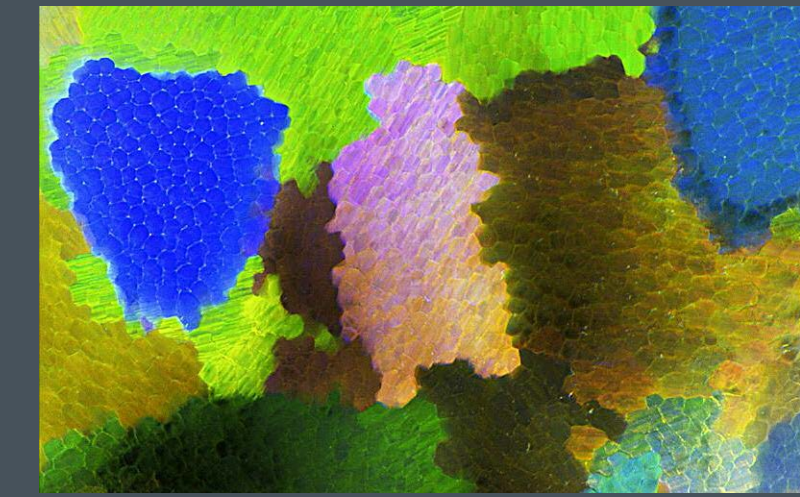
Synthetic and Imitation

Slocum Stone opal imitation glass was manufactured by John Slocum of Michigan in the early 1970s. Thin layers of metallic film fragments suspended in the glass matrix are responsible for the interference colors observed. Field of view 5.75 mm.
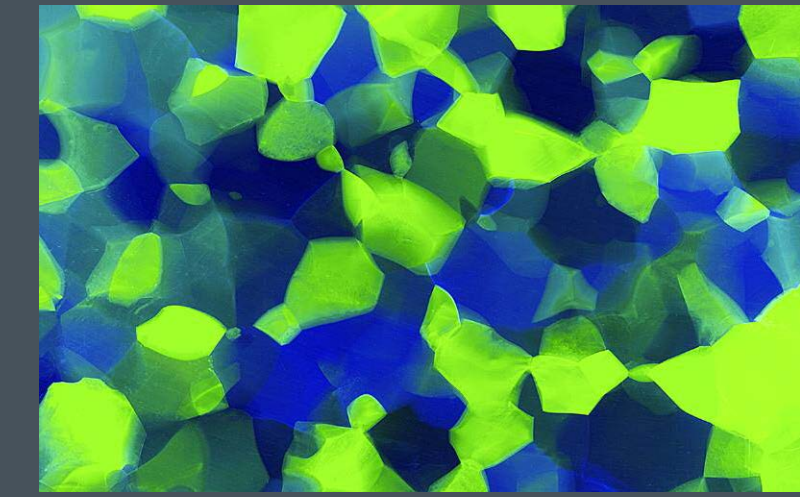

Randomly oriented polygonal play-of-color is distributed throughout this plastic imitation opal, which is composed of approximately 80% plastic and 20% silica. Field of view 14.40 mm.
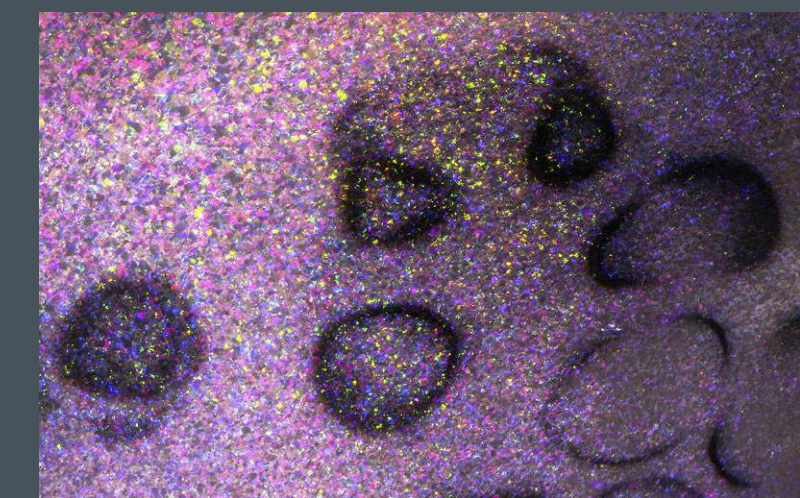
Manufactured by Almaztechnocrystal in Moscow under Professor M.I. Samoilovich, this synthetic opal shows a variety of patterns in its play-of-color, including the mottled black and dark brown growth zones seen here. Field of view 8.05 mm.

A snakeskin or "chicken-wire" cellular pattern is diagnostic for many types of synthetic opal, including this material manufactured by Gilson. Field of view 2.88 mm.
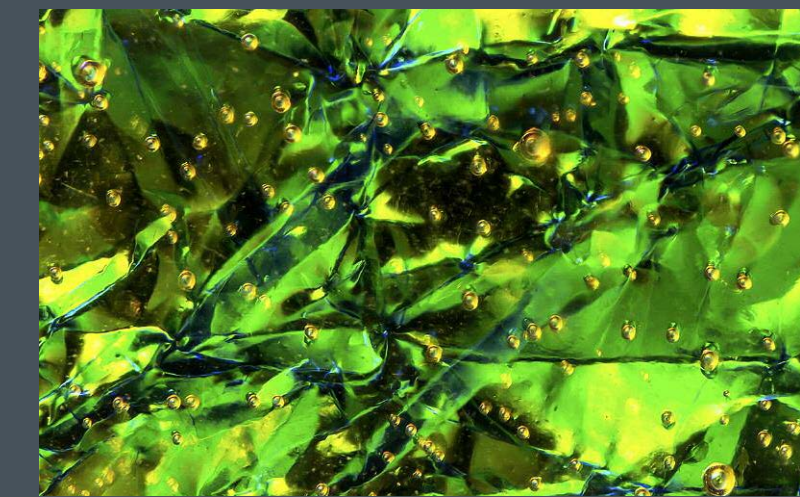
"Opalus" is a plastic imitation opal similar in appearance to Slocum Stone glass, as it also contains thin metallic foil responsible for thin-film interference colors. Numerous gas bubbles are also observable in this assembled opal imitation. Field of view 5.64 mm.

GIA